



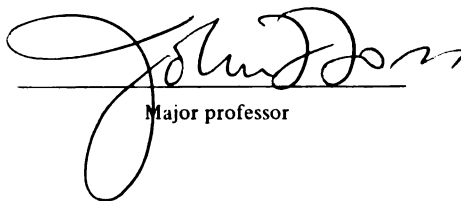
THESIS  
2  
2002

This is to certify that the  
thesis entitled  
**Velocity and Vorticity Measurements in an  
Atmospheric Boundary Layer**

presented by  
**Matthew C. Maher**

has been accepted towards fulfillment  
of the requirements for

MS degree in Mechanical Engineering

  
Major professor

Date August 19, 2002



**PLACE IN RETURN BOX** to remove this checkout from your record.  
**TO AVOID FINES** return on or before date due.  
**MAY BE RECALLED** with earlier due date if requested.

DATE DUE	DATE DUE	DATE DUE

VELOCITY AND VORTICITY MEASUREMENTS IN THE  
ATMOSPHERIC BOUNDARY LAYER

By

Matthew C. Maher

A THESIS

Submitted to

Michigan State University

in partial fulfillment of the requirements

for the degree of

MASTER OF SCIENCE

Department of Mechanical Engineering

2002



# ABSTRACT

## VELOCITY AND VORTICITY MEASUREMENTS IN THE ATMOSPHERIC BOUNDARY LAYER

By

Matthew C. Maher

Velocity and vorticity time series were measured in the near wall region of an atmospheric boundary layer. The measurements were acquired at the SLTEST site located in western Utah under thermally unstable, thermally stable, and thermally neutral ambient conditions. The surface was nearly flat and free of vegetation with a small scale surface roughness of approximately 2mm. The measurements were acquired at locations of 20cm and 40cm from the wall ( $y^+ = 3800$  and  $y^+ = 10,300$  respectively). The Reynolds number based on momentum thickness was approximately  $Re_\theta \approx 5 \times 10^6$  with a boundary layer thickness of approximately 200m.

The vorticity measurements indicated an extremely long correlation time of the near wall vorticity field. For example, the first zero of the autocorrelation of the spanwise vorticity component was found to be as large as 40m. The first zero of the wall normal vorticity autocorrelation was found to be as large as 220m. The gradient of the Reynolds shear stress was also investigated by measurement of the two contributing velocity-vorticity products ( $\overline{v'\omega_z'}$  and  $\overline{w'\omega_y'}$ ). The  $\overline{w'\omega_y'}$  product appeared to produce the dominant contribution to this gradient. Coherence spectral observations show that the relatively high wavenumber components produce the relatively large correlation ( $\approx 0.2$ ) between the lateral velocity fluctuations and the wall normal vorticity fluctuations.

## **ACKNOWLEDGEMENTS**

I would like to thank my advisor, John Foss, for his support and assistance over the past few years. My experiences at the Turbulent Shear Flows Laboratory are something I will never forget. The assistance of my colleagues, who have contributed their time and efforts, is greatly appreciated. I would like to thank Scott Morris, Al Lawrenz, Rich Prevost, Mike Dusel, Doug Neal and Scott Treat for their individual efforts.

I would like to thank my committee members, Ahmed Naguib and Charles Petty, for their contributions. The financial assistance of the Office of Naval Research (ONR) is also greatly appreciated.

Lastly, I would like to thank my family, who have been patient and supportive throughout this endeavor.

# TABLE OF CONTENTS

<b>List of Tables.....</b>	<b>vii</b>
<b>List of Figures.....</b>	<b>viii</b>
<b>Nomenclature .....</b>	<b>xviii</b>
<b>1.0 Introduction.....</b>	<b>1</b>
1.1 Boundary Layer Overview.....	3
1.2 Literature review .....	5
<b>2.0 Experimental Facility and Conditions .....</b>	<b>11</b>
2.1 Test Site Overview .....	11
2.2 Test Site Capabilities.....	12
2.2.1 Wind Monitoring.....	12
2.2.2 Thermal Effects.....	13
2.2.3 Shear Stress Measurements.....	16
<b>3.0 Experimental Equipment .....</b>	<b>21</b>
3.1 Mobile Data Cart .....	22
3.1.1 Cooling System.....	22
3.1.2 On-board Equipment.....	23
3.2 Calibration Facility .....	25
3.3 Three-Cup Anemometer .....	27

3.4	Wind Vane.....	28
3.5	Thermistor.....	28
<b>4.0</b>	<b>Hot Wire Techniques .....</b>	<b>37</b>
4.1	Single wire calibration and uncertainty .....	37
4.2	X-wire calibration, processing and uncertainty .....	41
4.2.1	X-wire processing algorithm .....	42
4.2.2	X-wire uncertainties.....	43
4.3	Vorticity Probe .....	44
4.3.1	Vorticity Algorithm.....	46
4.3.2	Vorticity probe uncertainties.....	49
<b>5.0</b>	<b>Results and Discussion.....</b>	<b>60</b>
5.1	Daily Specifics.....	60
5.1.1	18-July, 2001 .....	61
5.1.2	19-July, 2001 .....	63
5.1.3	25-July, 2001 .....	65
5.2	Mean flow statistics .....	67
5.2.1	Taylor microscale.....	69
5.2.2	Dissipation Measurement .....	70
5.2.3	Flow length and velocity scales .....	74
5.3	Spectral Properties .....	77
5.3.1	Spectral representation of the velocity field .....	77
5.3.1.1	u-component spectra.....	81

5.3.1.2 v-Component Spectra .....	83
5.3.1.3 w-Component Spectra.....	84
5.3.2 Spectral representation of the vorticity field.....	84
5.3.2.1 $\langle \omega_z \rangle$ Spectra .....	87
5.3.2.2 $\langle \omega_y \rangle$ spectra.....	89
5.3.3 Velocity-vorticity products .....	90
5.3.3.1 u'v' product .....	92
5.3.3.2 u'w' product .....	94
5.3.3.3 v' $\langle \omega_z \rangle$ product .....	95
5.3.3.4 w' $\langle \omega_y \rangle$ product .....	97
5.4 Vorticity Probability Density Functions.....	99
<b>6.0 Conclusions .....</b>	<b>149</b>
<b>Appendix A: Pre-Post Comparison .....</b>	<b>154</b>
<b>Appendix B: Combined Calibration Plots.....</b>	<b>162</b>
<b>References .....</b>	<b>172</b>

## LIST OF TABLES

Table 5.1 Data Set Properties .....	101
Table 5.2 Mean Dimensional Flow Parameters .....	108
Table 5.3 Mean Flow Properties .....	109
Table 5.4 Dissipation Estimates .....	109
Table 5.5 Normalized Flow Parameters .....	110
Table 5.6 Taylor Microscale Parameters .....	111
Table 5.7 Dimensional Flow Statistics .....	127
Table 5.8 Normalized Flow Statistics .....	128
Table 5.9 $\omega_z$ PDF Statistics .....	148
Table 5.10 $\omega_y$ PDF Statistics .....	148

## LIST OF FIGURES

Figure 1.1 The breakdown of a turbulent boundary layer [24].	8
Figure 1.2 Scaling collapse on the inner region of a turbulent boundary layer [24].	9
Figure 1.3 The Reynolds number dependence on the size of the overlap region [23].	10
Figure 2.1 Topographic map of the Dugway area.	18
Figure 2.2 Sensing capabilities of the SLTEST site [30].	19
Figure 2.3 Typical boundary layer profile at the SLTEST site [30].	19
Figure 2.4 A 2.4 meter drag plate was used to gather accurate values for the wall shear stress [30].	20
Figure 3.1 Schematic of Mobile Data Cart.	30
Figure 3.2 Interior view of Mobile Data Cart.	31
Figure 3.3 The Data Cart's portable calibration unit.	32
Figure 3.4 Top view of the calibration facility showing the flow conditioning.	32
Figure 3.5 Wiring diagram for the calibration unit.	33
Figure 3.6 Total pressure vs. the static tap reading for the calibration unit.	33
Figure 3.7 Three cup anemometer calibration	34
Figure 3.8 Tripod used to mount the three cup anemometer, wind vane and hot wire probes.	35

Figure 3.9 Thermistor re-calibration due to large ambient temperatures. ....	36
Figure 4.1 Geometry of spanwise vorticity probe. ....	51
Figure 4.2 Perspective view of spanwise vorticity probe. ....	51
Figure 4.3 Geometry of a single hot-wire probe.....	52
Figure 4.4 Sample calibration and fit.....	52
Figure 4.5 Normalized histogram of observed velocities from 25-July, 2001. ....	53
Figure 4.6 Example drift determination comparison taken on 19-July. ....	53
Figure 4.7 Pre-calibration data, post-calibration data, and the combined trend-line for 19-July. ....	54
Figure 4.8 Geometry of the X-wire probe. ....	54
Figure 4.9 Sample data demonstrating the angle locating algorithm for X-wire processing. ....	55
Figure 4.10 Example drift determination comparison for an X-wire taken on 19-July.....	55
Figure 4.11 Mean vertical angle measured over the evening of 18-July, 2001.....	56
Figure 4.12 Schematic of the micro-circulation domain used in the vorticity algorithm..	56
Figure 4.13 Velocity of each straight wire on the Mitchel Probe as it was traversed through the shear layer. ....	57
Figure 4.14 Collapse of shear layer traverse data used to compute ( $\Delta y$ ). ....	57
Figure 4.15 Vorticity probe and processing algorithm verification in a free stream of the	



calibration unit. ....	58
Figure 4.16 Vorticity probe and processing algorithm verification in a free stream. ....	58
Figure 4.17 Sample vorticity time series from 25-July, 2001. ....	59
Figure 5.1 Mean wind speed for 18-July, 2001. ....	102
Figure 5.2 Mean wind direction for 18-July, 2001. ....	102
Figure 5.3 Thermal stability parameter for 18-July, 2001. ....	103
Figure 5.4 Friction velocity as a function of time for 18-July, 2001. ....	103
Figure 5.5 Mean wind speed for 19-July, 2001. ....	104
Figure 5.6 Mean wind direction for 19-July, 2001. ....	104
Figure 5.7 Thermal stability parameter for 19-July, 2001. ....	105
Figure 5.8 Friction velocity as a function of time for 19-July, 2001. ....	105
Figure 5.9 Mean wind speed for 25-July, 2001. ....	106
Figure 5.10 Mean wind direction for 25-July, 2001. ....	106
Figure 5.11 Thermal stability parameter for 25-July, 2001. ....	107
Figure 5.12 Friction velocity as a function of time for 25-July, 2001. ....	107
Figure 5.13 Normalized autospectral density of the u-velocity fluctuation (25-July). ....	112
Figure 5.14 Compensated autospectral density of the u-velocity fluctuation (25-July). .	112
Figure 5.15 Normalized autospectral density of the u-velocity fluctuation (18-July). ....	113
Figure 5.16 Compensated autospectral density of the u-velocity fluctuation (18-July). .	113

Figure 5.17 Normalized autospectral density of the u-velocity fluctuation (19-July).....	114
Figure 5.18 Compensated autospectral density of the u-velocity fluctuation (19-July)..	114
Figure 5.19 Normalized autospectral density of the v-velocity fluctuation (25-July).....	115
Figure 5.20 Compensated autospectral density of the v-velocity fluctuation (25-July)..	115
Figure 5.21 Normalized autospectral density of the v-velocity fluctuation (18-July).....	116
Figure 5.22 Compensated autospectral density of the v-velocity fluctuation (18-July)..	116
Figure 5.23 Normalized autospectral density of the v-velocity fluctuation (19-July).....	117
Figure 5.24 Compensated autospectral density of the v-velocity fluctuation (19-July)..	117
Figure 5.25 Normalized autospectral density of the w-velocity fluctuation (18-July)....	118
Figure 5.26 Compensated autospectral density of the w-velocity fluctuation (18-July).	118
Figure 5.27 Normalized autospectral density of the w-velocity fluctuation (19-July)....	119
Figure 5.28 Compensated autospectral density of the w-velocity fluctuation (19-July).	119
Figure 5.29 Normalized autospectral density of the $\langle \omega_z \rangle$ vorticity (25-July).....	120
Figure 5.30 Compensated autospectral density of the $\langle \omega_z \rangle$ vorticity (25-July).....	120
Figure 5.31 Normalized autospectral density of the $\langle \omega_z \rangle$ vorticity (18-July).....	121
Figure 5.32 Compensated autospectral density of the $\langle \omega_z \rangle$ vorticity (18-July).....	121
Figure 5.33 Normalized autospectral density of the $\langle \omega_z \rangle$ vorticity (19-July).....	122
Figure 5.34 Compensated autospectral density of the $\langle \omega_z \rangle$ vorticity (19-July).....	122
Figure 5.35 Autocorrelation of the $\langle \omega_z \rangle$ vorticity for each day.....	123

Figure 5.36 Autocorrelation of the $\langle \omega_x \rangle$ vorticity in semilog format. ....	123
Figure 5.37 Normalized autospectral density of the $\langle \omega_y \rangle$ vorticity (18-July). ....	124
Figure 5.38 Compensated autospectral density of the $\langle \omega_y \rangle$ vorticity (18-July).....	124
Figure 5.39 Normalized autospectral density of the $\langle \omega_y \rangle$ vorticity (19-July). ....	125
Figure 5.40 Compensated autospectral density of the $\langle \omega_y \rangle$ vorticity (19-July).....	125
Figure 5.41 Autocorrelation of the $\langle \omega_y \rangle$ vorticity for each day. ....	126
Figure 5.42 Autocorrelation of the $\langle \omega_y \rangle$ vorticity in semilog format. ....	126
Figure 5.43 Normalized autospectral density of the $u'v'$ product (25-July).....	129
Figure 5.44 Compensated autospectral density of the $u'v'$ product (25-July).....	129
Figure 5.45 Normalized autospectral density of the $u'v'$ product (18-July).....	130
Figure 5.46 Compensated autospectral density of the $u'v'$ product (18-July).....	130
Figure 5.47 Normalized autospectral density of the $u'v'$ product (19-July).....	131
Figure 5.48 Compensated autospectral density of the $u'v'$ product (19-July).....	131
Figure 5.49 Normalized co-spectral density of the $u'$ and $v'$ velocity components (25-July). ....	132
Figure 5.50 Normalized co-spectral density of the $u'$ and $v'$ velocity components (18-July). ....	132
Figure 5.51 Normalized co-spectral density of the $u'$ and $v'$ velocity components (19-July). ....	133

Figure 5.52 Coherence of the $u'$ and $v'$ velocity components for all three data sets. ....	133
Figure 5.53 Normalized autospectral density of the $u'w'$ product (18-July).....	134
Figure 5.54 Compensated autospectral density of the $u'w'$ product(18-July).....	134
Figure 5.55 Normalized autospectral density of the $u'w'$ product (19-July).....	135
Figure 5.56 Compensated autospectral density of the $u'w'$ product (19-July).....	135
Figure 5.57 Normalized co-spectral density of the $u'$ and $w'$ velocity components (18-July). ....	136
Figure 5.58 Normalized co-spectral density of the $u'$ and $w'$ velocity components (19-July). ....	136
Figure 5.59 Coherence of the $u'$ and $w'$ velocity components (18, 19-July).....	137
Figure 5.60 Normalized autospectral density of the $v'<\omega_z'>$ product (25-July).....	137
Figure 5.61 Compensated autospectral density of the $v'<\omega_z'>$ product (25-July).....	138
Figure 5.62 Normalized autospectral density of the $v'<\omega_z'>$ product (18-July).....	138
Figure 5.63 Compensated autospectral density of the $v'<\omega_z'>$ product (18-July).....	139
Figure 5.64 Normalized autospectral density of the $v'<\omega_z'>$ product (19-July).....	139
Figure 5.65 Compensated autospectral density of the $v'<\omega_z'>$ product (19-July).....	140
Figure 5.66 Normalized co-spectral density of $v'$ and $<\omega_z'>$ (25-July).....	140
Figure 5.67 Normalized co-spectral density of $v'$ and $<\omega_z'>$ (18-July).....	141
Figure 5.68 Normalized co-spectral density of $v'$ and $<\omega_z'>$ (19-July).....	141

Figure 5.69 Coherence of $v'$ and $\langle \omega_z' \rangle$ over all three evenings. ....	142
Figure 5.70 Normalized autospectral density of the $w'\langle \omega_y' \rangle$ product (18-July). ....	142
Figure 5.71 Compensated autospectral density of the $w'\langle \omega_y' \rangle$ product (18-July).....	143
Figure 5.72 Normalized autospectral density of the $w'\langle \omega_y' \rangle$ product (19-July). ....	143
Figure 5.73 Compensated autospectral density of the $w'\langle \omega_y' \rangle$ product (19-July).....	144
Figure 5.74 Normalized co-spectral density of $w'$ and $\langle \omega_y' \rangle$ (18-July).....	144
Figure 5.75 Normalized co-spectral density of $w'$ and $\langle \omega_y' \rangle$ (19-July).....	145
Figure 5.76 Coherence of $w'$ and $\langle \omega_y' \rangle$ for 18, 19-July.....	145
Figure 5.77 Compensated autospectral densities of the velocity-vorticity products for 18-July. ....	146
Figure 5.78 Compensated autospectral densities of the velocity-vorticity products for 19-July. ....	146
Figure 5.79 Compensated autospectral densities of the velocity-vorticity products for 25-July. ....	147
Figure 5.80 Normalized PDF of the $\langle \omega_z' \rangle$ vorticity for each day. ....	147
Figure 5.81 Normalized PDF of the $\langle \omega_y' \rangle$ vorticity for each day. ....	148
Figure A.1 Drift determination comparison taken on 18-July ( $\langle \omega_z' \rangle$ probe, first straight wire). ....	154
Figure A.2 Drift determination comparison taken on 18-July ( $\langle \omega_z' \rangle$ probe,	

second straight wire). .....	154
Figure A.3 Drift determination comparison taken on 18-July ( $\langle\omega_y\rangle$ probe, first straight wire). .....	155
Figure A.4 Drift determination comparison taken on 18-July ( $\langle\omega_y\rangle$ probe, second straight wire). .....	155
Figure A.5 Drift determination comparison taken on 19-July ( $\langle\omega_z\rangle$ probe, first straight wire). .....	156
Figure A.6 Drift determination comparison taken on 19-July ( $\langle\omega_z\rangle$ probe, second straight wire). .....	156
Figure A.7 Drift determination comparison taken on 19-July ( $\langle\omega_y\rangle$ probe, first straight wire). .....	157
Figure A.8 Drift determination comparison taken on 19-July ( $\langle\omega_y\rangle$ probe, second straight wire). .....	157
Figure A.9 Drift determination comparison taken on 25-July ( $\langle\omega_z\rangle$ probe, first straight wire). .....	158
Figure A.10 Drift determination comparison taken on 25-July ( $\langle\omega_z\rangle$ probe, second straight wire). .....	158
Figure A.11 X-wire drift determination comparison taken on 18-July ( $\langle\omega_z\rangle$ probe). ..	159
Figure A.12 X-wire drift determination comparison taken on 18-July ( $\langle\omega_y\rangle$ probe). ..	159

Figure A.13 X-wire drift determination comparison taken on 19-July ( $\langle\omega_z\rangle$ probe).	..160
Figure A.14 X-wire drift determination comparison taken on 19-July ( $\langle\omega_y\rangle$ probe).	..160
Figure A.15 X-wire drift determination comparison taken on 25-July ( $\langle\omega_z\rangle$ probe).	..161
Figure B.1 Combined calibration data for 18-July ( $\langle\omega_z\rangle$ probe, first straight wire).	....162
Figure B.2 Combined calibration data for 18-July ( $\langle\omega_z\rangle$ probe, second straight wire).	.....162
Figure B.3 Combined calibration data for 18-July ( $\langle\omega_z\rangle$ probe, first X-wire).	.....163
Figure B.4 Combined calibration data for 18-July ( $\langle\omega_z\rangle$ probe, second X-wire).	.....163
Figure B.5 Combined calibration data for 18-July ( $\langle\omega_y\rangle$ probe, first straight wire).	....164
Figure B.6 Combined calibration data for 18-July ( $\langle\omega_y\rangle$ probe, second straight wire).	.....164
Figure B.7 Combined calibration data for 18-July ( $\langle\omega_y\rangle$ probe, first X-wire).	.....165
Figure B.8 Combined calibration data for 18-July ( $\langle\omega_y\rangle$ probe, second X-wire).	.....165
Figure B.9 Combined calibration data for 19-July ( $\langle\omega_z\rangle$ probe, first straight wire).	....166
Figure B.10 Combined calibration data for 19-July ( $\langle\omega_z\rangle$ probe, second straight wire).	.....166
Figure B.11 Combined calibration data for 19-July ( $\langle\omega_z\rangle$ probe, first X-wire).	.....167
Figure B.12 Combined calibration data for 19-July ( $\langle\omega_z\rangle$ probe, second X-wire).	.....167
Figure B.13 Combined calibration data for 19-July ( $\langle\omega_y\rangle$ probe, first straight wire).	..168

Figure B.14 Combined calibration data for 19-July ( $\langle\omega_y\rangle$ probe, second straight wire). .....	168
Figure B.15 Combined calibration data for 19-July ( $\langle\omega_y\rangle$ probe, first X-wire). .....	169
Figure B.16 Combined calibration data for 19-July ( $\langle\omega_y\rangle$ probe, second X-wire). .....	169
Figure B.17 Combined calibration data for 25-July ( $\langle\omega_z\rangle$ probe, first straight wire). ..	170
Figure B.18 Combined calibration data for 25-July ( $\langle\omega_z\rangle$ probe, second straight wire). .....	170
Figure B.19 Combined calibration data for 25-July ( $\langle\omega_z\rangle$ probe, first X-wire). .....	171
Figure B.20 Combined calibration data for 25-July ( $\langle\omega_z\rangle$ probe, second X-wire). .....	171



# NOMENCLATURE

## ARABIC

$A, B, n$	Coefficients of hot-wire calibration, equation 4.1.
$B$	Log law constant, equation 1.6 (Chapter 1 only).
$E$	Voltage output of the anemometer, equation 4.1 (Chapter 4 only).
$E_{11}$	Autospectral density of the $u$ component of velocity, equation 5.21.
$E_{12}$	Co-spectral density of the $u$ and $v$ velocity components, equation 5.37.
$E_{\omega_z}$	Autospectral density of the $z$ component of vorticity, equation 5.31
$f$	Data acquisition frequency.
$g$	Gravitational constant.
$H$	Coherence spectra, equation 5.39.
$k_1$	Wavenumber in the $x$ -direction, equation 5.23.
$L$	Monin-Obukhov length, equation 2.3.
$l^+$	Viscous length scale, equation 1.2.
$M$	Integer number of time records for $1/2$ micro-circulation domain, equation 4.6.
$R$	Normalized correlation function, equation 5.22.
$R_\lambda$	Reynolds number based on the Taylor microscale.
$Re_\theta$	Reynolds number based on the boundary layer momentum thickness.

$Q$	Velocity magnitude of calibration free stream, equation 4.1.
$q$	Magnitude of velocity measured by hot-wire sensors.
$s_{ij}$	Rate of strain tensor, equation 5.5
$U_o$	Free-stream velocity.
$u,v,w$	Components of the velocity vector.
$u_\tau$	Friction velocity computed in the thermally neutral condition, equation 1.1.
$(u_\tau)_s$	Friction velocity computed in the thermally stable condition, see Section 2.2.3.
$(u_\tau)_u$	Friction velocity computed in the thermally unstable condition, see Section 2.2.3.
$u_\eta$	Kolmogorov velocity, equation 5.20.
$\vec{V}$	Velocity vector.
$x, y, z$	Cartesian coordinates.

## GREEK

$\Delta s$	Size of the micro-circulation domain used in the vorticity calculation, equation 4.6.
$\Delta y$	Separation distance of straight wire sensors in the vorticity probe.
$\delta$	Boundary layer thickness.
$\varepsilon$	Dissipation, Section 5.2.2.

$\Phi_{uv}$	Autospectral density of the uv velocity product, Section 5.3.3.
$\Gamma$	Circulation, equation 4.7.
$\eta$	Kolmogorov length scale, equation 5.19.
$\kappa$	Log law constant, equation 1.6 (Chapter 1 only).
$\kappa$	von Karmen constant, equation 2.3.
$\lambda$	Taylor microscale length.
$\theta$	Boundary layer momentum thickness.
$\theta$	Potential temperature, equation 2.1 (Section 2.2.2 only).
$\theta_v$	Virtual potential temperature, equation 2.3.
$\tau_w$	Wall shear stress.
$\rho$	Density of air.
$\nu$	Kinematic viscosity of air.
$\omega$	Vorticity, equation 4.10.
$\zeta$	Thermal stability parameter.

## **SUPERSCRIPTS**

$+$	Wall units.
-----	-------------

## SUBSCRIPTS

1,2                  Differentiates between two hot wires on the same probe.

## SYMBOLS

For quantity  $a$

$a'$                   Fluctuating value.

$\tilde{a}$                   Root-mean-square value

$\bar{a}$                   Time averaged value

## 1.0 Introduction

The current research serves to quantitatively describe near wall velocity and vorticity characteristics in a very high Reynolds number turbulent boundary layer flow. This thesis will also examine the characteristics of local isotropy under these inherently anisotropic conditions. Applications of this research include submarine and aircraft travel which exhibit Reynolds numbers on the order of  $Re_\theta \sim 10^6$ . The current research was sponsored by the Office of Naval Research (ONR), in hopes that a better understanding of the near wall motions of these phenomena would help to reduce noise and drag on their submarines.

The study of the turbulent motions in high Reynolds number boundary layer flows is made difficult because of the extremely small scales which are present in typical laboratory conditions. In order to achieve very high Reynolds number ( $Re_\theta$ ) flow, current methods include increasing the free stream velocity  $U_\infty$  or decreasing the kinematic viscosity  $\nu$  of the observed fluid. Achieving a Reynolds number on the order of  $Re_\theta \sim 10^6$  (typical of a Los Angeles class submarine) with the aforementioned methods would cause the smallest length scales and time scales of the problem to drop significantly below current measurement capabilities [17].

The present research is motivated by the lack of data existing for such high Reynolds number flows. Characteristic trends that have been previously established for boundary layer flow hold true for a large range of Reynolds numbers. However, the trends developed from existing data must be extrapolated to cover a range of Reynolds

numbers not achievable with current laboratory techniques. Extending these trends to cover larger Reynolds numbers without physical evidence is not accurate since many flow phenomena display a Reynolds number dependence already.

The current research was conducted at the Surface Layer Turbulence and Environmental Science Test (SLTEST) site on the salt flats of western Utah. The SLTEST site offers a unique opportunity to examine very high Reynolds number flows with large length scales and relatively smooth walls. This newly founded site utilizes a very large atmospheric boundary layer developing over the flat desert floor to produce the large scales crucial for the detailed observations of a high Reynolds number boundary layer flow. The data were taken over a period of two years (spanning one month each year), and they were acquired with the Michigan State University (M.S.U.) compact vorticity probe. The outdoor nature of the SLTEST site made acquiring data a difficult process. As a result, three days of data were acquired for the current research. Throughout the rest of this thesis, these three data sets will be referred to by the date on which the data were taken: 18-July, 19-July, or 25-July, 2001. Chapter 2 will describe the conditions of the SLTEST site in more detail. The experimental equipment will be discussed in Chapter 3, and Chapter 4 will serve to explain the hot-wire anemometry techniques used to acquire and process the data. Chapter 5 will cover the results obtained at the SLTEST site and Chapter 6 will present the conclusions. The following subsections of this chapter will serve to review the turbulent boundary layer characteristics which are relevant to this research.

## 1.1 Boundary Layer Overview

Fluid travelling over a flat plate develops a transitional region between the uniform velocity of the free-stream and the zero velocity at the wall. The latter condition is a result of the no-slip phenomenon. This transitional region is termed the *boundary layer* and can be described as the region of the fluid “where friction plays an essential part” [28]. Turbulent boundary layers have been the focus of a wide range of investigations (see Schlichting [28], Schetz [27], Pope [24], etc.) which have served to establish characteristics of these boundary layers under specific conditions. The focus of the current research is to extend the investigation of these characteristics into a range of much higher Reynold’s number ( $Re_\theta \sim 10^6$ ).

Turbulent boundary layers are typically divided into two regions: the *outer layer* and the *inner layer*. A sizable overlap region exists between these two layers properly termed the *overlap region*. The inner layer starts at the wall and extends to include the *viscous sublayer*, the *buffer layer* and the overlap region. The outer layer begins with the overlap region and ends at the free stream (the end of the boundary layer). Fig 1.1 better illustrates the various layers of a turbulent boundary layer [24]. The shear stress of the *viscous wall region* is directly influenced by molecular viscosity, while in the outer layer the direct effect of viscosity on the shear stress is negligible [24].

Experimental data, taken in a turbulent boundary layer, are typically scaled with appropriate lengths and velocities. Close to the wall, where viscous effects are important, it is common to describe boundary layer characteristics in *plus units* or *wall units*. A friction velocity,  $u_\tau$ , can be defined from the wall shear stress  $\tau_w$  and fluid density  $\rho$  as [24]:

$$u_\tau \equiv \sqrt{\frac{\tau_w}{\rho}} \quad 1.1$$

With this, a viscous length scale can be defined as:

$$l^+ \equiv \frac{\nu}{u_\tau} \quad 1.2$$

where  $\nu$  is the kinematic viscosity of the fluid.

The distance away from the wall can then be defined (in wall units) as

$$y^+ \equiv \frac{y}{l^+} \quad 1.3$$

and the velocity in wall units can be defined as

$$u^+ \equiv \frac{u}{u_\tau} \quad 1.4$$

The inner layer of a turbulent boundary layer has been observed to exhibit a universal behavior in both the viscous sublayer and the overlap region. In the viscous sublayer (the very near wall region),  $u^+$  varies directly with  $y^+$ , or

$$u^+ = y^+ \quad 1.5$$

for very small  $y^+$  (up to  $y^+ \sim 10$ ).

The overlap region has also been noted to exhibit a universal behavior when scaled with inner wall units. In the overlap region of smooth wall turbulent boundary layers, the *log law* can be expressed as

$$u^+ = \frac{1}{\kappa} \ln y^+ + B \quad 1.6$$

where  $B$  and  $\kappa$  are constants, commonly taken to be [24]



$$\kappa = 0.41 \quad B = 5.2$$

These two regions join each other in the buffer layer, where neither equation holds true. Figure 1.2 demonstrates the universal behavior of the viscous sublayer and the overlap region. The linear trend (equation 1.5) can be seen in the very near wall region, and the log law behavior (equation 1.6) can be seen further away from the wall. The scaling collapse for a range of Reynolds numbers is also evident in the figure.

Turbulent boundary layers display a Reynolds number dependence in many characteristic trends and statistics. One example of this Reynolds number dependence is the size of the overlap region in a turbulent boundary layer. Figure 1.3 shows the dependence of the size of the overlap region as a function of Reynolds number [23]. The experimental data exhibit a straight line for  $yu_\tau/\nu > 30$ . This straight line represents the log law. Deviations from this line mark the end of the overlap region. The location where the data deviate from the log law is dependant on the Reynolds number.

## 1.2 Literature review

The current research examines the near-wall velocity and vorticity characteristics in a high Reynolds number turbulent boundary layer. This section will serve to briefly review the current literature relevant to the present study. Turbulent boundary layers and the concept of local isotropy have been studied extensively, but rarely at a Reynolds number comparable to that of the current research. The concept of local isotropy was presented by Kolmogorov in 1941 as a hypothesis concerning the characteristics of turbulent flows. Kolmogorov's hypothesis states that "at sufficiently high Reynolds numbers, the

small scale turbulent motions are isotropic” [13]. In other words, at high Reynolds number the statistics of the very small scale motions in turbulent flow are “invariant with respect to rotations and reflections of the coordinate axis,” i.e. independent of direction [24]. This hypothesis was made in the assumption of extremely high Reynolds number ( $Re_\theta \rightarrow \infty$ ) and has been tested up through current laboratory limitations.

The velocity and vorticity characteristics of turbulent boundary layers have been extensively studied over a range of Reynolds numbers. Those that involve vorticity measurements include Ong and Wallace (1998) who examined the structure and dynamics of the vorticity field of a turbulent boundary layer at  $R_\theta = 1070$  [22]. Honkan and Andreopoulos (1997) studied vorticity and dissipation in a turbulent boundary layer at  $R_\theta = 2790$  [14]. Andreopoulos and Agui (1996) studied the wall vorticity flux dynamics in a turbulent boundary layer at  $R_\theta = 5400$  [1]. Klewicki and Metzger (2001) were able to extend the study of turbulent boundary layers into the range of  $R_\theta \approx 5 \times 10^6$  by the use of the SLTEST site [16].

The concept of local isotropy in turbulent boundary layers has also been the subject of extensive investigations covering a range of Reynolds numbers. Mestayer (1982) studied local isotropy and anisotropy in a high Reynolds number turbulent boundary layer at  $R_\lambda = 616$  [18]. Saddoughi and Veeravalli investigated Kolmogorov’s 1941 hypothesis of local isotropy in a turbulent boundary layer at  $R_\theta = 370,000$  ( $R_\lambda = 1450$ ) [26]. These were the largest Reynolds numbers ever attained under laboratory conditions. The current research extends the investigation of turbulent boundary layers and the concept of

local isotropy up to  $R_\theta \approx 5 \times 10^6$  and  $R_\lambda = 2500$  by use of the SLTEST site. The following chapters detail this investigation.

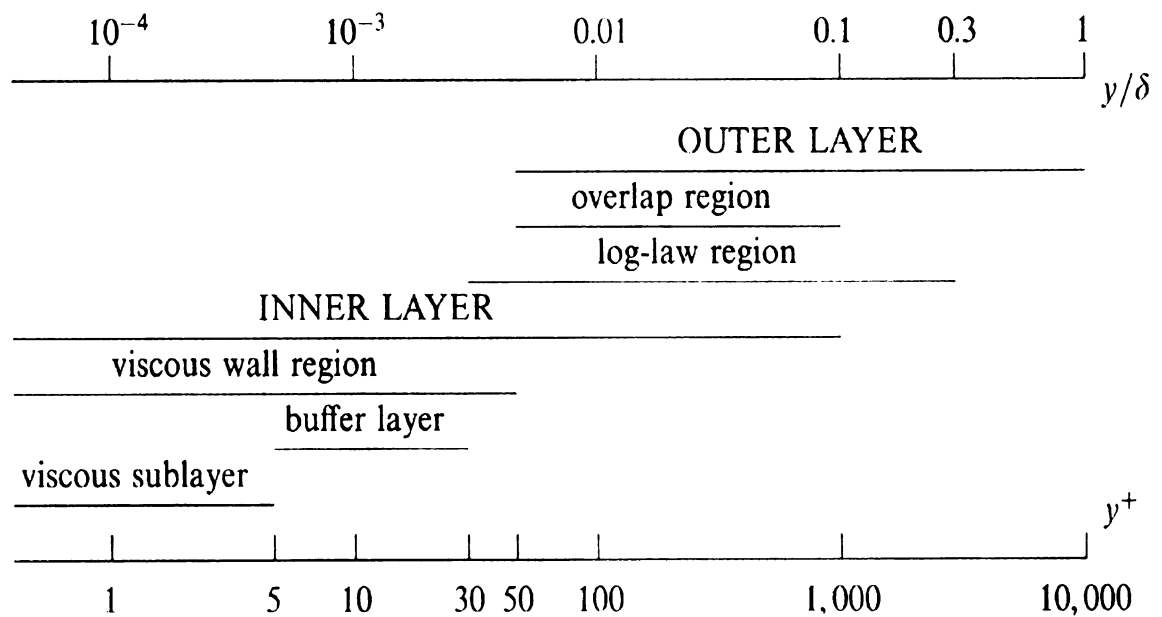


Figure 1.1 The breakdown of a turbulent boundary layer [24]. The inner  $y^+$  and the outer  $y/\delta$  are universal [  $\neq f(R_\theta)$  ], but the extents of these regions are  $R_\theta$  dependent.

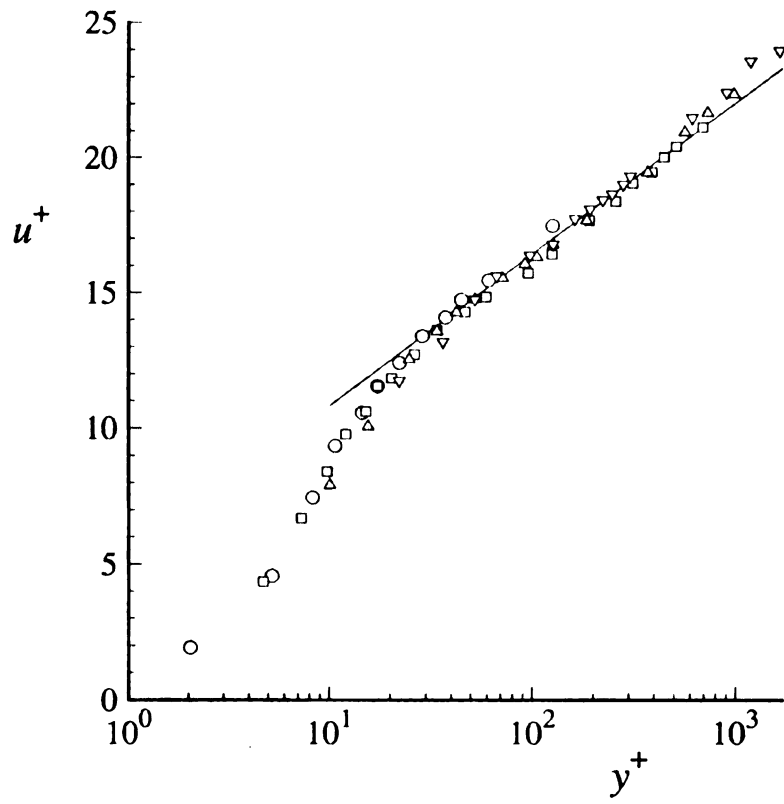


Figure 1.2 Scaling collapse on the inner region of a turbulent boundary layer [24]. O,  $Re_\delta = 2,970$ ;  $\square$ ,  $Re_\delta = 14,914$ ;  $\triangle$ ,  $Re_\delta = 22,776$ ; line, the log law.

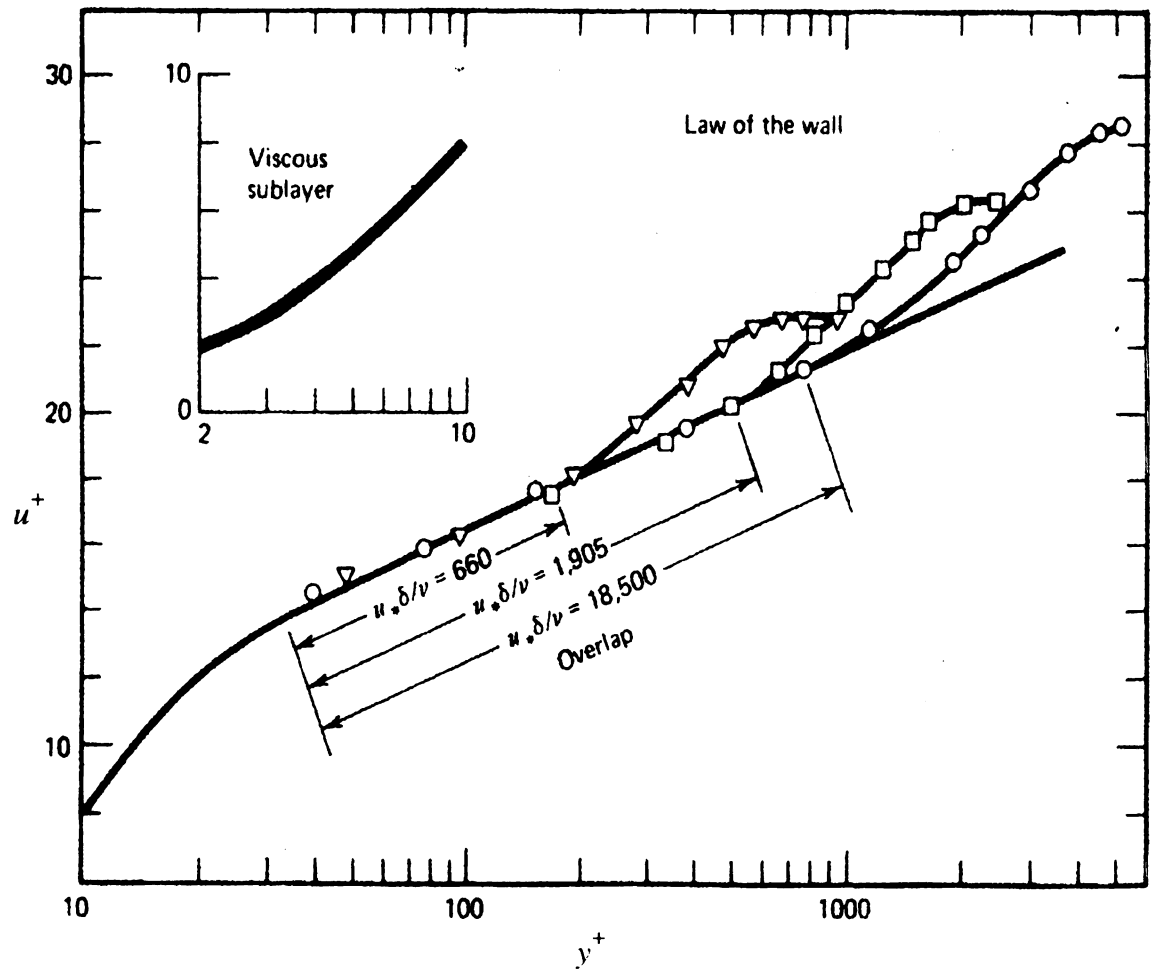


Figure 1.3 The Reynolds number dependence on the size of the overlap region [23].

## **2.0 Experimental Facility and Conditions**

The current research was conducted at the SLTEST site in western Utah. The SLTEST site utilizes a large atmospheric boundary layer which develops over the very flat desert floor. This unconventional test site allowed for high resolution, near wall velocity and vorticity measurements in a high Reynolds number turbulent boundary layer. However, the outdoor atmospheric environment also brought about new issues to address, including thermal effects and very low-frequency motions.

This chapter serves to describe the SLTEST site in detail and address the new issues which presented themselves during this research. Section 2.1 presents a general overview of the SLTEST site. Section 2.2 describes the test site's data acquisition equipment, including wind monitoring, thermal profiling and shear stress measurements.

### **2.1 Test Site Overview**

The SLTEST facility is located on the U.S. Army Dugway Proving Grounds in the Great Salt Lake Desert of western Utah. This region has been observed to provide desirable wind and surface conditions for accurate near-wall boundary layer measurements. The SLTEST site is located at  $113^{\circ} 16' W$ ,  $40^{\circ} 8.5' N$  and is situated between mountain ranges (forming crude sidewalls to the east and west) as seen in Figure 2.1 [19]. The SLTEST site is actually the floor of the ancient Lake Bonneville and consists of a very flat surface. This surface, devoid of vegetation, is formed by the recession of a relatively high water table in late Spring. This recession leaves the playa smooth, solid and virtually dust free (playa is defined as a mixture of mud, clay and salt). Measurements reported by the

University of Utah approximate the surface variation of the test site to be less than 1 meter per kilometer, or about 0.1% [30].

The observed boundary layer develops over a distance of nominally 150 kilometers for northerly winds and about 50 kilometers when the wind is blowing from the south [17]. These conditions typically result in a boundary layer thickness,  $\delta$ , on the order of 150 meters and a momentum thickness,  $\theta$ , on the order of 10 meters [15]. The large scales associated with this boundary layer contribute to typical Reynolds numbers (based on the momentum thickness  $\theta$ ) on the order of  $Re_\theta \approx 5 \times 10^6$ . These large scales along with the relatively low flow speeds (between 3 and 6 m/s at our probe locations) also allow for very good spatial resolution of the measurements [15].

## **2.2 Test Site Capabilities**

The conditions at the SLTEST site were continually monitored to characterize the data taken. The ambient conditions present during the acquisition of each data set were documented to allow for accurate comparisons to well controlled laboratory results. The monitored conditions included the wind speed, wind direction, velocity profiles, temperature profiles, and shear stress measurements at the wall. The following subsections will discuss the available information at the SLTEST site and how it was acquired.

### **2.2.1 Wind Monitoring**

The SLTEST facility offered equipment to monitor the wind conditions at a range of elevations above the desert floor. Figure 2.2 demonstrates the four types of measurements available to profile the boundary layer (Sonic tower, Echosonde, Radar wind pro-



filer, and FMCW radar) and their active ranges. Hot wire anemometry (the focus of this research) allowed for accurate measurements in the boundary layer ranging from 1mm to 2m off the surface [30]. Figure 2.3 shows a typical boundary layer profile taken at the SLTEST site under neutral conditions and averaged over a 1 hour period, courtesy of the University of Utah's echosonde equipment.

The outdoor nature of the SLTEST site did not allow for control over the steadiness of the free stream. The facility was equipped, however, with instrumentation to monitor the 'driving' atmospheric wind. Questions related to steadiness of the free stream velocity at the SLTEST site were sufficiently answered by monitoring the prevailing wind speed and direction. For each of the three days data were acquired, a three-cup anemometer and wind vane (discussed in Chapter 3) were used to verify the steadiness of the wind. The results for each day are discussed in Section 5.1.

### **2.2.2 Thermal Effects**

This section will address the thermal concerns brought about by the outdoor nature of the SLTEST facility. Thermal effects can be controlled under typical laboratory conditions to play a minimal role in boundary layer characteristics. However, this was not the case at the SLTEST site. During the day, the hot desert sun heated the test site floor to a temperature well above the ambient air. Such a condition is known as *unstable*, since a positive buoyancy flux results due to the temperature (and hence a density:  $\rho \sim 1/T$ ) gradient. This density gradient causes the lower, warmer air to move away from the wall. The fluctuations measured in a boundary layer under unstable conditions are amplified as a result of the effects of the positive buoyancy flux. As the sun sets, the ground cools off and eventually a state of thermal equilibrium is reached. This case is known as the *neutral*

condition. Thermal effects do not play a role in the boundary layer motions under the neutral condition. Following the neutral condition, the ground continues to cool and it eventually reaches a temperature lower than that of the surrounding air. The cool ground creates what is known as a *stable* condition. In this case, the cooler air initially near the wall tends to stay near the wall due to the density stratification. This negative buoyancy flux has a damping effect on the velocity fluctuations within the boundary layer.

The condition of thermal equilibrium was defined by  $\frac{\partial \theta}{\partial y} \approx 0$ , where  $\theta$  is the potential temperature of the air. Potential temperature is defined as the temperature a parcel of dry air would have if it was brought adiabatically from its initial state to the standard sea level pressure of 1000mb. The potential temperature removes the temperature variation caused by changes in pressure altitude of an air parcel, and is given by [29]:

$$\theta \equiv T \left( \frac{P_o}{P} \right)^{\frac{\gamma-1}{\gamma}} \quad 2.1$$

In this formulation,  $T$  and  $P$  are the temperature and pressure of the air parcel respectively,  $P_o$  is the reference pressure of 1000mb, and  $\gamma$  is the heat capacity ratio of the air.

The *virtual* potential temperature  $\theta_v$  is similar to the potential temperature  $\theta$  defined in equation 2.1, but uses the virtual temperature of the air in its computation. The virtual temperature of moist air is defined as the temperature that dry air must have to equal the density of the moist air at the same pressure. The virtual potential temperature is related to the potential temperature by [29]:

$$\theta_v = \theta (1 + 0.61 r_{sat} - r_L) \quad 2.2$$

where  $r_{sat}$  is the water-vapor saturation mixing ratio of the air parcel and  $r_L$  is the liquid-water mixing ratio [29].

The relative buoyancy effects were assessed according to the stability parameter  $\zeta \equiv \frac{y}{L}$ . In this stability parameter,  $y$  is the distance of the measurement away from the wall and  $L$  is the Monin-Obukhov length [19],

$$L = \frac{-u_\tau^3}{\kappa(g/\overline{\theta_v})v'\theta_v'} \quad 2.3$$

In the Monin-Obukhov length,  $u_\tau$  is the friction velocity (see the next section),  $g$  is the gravitational constant,  $v'$  is the wall-normal velocity fluctuation,  $\kappa$  is the von Karmen constant,  $\overline{\theta_v}$  is the time averaged virtual potential temperature and  $\theta_v'$  is its fluctuating counterpart. The Monin-Obukhov length  $L$  is physically the height at which the buoyancy term equals the shear production term in the turbulent kinetic energy balance [19]. Positive  $\zeta$  indicates the presence of a stable atmospheric condition while negative  $\zeta$  indicates the presence of an unstable atmospheric condition. The “neutral” condition was taken to be  $|\zeta| \leq 0.1$  as was found to be common practice in atmospheric boundary layer research [13].

Previous work by Klewicki [15] has indicated that a range of up to 2 hours can exist during the evening where the ambient atmospheric conditions are very close to neutral. The thermal stability parameter was evaluated for each of the three days that data were acquired. These results are discussed in Section 5.1. It should be noted that this stability parameter was calculated from the data acquired by a sonic anemometer located at  $y$

= 3.185m. This is not the same location of the probes, but still gives a good indication of the stability condition at the SLTEST site for each evening. Differences between the stability parameter at  $y = 3.185$  m (the parameter measurement location) and  $y = 20$  cm (probe location) are assumed to be relatively small.

### **2.2.3 Shear Stress Measurements**

The mean wind shear stress was also monitored in order to accurately normalize the data for comparison with laboratory measurements. A drag plate (Figure 2.4) consisting of a thin (thickness = 1.27mm) polyethylene cylinder 2.4 meters in diameter was mounted on a styrofoam base and placed in a shallow pool of water (0.2m). The drag plate was mounted flush with the surface of the surrounding salt flats. A small amount of playa was then scattered on the drag plate surface to mimic the surface roughness of the surrounding 'wall.' Force transducers were mounted near the edges of the cylinder on 3 sides of the plate, each separated by 90 degrees. These force transducers recorded the mean wall shear stress when the wind was blowing from a northerly direction. The drag plate was able to extract shear stress values as small as 0.01 Pa [19].

The drag plate was located on the north side of the raised access road. As a result, accurate shear stress measurements could only be acquired with wind blowing from the northerly direction. However, all three data sets for this research were taken when the wind blew from the south. To account for this, the drag plate data were previously correlated with a propeller anemometer located 2 meters above the ground. An identical propeller anemometer was then located on the south side of the test site and used to extract the mean shear stress data in the case of southerly winds. The friction velocity,  $u_\tau$ , could

then be computed from the measured mean shear stress and the density of the air by using equation 1.1.

Data from the University of Utah indicated that the correlation between the drag plate and propeller anemometer was only valid under the condition of thermal neutrality. However, some of the data presented were also acquired under thermally stable and thermally unstable conditions. Correlating the propeller anemometer to the drag plate under thermally stable and thermally unstable conditions would have proven difficult, since the correlation is dependant on the degree of thermal stability present. The aforementioned correlation over thermally stable and thermally unstable conditions was not complete at the time of this work. As a result, the value of the friction velocity that was used for each data set was computed through a correlation which assumed thermal neutrality, regardless of the present thermal condition.

To distinguish between the known friction velocity (for the thermally neutral condition) and the estimated friction velocity (for thermally stable or unstable conditions), the following notation is used. In the condition of thermal neutrality, the friction velocity will be denoted by  $u_\tau$ . In the thermally unstable condition, the friction velocity will be denoted by  $(u_\tau)_u$ . In the thermally stable condition, the friction velocity will be denoted by  $(u_\tau)_s$ . The friction velocity for each day is discussed in Section 5.1.

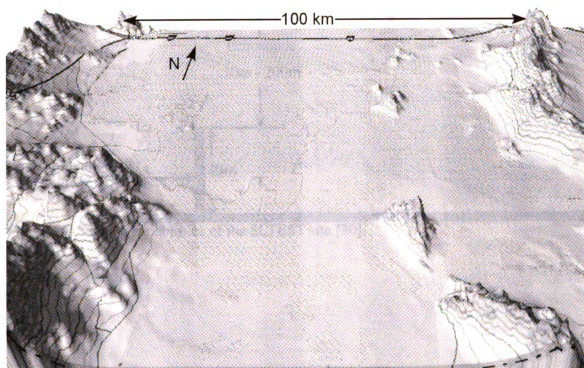


Figure 2.1 Topographic map of the Dugway area. The SLTEST site is denoted by  $\oplus$ .

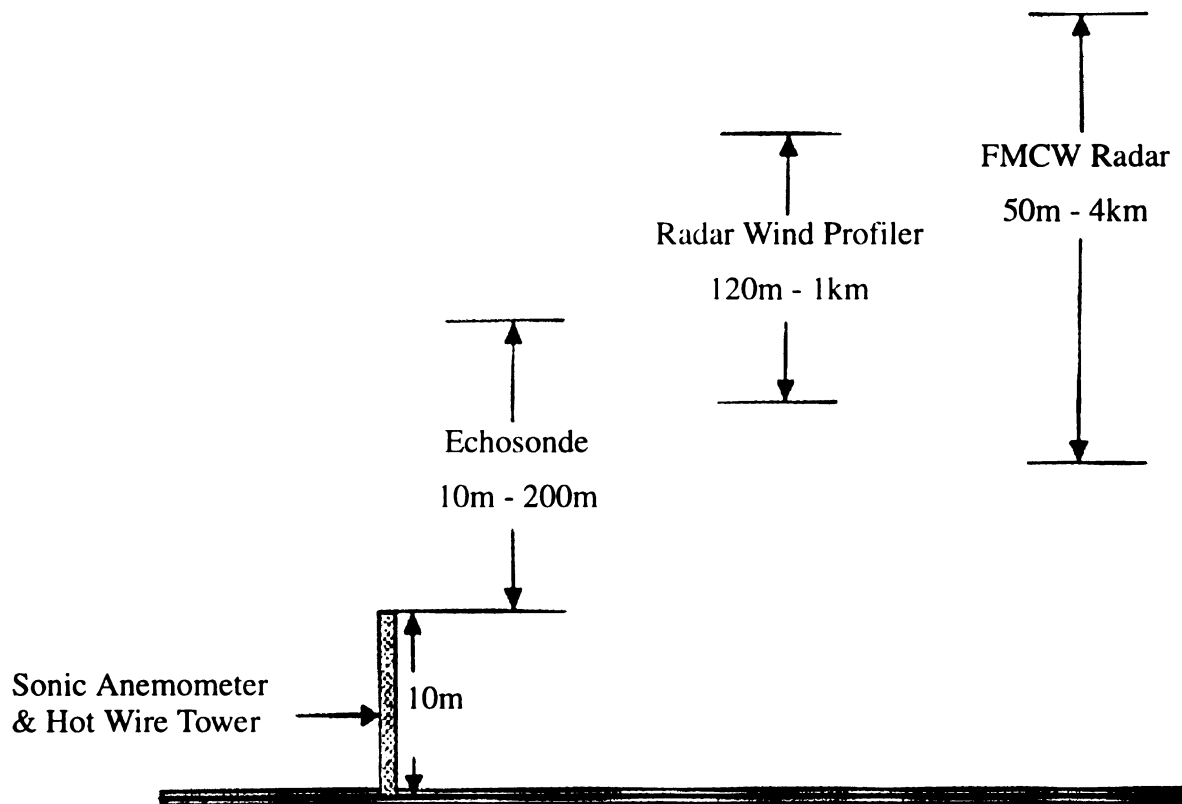


Figure 2.2 Sensing capabilities of the SLTEST site [30].

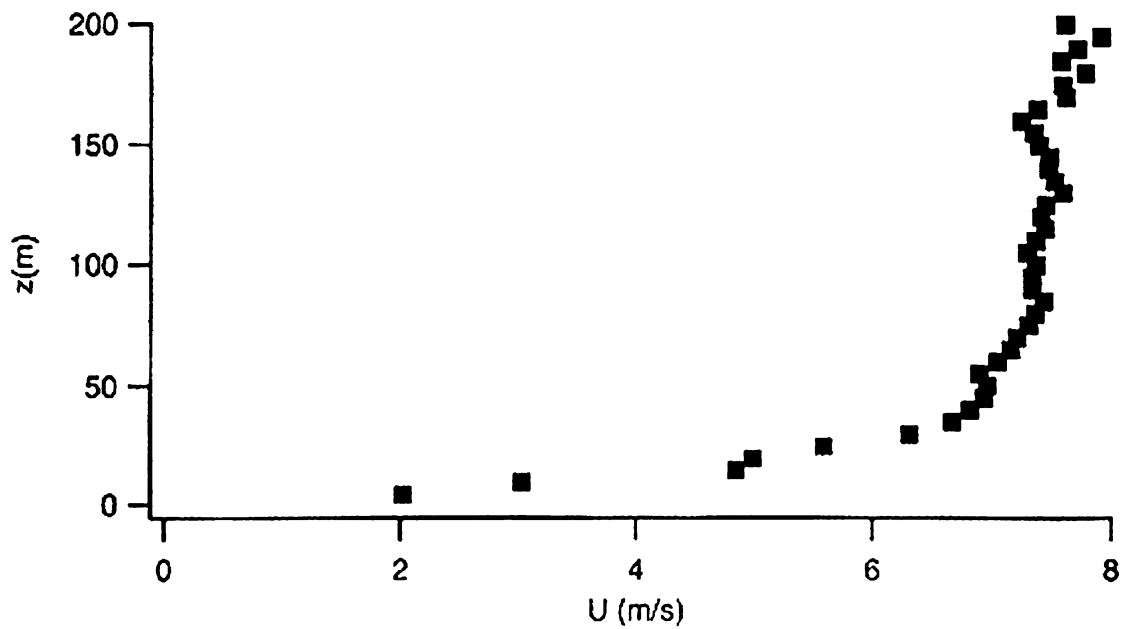


Figure 2.3 Typical boundary layer profile at the SLTEST site [30].

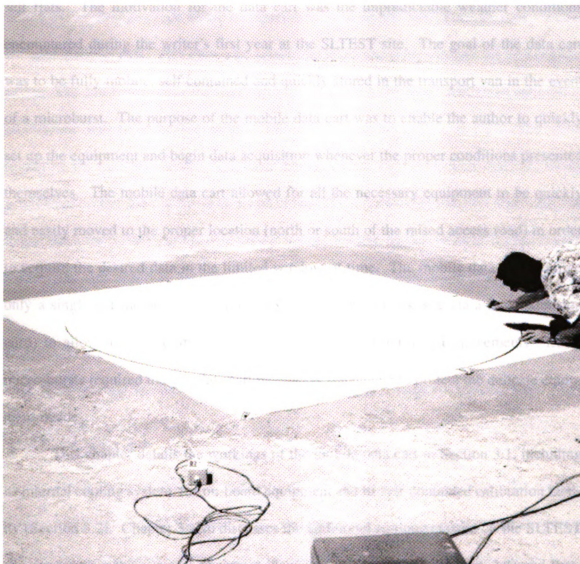


Figure 2.4 A 2.4 meter drag plate was used to gather accurate values for the wall shear stress [30]. (J. Klewicki is shown smoothing the playa to the edge of the housing for the drag plate.)



### **3.0 Experimental Equipment**

A mobile data cart was created to aid in the acquisition of data on the SLTEST site salt flats. The motivation for the data cart was the unpredictable weather conditions encountered during the writer's first year at the SLTEST site. The goal of the data cart was to be fully mobile, self contained and quickly stored in the transport van in the event of a microburst. The purpose of the mobile data cart was to enable the author to quickly set up the equipment and begin data acquisition whenever the proper conditions presented themselves. The mobile data cart allowed for all the necessary equipment to be quickly and easily moved to the proper location (north or south of the raised access road) in order to acquire the desired data in the limited window of time. The mobile data cart required only a single outside power source (110 V supplied by the test site via a long extension cord) to allow for the equipment to remain powered up during the movements. Local micro-bursts required that the data cart be quickly retractable to protect the delicate equipment inside.

This chapter details the workings of the mobile data cart in Section 3.1, including its internal cooling system, the on-board equipment and its self-contained calibration facility (Section 3.2). Chapter 3 also discusses the additional equipment used on the SLTEST site, including a three cup anemometer (Section 3.3), wind vane (Section 3.4) and thermistor (Section 3.5).

### **3.1 Mobile Data Cart**

The mobile data cart (Figure 3.1) was fabricated from a set of 2' X 4' steel storage shelves and the base of a heavy duty pull cart. The maximum height of the cart was determined by the storage space of the transport vehicle to be 45" tall. The cart rode on 25.4 cm pneumatic wheels. This choice of wheels made maneuvering through the desert playa easier. The lower region of the data cart was designed to be a self-contained calibration facility and will be discussed more in the following section (Section 3.2). The upper region of the cart housed the equipment necessary for data collection and was easily accessible through the flip-down doors on either side of the cart (Figures 3.1 and 3.2). The upper and lower regions of the data cart were kept isolated from each other for fewer calibration disturbances. The outside of the cart was covered in thin sheets of white plastic to keep the cart as cool as possible. The front of the cart was comprised of a flip-down shelf designed to support a portable personal computer and keyboard. It was also designed to include an optional sun-blocking roof to eliminate glare on the face of the monitor.

#### **3.1.1 Cooling System**

The mobile data cart was equipped with an internal cooling system. The cooling system was required because of the high ambient temperatures (typically  $95^{\circ}F = 35^{\circ}C$ ) present at the SLTEST site. The equipment on the mobile data cart was calibrated and typically operated at laboratory temperatures. The purpose of the cooling system was to provide a similar operating temperature to avoid any thermally related problems with the equipment. The cooling system worked as follows.

Additional space was added to the back of the cart in the form of an extension and divided into two regions; see Figure 3.1, sections B and D. The lower extension region

(D) was used for both the calibration facility as well as storage of the three-cup anemometer and wind vane. The upper extension region (B) housed the data cart's cooling system, and both were accessible through a large (61mm x 77.5mm) door on the back of the cart. A large (20mm x 20mm x 51mm) basin was constructed and mounted in the upper extension region of the data cart. The basin was filled with water through a hole in the roof; see Figure 3.1, label A. A 17" X 10" square of cloth filter material was mounted partially in the basin and used to wick up the water stored in the basin. A small blower was mounted outside of the data cart and attached to a diffuser leading into the cooling system. As air entered the cooling system, it absorbed water from the wet filter material (due to the low ambient humidity in the desert) and then quickly evaporated, significantly lowering the temperature of the air stream. This cooled air then travelled throughout the cart (over both levels of equipment), eventually exiting out the front of the cart. The system was loosely tested at the SLTEST site with temperature sensing equipment and the temperature immediately behind the cooling system was found to be significantly cooler than the ambient air. The humidity level was also monitored and observed to be only slightly higher than the ambient air.

### **3.1.2 On-board Equipment**

The mobile data cart housed all equipment necessary for data acquisition at the SLTEST site. The data acquisition equipment was stored in the upper region of the cart; see Figure 3.2. The upper region of the data cart was separated into two levels. The lower level housed 8 DISA 55m10 anemometers (which were used to control the hot wire probes utilized in this research) as well as the A/D board (labels B and C). The anemometers had electrical noise levels on the order of 2 mvolts RMS and frequency responses always in

excess of 30 kHz [20]. The A/D board used was an Iotech WaveBook 516, which had 16-bit resolution and 1MHz total sampling capabilities over 16 channels. Eight of the channels were equipped with a sample-and-hold card to allow for simultaneous measurements. The Iotech board had a range of  $\pm 10$  volts and typical electrical noise of about 10 mV. The A/D board transferred all data to a BSI FieldGo “luggable” computer for permanent storage and processing.

The upper level of the data cart contained the pressure transducer, DISA power supplies, stepper motor control (for the calibration unit described below), probe case, and drivers for the thermistor, three-cup anemometer and wind vane. The pressure transducer was an MKS Baratron 220BD differential manometer, with a full scale range of 0.53 in H<sub>2</sub>O, a resolution of 0.01% of the full scale range ( $5.3 \times 10^{-6}$  in H<sub>2</sub>O) and an accuracy of  $\pm 0.15\%$  the reading.

The data cart was wired to run off a single 110 volt power supply. Surge protection strips provided 12 outlets for the equipment. Power for the calibration facility blowers as well as additional cooling fans was supplied directly from the cart’s wiring scheme. All electronics on the cart connected to a single ground. This single ground was then connected to a grounding rod. Taking advantage of the water table just beneath the test surface (as well as the salty conditions), the rod was driven into the desert floor in order to properly ground all of the equipment.

### **3.2 Calibration Facility**

The hot wire sensors were calibrated using a facility located on the lower level of the mobile data cart; see Figure 3.1 (F). The calibration facility was designed to provide the proper range of air speeds to the hot wire probes without interference from the ambient wind. This section will discuss the construction of the calibration facility while the actual calibration procedures will be discussed in Chapter 4.

The lower region of the data cart was covered with filter material; see Figure 3.1. This filter material eliminated the effects of ambient winds on the calibration of the hot wires and still allowed for the higher pressure air inside the lower region of the unit to escape. Two small doors on the front of the data cart allowed for access to the front of the calibration unit. The front half of the calibration facility detached from the fixed base and rolled forward for probe mounting and alignment; see Figure 3.3. Doors on either side of the lower region of the data cart (3/4 of the way back, see Figure 3.1) allowed for access to attach and detach the front half of the calibration unit from the fixed base. The blowers were mounted on the fixed base of the calibration unit and hung off the back of the data cart, enclosed in the lower extension region. This allowed for ambient air to be induced into the facility, used to calibrate the wires, and then be returned through the filter material to the surroundings.

The calibration unit seen in Figure 3.3 was designed and built specifically for the mobile data cart. The unit was composed of two parts: a stationary back portion and the detachable front portion. The two halves were latched together while in use, sandwiching a thin layer of foam which sealed the connection as well as reduced the vibrational effects of the blowers. The back half of the calibration unit was secured to the bottom floor of the

data cart and utilized two Dayton 4C015 Dual Shaded Pole Blowers, with outputs of 72 CFM at 0.5" H<sub>2</sub>O each. The blowers were throttled by four aluminum plates connected to a threaded rod. The external end of the threaded rod was connected to a 1/20th horsepower gear reduction D.C. motor. Limit switches were mounted inside the unit to stop the throttle plate at fully open and fully closed positions. A 24 volt power supply and main control switch were added to the system (Figure 3.5) to allow throttling of the motor to occur from the front of the cart with the flip of a switch.

The calibration facility contained several flow conditioning devices that were used to ensure a steady and uniformly distributed calibration flow. A top view of the calibration facility, along with the flow conditioning elements, can be seen in Figure 3.4. Two vertical pieces of angle stock were mounted directly in front of the blower exits (downstream of the throttle plate) in order to disperse the jets formed from the blowers. Additional elements: a layer a filter material, a 1" thick honeycomb (used to straighten the flow) and two layers of screen, were place downstream of the vertical angle stock obstructions. The back plate of the calibration unit (which held the blowers) was mounted to the unit with a slight air gap on all four sides. This allowed for stable operation at very low calibration air flow speeds since, for low fan speeds, air would escape out of the back gaps instead of travelling through the more restrictive passage into the front of the unit.

The front half of the calibration unit was made detachable and designed to roll from the back position (used for calibration) to the forward position (used for probe mounting) along a track mounted on the data cart floor. The uniform and steady airflow received from the back portion underwent a smooth contraction and exited the unit with a width of 2.54 cm. The probes were mounted to a vertical "D-bracket" which was sus-

pendent from a rotatable rod with its pivot point located directly over the exit plane. An 11.43 cm gear was also connected to the same rod and connected to a stepper motor by means of a belt. The stepper motor was computer controlled and used to control the angle of the probe with respect to the flow. This angle traverse was found to have a resolution of 0.15 degrees, and was adjusted in six degree increments.

Pressure taps located on the front wall of the calibration unit were used to monitor the pressure change across the contraction. Since the calibration facility's settling chamber did not represent true plenum, the measured pressure difference,  $\Delta p_m$ , could not be used for the velocity calculation as  $V = \left[ \frac{2}{\rho} \Delta p \right]^{1/2}$ . Instead, an auxiliary calibration:  $\Delta p = f(\Delta p_m)$  was implemented. The static tap readings across the contraction were compared to readings from a pitot tube located at the exit plane of the facility for a range of pressures. The data were then curve fit in order to calculate a linear compensation factor used to transform the static readings into the true total pressure readings. Figure 3.6 displays this calibration information.

### 3.3 Three-Cup Anemometer

A three-cup anemometer was also used at the SLTEST site to monitor ambient wind conditions. An R.M. Young #03101-X three cup anemometer was calibrated in a 2' x 2' wind tunnel for a range up to 15 m/s. Figure 3.7 shows the calibration curve used for the three cup anemometer. The anemometer was mounted on a modified tripod 1.5 meters above the test surface; see Figure 3.8. The three-cup anemometer acquired data at the same rate of the hot wires and was used to verify trends in the data.

### **3.4 Wind Vane**

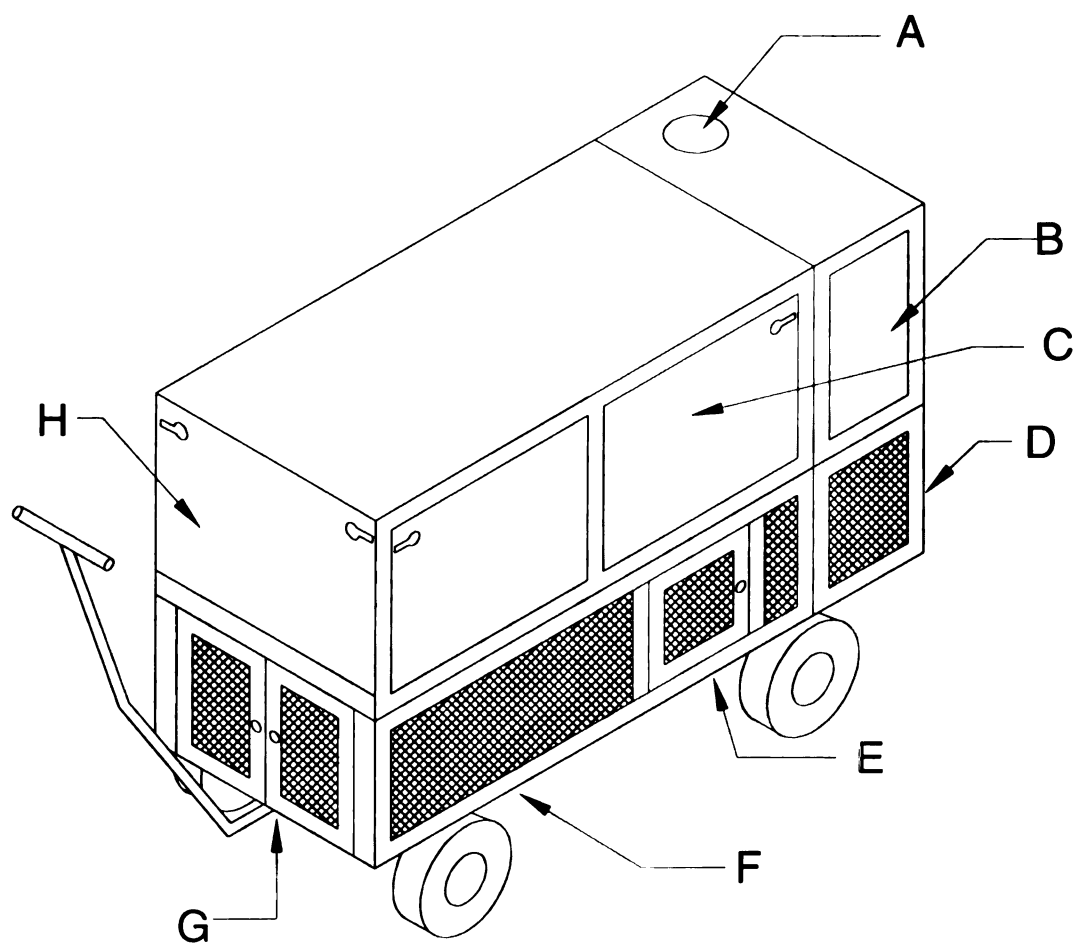
An R.M. Young 03101 wind vane was used on the SLTEST site in order to monitor the direction of the wind during data acquisition. The vane had 360 degree capabilities with a discontinuity between the 360 degree and 0 degree readings. The wind vane had a resolution of 1 degree. The vane was also mounted on the modified tripod 1.5 meters above the test surface; see Figure 3.8. Once the hot wire probe was aligned into the direction of the wind, a baseline angle reading was taken from the vane. The vane direction was then monitored over the period of data taking and later used to verify the location of the probe with respect to the mean wind direction. The readings from the wind vane were also used to verify trends in the wind shifts observed by the probes. The vane was quoted to have an accuracy of  $\pm 5$  degrees.

### **3.5 Thermistor**

A thermistor was used to compensate all hot wire probe measurements in order to account for ambient temperature variations. The thermistor was pre-calibrated and found to have a sensitivity of 2.03K/Kohm [20]. At the SLTEST site, comparison of the thermistor reading to a portable thermometer showed a large disagreement. The circuitry of the thermistor was temperature dependant. The discrepancy resulted from the thermistor driver box being operated at a higher temperature than that of its laboratory calibration. To account for this, simultaneous readings from both the thermistor and hand-held thermometer unit were taken over a range of ambient temperatures. The temperature pre-

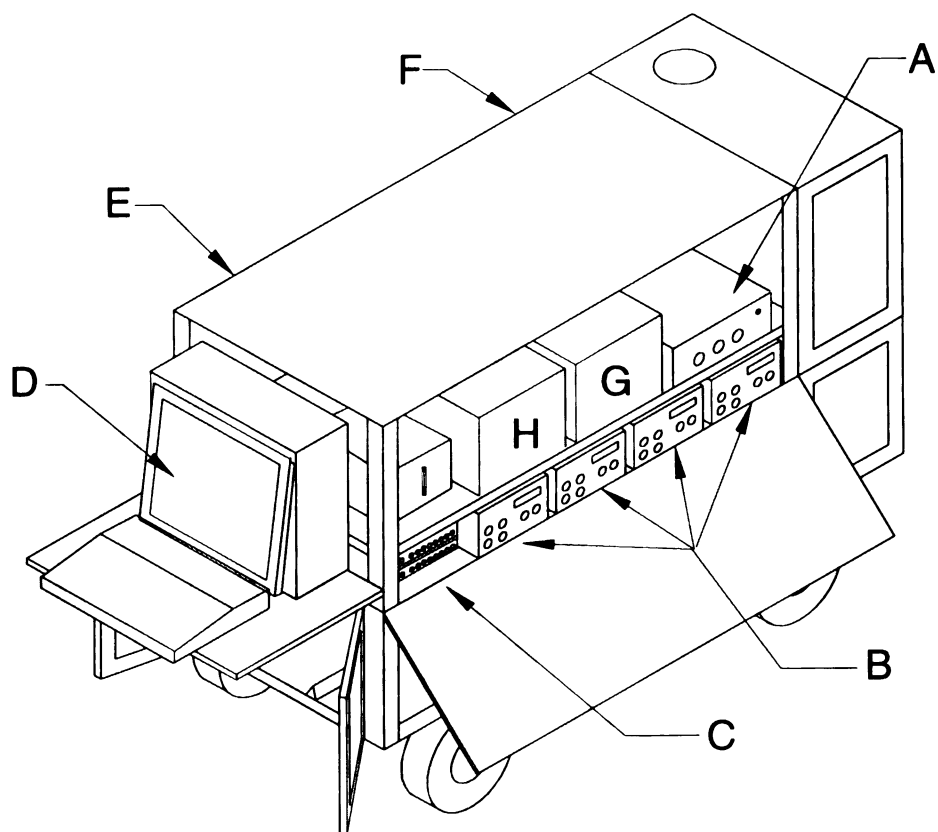


dicted by the recorded thermistor voltage was compared to the actual temperature over this range. The thermistor data were found to differ from the actual temperature by a constant value for the entire range of observed temperatures. The thermistor data were then offset by this constant value to achieve the actual temperature. Figure 3.9 shows the actual temperature reading (taken with the hand-held thermometer) compared to the adjusted thermistor reading for a range of thermistor voltages. All the data were then curve fit and used to extract the actual temperature from the thermistor voltage.



- A Cooling System Fill Hole
- B Upper Extension Region
- C Access to Upper Region
- D Lower Extension Region
- E Side Access to Calibration Facility
- F Lower Region
- G Front Access to Calibration Facility
- H Flip-Down Computer Shelf

Figure 3.1 Schematic of Mobile Data Cart.



- A Cup / Vane Driver
- B DISA Anemometers (not shown)
- C A/D Board
- D Computer
- E Thermistor Driver (not shown)
- F Stepper Motor Driver (not shown)
- G DISA Power Supply
- H Probe Case
- I Pressure Transducer

Figure 3.2 Interior view of Mobile Data Cart.

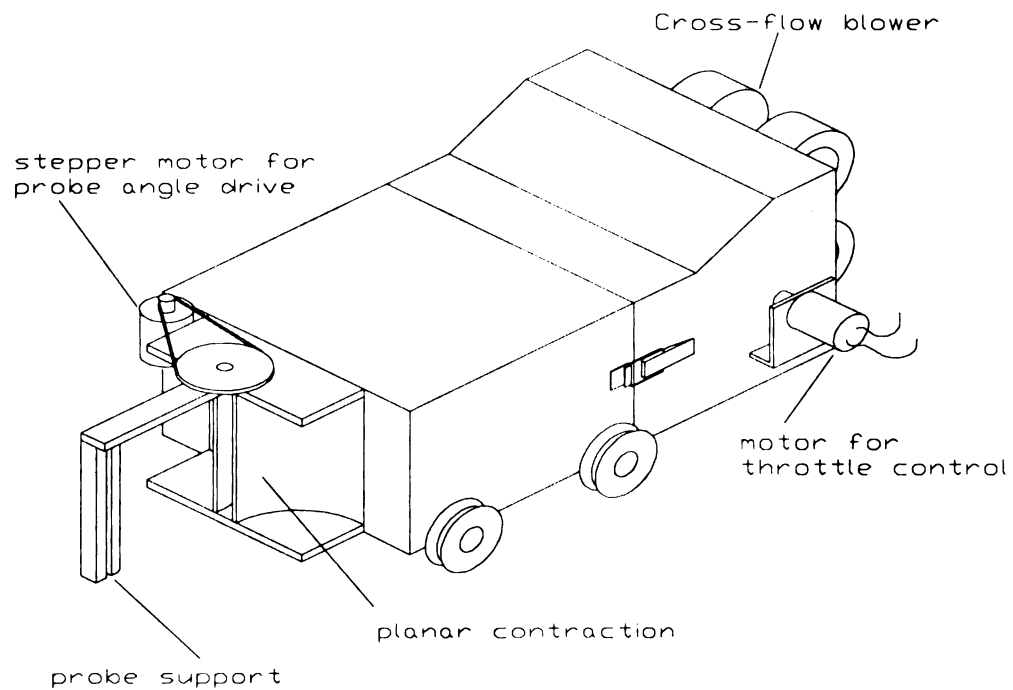


Figure 3.3 The Data Cart's portable calibration unit.

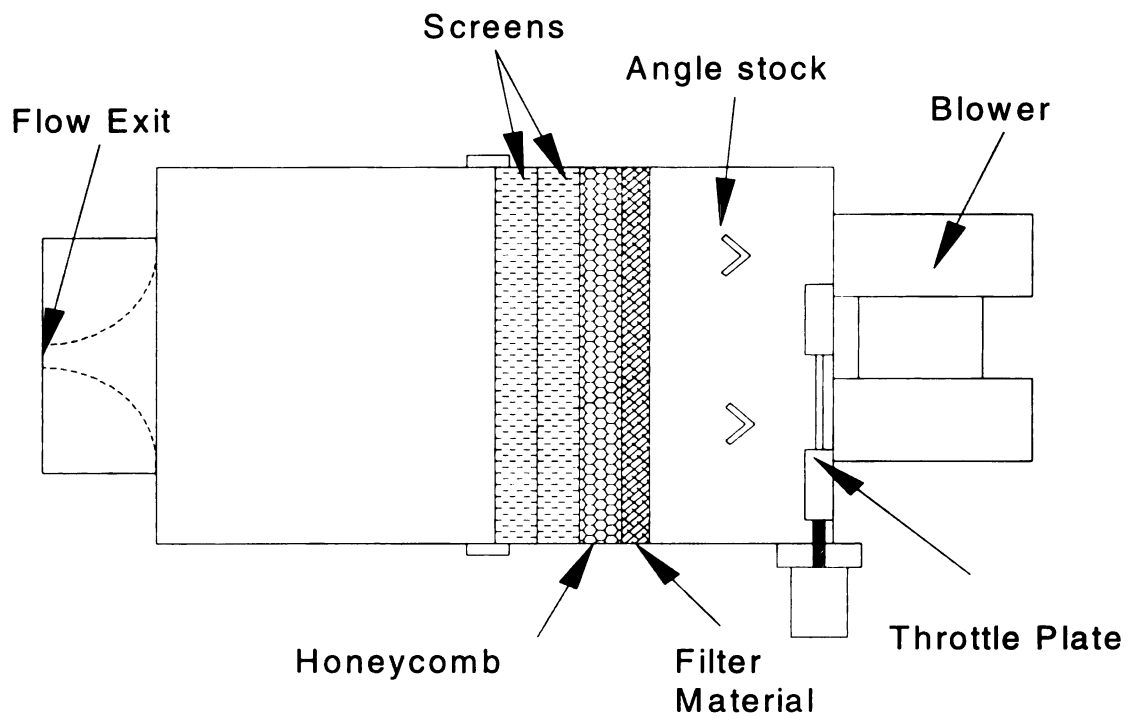


Figure 3.4 Top view of the calibration facility showing the flow conditioning.

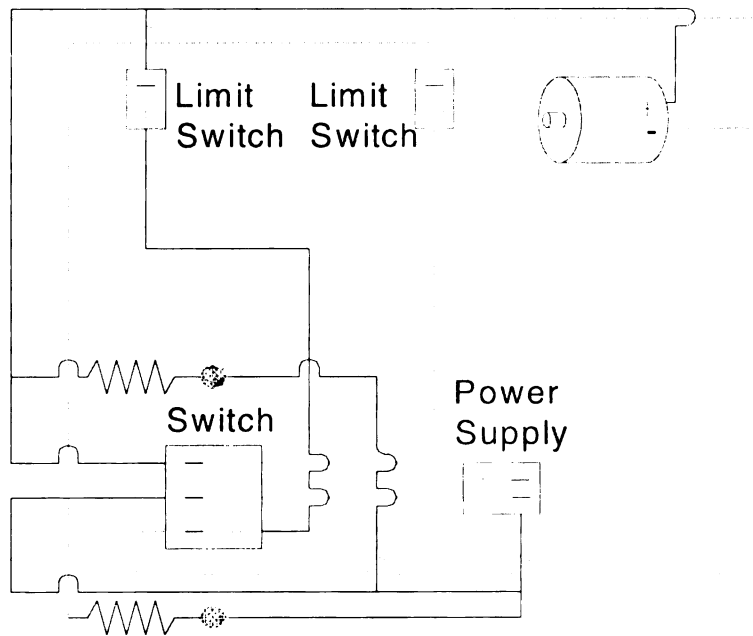


Figure 3.5 Wiring diagram for the calibration unit.

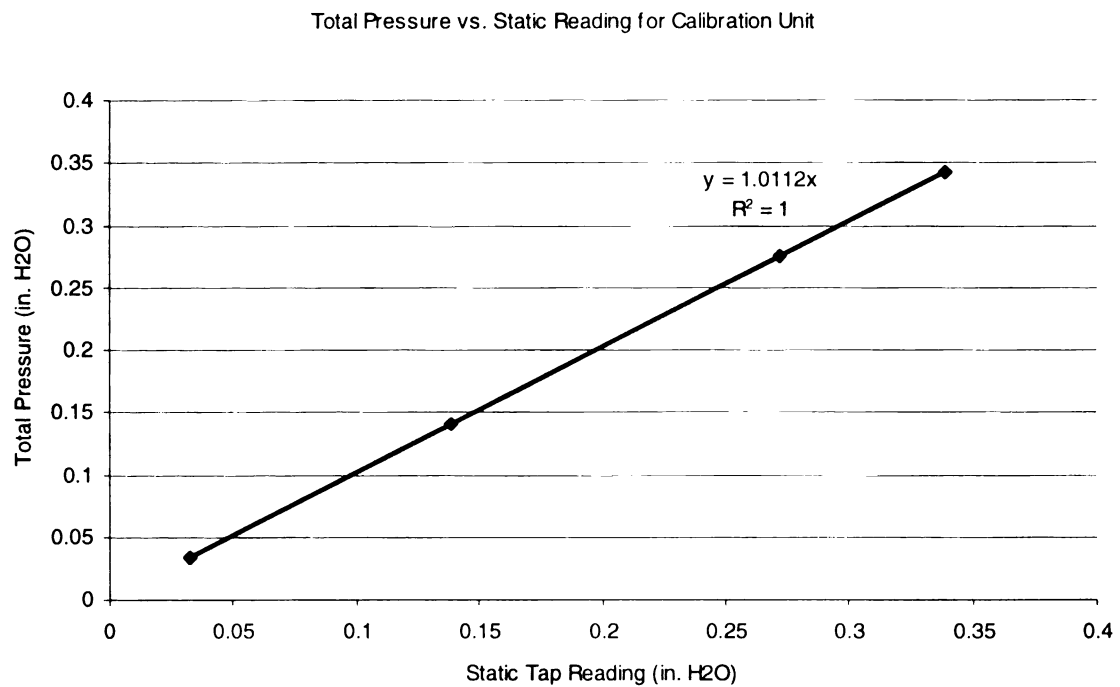


Figure 3.6 Total pressure vs. the static tap reading for the calibration unit.

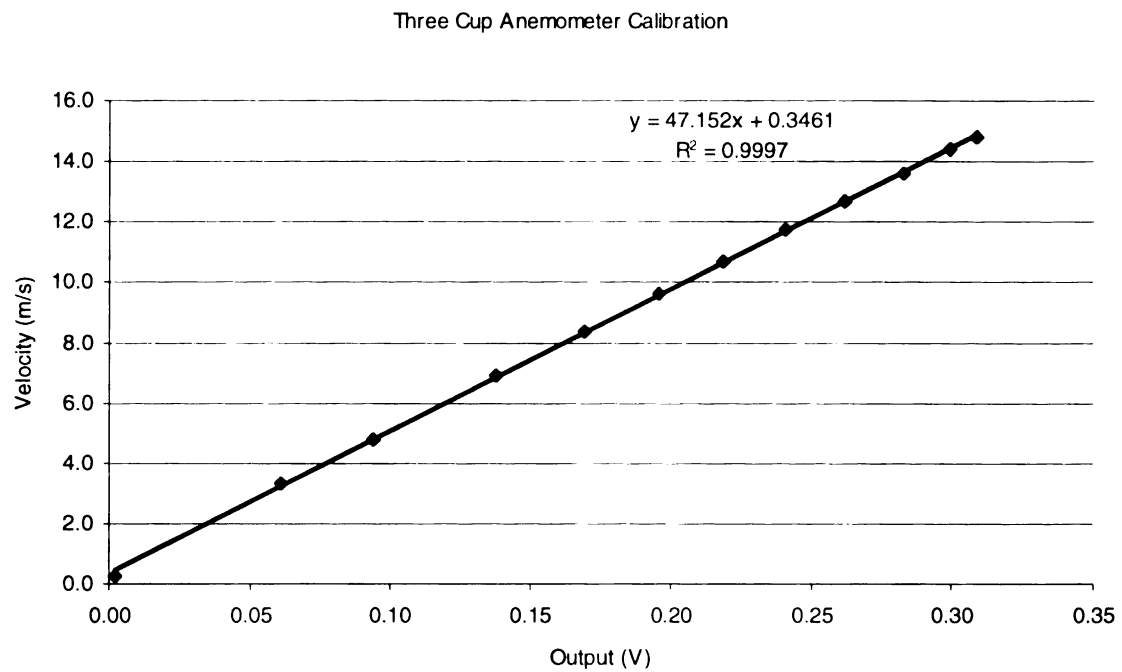


Figure 3.7 Three cup anemometer calibration.

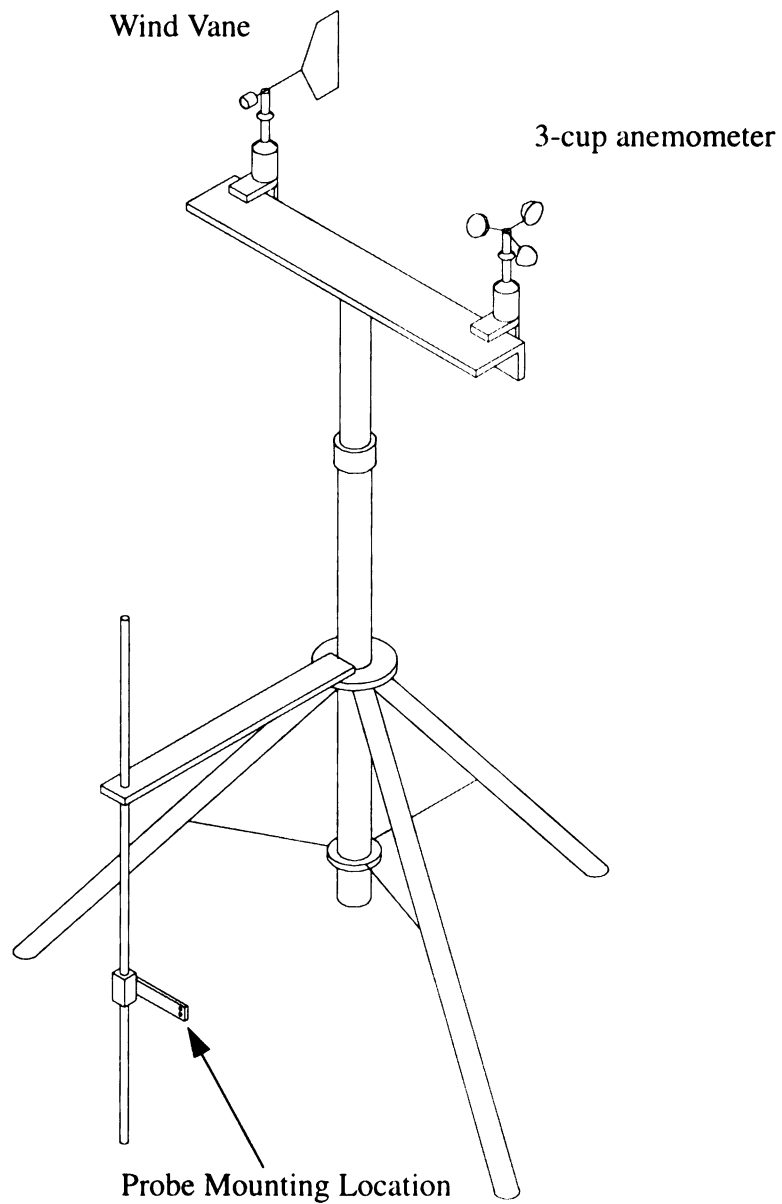


Figure 3.8 Tripod used to mount the three cup anemometer, wind vane and hot wire probes.

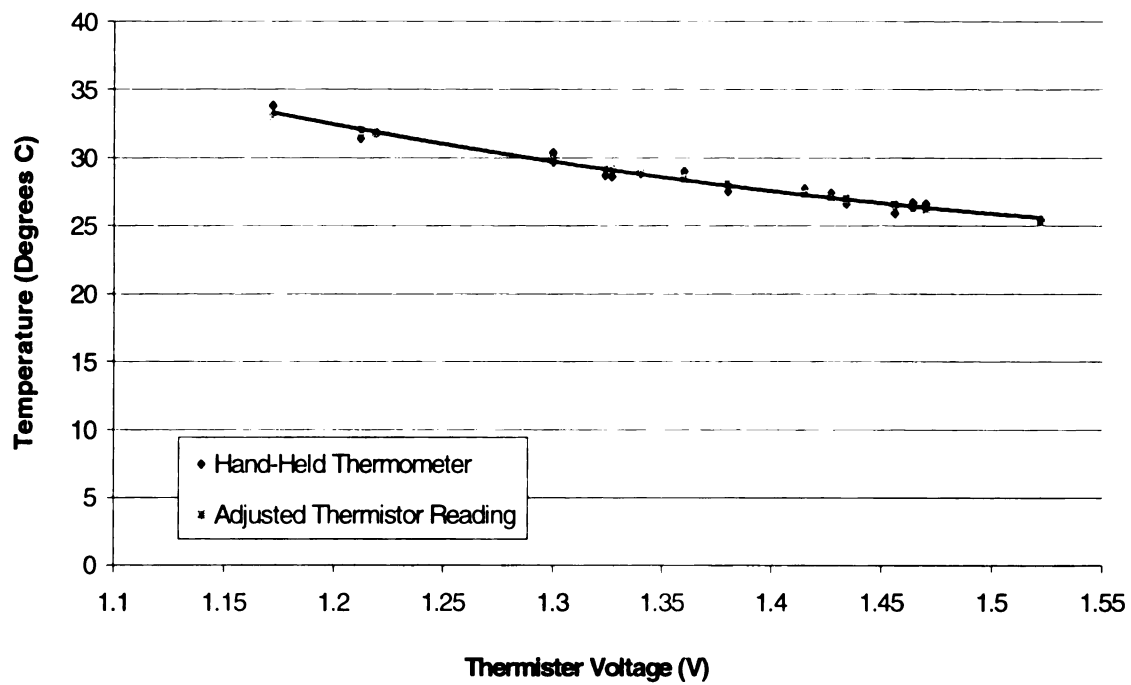


Figure 3.9 Thermistor re-calibration due to large ambient temperatures.



## 4.0 Hot Wire Techniques

The data recorded at the SLTEST site were acquired with the Michigan State University compact vorticity probe developed by Foss et. al. [11]. This probe consists of two parallel hot-wires mounted in conjunction with an X-wire array; see Figures 4.1 and 4.2. The two parallel wires of the compact vorticity probe, separated by a nominal distance of 1 mm, were used to measure two independent velocity magnitudes of the approaching fluid. The X-wire array is used to measure the angle between the resolved velocity (in the plane of the X-array) and the probe axis. From these three values, two components of the velocity vector as well as the corresponding vorticity component could be computed. Section 4.1 presents the operation of a single hot-wire sensor, including the calibration at the SLTEST site and a detailed uncertainty analysis. Section 4.2 presents the workings of an X-array hot-wire sensor, including its calibration, processing algorithm and uncertainties. Section 4.3 will cover the M.S.U. compact vorticity probe, its calibration, processing algorithms and the resulting measurement uncertainties.

### 4.1 Single wire calibration and uncertainty

A typical single wire hot wire sensor is shown schematically seen in Figure 4.3. The probes were fabricated using  $5\mu\text{m}$  diameter, 3mm long Tungsten wire in the Turbulent Shear Flows Laboratory (TSFL), MSU. The active region of the sensor was constructed of Tungsten to be 1mm long and  $5\mu\text{m}$  in diameter. Each end (1mm length) of the Tungsten was plated with copper to  $30\mu\text{m}$  in order to ensure the main resistance of the

sensor was concentrated in the 1 mm active region. The copper plating also allowed the Tungsten sensor to be easily soldered to the supporting broaches.

The calibration of the sensors was performed in a “quasi-steady” manner. This quasi-steady calibration involved slowly traversing a throttle plate across the blower exit, see Figure 3.4. This process was performed at a constant rate by a DC motor. The velocity of the calibration stream was varied continuously (albeit non-linearly) from 0.5 m/s to 12 m/s over a 50 second period. The calibration was termed either a ‘spin-up’ (velocity increasing) or ‘spin-down’ (velocity decreasing). Data samples from the hot-wire sensors, the pressure transducer and the thermistor were acquired at 200 Hz over this 50 second period. The pressure reading across the contraction of the calibration facility was used with the Bernoulli equation to predict the velocities seen by the sensors. Previous work has shown that under slow throttle plate movements the steady Bernoulli equation is still valid. The calibration time of 50 seconds was chosen for this reason.

The recorded calibration data were used in conjunction with the modified Collis and Williams equation [21]

$$E^2 = A + BQ^n \quad 4.1$$

where E is the voltage recorded from the hot-wire anemometer and Q is the exit velocity of the calibration stream. The processing algorithm cycled through a range of ‘n’ values (from 0.3 to 0.7 in steps of 0.02) while linearly curve fitting  $E^2$  verses  $Q^n$ . The curve fit with the smallest standard deviation was selected and the corresponding values of A, B, and n were assigned to the wire. An example of a single calibration can be seen in Figure 4.4.

The Bernoulli equation was used for the calibration of one sensor on the compact vorticity probe. This sensor then served as the reference signal for the other three sensors on the same probe (the other straight wire as well as the X-array). This process allowed for the sensors to be calibrated over the high frequency fluctuations in the calibration stream not observable through the less sensitive pressure reading. This high frequency calibration was necessary to ensure instantaneous velocity differences between the sensors were real and not a result of the calibration method.

The range of velocities over which the calibrations coefficients were determined was dependant on the range of velocities observed by the probe during the data acquisition period. All probes were initially calibrated from 0.5 m/s to 12 m/s in the calibration stream before (*pre-calibration*) and after (*post-calibration*) the data acquisition. The data recorded from each specific day were then examined to see the range of velocities the hot wire sensors saw over the period of data acquisition. Figure 4.5 shows an example histogram of the observed velocities for the evening of 25-July, 2001. For this specific example, the calibration was then performed spanning a range from 2.5 m/s to 9 m/s. Calibrations for the other two days (18-July and 19-July) were performed from 2 m/s to 8 m/s.

The accuracy of the recorded data set was determined through examination of the pre- and post-calibration data. Under laboratory conditions, if any discrepancies about the acquired data were to arise, one could easily discard the existing data set and re-take the data without hesitation. This was not the case for the current research. As a result, the discrepancies must be quantified so one may assess the accuracy of the resulting data.

The pre-calibration and the post-calibration data sets were examined for each day data were acquired. The pre-calibration and post-calibration of a sensor produced two independent sets of A,B, and n constants. For a range of inputted voltages, equation 4.1 was used along with each set of constants to produce two sets of predicted velocities. If a sensor predicted the same velocities using both the pre- and post-calibration constants, then the data set was considered accurate. If not, drift had occurred on the sensor. Drift occurs from a change in the resistance of the sensor over the period of data acquisition. Drift cannot be accounted for in the data processing routine since one cannot determine when in the data set the drift occurred. As a result, data sets with large amounts of drift were discarded.

The amount of drift that a wire had experienced was gauged as follows. The voltage data recorded during the post-calibration was processed with the A,B, and n constant values that were determined from the pre-calibration. A velocity was then calculated from these data (using equation 4.1) and compared to the Bernoulli velocity calculated from the recorded pressure. From this, the quality of the data set recorded between the two calibrations could be accurately determined. Figure 4.6 shows an example drift comparison taken on 19-July. In this plot, it can be seen that the accuracy of this wire is within  $\pm 2\%$  over the entire data range. Differences between the pre- and post-calibrations of up to 10% were accepted for this research. The accuracy of all the straight wire sensors used for the three data sets can be seen in Appendix A.

The slight offset in most of the pre- and post-calibration data visible in the three data sets prompted the author to combine the pre- and post-calibrations. Since drift is non-linear and may occur at any point throughout the data acquisition (be it right after pre-cal-

ibration, or right before post-calibration), it was decided that combining the pre-and post-calibration data would produce the most accurate results. Figure 4.7 demonstrates the pre-calibration data (lower diamonds), the post-calibration data (upper open circles), and the best fit trend line through both sets. Using the pre-calibration data alone, typical standard deviations were on the order of less than 0.05 m/s. Using the combination of both the pre- and post-calibration data, typical standard deviations increased to a range of 0.05 m/s to 0.20 m/s. The entire set of plots showing the combination of the pre- and post-calibration data for all the sensors used over the three days can be seen in Appendix B.

#### **4.2 X-wire calibration, processing and uncertainty**

An X-wire probe consisted of two hot-wire sensors mounted in an X pattern; see Figure 4.8. The two wires were oriented at  $\pm 45^\circ$  to the probe axis and separated by a distance of 1 mm (into the page). Each sensor of the X-wire probe was fabricated in the same manner as a single hot-wire with the same 1 mm active region. Each X-array had the outputs  $E_1$  and  $E_2$  corresponding to the output voltages of each sensor in the array. Processing techniques discussed in the following paragraphs allowed for these outputs to be transformed into the speed and angle of the approaching fluid. This allowed for the simultaneous measurement of two velocity components. However, since the compact vorticity probe contained two parallel hot-wires as well as the X-array, the speed predicted by the X-array was not used.

Each X-array had to be calibrated for a range of angles as well as a range of velocities. To do this, the vorticity probe(s) was affixed to a D-shape bracket attached to the calibration unit. The probe was aligned so that the X-array was centered under the pivot

point, just downstream of the exit plane. The zero angle alignment was held constant throughout pre- and post-calibrations by an alignment mark made on the floor of the data cart. The probes were then rotated to an angle of -36 degrees with respect to the exiting fluid and either a 'spin-up' or 'spin-down' was performed on the probes. The probes were calibrated at 13 discrete angles from -36 degree to +36 degrees in 6 degree increments. For each specific angle, two sets of A,B, and n constants could then be computed, one for each wire in the X-array. The calibrations were performed for each angle in the same manner as described in Section 4.1.

#### 4.2.1 X-wire processing algorithm

The most accurate algorithm for X-array processing has been the subject of considerable debate. The current research utilizes a "curve-intersection" method proposed by Morris [21] as an adaptation to the "speed-wire / angle-wire" method proposed by Foss [9]. In the current method, the X-wire probe is calibrated for 13 angles ranging from  $-36^\circ \leq \gamma \leq 36^\circ$  in  $6^\circ$  increments. This results in 13 sets of constants (A,B,n) for each sensor in the X-array, corresponding to the 13 calibration angles. The experimental data are acquired as time series values of the voltage pair  $E_1, E_2$ . The processing algorithm begins by picking out the  $E_1, E_2$  voltage pair for each time step. Using this  $E_1, E_2$  pair, equation 4.1 is then solved for  $Q_1(E_1, \gamma_i)$  and  $Q_2(E_2, \gamma_i)$ , where  $i = 1, 2, \dots, 13$ . In other words, for each time step, the algorithm uses the measured voltage and the corresponding A, B, n values (for each of the 13 calibration angles) along with in equation 4.1 to solve for the flow speed. This was done each sensor. It is then possible to plot the predicted velocity verses the corresponding angle (associated with the specific A, B, n constants) for

both sensors. The “true” velocity and thus the “true” angle are then represented by the intersection of these two functions. This is found by curve fitting the nearest points of each curve with a second order polynomial and then solving for the intersection point. Figure 4.9 shows an example plot of the 13 predicted velocities of each wire for a given voltage pair.

#### 4.2.2 X-wire uncertainties

The accuracy of the X-array was determined by the amount of drift the array had experienced. However, since the current research used X-wires to measure the flow angle  $\gamma$  and not the speed, determining their drift based on predicted velocity would not suffice. The amount of X-wire drift was determined using the same method as described in Section 4.1, but the predicted angles were examined as opposed to the predicted velocity. Again, the 13 sets of constants (A, B, and n) for each wire were taken from the pre-calibration data along with the 13 time series from the post-calibration data (one time series for each angle). The data were then processed using the algorithm described previously in Section 4.2.1. For each time series, the predicted angle from the processing algorithm was then compared to the mechanical angle determined by the physical probe orientation. The quality of the data set recorded between the two calibrations was then determined from this comparison.

Figure 4.10 shows an example drift comparison from an X-array taken on 19-July. It can be seen that the X-wire shows no visible drift, since the pre-calibration A,B, and n constants correctly predict all 13 angles given the post-calibration time series. In this case, the lines are all constant over the entire range of data (2 - 8 m/s), and equally spaced over the entire range of  $-36^\circ \leq \gamma \leq 36^\circ$ . Typical angle drift on accepted data sets was less

than 2 degrees over the range of  $-18^\circ \leq \gamma \leq 18^\circ$ . Larger variations outside of this range were accepted due to the difficulty in the measurement of larger angles. The variations of all the X-wires used for all three data sets can be seen in Appendix A.

The slight offset in most of the pre- and post-calibration data visible in the three data sets prompted the author to combine the pre- and post-calibration data. The two pre- and post- calibration data sets were combined into one data set used for calibration following the same method described in the straight wire section. The entire set of plots showing the combination of the pre- and post-calibration data for all the sensors used in the three data sets can be seen in Appendix B.

### **4.3 Vorticity Probe**

The data for the current research were acquired at the SLTEST site using a four-wire spanwise vorticity probe, or a “Mitchell” Probe. The probe is a combination of two parallel hot-wires interlaced within the spacings of an X-wire probe. Figure 4.1 shows the two dimensional geometry of the Mitchell Probe, while Figure 4.2 shows a perspective view.

The two straight wires were calibrated as discussed in Section 4.1. The processed output from these two straight hot-wires gave a time series of the magnitude of the velocity at each sensor location (these two magnitudes will be referred to as  $q_1$  and  $q_2$ ). The X-wire within the Mitchell probe was calibrated using the methods described in Section 4.2 for 13 angles spanning  $-36^\circ \leq \gamma \leq 36^\circ$ . The processed X-array data yielded a time series of the angle  $\gamma$  acquired at the same instant as  $q_1$  and  $q_2$ . The following paragraphs



describe the processing used to transform the time series of  $(q_1, q_2, \gamma)$  into the desired velocity time series. Section 4.3.1 will review the algorithm used to transform the time series of  $(q_1, q_2, \gamma)$  into the vorticity time series and Section 4.3.2 will cover the probe uncertainties. The spanwise vorticity probe and the corresponding processing algorithm were originally developed by Foss et al. and are more thoroughly described in references [12] and [10].

The coordinate system used throughout the current research was a standard laboratory coordinate system as opposed to the standard atmospheric coordinate system. The x-axis was assumed positive in the flow direction. The y-axis was taken as positive extending outward normal from the wall (desert floor) and the z-axis was then computed from the right-hand rule. From the time series of  $(q_1, q_2, \gamma)$  taken from each probe, the specific u, v, and w velocity components could be computed as:

$$u = \left( \frac{q_1 + q_2}{2} \right) \cos(\gamma) \quad 4.2$$

$$v = \left( \frac{q_1 + q_2}{2} \right) \sin(\gamma) \quad 4.3$$

for a probe oriented to measure the vorticity in the z-direction ( $\langle \omega_z \rangle$ ), or:

$$u = \left( \frac{q_1 + q_2}{2} \right) \cos(\gamma) \quad 4.4$$

$$w = \left( \frac{q_1 + q_2}{2} \right) \sin(\gamma) \quad 4.5$$

for a probe oriented to measure the vorticity in the y-direction ( $\langle \omega_y \rangle$ ). All statistical quantities were averaged over the entire range of files for which the ambient conditions were considered constant (see Section 5.1).

It should be noted that the angle  $\gamma$  used to compute the velocity and vorticity components was the *adjusted* angle of the fluid with respect to the probe axis (the x-axis). For the probes oriented to measure  $\langle \omega_y \rangle$ , the angle of the fluid measured by the X-array was the horizontal (left-right) angle of the fluid. The angles for the  $\langle \omega_y \rangle$  probes were detrended according to the analysis presented in Section 5.1 for each independent data set. For probes oriented to measure  $\langle \omega_z \rangle$ , the angle of the fluid measured by the X-array was the vertical (up-down) angle of the fluid with respect to the probe axis. Slight deviations from a zero mean reading in the vertical angle meant the  $\langle \omega_z \rangle$  probe was not oriented exactly parallel to the wall. The mean value observed in the  $\langle \omega_z \rangle$  angle measurement was subtracted from the probe for each day, giving the *adjusted* angle  $\gamma$  used in the data processing. Figure 4.11 shows the typical distribution of the mean vertical angle. This specific data set was taken on 18-July, 2001, and had an overall mean value of -0.1 degrees which was subsequently subtracted from each file taken over that evening.

#### 4.3.1 Vorticity Algorithm

A vorticity time series was also computed from the measured values of  $(q_1, q_2, \gamma)$ . A modified “Taylor’s frozen flow hypothesis” was used along with the convection velocity of the flow to create a parallelogram shaped micro-circulation domain (in time). Specifically, unlike the original hypothesis (which was used for the flow downstream of a turbulence generating grid in a wind tunnel and made use of the time averaged velocity as the convection speed), the present study has used the average of the two recorded velocity magnitudes  $[\langle U \rangle = (q_1 + q_2)/2]$  as the convection velocity to create this parallelogram; see Figure 4.12. The velocities  $q_1$  and  $q_2$  are known at the top and bottom of the micro-

circulation domain, indicated by dark circles in the figure. The normal component of velocity,  $v$ , was computed at the left and right sides of the mirco-circulation domain, indicated by open circles. The height of the micro-circulation domain ( $\Delta y$ ) was a fixed physical distance defined by the separation of the two straight wires. The measurement of this distance will be described in the following section. The length of the mirco-circulation parallelogram ( $\Delta s$ ) was set to be roughly equal to the domain height ( $\Delta y$ ). This was accomplished as follows.  $\Delta s$  was defined from the velocities [ $q_1(t_n)$  and  $q_2(t_n)$ ] at an instantaneous time  $n$  to be

$$\Delta s_n(m) = \frac{1}{2m+1} \sum_{i=n-m}^{i=n+m} \left( \frac{q_1(t_i) + q_2(t_i)}{2} \right) \Delta t \quad 4.6$$

where  $m$  was increased, starting from  $m = 1$ , until  $\Delta s_n > \Delta y$ . When this was accomplished, the number of data points spanning  $\Delta s$  was defined as  $2M$  ( $M$  being the integer number of time records needed to create one half of the mirco-circulation domain). The number of points spanning  $\Delta s$  ( $= 2M$ ) was variable and was dependant on the convective velocity of the fluid as well as the sampling frequency. Typical values of  $2M$  were between 6 and 20 time steps [21].

The physical value of  $\Delta y$  and the calculated value of  $\Delta s$  determined the final size of the micro-circulation domain. Once this was accomplished, the average value of the vorticity within that domain was calculated from the velocity circulation around the domain since

$$\Gamma = \oint_C \vec{V} \cdot d\vec{s} \quad 4.7$$

and

$$\Gamma = \int_A \omega dA = \langle \omega_n \rangle (\Delta s)(\Delta y) \quad 4.8$$

where  $\Gamma$  is the circulation and  $V$  is the magnitude of velocity. For notation purposes, the mean value of a given quantity during the time interval  $t_{n-M} < t < t_{n+M}$  will be expressed within brackets  $\langle \rangle$ . For example, the angle of the micro-circulation parallelogram was the mean value of  $\gamma$  during the time period of the mirco-circulation:

$$\langle \gamma_n \rangle = \frac{1}{2M+1} \sum_{i=n-M}^{i=n+M} \gamma(t_i) \quad 4.9$$

The instantaneous average vorticity  $\langle \omega_n \rangle$  was computed by integrating the velocities  $q_1$  and  $q_2$  along the top and bottom of the mirco-circulation domain. The normal velocity component at the left and right sides of the micro-circulation interval was computed from  $v = (q_1 + q_2)(\sin \gamma)/2$ . Combining this with equations 4.7 and 4.8, the instantaneous average vorticity at time  $n$  is calculated as:

$$\langle \omega_n \rangle = \frac{1}{(\Delta s)(\Delta y)} \oint (\vec{V} \cdot d\vec{s}) = \frac{v(t_{n+M}) - v(t_{n-M})}{\Delta s} - \frac{\langle q_2 \rangle - \langle q_1 \rangle}{\Delta y} \quad 4.10$$

The process of calculating the instantaneous average vorticity  $\langle \omega_n \rangle$  involves dividing the circulation integral by a very small number  $[(\Delta s)(\Delta y)]$ ; see equation 4.10. The accuracy of  $\langle \omega_n \rangle$  therefore depends heavily on the accuracy of the  $(\Delta s)(\Delta y)$  product. Of the  $(\Delta s)(\Delta y)$  product,  $(\Delta s)$  is a mathematically computed from the size of  $(\Delta y)$ . However,  $(\Delta y)$  is a physically measured quantity and its accuracy is limited to the accuracy of the technique used to measure it. To account for this, a new technique was implemented for a more accurate measurement.

An accurate measurement of the distance separating the two straight wires ( $\Delta y$ ) was obtained by traversing the probe through the shear layer of the calibration facility. A threaded screw traverse mechanism was used to traverse the Mitchell Probe through the shear layer, which was very thin with a high velocity gradient. The resulting data were used to create the plot seen in Figure 4.13. As can be seen in this plot, the two wires produce identical representations of the shear layer, separated by a small distance. This distance is the distance which separates the two wires, or ( $\Delta y$ ). To compute ( $\Delta y$ ), one curve was shifted along the abscissa by small increments until the two curves lined up (Figure 4.14). For this particular probe, the ( $\Delta y$ ) measurement was 1.40 mm. For the other probe used in the current research, the ( $\Delta y$ ) measurement was 1.70 mm. The accuracy of this measurement was estimated at  $\pm 0.04$  mm, or a 2.5% uncertainty.

#### 4.3.2 Vorticity probe uncertainties

The amount of uncertainty present in the vorticity measurement was best estimated by examining the amount of drift that occurred in the straight wires and X-array that comprised each probe. The comparison of the pre- and post-calibrations for each straight wire and each X-array are available to the reader in Appendix A. The combination of both the pre- and post-calibration data for each wire can be seen graphically in Appendix B.

The spanwise vorticity measurement techniques were not developed as part of the current research and therefore will only be briefly discussed in this section. A detailed account of the uncertainty analysis of both the probe and the processing algorithm can be found in Foss and Haw [12]. From their research, the main source of error in the vorticity calculation was found to be electronic noise present in the time series data. The contribution of this electronic noise to the uncertainty of the calculation was found to be on the

order of 20 (1/sec.) [12]. The vorticity processing algorithm was performed on data acquired in the free stream of the calibration unit (at  $\gamma = 0^\circ$ ), which should theoretically contain little or no vorticity. Figures 4.15 and 4.16 show this result plotted from a range of 2 m/s to 8 m/s for the two vorticity probes used in this research. It can be seen that at the higher velocities, the noise level is on the order of 20 (1/sec.). This is relatively small, since a typical vorticity time series has a standard deviation on the order of 80-90 (1/sec.) with excursions over 500 (1/sec.) (Figure 4.17).

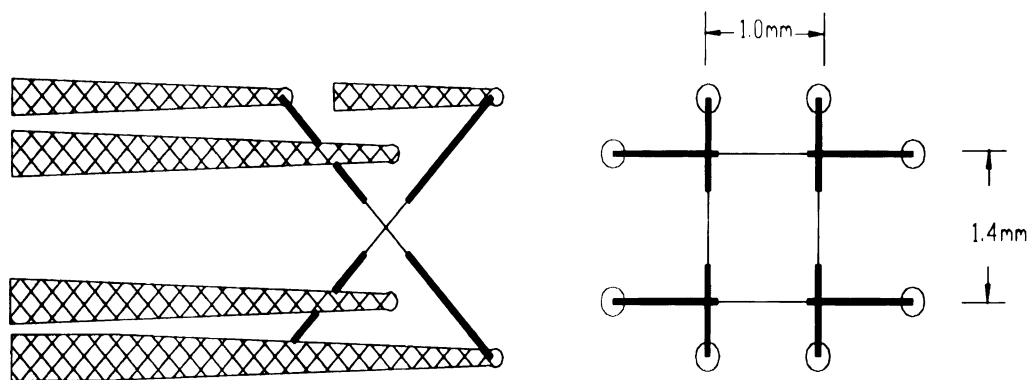


Figure 4.1 Geometry of spanwise vorticity probe.

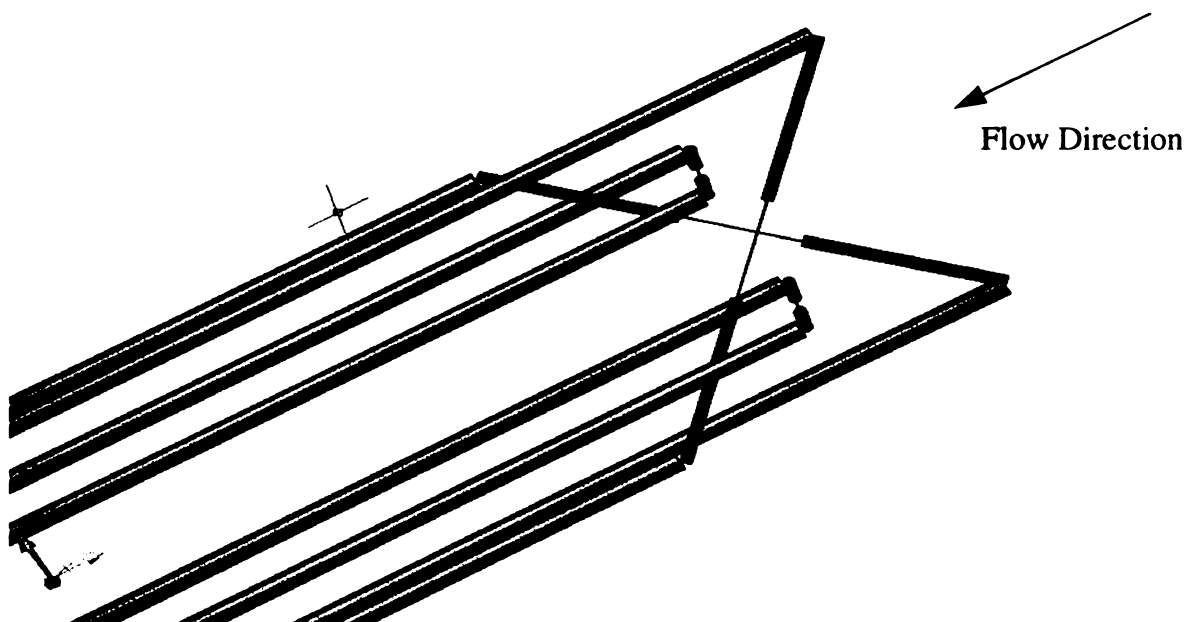


Figure 4.2 Perspective view of spanwise vorticity probe.

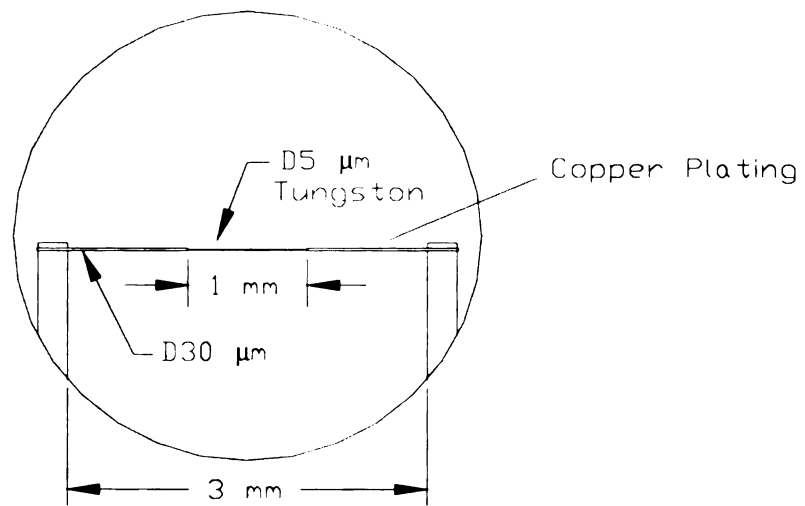


Figure 4.3 Geometry of a single hot-wire probe.

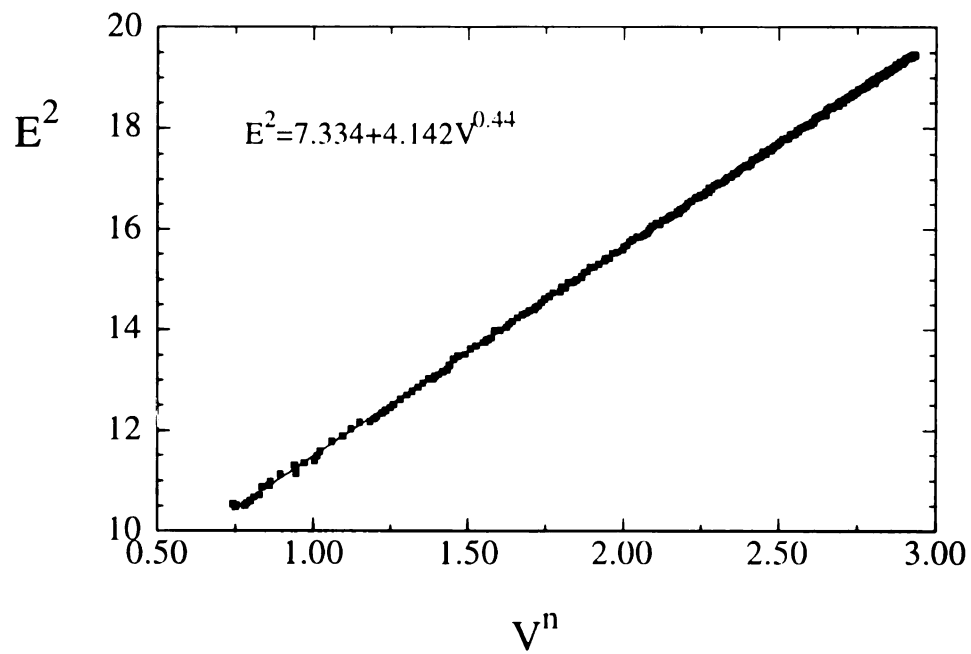


Figure 4.4 Sample calibration and fit.



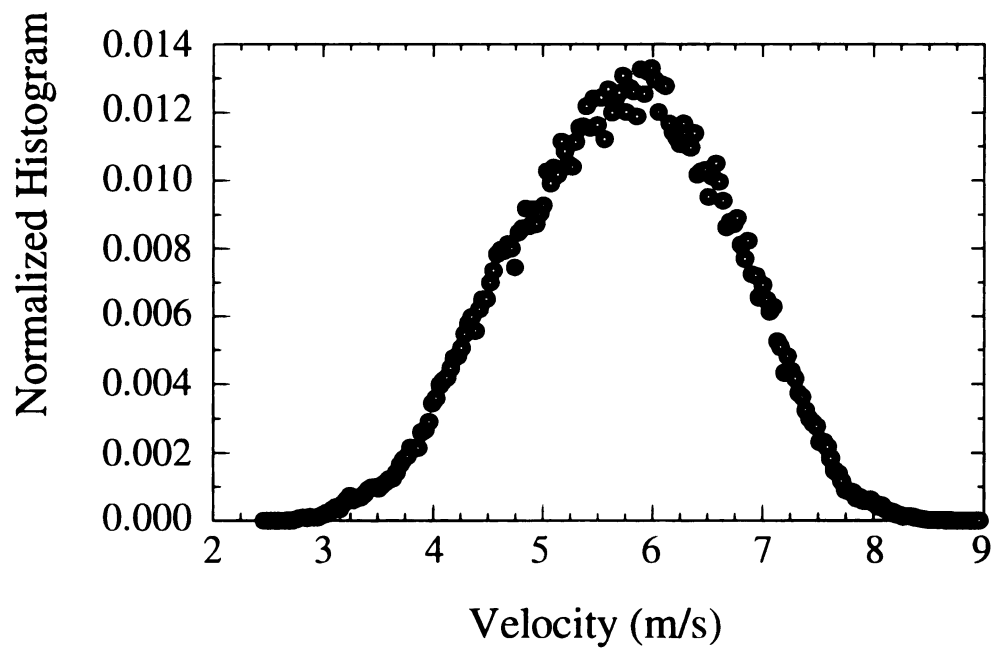


Figure 4.5 Normalized histogram of observed velocities from 25-July, 2001.

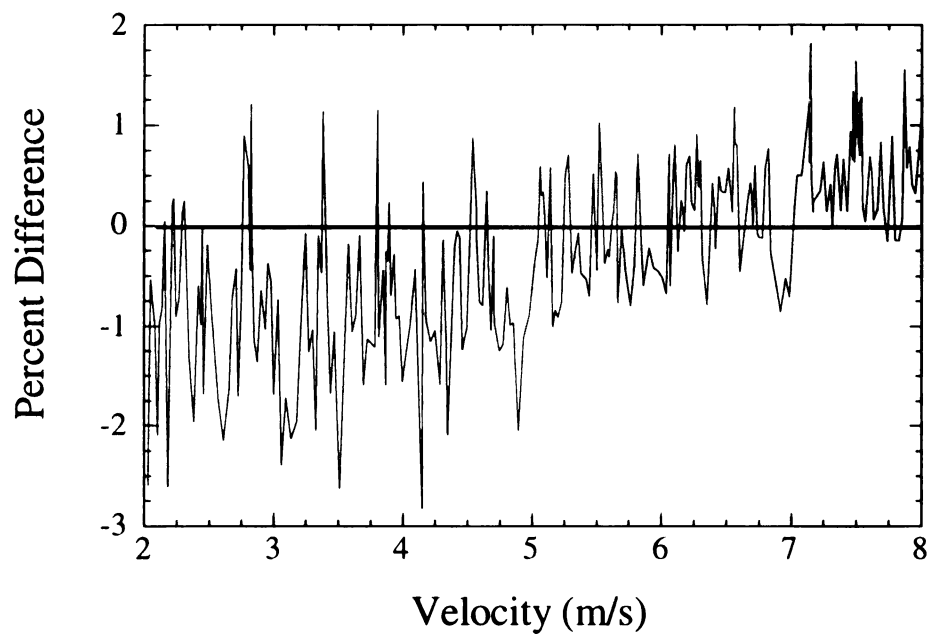


Figure 4.6 Example drift determination comparison taken on 19-July ( $\langle \omega_z \rangle$  probe, second straight wire).

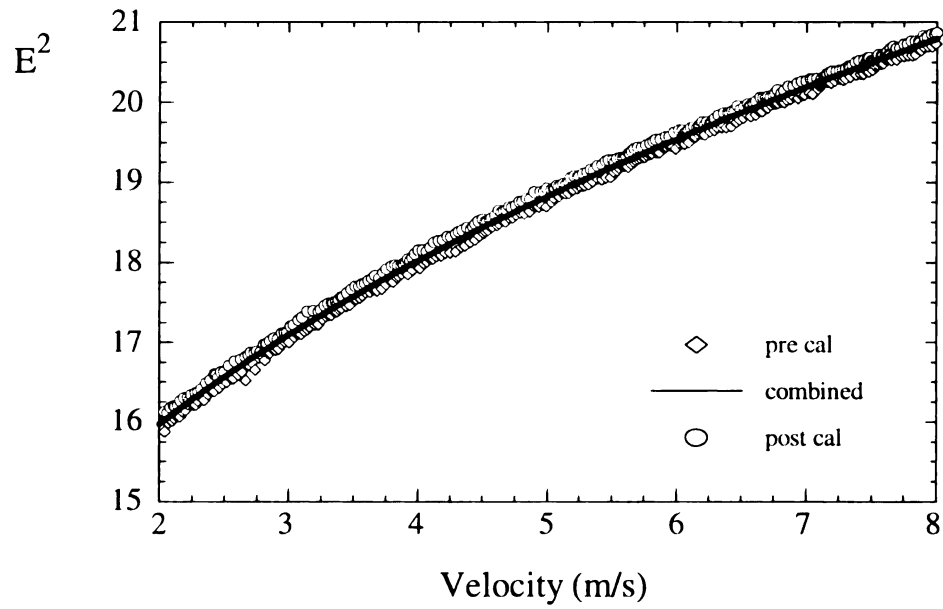


Figure 4.7 Pre-calibration data, post-calibration data, and the combined trend-line for 19-July ( $\langle \omega_y \rangle$  probe, first straight wire).

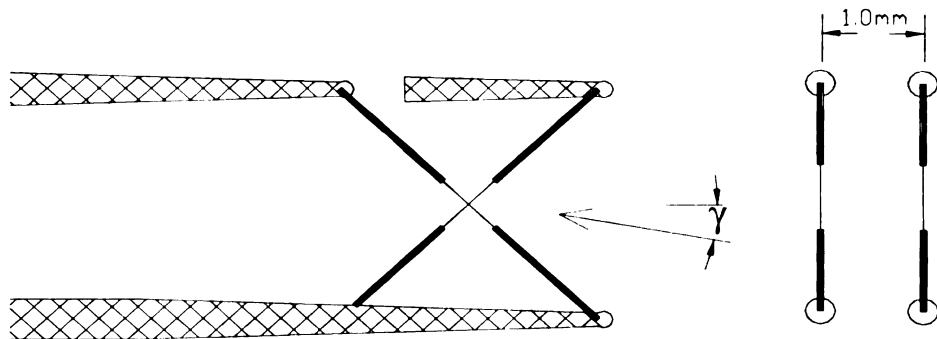


Figure 4.8 Geometry of the X-wire probe.

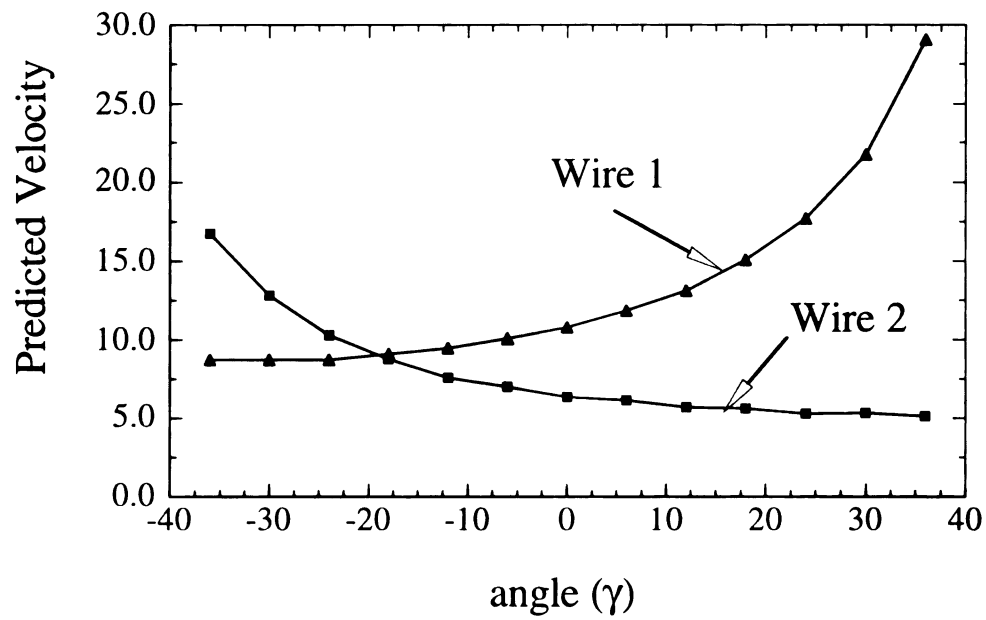


Figure 4.9 Sample data demonstrating the angle locating algorithm for X-wire processing.

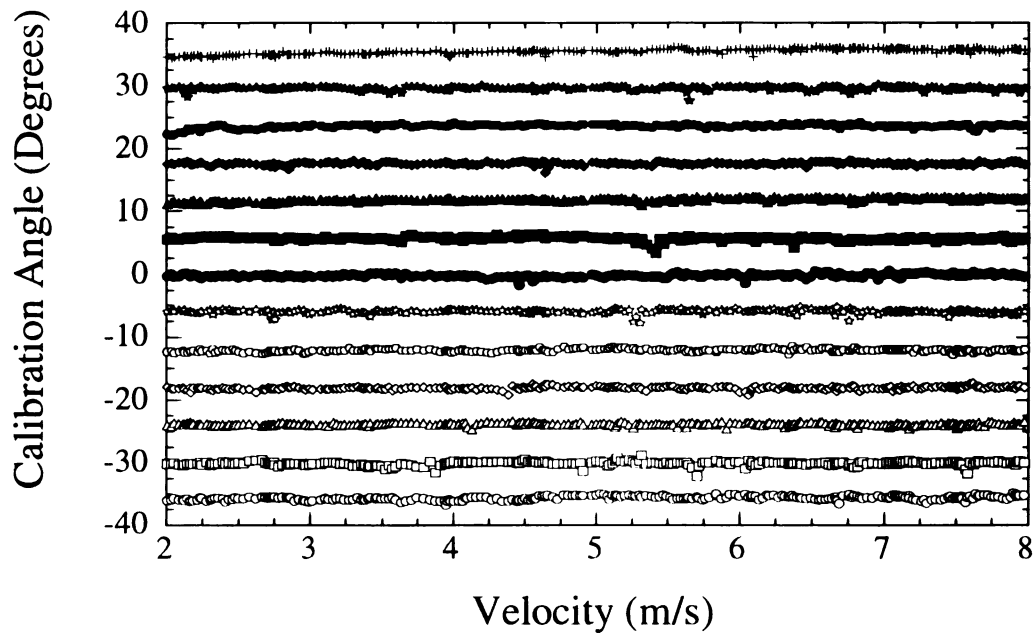


Figure 4.10 Example drift determination comparison for an X-wire taken on 19-July ( $\langle \omega_y \rangle$  probe).

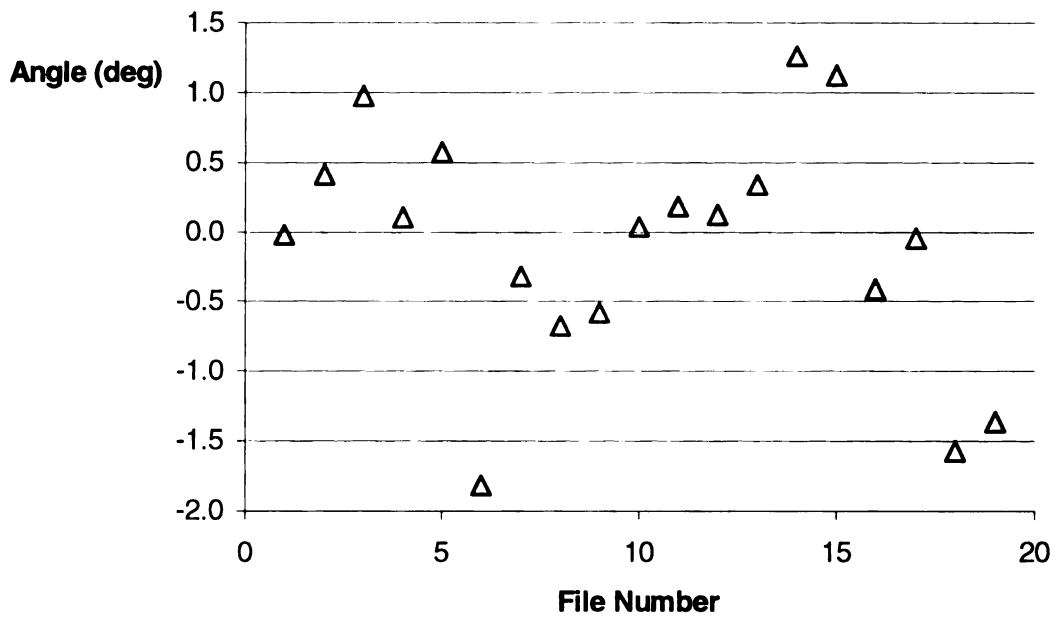


Figure 4.11 Mean vertical angle measured over the evening of 18-July, 2001.

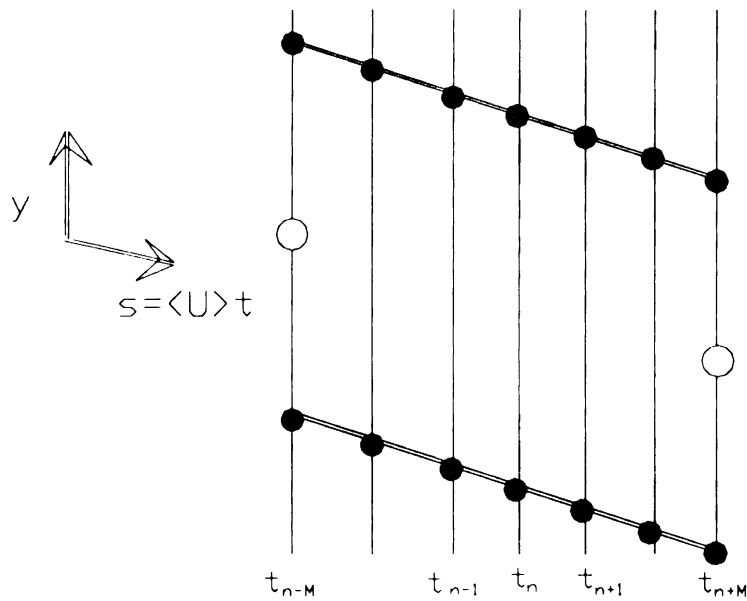


Figure 4.12 Schematic of the micro-circulation domain used in the vorticity algorithm.

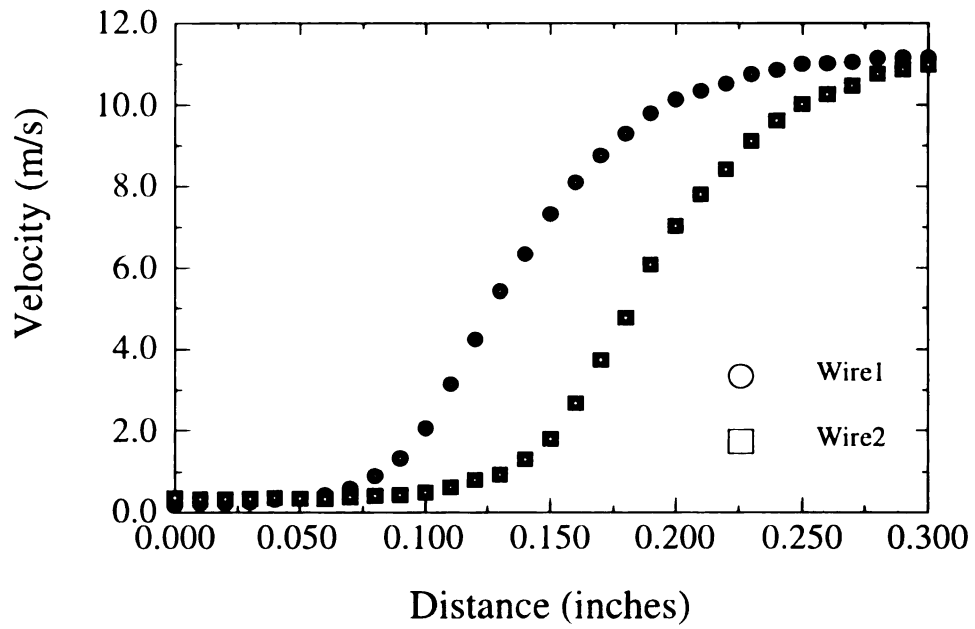


Figure 4.13 Velocity of each straight wire on the Mitchel Probe as it was traversed through the shear layer.

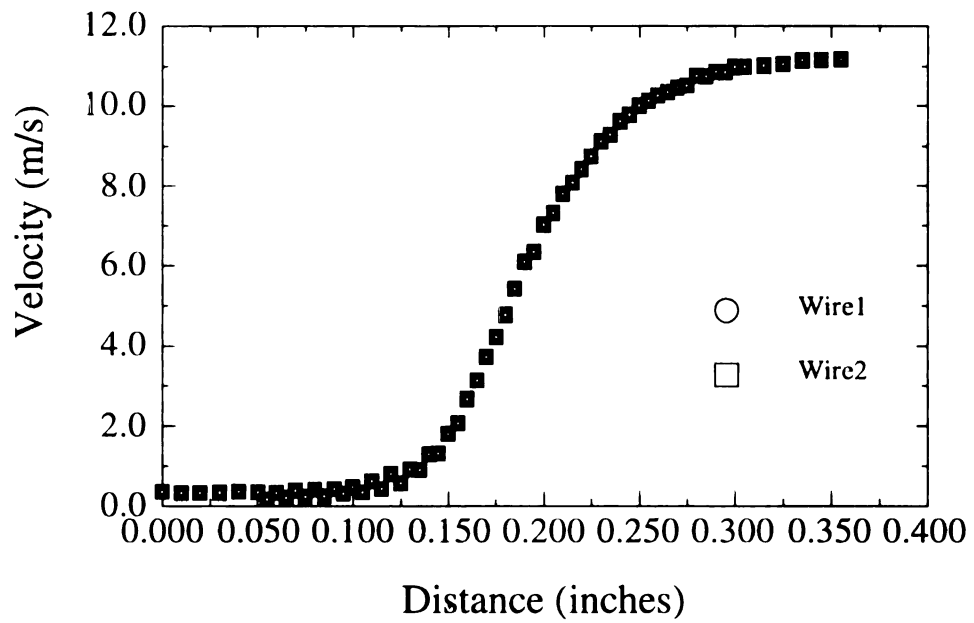


Figure 4.14 Collapse of shear layer traverse data used to compute  $(\Delta y)$ .

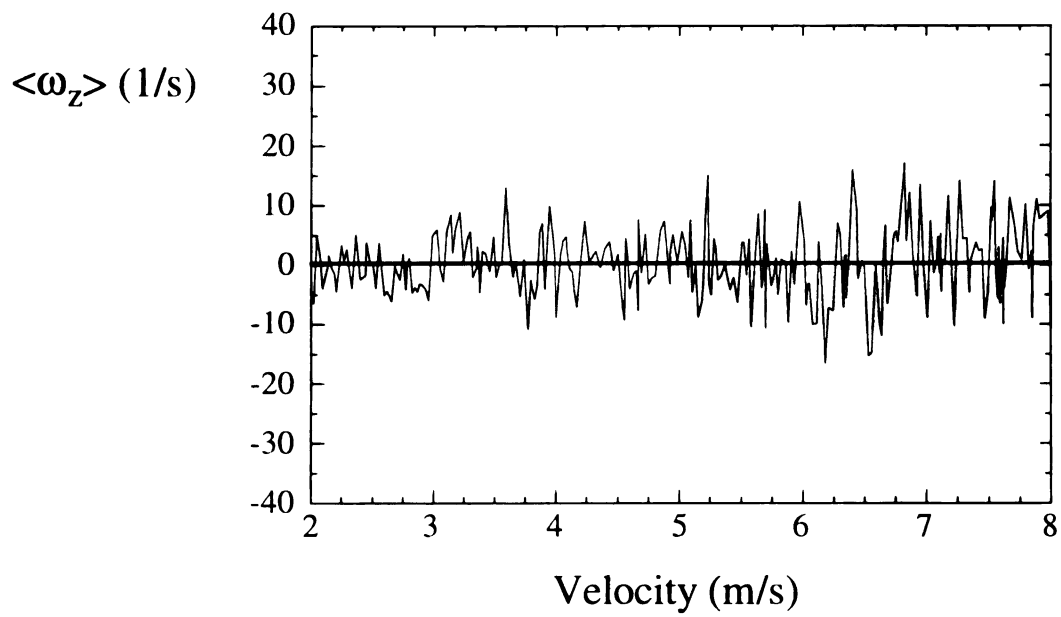


Figure 4.15 Vorticity probe and processing algorithm verification in a free stream of the calibration unit.

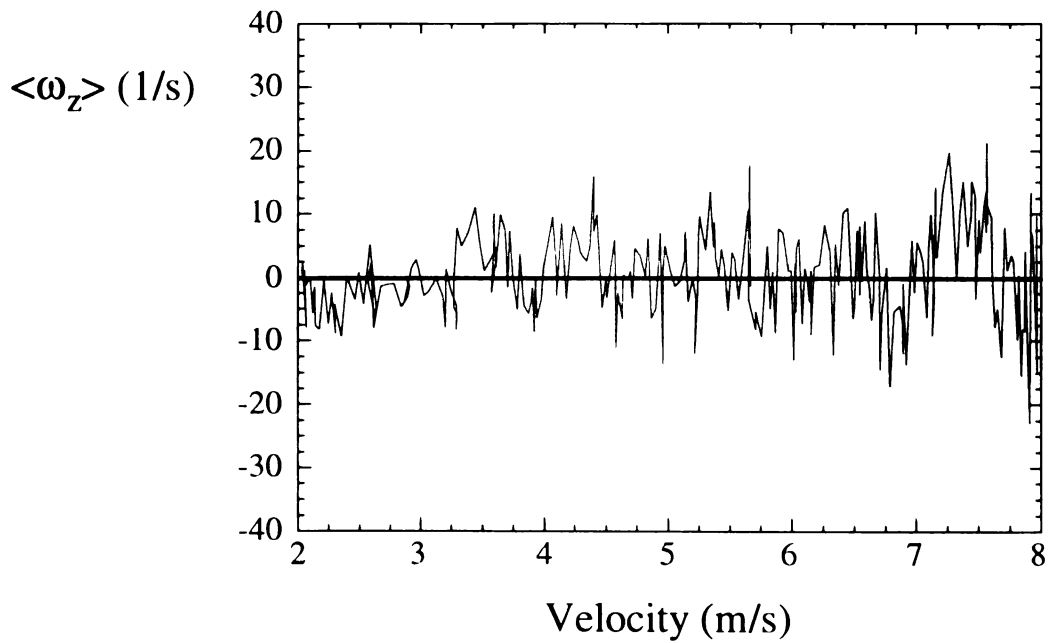


Figure 4.16 Vorticity probe and processing algorithm verification in a free stream.

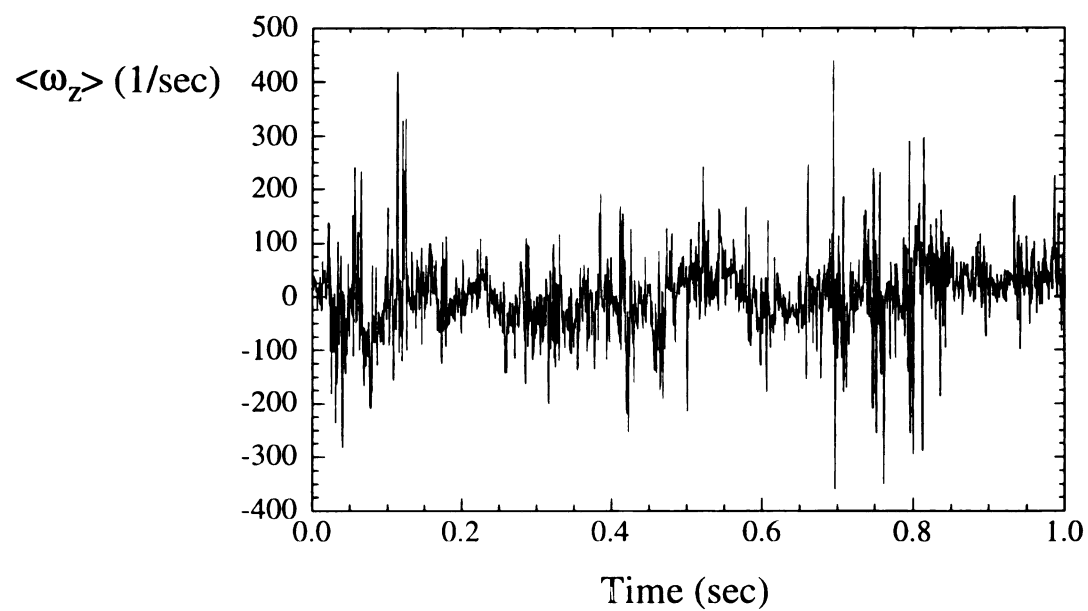


Figure 4.17 Sample vorticity time series from 25-July, 2001.

## 5.0 Results and Discussion

This chapter will serve to identify the characteristics of the near wall velocity and vorticity measurements taken in a high Reynolds number boundary layer flow. The data for the current research were acquired during three days at the SLTEST site. The ambient conditions present at the SLTEST site varied with each day. Section 5.1 will review the specific conditions which characterize each day that data were taken. Section 5.2 will describe the statistics derived from the velocity and vorticity measurements which are relevant to turbulence for these days. Section 5.3 will discuss the spectral properties of the data taken at the SLTEST site. Section 5.4 will discuss the probability density functions (PDF's) of the vorticity and their relevance to this research.

### 5.1 Daily Specifics

The data that were acquired at the SLTEST site were examined using methods described in the previous chapters. Acceptable conditions (constant ambient conditions and accurate hot-wire measurements) existed on three days of experimentation, resulting in three sets of data (to be referred to as 18-July, 19-July, and 25-July). Two probes were used for the data taken on 18-July and 19-July, and one probe was used on 25-July. When two probes were used simultaneously, one probe was used to measure  $\langle \omega_z \rangle$  and the other probe was rotated 90 degrees and used to measure  $\langle \omega_y \rangle$ . For convenience and organization, the probes will be referred to as the  $\langle \omega_z \rangle$  probe or the  $\langle \omega_y \rangle$  probe throughout the rest of this thesis. The purpose of this chapter is to cover in detail the results obtained from these data sets and compare statistical quantities over the three days. First, however,



the specific conditions of each day will be noted followed by the detailed analysis of the data. Table 5.1 displays the specific properties of each data set, including the probe measurement location ( $y_{measure}$ ), the time duration of the data set ( $T_{Duration}$ ), the Monin-Obukov length  $L_{Monin - Obukov}$  and the corresponding thermal stability parameter  $\zeta$  described in Chapter 2. A streamwise length scale  $L_x$  was also computed as

$$L_x = \bar{u} T_{Duration} \quad 5.1$$

where  $\bar{u}$  is the mean velocity over the entire data set.

### 5.1.1 18-July, 2001

Two vorticity probes were used on 18-July, 2001 to measure  $\langle \omega_z \rangle$  and  $\langle \omega_y \rangle$ .

Both probes were mounted 20 cm above the desert floor ( $y^+ = 3800$ ) separated by a spanwise distance of 2.2 cm. The wind direction was from the south. Twenty-eight files were acquired at 40 kHz, 60 seconds each. An analysis of the ambient conditions present during the acquisition of these data showed that the mean friction velocity shifted significantly after the 19th file had been acquired. The remaining 9 files were subsequently discarded. The streamwise distance  $L_x$  for these 19 files was nominally 4500m. This allowed for the small scale turbulent quantities to be well converged for this day. For example, the 18-July data contained over 24,000 records of the streamwise Taylor microscale ( $L_x/\lambda_u \approx 24,000$ ). Conversely, it was not possible to resolve the large scales present at the SLTEST site as a result of the extremely large scales present and the limited window of time for data acquisition. For example, the 18-July data contained only 20

records of a typical boundary layer thickness ( $L_x/\delta \approx 20$ ). The following paragraphs present the ambient conditions of 18-July, including the mean wind speed, wind direction, thermal stability parameter and friction velocity.

Figure 5.1 shows the steadiness of the prevailing wind on 18-July, spanning the time period that data were acquired. The top triangles represent the data taken by the three cup anemometer (located at  $y = 1.5$  m), and the bottom circles and x's represent the velocity measured by the two probes (located at  $y = 20$  cm). Data were averaged over 19 one-minute intervals. Figure 5.2 shows the direction of the wind over this same time period (again averaged over 19 one-minute intervals) measured by both the wind vane and the  $\langle \omega_y \rangle$  probe. From this graph, it can be seen that the wind direction was not constant. The variations were bounded by  $-8^\circ \leq \gamma \leq 1^\circ$  with a mean value of  $-4.41^\circ$  and an RMS of  $2.59^\circ$  as observed by the  $\langle \omega_y \rangle$  probe. Since a visible trend was not observed in the horizontal angle measurement, deviations from a mean value were assumed to be a result of the one-minute averaging technique and not a result of a shift in the mean wind direction (a shift in the mean wind direction was observed in the 19-July data, see the next section for how this was handled). For the 18-July horizontal angle data, the mean angle over the entire evening was subtracted from each individual data file, setting the mean flow angle over the 19 files to zero.

Figure 5.3 shows the thermal stability parameter,  $\zeta$ , plotted against time for 18-July, 2001, courtesy of the University of Utah. Data for this day were acquired from 7:50 to 8:12 p.m. As the figure shows, the MSU vorticity data were acquired in a period of unstable thermal conditions in the range  $-3 < \zeta < -2$ .

Figure 5.4 shows the friction velocity  $(u_{\tau})_{\text{II}}$  as a function of time throughout the evening of 18-July, 2001. The horizontal bars represent the mean friction velocity over the entire time period that data were taken. The solid circles overlaid on top of the bars corresponds to the mean friction velocity over the range of “accepted” files. Accepted files were files under which the ambient conditions appeared constant (such as the thermal stability parameter, the mean wind speed and direction, and the friction velocity). From this figure, it can be seen that after the “accepted” range of files, the mean friction velocity deviates from what appears to be a constant value, decreasing over time. The mean value of the friction velocity over these “accepted” files was taken as a constant value for the evening.

### 5.1.2 19-July, 2001

Two vorticity probes were also used on 19-July, 2001 to measure  $\langle \omega_z \rangle$  and  $\langle \omega_y \rangle$ . The probes were again mounted 20 cm above the desert floor ( $y^+ = 3800$ ) and separated in the spanwise direction by the same distance of 2.2 cm. The wind direction was from the south. Sixty files were originally acquired at 40 kHz, 60 seconds each. These files were reduced to 50 files due to a shift in the mean wind direction after the first 10 files had been taken (these first 10 files were subsequently discarded). The spanwise distance  $L_x$  for these 50 files was nominally 11,000m. This allowed for the small scale turbulent quantities to be well converged for this day. For example, the 19-July data contained over 336,000 records of the streamwise Taylor microscale ( $L_x/\lambda_{\text{II}} \approx 336,000$ ). The resolution of the large scales present at the SLTEST site for 19-July was better than 18-July, but still

not enough to fully resolve the large scale motions. For example, the 19-July data contained 55 records of a typical boundary layer thickness ( $L_x/\delta \approx 55$ ). The following paragraphs present the ambient conditions of 19-July, including the mean wind speed, wind direction, thermal stability parameter and friction velocity.

Figure 5.5 shows the mean wind speed (in one-minute averages) over the period that data were acquired on 19-July, 2001. The three cup anemometer and both probes are represented on this graph. The wind speed appears very steady over the fifty one-minute intervals. Figure 5.6 shows the mean wind direction, in one-minute averages, over this same period. A general trend was observed in the wind direction data over this time period. This very low-frequency motion is commonly observed in atmospheric work. The mean wind direction for 19-July was de-trended by methods frequently used in atmospheric boundary layer work. De-trending is a common practice used to eliminate the ‘red noise,’ or extremely low-frequency fluctuations, from the data [29]. De-trending basically involves eliminating the visible trend to produce a constant mean value. The wind direction data that were acquired at the SLTEST site on 19-July were de-trended as follows.

The one minute averages of the horizontal flow angle throughout the evening were independently curve fit for both the wind vane and the probe (see Figure 5.6). A mean difference was taken between the two curve fits, and the (negative) difference was then added to the angle measurements recorded by the probe. This in essence shifted the probe measurements down to the level of the recorded vane measurements. Finally, the (negative) value of the vane curve fit (corresponding to the proper abscissa location) was subtracted from these readings, de-trending the parabolic shape and placing the mean value of the probe angle measurements at zero degrees. This process effectively took the parabolic

shape of the wind direction measured by the probe and flattened it out across the abscissa. This process allowed for the use of surrounding information to get more accurate approximations of the local mean values.

Figure 5.7 shows the stability parameter for the evening of 19-July, 2001. Data for this evening were acquired between 9:41 and 10:41 p.m. As shown, the stability parameter increased quickly on this evening and reached a value near 0.6 over the period that the data were acquired. This is a significantly large value, indicating a stable (or stratified) ambient condition. The extent to which this thermal stratification affected the data will be discussed throughout the rest of this chapter.

Figure 5.8 shows the mean friction velocity  $(u_\tau)_s$  for the evening of 19-July, 2001. In this case, the friction velocity appears semi-constant across the entire range of data taken. However, the “accepted” range did not include the first few files taken during this evening due to a large direction change in the mean wind direction after the first 15 minutes.

### 5.1.3 25-July, 2001

On 25-July, 2001, only one probe was used to acquire data. The second probe (used to acquire data on the previous days) was damaged beyond repair between data sets, and therefore only records  $\langle \omega_z \rangle$  vorticity were recorded. The probe was mounted at  $y = 40$  cm this time ( $y^+ = 10, 300$ ), and the wind direction was again from the south. Sixty-five files were originally taken at 40 kHz, 90 seconds each. These files were reduced to 36 acceptable files due to a large shift in both the mean wind speed and direction (as well as the friction velocity) after the first 36 files had been taken. The remaining files were dis-

carded. The spanwise distance  $L_x$  for these 36 files was nominally 19,000m. This allowed for the small scale turbulent quantities to be well converged for this day. For example, the 25-July data contained over 481,000 records of the streamwise Taylor microscale ( $L_x/\lambda_u \approx 481,000$ ). The 25-July data produced the largest streamwise distance  $L_x$ , but still was not large enough to accurately resolve the largest motions as evidenced by the very low wavenumber ( $k_1 \eta \approx 10^{-3}$ ) spectral distributions. However, the statistical quantities ( $\bar{u}$ ,  $\bar{v}$ , etc.) indicated that convergence was achieved for all three data sets. For example, the 25-July data contained 94 records of a typical boundary layer thickness ( $L_x/\delta \approx 94$ ). The following paragraphs present the ambient conditions of 25-July, including the mean wind speed, wind direction, thermal stability parameter and friction velocity.

Figure 5.9 shows the mean wind speed (one-minute averages) taken on 25-July, 2001. This plot shows a very steady velocity reading from both the three cup anemometer (located at  $y = 1.5$  m) and the one probe used to acquire data on this day (located at  $y = 40$  cm). Figure 5.10 shows the mean direction of the wind over this period, measured by the wind vane. Only one probe was used on this day, so a probe measurement of the angle was not recorded; see Chapter 4 for more detail. The mean wind direction as measured by the vane was fairly constant, indicating the  $\langle \omega_z \rangle$  probe was well aligned with the flow direction throughout the data set.

The thermal stability parameter for the evening of 25-July, 2001 can be seen in Figure 5.11. Data were acquired on this evening from 8:20 until 9:24 p.m. This figure

e

e

t

th

a

5.

P

ve

T

de

ve

lat

no

frop

shows that the entire data set fell within the accepted range to be called a neutral condition ( $|\zeta| \leq 0.1$ ). Figure 5.12 shows the mean friction velocity for the evening of 25-July, 2001. Here, the friction velocity remained constant for the first hour, but steadily decreased after that. As a result, the “accepted” files were limited to the first hour of data acquisition (36 files).

The format used to discuss the results will present the thermally neutral data set (25-July) first followed by the thermally unstable (18-July) and thermally stable (19-July) conditions respectively. Although the thermally neutral data were acquired at a larger distance away from the wall, they will still serve as the baseline condition when compared to the two other conditions. An attempt to distinguish between the effects of probe location and the effects of thermal stability will also be made.

## **5.2 Mean flow statistics**

This section describes the mean flow statistics for each data set. The following paragraphs will present the mean and root-mean-squared (RMS) values of the velocity and vorticity components for each data set. Section 5.2.1 will describe the formulation of the Taylor microscale and corresponding Reynolds numbers. Section 5.2.2 will provide a detailed analysis of the dissipation estimate, and Section 5.2.3 will discuss the length and velocity scales for each day.

Table 5.2 displays these mean and RMS velocity and vorticity quantities calculated from the data acquired on the three specific days. The data acquired on 25-July has noticeably higher mean and RMS values of the velocity than the other two days. The data from 25-July were taken at a probe location of  $y = 40\text{cm}$ , while the data from the 18th and



2

3

4

5

6

7

8

9

10

11

12

13

14

15

16

17

18

19

20

21

22

19th of July were taken at probe locations much closer to the wall ( $y = 20\text{cm}$ ). When compared to each other, 18-July and 19-July had similar mean values for the three components of velocity. However, the RMS values of 18-July were noticeably higher than 19-July. This difference in the RMS values may be explained by the thermal effects discussed in Section 5.1. Data taken on 18-July were acquired under conditions that were considered unstable ( $\zeta < -0.1$ ) while the 19-July data were taken under stable conditions ( $\zeta \approx 0.6$ ). The unstable condition present in the 18-July data would cause higher fluctuations from buoyancy effects. The stratification that occurs during the stable condition would have suppressed the larger fluctuations on 19-July, causing the observed differences in the fluctuations between the two days.

The mean values of vorticity were not examined. From analysis of the vorticity probe [12], the mean values have an uncertainty of  $\pm 20$  (1/s). The calibration techniques used on the probe did not ensure an accurate mean vorticity measurement. These techniques did, however, ensure accurate fluctuation measurements. The RMS values of the spanwise and transverse vorticity can be seen in Table 5.2 as well. The vorticity RMS values for all three days was fairly consistent around 90 (1/sec.).

Table 5.5 displays these same flow data normalized by the friction velocity [ $u_\tau$ ,  $(u_\tau)_u$  or  $(u_\tau)_s$ ] for each data set. Compared to the neutral condition (25-July), it can be seen that data from 18-July have significantly higher normalized fluctuation values. This is due to the unstable thermal condition present during the time those data were acquired. Conversely, data from 19-July show normalized fluctuation values that are lower than the neu-

tral baseline condition as a result of the thermally stable condition present over the data set.

### 5.2.1 Taylor microscale

The Taylor microscale  $\lambda$  and corresponding Reynolds number based on the microscale  $R_\lambda$  were computed for each evening of data. The Taylor microscale is a well-defined quantity that is often used to characterize a turbulent flow [24]. Measurements of the Taylor microscale were available for each data set and were used to quantitatively describe the flow by the corresponding Reynolds number,  $R_\lambda$ .

The Taylor microscale was computed for all three velocity components (if applicable) from the respective autocorrelation of each time series measurement. The corresponding Reynolds number based on this microscale was defined by

$$R_{\lambda_u} = \frac{\tilde{u}\lambda_u}{\nu} \quad 5.2$$

$$R_{\lambda_v} = \frac{\tilde{u}\lambda_v}{\nu} \quad 5.3$$

$$R_{\lambda_w} = \frac{\tilde{u}\lambda_w}{\nu} \quad 5.4$$

for each velocity component. Table 5.6 shows the values of the Taylor Microscale and Reynolds number for each day data were acquired.

The Taylor length scales and the Reynolds numbers follow the same trends -- 19-July has the smallest microscales and also the smallest  $R_\lambda$  values. The data from 18-July, which appeared to be a very similar day initially, has similar  $\lambda$  values but significantly

larger  $R_\lambda$  values when compared to 19-July. This trend may be due to the thermal stability issues, which suppressed  $\tilde{u}$  on 19-July and increased  $\tilde{u}$  on 18-July, causing the difference observed in the  $R_\lambda$  values. The data acquired on 25-July had the largest Taylor microscale and also the largest  $R_\lambda$  values.

An interesting trend was observed between the values of  $\lambda_u$  and  $\lambda_v$  for each data set. The ratio of  $\lambda_v / \lambda_u$  for all three days on the SLTEST site was very near 1/3. However, for isotropic turbulence, this ratio is defined to be  $1/\sqrt{2}$  (see equation 5.11) [24]. This relationship between also  $\lambda_u$  and  $\lambda_v$  explains the large discrepancy found between the dissipation estimates “a” and “b” discussed in the next section. The relationship between these two estimates is based on the  $\lambda_v = \lambda_u / \sqrt{2}$  isotropic relationship.

### 5.2.2 Dissipation Measurement

The dissipation estimate was treated separately due to the difficulty of the measurement and its importance in the scaling of turbulence quantities treated in the following sections. This section will discuss in detail the evaluation of the turbulent kinetic energy dissipation at the SLTEST site.

As shown in Pope [24], the dissipation can be expanded as:

$$\epsilon = 2\nu \overline{s_{ij}s_{ij}} = \nu \overline{\left( \frac{\partial u_i}{\partial x_j} \frac{\partial u_i}{\partial x_j} + \frac{\partial u_i}{\partial x_j} \frac{\partial u_j}{\partial x_i} \right)} = \tilde{\epsilon} + \nu \overline{\frac{\partial^2 u_i u_j}{\partial x_i \partial x_j}} \quad 5.5$$

where  $\tilde{\epsilon}$  is the “pseudo-dissipation”. The last term of equation 5.5 is very small in virtually all circumstances and the consequent distinction between  $\epsilon$  and  $\tilde{\epsilon}$  is seldom made [24]. As a result, the dissipation estimate becomes:

$$\epsilon \equiv \nu \overline{\left( \frac{\partial u_i}{\partial x_j} \frac{\partial u_i}{\partial x_j} \right)} \quad 5.6$$

In Cartesian coordinates, equation 5.6 can be expanded as nine derivatives of the fluctuating velocity components as:

$$\frac{\epsilon}{\nu} = \overline{\left( \frac{\partial u}{\partial x} \right)^2} + \overline{\left( \frac{\partial u}{\partial y} \right)^2} + \overline{\left( \frac{\partial u}{\partial z} \right)^2} + \overline{\left( \frac{\partial v}{\partial x} \right)^2} + \overline{\left( \frac{\partial v}{\partial y} \right)^2} + \overline{\left( \frac{\partial v}{\partial z} \right)^2} + \overline{\left( \frac{\partial w}{\partial x} \right)^2} + \overline{\left( \frac{\partial w}{\partial y} \right)^2} + \overline{\left( \frac{\partial w}{\partial z} \right)^2} \quad 5.7$$

Because the direct measurement of all nine terms with adequate spatial resolution is difficult, equation 5.7 is seldom used to estimate dissipation. Instead, various assumptions are made which allow for the terms to be reduced and combined. This allows for dissipation to be more easily measured and estimated with less than nine derivatives.

The dissipation at the SLTEST site measurement location was computed using a number of assumptions. Each method required the measurement of the spatial derivatives of the velocity components in the streamwise, spanwise, and / or traverse directions. Spatial derivatives in the streamwise direction were computed using the Taylor microscale formation [21]

$$\overline{\left( \frac{\partial u_i}{\partial x} \right)^2} = 2 \frac{\tilde{u}_i^2}{\lambda_{u_i}^2} \quad 5.8$$

where  $\lambda_{u_i}$  is the Taylor microscale of the  $u_i$  velocity component. Spatial derivatives in the transverse and spanwise directions were only available for the u component of veloc-

ity. These derivatives were computed directly from the vorticity probe straight wires that were separated by a fixed distance ( $\Delta y$  or  $\Delta z$ , depending on probe orientation).

The following paragraphs will describe the various assumptions and corresponding methods used to compute the dissipation estimates. Each estimate will be denoted by an alphabetical subscript to differentiate between the various methods. Table 5.4 displays the results of these various estimates.

The most common method used to obtain  $\epsilon$  is to assume that the velocity fluctuations and their derivatives are isotropic. With this assumption, the relationships among the terms in equation 5.7 leads to the approximation:

$$\epsilon = 15\nu \overline{\left(\frac{\partial u'}{\partial x}\right)^2} \quad 5.9$$

Substituting in the result of the streamwise derivative from equation 5.8, the dissipation can be computed from the u component of velocity as:

$$\epsilon_u = 30\nu \frac{\overline{u'^2}}{\lambda_u^2} \quad 5.10$$

where  $\lambda_u$  is the streamwise Taylor microscale. Given the assumption of isotropic turbulence, the relationship

$$\lambda_v = \lambda_u / \sqrt{2} \quad 5.11$$

is valid, and an equivalent statement of the dissipation can be computed as:

$$\epsilon_b = 15\nu \frac{\overline{u'^2}}{\lambda_v^2} \quad 5.12$$

using the measured wall normal Taylor microscale.

In flow that is isotropic over all measured wavelengths,  $\overline{v'^2} = \overline{u'^2}$ , and the dissipation can be estimated as:

$$\varepsilon_b' = 15\nu \frac{\overline{v'^2}}{\lambda_v^2}. \quad 5.13$$

using the measured wall normal velocity fluctuations.

Similarly, in the assumption of isotropic turbulence  $\lambda_v = \lambda_w$ , and the dissipation can be estimated as:

$$\varepsilon_c = 15\nu \frac{\overline{u'^2}}{\lambda_w^2} \quad 5.14$$

using the measured spanwise Taylor microscale.

In homogeneous, isotropic turbulence, the dissipation can be directly related to the spanwise vorticity by [21]

$$\varepsilon_d = 3\nu \tilde{\omega}_z^2. \quad 5.15$$

This was calculated using the variance of the spanwise vorticity measured by the compact vorticity probe.

The next group of estimates attempt to measure several of the terms of equation 5.7 with assumptions that are less stringent than perfect local isotropy. These are referred to as the “semi-isotropic” relationships. The first assumption is that of “axisymmetric turbulence.” A “semi-isotropic” approximation of  $\varepsilon$ , as given by equation (14) of Browne et al. [6], is given by:

$$\varepsilon_e = 3\nu \left[ \overline{\left(\frac{\partial u'}{\partial x}\right)^2} + 2\overline{\left(\frac{\partial u'}{\partial y}\right)^2} + \overline{\left(\frac{\partial u'}{\partial z}\right)^2} \right] \quad 5.16$$

Wyganski and Fiedler [33] used a semi-isotropic calculation that imposed the condition:

$$\overline{\left(\frac{\partial v}{\partial y}\right)^2} = \overline{\left(\frac{\partial v}{\partial z}\right)^2} = \overline{\left(\frac{\partial w}{\partial y}\right)^2} = \overline{\left(\frac{\partial w}{\partial z}\right)^2} = \overline{\left(\frac{\partial w}{\partial x}\right)^2} \quad 5.17$$

where only the last of these terms is measured. Equation 5.7 then takes the form:

$$\varepsilon_f = \nu \left[ \overline{\left(\frac{\partial u}{\partial x}\right)^2} + \overline{\left(\frac{\partial u}{\partial y}\right)^2} + \overline{\left(\frac{\partial u}{\partial z}\right)^2} + \overline{\left(\frac{\partial v}{\partial x}\right)^2} + 5\overline{\left(\frac{\partial w}{\partial x}\right)^2} \right] \quad 5.18$$

The results of these six methods (a -- f) are presented in Table 5.4. From these results, it can be seen that the dissipation estimates span a large range of values. The isotropic dissipation estimate from the streamwise velocity measurement ( $\varepsilon_a$ ) predicted the lowest value while the isotropic dissipation estimate from the lateral velocity measurement ( $\varepsilon_b$ ) predicted the highest value. The semi-isotropic predictions fell between the isotropic estimates. The dissipation estimated based on the streamwise velocity component ( $\varepsilon_a$ ) was found to be the most commonly used estimate throughout the reference literature. For the present data, this estimate was also consistent with the values inferred from several of the other techniques. Hence, it was selected by the authors as the dissipation value used to scale the turbulent quantities covered in the remaining sections.

### 5.2.3 Flow length and velocity scales

This section describes the physical scales of the flow averaged over each data set and explains how they were calculated. This section will describe the friction velocity



$[u_\tau, (u_\tau)_s, \text{ or } (u_\tau)_u]$  depending on the ambient thermal condition: see Section 2.2.3], the kinematic viscosity  $\nu$ , the viscous length scale  $l^+$ , and the Kolmogorov length and velocity scales,  $\eta$  and  $u_\eta$  respectively.

Table 5.3 shows the mean flow properties for the three evenings that data were acquired. The friction velocity was derived from a propeller anemometer correlation to the drag plate acquired by the University of Utah. The friction velocity recorded on 25-July ( $u_\tau \approx 0.41$  m/s) was significantly higher than the friction velocities measured over the other two days due to the larger streamwise velocity present on this day. The friction velocities for 18-July and 19-July were very similar to each other  $[(u_\tau)_s \approx (u_\tau)_u \approx 0.3$  m/s] as a result of similar wind conditions.

The kinematic viscosity  $\nu$  was dependant on the ambient temperature of the SLT-EST site and was supplied to M.S.U. by the University of Utah. The temperatures over the three days were very similar. The ambient temperature during the data acquisition for 18-July was 30.1 degrees celsius. The data from 19-July and 25-July were acquired under ambient temperatures of 26.7 and 31.0 degrees celsius respectively. The kinematic viscosity of air did not experience a significant difference over this range of temperatures and therefore a constant value of  $\nu = 1.6 \times 10^{-5} \text{ m}^2/\text{s}$  was used.

From the kinematic viscosity and the dissipation (discussed in the previous section), the Kolmogorov length scale,  $\eta$ , was then computed as

$$\eta \equiv (\nu^3/\epsilon)^{1/4} \quad \mathbf{5.19}$$

and the kolmogorov velocity as

$$u_{\eta} \equiv (\epsilon \nu)^{1/4} \quad 5.20$$

Table 5.3 shows the Kolmogorov length scale  $\eta$  for each data set. It can be seen that this length scale was similar for 18-July and 19-July. It should be noted that  $\eta$  was very insensitive to which dissipation estimate was used in the computation. The Kolmogorov length on 25-July was slightly smaller than the other two days.

The resolution of the vorticity probe used to acquire these data can now be compared to the smallest length scales of the flow. More specifically, was the probe micro-circulation region small enough to resolve scales this small? From Chapter 4, the two probes had  $\Delta y$  values of 1.397 mm and 1.702 mm respectively. This resulted in a range of  $3\eta < \Delta y < 4.5\eta$ , depending on the specific probe and the specific day. Wallace and Foss presented an optimal range of  $2\eta < \Delta y < 4\eta$  for the best resolution and accuracy of velocity gradients [32]. Therefore, the vorticity probes used to acquire the data at the SLTEST were determined to have adequate spatial resolution to resolve even the smallest flow scales.

The viscous length scale  $l^+$  was defined by equation 1.2. The viscous length scales of 18-July and 19-July were very close to each other with vales of  $l^+ \approx 0.05mm$  for each day. The viscous length of 25-July was significantly smaller at  $l^+ \approx 0.04mm$ .

### **5.3 Spectral Properties**

The focus of the current research involved studying the characteristics of local isotropy under inherently anisotropic conditions. Kolmogorov's hypothesis states that "at sufficiently high Reynolds numbers, the small scale turbulent motions are isotropic" [13]. In the current research, the probes were located at relatively near wall positions which would prevent the condition of isotropy to occur over larger wavelengths. The current research will investigate if Kolmogorov's hypothesis of local isotropy does hold true for the near wall data acquired at the SLTEST site, and if so, over what wavelengths does the condition of local isotropy exist?

This section serves to analyze the spectral representation of the velocity and vorticity components measured at the SLTEST site. Section 5.3.1 will present the spectral representation of the velocity components. Section 5.3.2 will follow with the spectral representation of the vorticity components of the flow. Section 5.3.3 will examine the spectral properties of velocity and vorticity products.

#### **5.3.1 Spectral representation of the velocity field**

This section details the spectral representation of the velocity measurements acquired at the SLTEST site. The following paragraphs will discuss the equations used to perform this analysis. An isotropic model will also be formulated in this section and used to serve as a point of contrast between the SLTEST data and purely isotropic turbulence. Section 5.3.1.1 will discuss the results of the  $u$  component of velocity, while Sections 5.3.1.2 and 5.3.1.3 will discuss the  $v$  and  $w$  velocity components respectively.

The autospectral density (power spectrum) of each velocity component was defined as [5]

$$E_{u_i u_i}(f) = \int_{-\infty}^{\infty} R_{u_i u_i}(\tau) e^{-j2\pi f \tau} d\tau \quad 5.21$$

where  $R_{u_i u_i}$  is the autocorrelation of the  $i$ th-component of velocity and  $f$  is the frequency under which the data were acquired. The correlation function  $R$  was defined as

$$R_{ab}(\Delta \tau) = \frac{\overline{a(\tau)b(\tau + \Delta \tau)}}{\tilde{a}\tilde{b}} \quad 5.22$$

where  $a$  and  $b$  represent the two signal of interest. If  $a = b$ , then  $R$  is the *autocorrelation* of signal  $a$ . If  $a \neq b$ , then  $R$  is the *cross correlation* between signals  $a$  and  $b$ . For the present data, the *pwelch* command in Matlab was used to compute the autospectral densities.

The wavenumber,  $k_1$ , was computed from the frequency  $f$  as:

$$k_1 = 2\pi f / \bar{u} \quad 5.23$$

where  $\bar{u}$  is the mean velocity for the given data set. Wavenumbers have the units of  $m^{-1}$ , so very low wavenumbers correspond to very large motions in the boundary layer. The wavenumbers were normalized by multiplying  $k_1$  by the Kolmogorov lengthscale,  $\eta$ . The autospectral density was then computed as a function of wavenumber and normalized by the kinematic viscosity and dissipation as:

$$E_{u_i u_i}(k_1) / (\epsilon \nu^5)^{1/4} \quad 5.24$$

for each  $E_{u_i u_i}$  component.

An isotropic model was formulated based on the assumptions of homogeneous isotropic turbulence. The model spectrum was computed from Pope as [24]:

$$E(\kappa) = [C\varepsilon^{2/3} \kappa^{-5/3}] f_L(\kappa L) f_\eta(\kappa \eta_K) \quad 5.25$$

where  $\kappa$  is the wave number in three dimensional wave number space. The “universal equilibrium” is represented by the function in square brackets, where  $C=1.5$  represents the universal constant. The value of  $\eta_K$  was determined for each day using equation 5.19 and the dissipation value ( $\varepsilon_a$ ). The functions  $f_L$  and  $f_\eta$  are given by:

$$f_L(\kappa L) = \left( \frac{\kappa L}{\sqrt{\kappa L^2 + c_L}} \right)^{\frac{11}{3}} \quad 5.26$$

and

$$f_\eta(\kappa \eta_K) = \exp \left\{ \beta c_\eta - \beta [(\kappa \eta_K)^4 + c_\eta^4]^{1/4} \right\}. \quad 5.27$$

These are effectively curve fits to the large and smallest scale motions respectively. The value of  $c_L=6.78$  was used as suggested by Pope [24]. The value of  $L$  represents the integral, or largest scale of motion, and it is specified in terms of the ratio to the Kolmogorov length scale:  $L/\eta_K$ . This ratio was selected to provide the best agreement between the model spectra and the large scale portion of the experimental spectra, using the measured  $E_{11}$  spectra as described below. The resulting value was  $L = 6000 \cdot \eta_K$ .

The values  $\beta=5.2$ ,  $c_\eta=0$  were suggested by Saddoughi and Veeravalli [26] in their measurements of the spectra in a high Reynolds number boundary layer. Pope [24] sug-

gested  $\beta=2.1$ ,  $c_\eta=0.4$ . The values of  $\beta$  and  $c_\eta$  for the SLTEST data were selected to provide the best agreement between the model spectra and the small scale portion of the experimental spectra. This resulted in values of  $\beta=5.2$ ,  $c_\eta=0.25$  (18-July),  $\beta=4$ ,  $c_\eta=0.25$  (19-July), and  $\beta=5.2$ ,  $c_\eta=0.2$  (25-July). It should be noted that only the large scale and small scale portions of the model spectra were best fit. The amplitude of the spectra for the intermediate scales was determined by the universal constant  $C=1.5$  for all three data sets.

The modeled one dimensional energy spectra was calculated from  $E(\kappa)$  from the isotropic relation:

$$E_{uu}(\kappa_1) = \int_{\kappa_1}^{\infty} \frac{E(\kappa)}{\kappa} \left[ 1 - \left( \frac{\kappa_1}{\kappa} \right)^2 \right] d\kappa \quad 5.28$$

The one dimensional model spectrum of the v and w velocity components were also calculated as:

$$E_{vv}(\kappa_1) = E_{ww}(\kappa_1) = \frac{1}{2} \int_{\kappa_1}^{\infty} \frac{E(\kappa)}{\kappa} \left[ 1 + \left( \frac{\kappa_1}{\kappa} \right)^2 \right] d\kappa \quad 5.29$$

The isotropic model spectra demonstrate a large region of -5/3 slope for all three velocity components. A similar slope is apparent in the SLTEST velocity data, but the log scale of the normalized plots make distinguishing the actual slope difficult. The autospectral densities of the velocity components were compensated by multiplying the spectra by  $k_1^{5/3}$ . This compensation better differentiates between the isotropic model slope of -5/3 and the actual slope of the SLTEST data. Any region of -5/3 slope would flatten out into a

horizontal line, making deviations from this isotropic slope more apparent. The compensated spectrum was obtained for the  $E_{u_i u_i}$  component as:

$$\epsilon^{-2/3} k_1^{5/3} E_{u_i u_i}(k_1) \quad 5.30$$

for both the modeled and experimental spectra.

### 5.3.1.1 u-component spectra

This section presents the spectral representation of the u-component of velocity compared to the isotropic model spectrum. The thermally neutral condition (25-July) will be presented first followed by the thermally unstable (18-July) and stable (19-July) conditions respectively. Both the normalized and compensated spectra will be presented for these data.

Figures 5.13 through Figure 5.18 show the normalized autospectral densities of the fluctuations of the u-component of velocity for all three data sets. From the normalized autospectral density on 25-July, it appears that the model spectra accurately resembles the longitudinal velocity spectra measured at the SLTEST site for high wavenumbers. The data appear to follow the  $-5/3$  power law over a large range of wavenumbers (over 3 decades of  $k_1 \eta$ ) corresponding to the very high Reynolds number trends observed through experiments [24]. The compensated spectrum for the same data show the same character as the model spectrum, but the experimental spectrum never reaches the amplitude of the model spectrum. The experimental spectrum also appears to fall off for lower wavenumbers faster than the model spectra. The model spectra breaks away from the  $-5/3$

region very abruptly, whereas the experimental spectra drifts out of the  $-5/3$  region very gradually.

Figures 5.15 and 5.16 show the normalized and compensated longitudinal autospectral densities for 18-July. As can be seen, the two follow the same trend over larger wavenumbers, but the experimental spectrum overshoots the predicted peak value. Experimental data by Saddoughi and Veeravalli demonstrate a similar characteristic [26], but show a flatter region for moderate wavenumbers. The SLTEST data for 18-July does not appear to contain a region of  $-5/3$  slope. This is very evident by examination of the compensated spectrum. This lack of a constant region is contrary to what is expected from high Reynolds number isotropic data (as the Reynolds number is increased, one would expect the wavenumber range over which this “flat” region covers to expand). Since the probes were located much closer to the wall on this day (when compared to the 25-July data), the anisotropic effect is much more evident. This can be seen in Figure 5.16 where the magnitude of the compensated spectrum tails off quickly for lower wavenumbers.

Figures 5.17 and 5.18 show the normalized and compensated longitudinal autospectral densities for 19-July. Similar to the 18-July data, these data compare well to the isotropic model spectra at high wavenumbers, but deviate over the range of moderate to low wavenumbers. The data exhibit the same overshoot in the compensated spectra and no distinguishable  $-5/3$  slope. The effect of the wall on the moderate to large scale motions can be readily observed in the compensated spectrum.

Thermal effects appear to have played little role in the  $u$  component velocity spectra. The data acquired under an unstable condition (18-July) closely resemble the data acquired under the stable condition (19-July). The neutral condition data show a smaller



amplitude and a more evident  $-5/3$  slope, but were also acquired farther away from the wall.

### 5.3.1.2 v-Component Spectra

The spectral representation of the v-component of velocity compared to the isotropic model spectrum are presented in this section. The thermally neutral condition will again be presented first followed by the thermally unstable and stable conditions respectively. Both the normalized and compensated spectra will be presented for these data.

Figures 5.19 through 5.24 show the normalized and compensated autospectral density of the v-component of velocity for all three data sets. The data acquired on 25-July have a much lower amplitude than the isotropic model. However, the general shape of the compensated spectrum resembles the experimental data presented by Saddoughi and Veeravalli [26]. A region exists over moderate wavenumbers where the  $-5/3$  compensated spectrum appears flat. The wall still appears to effect the lower-to-moderate wavenumbers.

For 18-July and 19-July, the general character of the spectra appear very similar to each other, but they are very different than the model spectra. The effect of the wall is more evident when compared to the u-component spectra for each data set since we are now dealing with motions in the wall-normal direction. The data appear to follow the isotropic model for very high wavenumbers, but break away from the model spectra very early. The compensated spectra show a distinguishable hump for wavenumbers just outside of the dissipation range. This trend was also observed by Saddoughi and Veeravalli [26]. However, the experimental spectra never reach the predicted amplitude of the model

spectra and drop off quickly as the wavenumber decreases. In fact, there is little contribution to the autospectral density from the very low wavenumbers.

Again, thermal stability does not appear to play a large role in the spectral representation of the v-component of the velocity. Data from 18-July and 19-July demonstrate very similar trends, but differ from 25-July. The main differences between these three data sets are attributed to the probe location.

### **5.3.1.3 w-Component Spectra**

The autospectral densities representing the w-component of velocity were available for the two evenings when two probes were used to acquire data (18-July and 19-July). Figures 5.25 through 5.28 show the normalized and compensated spectra for these two days. The 19-July data show the large spectral hump consistent with the previous component spectra. The data also appear to level off before dropping off quickly for lower wavenumbers. The data from 18-July show a different trend, never reaching the amplitude of 19-July. These data do not show a pronounced spectral hump. Instead, the data exhibit what appears to be a constant slope ( $k^n$  with  $n < -5/3$ ) over moderate wavenumbers. The data then tail off quickly for low wavenumbers. The effect of the thermal condition between these two days cannot be determined since the neutral condition was not recorded to serve as a baseline condition.

### **5.3.2 Spectral representation of the vorticity field**

The vorticity data taken at the SLTEST site were also analyzed in the frequency domain. This section serves to present the spectral representation of the vorticity components measured over the three days. The following paragraphs will discuss the equations

used to perform this analysis as well as formulate the isotropic model to which the results were compared. Section 5.6.1 will discuss the results of the  $\langle \omega_z \rangle$  vorticity component while Section 5.6.2 will discuss the  $\langle \omega_y \rangle$  vorticity component.

The autospectral density of each vorticity component was defined as [5]:

$$E_{\omega_i}(f) = \int_{-\infty}^{\infty} R_{\omega_i \omega_i}(\tau) e^{-j2\pi f \tau} d\tau \quad 5.31$$

where  $R_{\omega_i \omega_i}$  is the autocorrelation of the  $i$ th-component of vorticity (computed according to equation 5.22) and  $f$  is the frequency with which the data were acquired. For the present data, the *pwelch* command in Matlab was used to compute the autospectral densities.

The autospectral density was normalized by the kolmogorov length  $\eta$  and velocity  $u_\eta$  as

$$E_{\omega_i}(k_1) \eta / u_\eta^2 \quad 5.32$$

(for the  $\langle \omega_i \rangle$  vorticity component) and computed as a function of the wavenumber,  $k_1$ , computed from equation 5.23. This autospectral density was plotted against the normalized wavenumber.

The model spectra, which assumes homogeneous isotropic turbulence, was calculated using the same constants which best fit the  $u$  component of velocity for that day (see Section 5.5). Antonia et al. [3] derived the isotropic relationship between the one dimensional vorticity spectra and the energy spectra:

$$\phi_{\omega_z}(\kappa_1) = \frac{\kappa_1}{2} \int_{\kappa_1}^{\infty} \frac{E(\kappa)}{\kappa} d\kappa + \frac{1}{4} \int_{\kappa_1}^{\infty} \frac{E(\kappa)}{\kappa} [\kappa^2 + \kappa_1^2] d\kappa. \quad 5.33$$

In the assumption of isotropic turbulence, the vorticity spectrum is independent of orientation. Therefore, the model used to compute  $\omega_y$  is the same model used to compute  $\omega_z$ .

The u,v, and w velocity autospectral densities were compensated with  $k_1^{5/3}$  to better differentiate between the -5/3 slope of the model and the actual slope of the SLTEST data. A similar power law does not exist for the vorticity data. However, it is instructive to plot the vorticity autospectral densities compensated as  $k_1 \phi_{\omega}$ . This compensated spectrum better demonstrates the relative contributions of the different scales of motion to the vorticity variance:

$$\overline{(\omega')^2} = \int_0^{\infty} \phi_{\omega}(k_1) dk_1 = \int_0^{\infty} k_1 \cdot \phi_{\omega}(k_1) d(\ln(k_1)) \quad 5.34$$

The integrand of the second right hand side of equation 5.34 is plotted (in semilog format) to show the contributions from each normalized wavenumber.

The autospectral densities of the vorticity showed a large contribution from very low wavenumbers. The autocorrelation of the vorticity data was also included in this section for a more complete description of this low wavenumber contribution. The autocorrelation was performed according to equation 5.22, and is presented at the ends of Sections 5.6.1 and 5.6.2.

### 5.3.2.1 $\langle \omega_z \rangle$ Spectra

This section presents the spectral representation of the  $\langle \omega_z \rangle$  component of the vorticity compared to the isotropic model spectrum. The thermally neutral condition (25-July) will be presented first followed by the thermally unstable (18-July) and stable (19-July) conditions respectively. Both the normalized and compensated spectra will be presented for these data. This section concludes with the presentation of the autocorrelation of the  $\langle \omega_z \rangle$  vorticity component.

Figures 5.29 through 5.34 and show the normalized and compensated  $\langle \omega_z \rangle$  autospectral densities for all three data sets. The normalized model spectra do not accurately predict the measured spectra for any data set. The model spectra level off asymptotically as the wavenumber decreases, whereas the measured spectra continues to rise. This behavior indicates major contributions from wavenumbers much larger than the distance between the probe and the wall. This phenomenon is likely due to the pressure distribution along the wall. According to Panton, “a vorticity flux from a wall results from the pressure gradients along the wall” [23]. This relationship is described by the following equation [23]:

$$\frac{\partial p}{\partial x} = -\mu \frac{\partial \omega_z}{\partial y} \quad 5.35$$

The compensated autospectral densities show the actual contribution of these observed large scale motions to the vorticity variance. The data acquired on 25-July compares well to the isotropic model spectrum. These data show the same general shape as the model spectrum but with a larger contribution from the lower wavenumbers. The

compensated vorticity spectrum for 18-July follows the same basic trend as the model spectrum, but demonstrates a much larger amplitude. Given that the unstable boundary layer involves density variations and given the non-barotropic source term in the vorticity transport equation, it is rational that the vorticity variance is larger for 18-July. These data also show the larger contribution from the low wavenumbers. The experimental spectrum from the 19-July data does not follow the model spectra well. Instead, the experimental spectra demonstrates a large initial spectral hump followed by a second spectral hump occurring at a much lower wavenumber.

Autocorrelations of the  $\langle \omega_z \rangle$  vorticity were calculated to more thoroughly investigate the size of the large scale motions contributing to the vorticity. The autocorrelations were determined from equation 5.22. Figures 5.35 and 5.36 show the autocorrelations of the  $\langle \omega_z \rangle$  vorticity for each day. In these figures, the 19-July data show the first zero of the  $\langle \omega_z \rangle$  vorticity autocorrelation to be at a location corresponding to 13m. The 18-July data show the first zero of the autocorrelation occurring at a location corresponding to 35m. Both of these measurements were at 20cm above the desert floor and their nominal  $y^+$  values were 3800. The 25-July data, from a distance of 40cm above the desert floor, shows the first zero crossing of the autocorrelation at 43m. The observed differences in these data may be caused by some combination of the thermal effects, a Reynolds number dependence, or the distance from the floor. The Reynolds number based on the Taylor microscale  $R_\lambda$  increases from 19-July to 18-July to 25-July (see Table 5.6), meaning that the first zeros in the autocorrelations of the  $\langle \omega_z \rangle$  vorticity time series' increase with  $R_\lambda$ . The data appear to show a similar Reynolds number dependence when plotted in semilog

format. The initial correlation of the vorticity decreases at a more rapid rate as  $R_\lambda$  increases.

### 5.3.2.2 $\langle \omega_y \rangle$ spectra

This section presents the spectral representation of the  $\langle \omega_y \rangle$  component of the vorticity. The  $\langle \omega_y \rangle$  component of the vorticity was not acquired over the thermally neutral condition (25-July). As a result, this section will only present the unstable (18-July) and stable (19-July) conditions. Both the normalized and compensated spectra will be presented for these data. This section concludes with the presentation of the autocorrelation of the  $\langle \omega_y \rangle$  vorticity component.

Figures 5.37 through 5.40 show the normalized and compensated  $\langle \omega_y \rangle$  autospectral densities measured on 18-July and 19-July. These data appear to exhibit the same character observed in the normalized  $\langle \omega_z \rangle$  spectra. The model spectra level off for lower wavenumbers while the measured spectra continue to increase over this range. This demonstrates a significant contribution from large scale motions to the vorticity fluctuations. Although  $\omega_y$  at the wall itself is zero, there may be a flux of  $\omega_y$  vorticity out of the wall. This flux is dependant on the distributions of  $\omega_x$  and  $\omega_z$  on the wall itself [23]. This relationship is described by [23]:

$$\frac{\partial \omega_y}{\partial y} = \frac{\partial \omega_x}{\partial x} + \frac{\partial \omega_z}{\partial z} \quad 5.36$$

evaluated at the wall.

The compensated  $\langle \omega_y \rangle$  vorticity spectra for 18-July exhibit two humps separated by over a decade of normalized wavenumber. This is not the trend observed in the compensated  $\langle \omega_z \rangle$  autospectral density for 18-July. This same anisotropic character was observed on 19-July. The compensated  $\langle \omega_y \rangle$  data exhibit only one peak at high wavenumbers. The  $\langle \omega_z \rangle$  data from the same day exhibited two peaks.

Autocorrelations of the  $\langle \omega_y \rangle$  vorticity component were computed in order to observe the larger length scales present. Figures 5.41 and 5.42 shows the autocorrelations of the  $\langle \omega_y \rangle$  vorticity for each day. The 19-July data show the first zero of the  $\langle \omega_y \rangle$  vorticity autocorrelation to be at a location corresponding to 225m. The 18-July data show the first zero of the autocorrelation to be at 240m. A typical boundary layer thickness was on the order of 150m.

### 5.3.3 Velocity-vorticity products

Spectral analysis was also conducted on the products of the velocity and vorticity flow components. The following paragraphs will discuss the methods used to examine the products of the velocity components as well as the velocity-vorticity products. These methods including the autospectral density of the product, the cross-spectral density of the two components and the coherence of the two components. Section 5.3.3.1 will cover the  $u'v'$  velocity product while Section 5.3.3.2 will cover the  $u'w'$  velocity product. The velocity-vorticity products that were examined in this study included  $v'\langle \omega_z' \rangle$  and  $w'\langle \omega_y' \rangle$ . Section 5.3.3.3 will discuss the significance of the velocity-vorticity products and present the results of the  $v'\langle \omega_z' \rangle$  product analysis. Section 5.3.3.4 presents the



$w'\omega_y'$  product. Table 5.7 displays the dimensional statistics of all the velocity and velocity-vorticity products while Table 5.8 shows the normalized correlation coefficients of these products.

The spectral representation of the velocity and velocity-vorticity products was examined in two ways. The autospectral density of the combined product was examined as well as the co-spectral density of the two components. The autospectral density ( $\Phi_{u_i u_j}$  for velocity products or  $\Phi_{u_i \omega_j}$  for velocity-vorticity products) of the product was computed as follows. A time series of the desired product was constructed by multiplying the two times series together. The autospectral density was then calculated from this single time series according to equation 5.21. Autospectral densities including only the velocity products were compensated by  $k_1^{5/3}$ . Autospectral densities of the velocity-vorticity products were compensated by  $k_1$ .

The co-spectral density was defined as [5]:

$$E_{u_i u_j}(f) = \int_{-\infty}^{\infty} R_{u_i u_j}(\tau) e^{j2\pi f \tau} d\tau \quad 5.37$$

or

$$E_{u_i \omega_j}(f) = \int_{-\infty}^{\infty} R_{u_i \omega_j}(\tau) e^{j2\pi f \tau} d\tau \quad 5.38$$

for the velocity product or the velocity-vorticity product respectively. In these equations,

$R_{u_i u_j}$  is the cross correlation of the velocity components and  $R_{u_i \omega_j}$  is the cross correla-

tion of the velocity-vorticity components, determined from equation 5.22. The co-spectral densities were calculated in Matlab using the *csd* function.

Further correlations between the velocity and vorticity components were investigated by examining the coherence the two signals. The coherence was defined by

$$H_{u_i u_j}(k_1) = \frac{|E_{u_i u_j}(k_1)|^2}{E_{u_i u_i}(k_1) E_{u_j u_j}(k_1)} \quad 5.39$$

where  $E_{u_i u_i}(k_1)$  is the autospectral density of the  $u_i$  component and  $E_{u_i u_j}(k_1)$  is the co-spectral density of the  $u_i$  and  $u_j$  components.

#### 5.3.3.1 $u'v'$ product

This section serves to present the results of the  $u'v'$  product for the three data sets. The statistical value of  $\overline{u'v'}$  will be presented for each day as well as the normalized coefficient. The autospectral density of the product, the co-spectral density and the coherence will also be examined. The data will be presented with the thermally neutral data first (25-July) followed by the thermally unstable and thermally stable data (18-July and 19-July respectively).

The dimensional value of  $\overline{u'v'}$  for all three days was fairly consistent, varying from -0.07 to -0.11 ( $\text{m}^2/\text{s}^2$ ). The normalized correlation coefficients, however, varied significantly between days. The neutral condition (25-July) had a value of  $\overline{u'v'}/u_\tau^2 = -0.67$ . The 18-July data had a normalized value of  $\overline{u'v'}/(u_\tau)_u^2 = -0.96$ . This larger value present

on 18-July was a result of the thermally unstable condition present. The data taken at the same probe location on 19-July had a coefficient of only  $\overline{u'v'}/(u_\tau)_s^2 = -0.77$ . This resulted from the stable condition that occurred on this day. The unstable condition caused larger fluctuations from buoyancy effects. The stable condition suppressed these fluctuations, causing the observed differences between the data sets acquired at the same location.

Figures 5.43 through 5.48 show the normalized and compensated autospectral densities of the  $u'v'$  product for the three data sets. The data follow a slope slightly different than the  $-5/3$  power law observed in the velocity spectra. The compensated spectra for all three cases show a peak between  $0.07 < k_1 \eta < 0.1$ , followed by a steady decline as wave-number decreases.

Figures 5.49 through 5.51 show the normalized co-spectral densities of the  $u'$  and  $v'$  velocity components for all three data sets. In isotropic turbulence, the  $u'v'$  co-spectral density is zero. For linear shear flows, the  $u'v'$  co-spectral density decays more rapidly than the  $E_{11}$  autospectral density (as  $k_1^{-7/3}$  compared to  $k_1^{-5/3}$ ) so that the anisotropy decreases with  $k_1$  [24]. The  $u'v'$  co-spectral density from the SLTEST site data decays at a faster rate than the predicted  $-7/3$  slope for high wavenumbers.

Figure 5.52 shows the coherence of the  $u'$  and  $v'$  velocity components for all three days. In this figure, all three sets of data steadily decrease until  $k_1 \eta \approx 0.02$ , where they level off just above zero. Zero coherence of the  $u'v'$  product is a necessary condition for local isotropy [26]. The SLTEST data indicate the presence of this necessary condition

for a region of local isotropy spanning nearly two decades of  $k_1 \eta$  (including the dissipation region).

Thermal effects did not appear to play a large role in the  $u'v'$  velocity product spectra, but were evident in the  $\overline{u'v'}/u_\tau^2$  statistic for each evening.

### 5.3.3.2 $u'w'$ product

This section presents the results of the  $u'w'$  product as determined from the two days during which data were acquired. The statistical value of  $\overline{u'w'}$  will be presented for each day as well as the normalized coefficient. The autospectral density of the  $\overline{u'w'}$  product, the co-spectral density and the coherence will also be examined. Since the thermally neutral data (25-July) was not acquired for these products, the data will be presented with the thermally unstable data (18-July) first followed by the thermally stable data (19-July).

The  $\overline{u'w'}$  product was available for 18-July and 19-July and showed a much lower correlation than the  $\overline{u'v'}$  statistic (see Table 5.7 and Table 5.8). Figures 5.53 through 5.56 show the normalized and compensated autospectral densities of the  $u'w'$  product for these two days of data. The data do not demonstrate the same region of  $-5/3$  slope observed in the single component velocity data. The compensated data peak around a normalized wavenumber of 0.15 with apparent linear slopes on either side.

Figures 5.57 and 5.58 show the normalized co-spectral densities of the  $u'$  and  $w'$  velocity components. Again, the data do not appear to follow the predicted  $-7/3$  slope for linear shear flows [24]. Figure 5.59 shows the coherence of the  $u'$  and  $w'$  velocity com-

ponents for 18 and 19-July. The data show virtually no coherence over the range of recorded wavenumbers, as is expected for a flow that is “two dimensional” in the time averaged sense. This character is evident in both sets of data, but it is more amplified in the data taken on 18-July. The  $u'w'$  product does not seem to be effected by the ambient thermal condition.

### 5.3.3.3 $v'<\omega_z'>$ product

The velocity-vorticity products are important when viewed in the context of the Reynolds averaged Navier Stokes equations. The time averaged momentum equation for the u component of velocity can be presented in the form [25]:

$$\frac{\bar{D}\bar{u}}{Dt} = -\frac{1}{\rho} + \nu \nabla^2 \bar{u} - \frac{\partial \overline{u'^2}}{\partial x} - \frac{\partial \overline{u'v'}}{\partial y} - \frac{\partial \overline{u'w'}}{\partial z} \quad 5.40$$

where

$$\frac{\bar{D}}{Dt} = \bar{u} \frac{\partial}{\partial x} + \bar{v} \frac{\partial}{\partial y} + \bar{w} \frac{\partial}{\partial z} + \frac{\partial}{\partial t} \quad 5.41$$

is the material derivative. Assuming the pressure gradient and viscous effects are negligible, and ignoring the streamwise and spanwise derivatives, equation 5.40 can be reduced to:

$$\frac{\bar{D}\bar{u}}{Dt} = -\frac{\partial \overline{u'v'}}{\partial y} \quad 5.42$$

where the right hand side of equation 5.42 is the gradient of the Reynolds shear stress.

Using the tensor identity [31]

$$\frac{\partial}{\partial x_j} \overline{u'_i u'_j} = -\epsilon_{ijk} \overline{u'_j \omega'_k} + \frac{1}{2} \frac{\partial}{\partial x_i} \overline{u'_j u'_j} \quad 5.43$$

the gradient of the Reynolds shear stress can be decomposed to include contributions from the velocity-vorticity products. Using  $i = 1$  and ignoring the streamwise gradients, equation 5.43 reduces to

$$-\frac{\partial}{\partial y} \overline{u'v'} \approx \overline{v'\omega_z} - \overline{w'\omega_y} \quad 5.44$$

This section serves to present the results of the  $v'\omega_z$  product as seen over the three days data were acquired. The following section will present the findings on the  $w'\omega_y$  product. The statistical value of  $\overline{v'\omega_z}/\tilde{v}\tilde{\omega}_z$  will be presented for each day. The autospectral density of the product, the co-spectral density and the coherence will also be examined. The data will be presented with the thermally neutral data first (25-July) followed by the thermally unstable and thermally stable data (18-July and 19-July respectively).

The correlation coefficient,  $\overline{v'\omega_z}/\tilde{v}\tilde{\omega}_z$ , was found to be a relatively small quantity over all three data sets. Data from 18-July indicated a positive quantity (0.02), while data from 19 and 25-July indicated a negative coefficient (-0.03 and -0.004 respectively). Figures 5.60 through 5.65 illustrate the normalized and compensated autospectral densities of the  $v'\omega_z$  product for the three days data were taken. The compensated spectra for 25-July and 18-July show a similar peak at high wavenumbers and a similar slope over moderate wavenumbers before tailing off over the smallest wavenumbers. The data for 19-July show the same initial peak at higher wavenumbers, but show a region of almost constant value over the moderate wavenumbers before finally tailing off for low wavenumbers.

Figures 5.66 through 5.68 show the co-spectral densities of the  $v'$  velocity component and the  $\langle \omega_z' \rangle$  vorticity component. These data appear very similar over all three days, and have a very small region demonstrating the  $-7/3$  slope. This  $-7/3$  slope is predicted for the co-spectral densities of the velocity components for linear shear flows [24], but was shown here to serve as a point of comparison.

Figure 5.69 shows the coherence of the  $v'$  and  $\langle \omega_z' \rangle$  components for all three days. It can be seen that all the data exhibit the same trend in the coherence. The  $v'$  and  $\langle \omega_z' \rangle$  components are highly correlated over a very small range of wavenumbers. The coherence peaks at a value of 0.8 for a normalized wavenumber of about  $k_1 \eta \approx 0.35$  (corresponding to  $k_1 l^+ \approx 0.05$ ). The trend drops off fairly quickly (but not symmetrically) on either side of the peak.

#### 5.3.3.4 $w' \langle \omega_y' \rangle$ product

This section serves to present the results of the  $w' \langle \omega_y' \rangle$  product as obtained from the two days for which data were acquired. The statistical value of  $\overline{w' \omega_y'} / \tilde{w} \tilde{\omega}_y$  will be presented for each day. The autospectral density of the product, the co-spectral density and the coherence will also be examined. The  $w' \langle \omega_y' \rangle$  product was not available on the day with thermal neutrality. Therefore, the thermally unstable data will be presented first followed by the thermally stable data (18-July and 19-July respectively).

The correlation coefficient,  $\overline{w'\omega_y'}/\tilde{w}\tilde{\omega}_y$ , was found to be a relatively large quantity over both data sets. The correlation coefficient ( $\overline{w'\omega_y'}/\tilde{w}\tilde{\omega}_y = 0.2$ ) indicates a significant correlation between the  $w'$  component of the velocity and the  $\langle\omega_y'\rangle$  component of the velocity.

Figures 5.70 through 5.73 show the normalized and compensated autospectral densities of the  $w'\langle\omega_y'\rangle$  product. The character of these plots appears similar to the  $v'\langle\omega_z'\rangle$  autospectral densities. The compensated spectrum from 18-July shows a flattened region over moderate wavenumbers. The 19-July data show a large hump at higher wavenumbers followed by the decline to an almost constant value. The spectrum then tails off for the lowest wavenumbers.

Figures 5.74 and 5.75 show the normalized co-spectral densities of  $w'$  and  $\langle\omega_y'\rangle$  for both days. The data show a linear decrease as the wavenumber increases, but the slope is visibly not  $-7/3$ . Figure 5.76 shows the spectral coherence of  $w'$  and  $\langle\omega_y'\rangle$  for both data sets. Both data sets show similar trends, although slightly offset in amplitude and wavenumber. The general shape of the coherence is a large correlation at high wavenumbers. The coherence peaks around  $k_1\eta \approx 0.25$  for 18-July and  $k_1\eta \approx 0.4$  for 19-July. The observed coherence drops to a value near zero for moderate wavenumbers before rising again for the lowest wavenumbers.

The correlation between the  $u'$  and  $\langle\omega_z'\rangle$  measurements was also examined, but provided no consistent character. Table 5.8 shows the correlation coefficient for  $u'\langle\omega_z'\rangle$



varies significantly between the three data sets. Spectral analysis showed no coherence between the two measurements. Figure 5.77 shows the three compensated autospectral densities of the velocity-vorticity products for 18-July plotted together. The  $u'\langle\omega_z'\rangle$  and  $v'\langle\omega_z'\rangle$  components show similar trend with a hump at higher wavenumbers, while the  $w'\langle\omega_y'\rangle$  data show no hump and a region of constant value.

Figure 5.78 shows the same data for 19-July. Here, all three spectra show the larger hump for higher wavenumbers and a fairly constant value over a range of moderate wavenumbers. Figure 5.79 shows this data for 25-July. The two spectra for 25-July show the same large hump and semi-constant range, offset by what appears a constant magnitude.

#### 5.4 Vorticity Probability Density Functions

The probability density functions (PDF's) for the measured  $\langle\omega_z'\rangle$  and  $\langle\omega_y'\rangle$  vorticity components were also analyzed. This section presents the normalized PDF's for the three data sets and it provides a discussion of the trends associated with Reynolds number and / or thermal stability.

Figure 5.80 shows the normalized PDF's for the  $\langle\omega_z'\rangle$  vorticity component. The three days of data do not collapse very well, but instead exhibit a dependence on  $R_\lambda$ . The kurtosis (flatness) of the  $\langle\omega_z'\rangle$  PDF seems to increase with higher  $R_\lambda$  values. The statistical values of the PDF can be seen in Table 5.9. The Reynolds number of each day is shown in Table 5.6 and increases from 19-July through 25-July. It should be noted that

this dependence on  $R_\lambda$  is assumed independent of the thermal effects which may also contribute to the skewness of the probability distribution functions.

Figure 5.81 shows the normalized PDF's for the  $\langle \omega_y' \rangle$  vorticity component. The two data sets do not collapse well. The statistics of the PDF can be seen in Table 5.10. The flatness appears to decrease with an increase in  $R_\lambda$ , but a specific trend could not be inferred due to the uncertainties of the thermal effects.

**Table 5.1 Data Set Properties**

	18-July	19-July	25-July
$y_{measure}$ (cm)	20	20	40
$y^+$	3800	3800	10,300
$T_{Duration}$ (min)	19	50	58.5
$L_x$ (m)	4583	11,108	18,779
$\frac{y_{measure}}{L_x}$	$4.36 \times 10^{-5}$	$1.8 \times 10^{-5}$	$2.13 \times 10^{-5}$
$L_{Monin - Obukov}$ (m)	-1.3	6.1	42.4
$\bar{\xi}$	-2.4	.52	.075

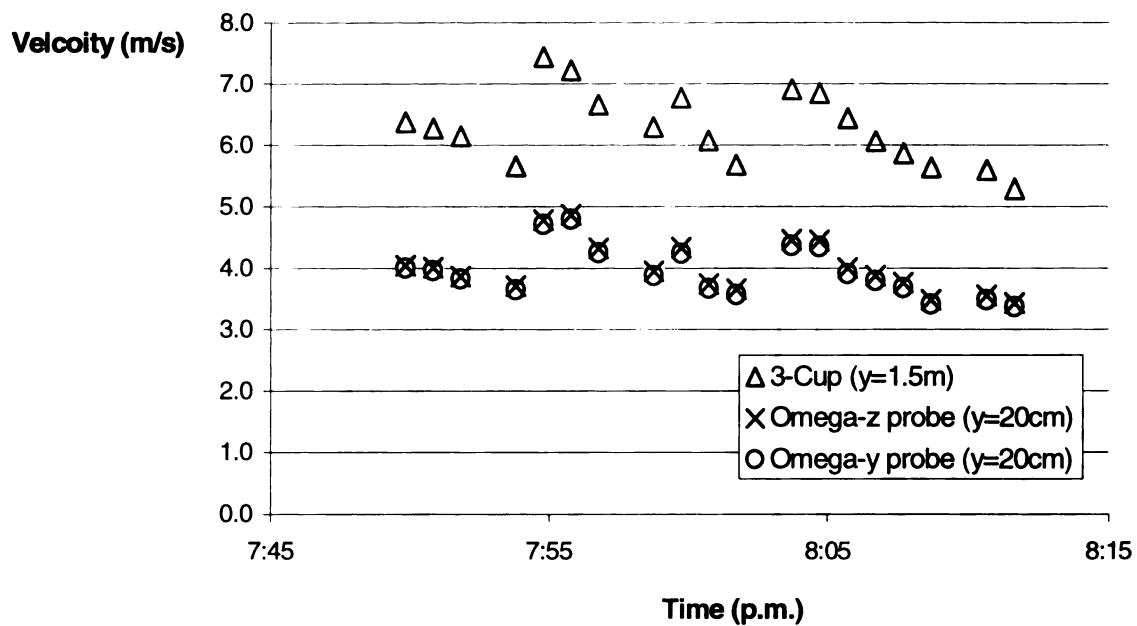


Figure 5.1 Mean wind speed for 18-July, 2001.

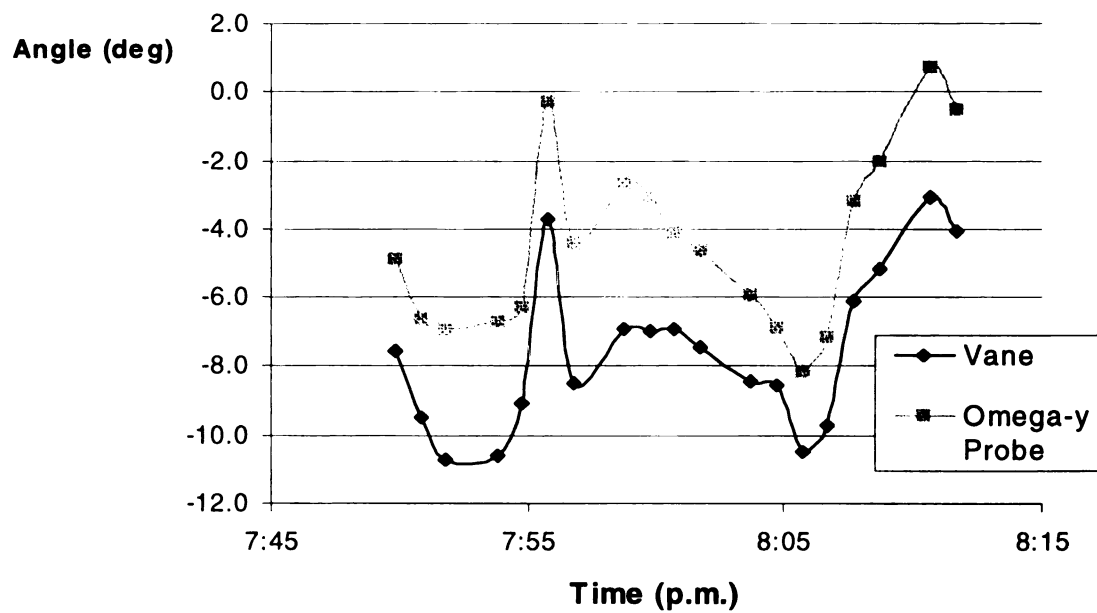


Figure 5.2 Mean wind direction for 18-July, 2001.

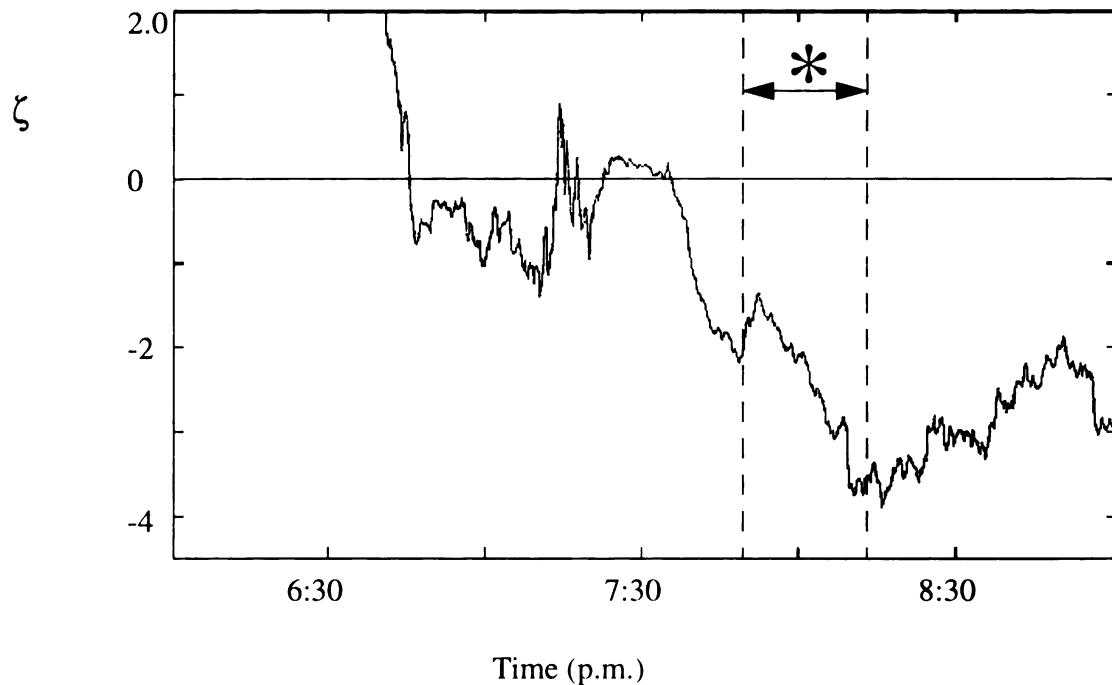


Figure 5.3 Thermal stability parameter for 18-July, 2001. (\* = Time period for MSU data acquisition.)

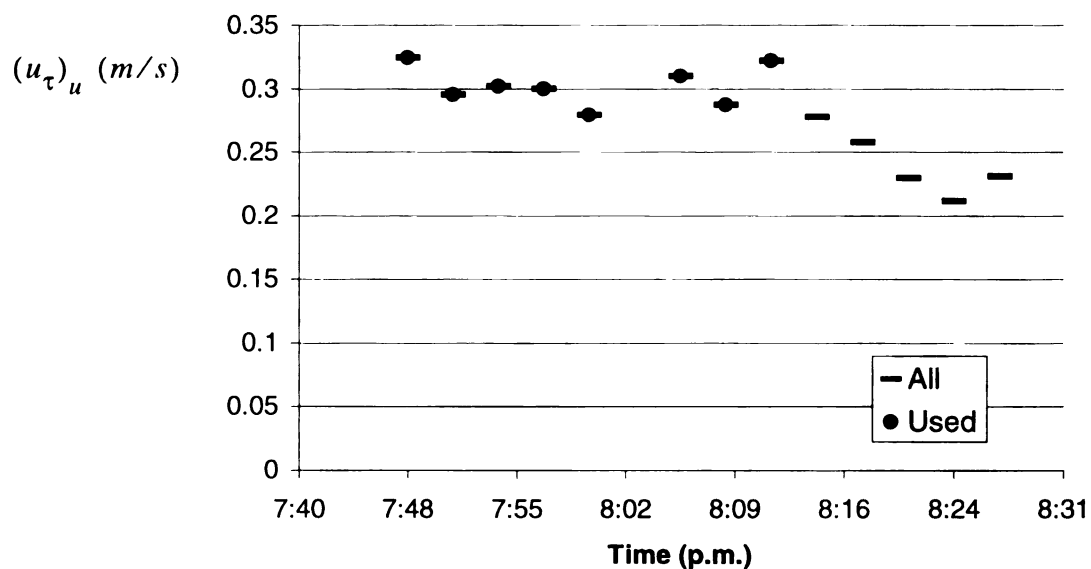


Figure 5.4 Friction velocity as a function of time for 18-July, 2001.

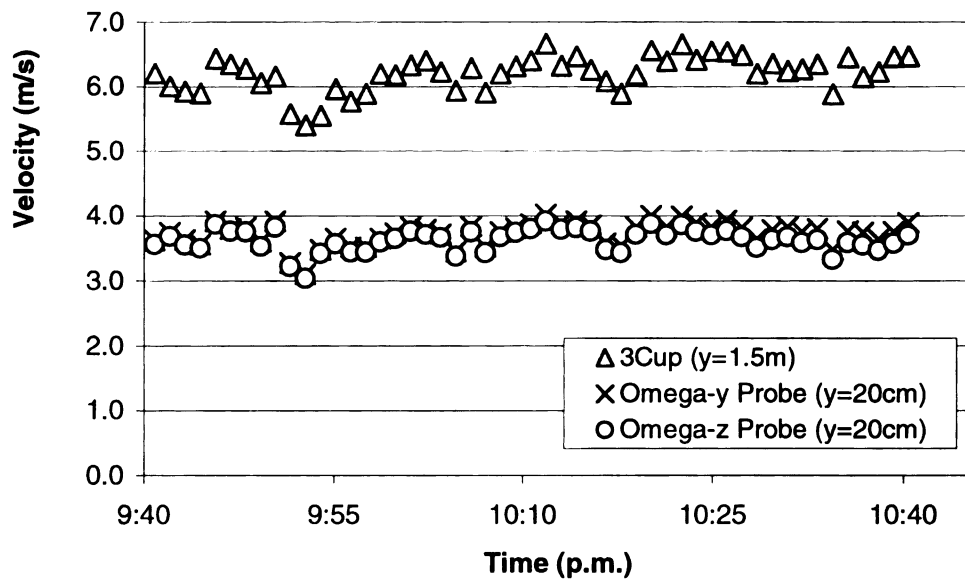


Figure 5.5 Mean wind speed for 19-July, 2001.

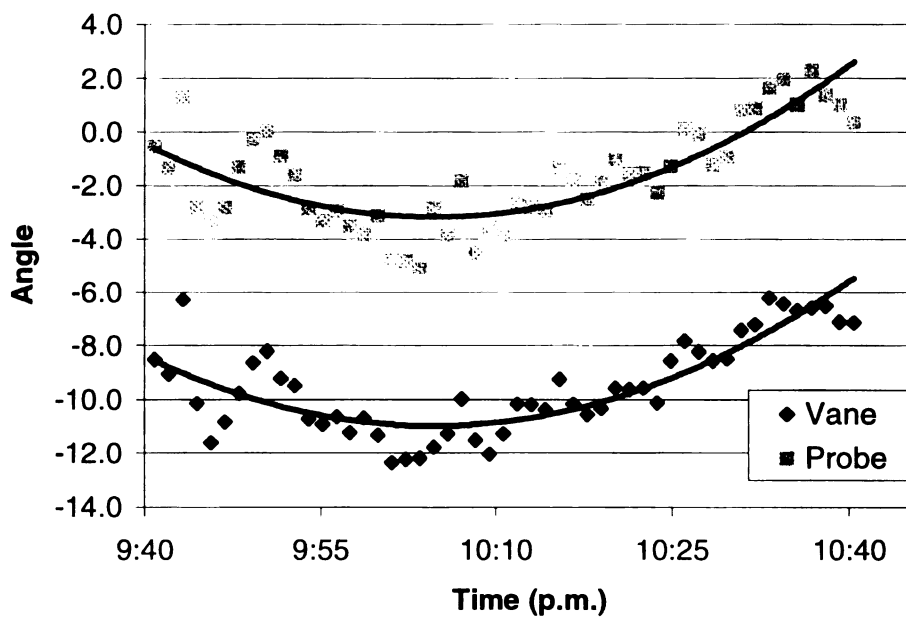


Figure 5.6 Mean wind direction for 19-July, 2001.

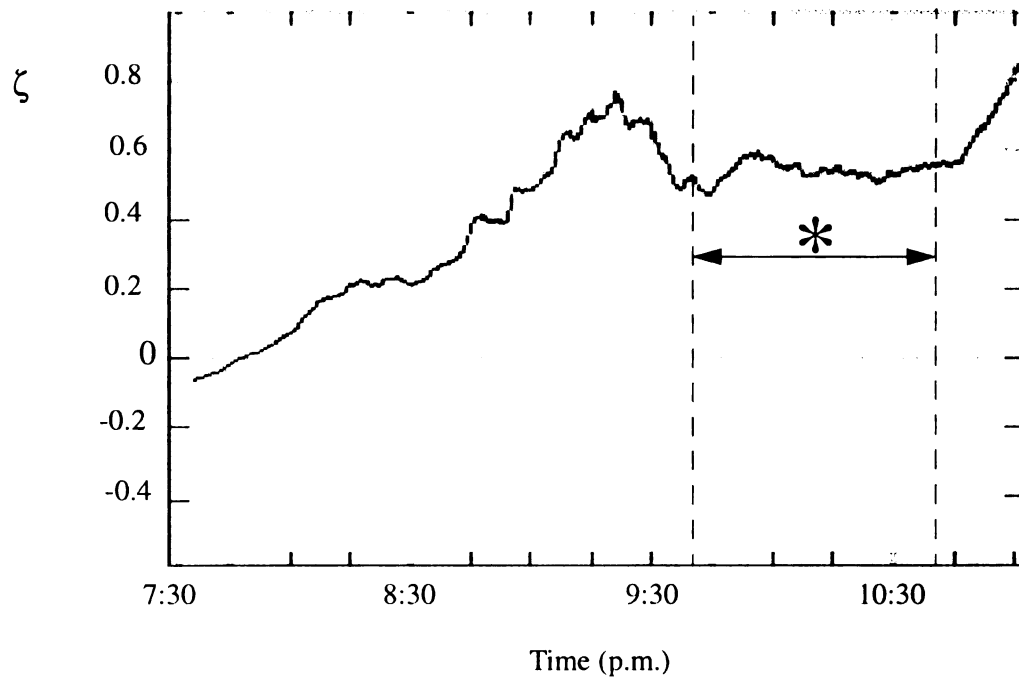


Figure 5.7 Thermal stability parameter for 19-July, 2001. (\* = Time period for MSU data acquisition.)

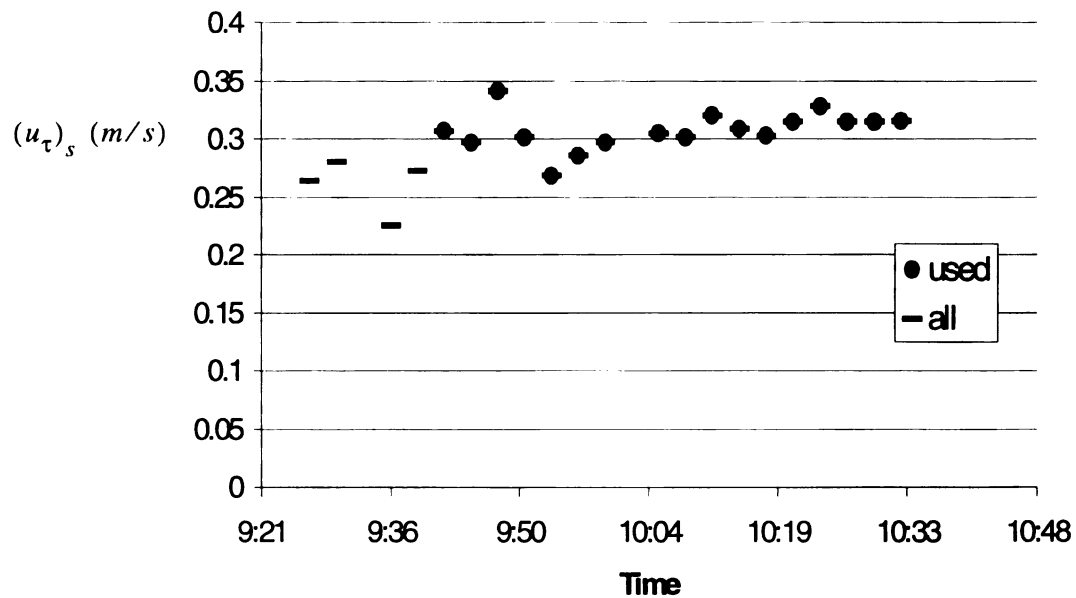


Figure 5.8 Friction velocity as a function of time for 19-July, 2001.

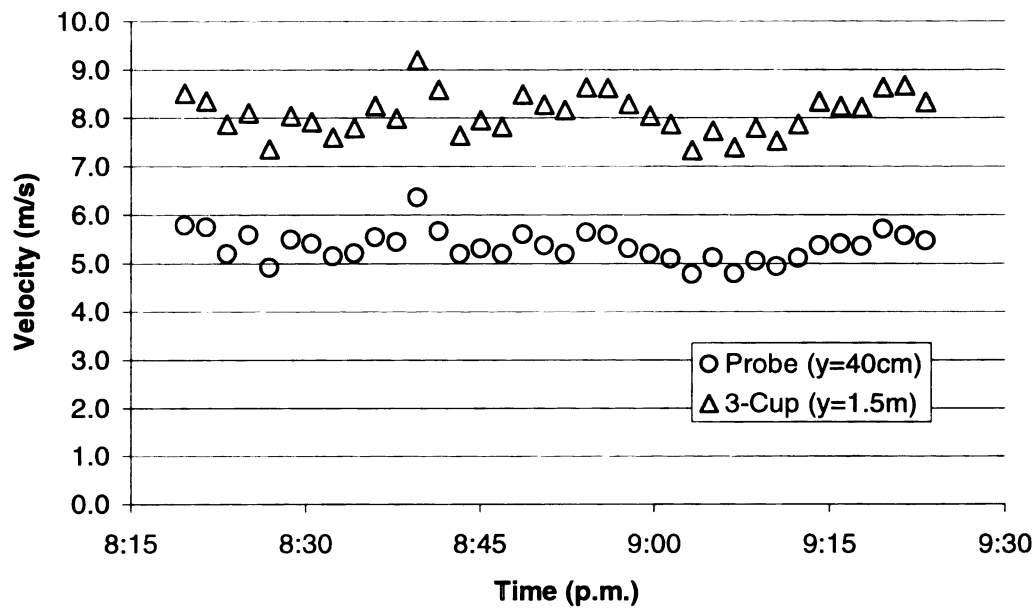


Figure 5.9 Mean wind speed for 25-July, 2001.

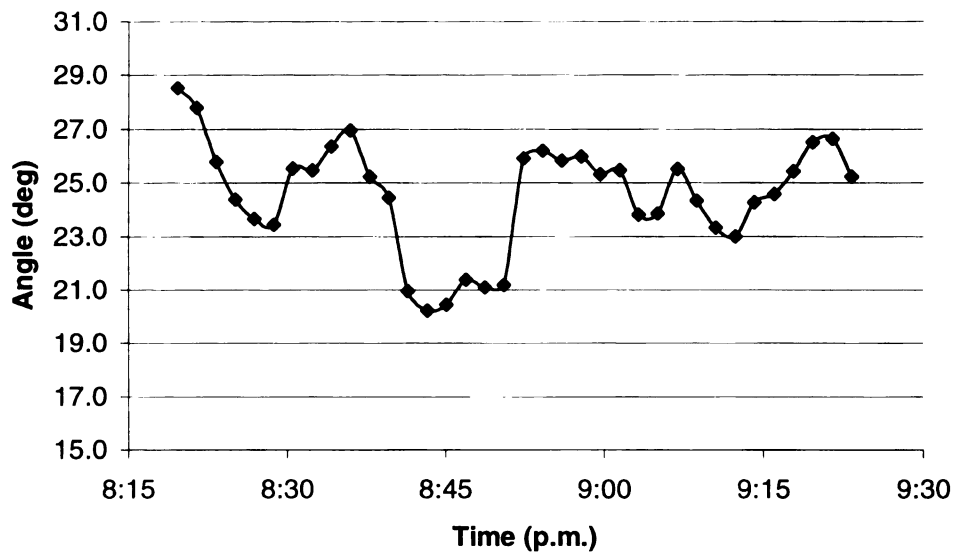


Figure 5.10 Mean wind direction for 25-July, 2001.



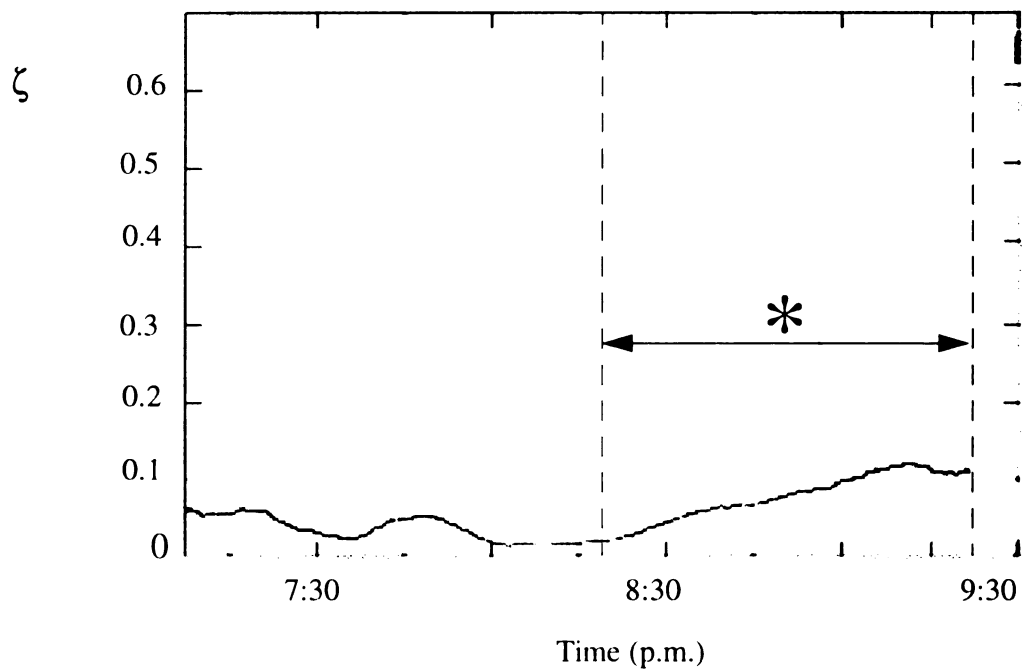


Figure 5.11 Thermal stability parameter for 25-July, 2001. (\* = Time period for MSU data acquisition.)

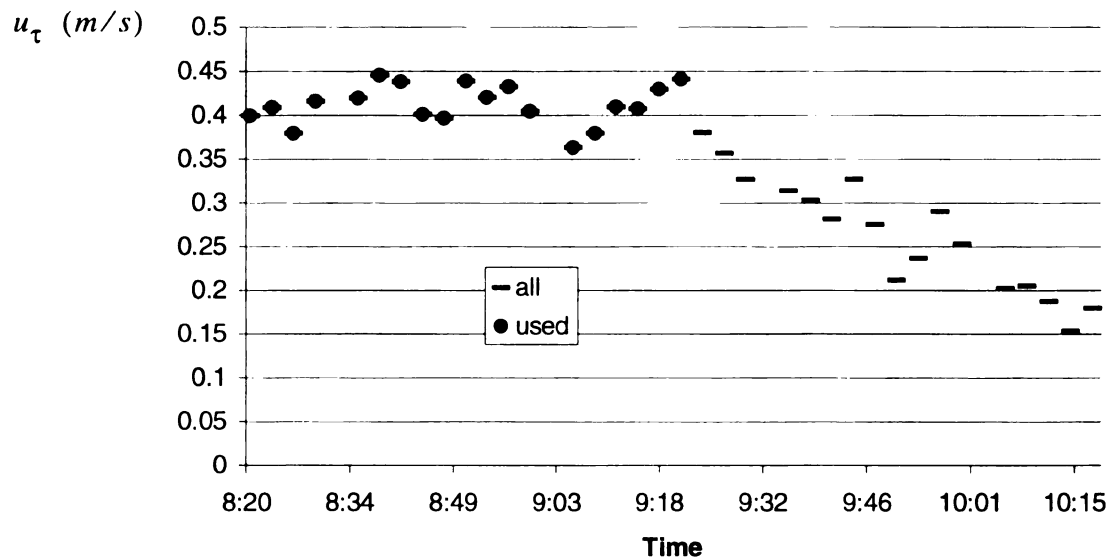


Figure 5.12 Friction velocity as a function of time for 25-July, 2001.

**Table 5.2 Mean Dimensional Flow Parameters**

	18-July	19-July	25-July
$\bar{u}$ (m/s)	4.02	3.63	5.35
$\bar{v}$ (m/s)	-0.02	-0.02	-0.02
$\bar{w}$ (m/s)	-0.003	-0.008	N/A
$\tilde{u}$ (m/s)	0.89	0.74	1.02
$\tilde{v}$ (m/s)	0.38	0.32	.046
$\tilde{w}$ (m/s)	0.55	0.51	N/A
$\overline{u'^2}$ (m <sup>2</sup> /s <sup>2</sup> )	0.79	0.54	1.04
$\overline{v'^2}$ (m <sup>2</sup> /s <sup>2</sup> )	0.14	0.10	0.21
$\overline{w'^2}$ (m <sup>2</sup> /s <sup>2</sup> )	0.31	0.26	N/A
$\tilde{\omega}_z$ (1/s)	84.5	94.1	84.7
$\tilde{\omega}_y$ (1/s)	97.0	75.3	N/A

**Table 5.3 Mean Flow Properties \***

	18-July	19-July	25-July
$u_{\tau}$ (m/s)	0.302	0.307	0.412
$v$ (m <sup>2</sup> /s)	$1.6 \times 10^{-5}$	$1.6 \times 10^{-5}$	$1.6 \times 10^{-5}$
$\eta$ (mm)	0.35	0.36	0.34
$u_{\eta}$ (m/s)	0.046	0.044	0.048
$l^+$ (mm)	0.053	0.052	0.039

\*The values of  $u_{\tau}$  were computed in the assumption of thermal neutrality. 18-July data were acquired under thermally unstable conditions and 19-July data were acquired under thermally stable conditions. See Section 2.2.3 for details.

**Table 5.4 Dissipation Estimates**

	18-July	19-July	25-July
$\epsilon_a$ (m <sup>2</sup> /s <sup>3</sup> )	0.27	0.24	0.32
$\epsilon_b$ (m <sup>2</sup> /s <sup>3</sup> )	1.1	1.0	1.4
$\epsilon_b'$ (m <sup>2</sup> /s <sup>3</sup> )	.20	.20	0.28
$\epsilon_c$ (m <sup>2</sup> /s <sup>3</sup> )	0.33	0.57	N/A
$\epsilon_d$ (m <sup>2</sup> /s <sup>3</sup> )	0.34	.043	0.34
$\epsilon_e$ (m <sup>2</sup> /s <sup>3</sup> )	0.62	0.61	N/A
$\epsilon_f$ (m <sup>2</sup> /s <sup>3</sup> )	0.32	0.41	N/A

**Table 5.5 Normalized Flow Parameters \***

	18-July	19-July	25-July
$\frac{\overline{u}}{u_\tau}$	13.28	11.8	13.0
$\frac{\bar{v}}{u_\tau}$	-0.08	-0.07	-0.06
$\frac{\bar{w}}{u_\tau}$	-0.01	-0.03	N/A
$\frac{\tilde{u}}{u_\tau}$	2.93	2.47	2.47
$\frac{\tilde{v}}{u_\tau}$	1.24	1.05	1.11
$\frac{\tilde{w}}{u_\tau}$	1.83	1.67	N/A
$\frac{\overline{u'^2}}{u_\tau^2}$	8.61	5.76	6.11
$\frac{\overline{v'^2}}{u_\tau^2}$	1.54	1.10	1.24
$\frac{\overline{w'^2}}{u_\tau^2}$	3.35	2.79	N/A

\*The values of  $u_\tau$  were computed in the assumption of thermal neutral-ity. 18-July data were acquired under thermally unstable conditions and 19-July data were acquired under thermally stable conditions. See Section 2.2.3 for details.

**Table 5.6 Taylor Microscale Parameters**

	18-July	19-July	25-July
$\lambda_u$ (m)	0.037	0.033	0.039
$\lambda_v$ (m)	0.013	0.011	0.013
$\lambda_w$ (m)	0.024	0.015	N/A
$R_{\lambda_u}$	2062	1533	2510
$R_{\lambda_v}$	725	514	850
$R_{\lambda_w}$	827	485	N/A

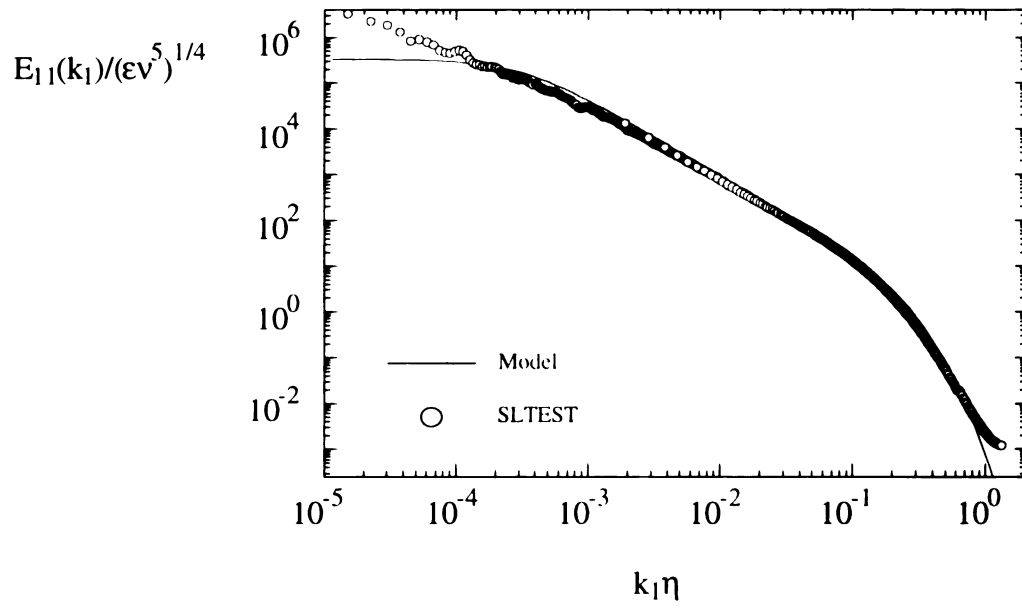


Figure 5.13 Normalized autospectral density of the u-velocity fluctuation (25-July).

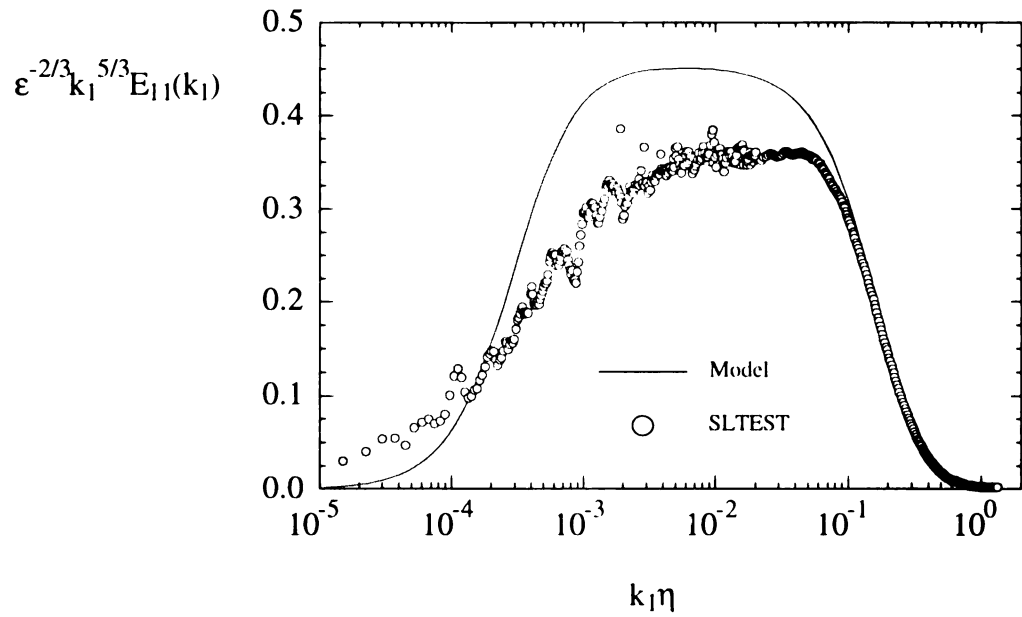


Figure 5.14 Compensated autospectral density of the u-velocity fluctuation (25-July).

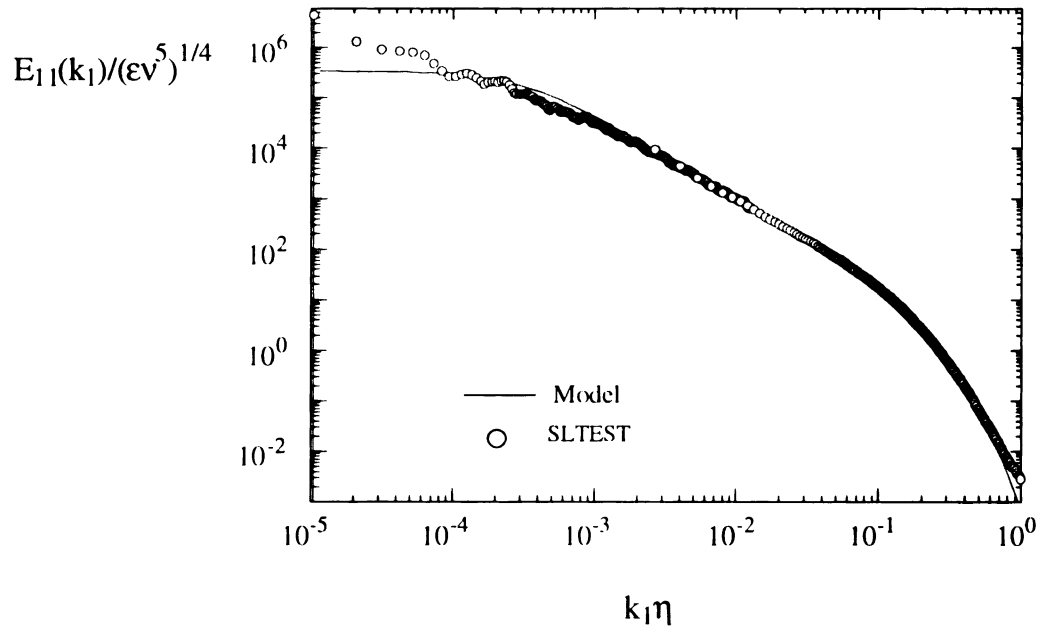


Figure 5.15 Normalized autospectral density of the u-velocity fluctuation (18-July).

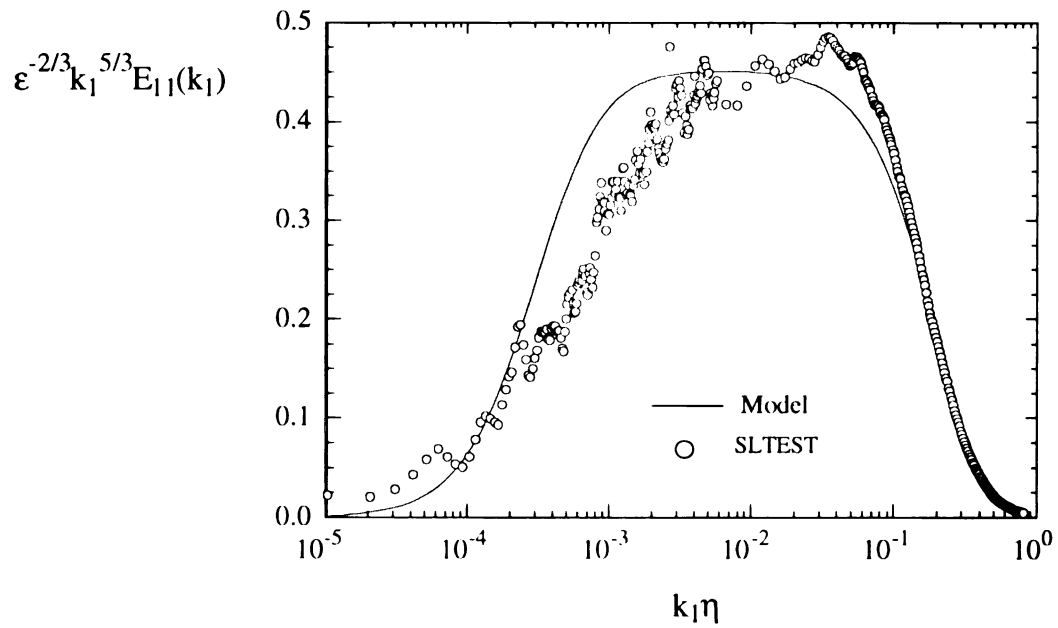


Figure 5.16 Compensated autospectral density of the u-velocity fluctuation (18-July).

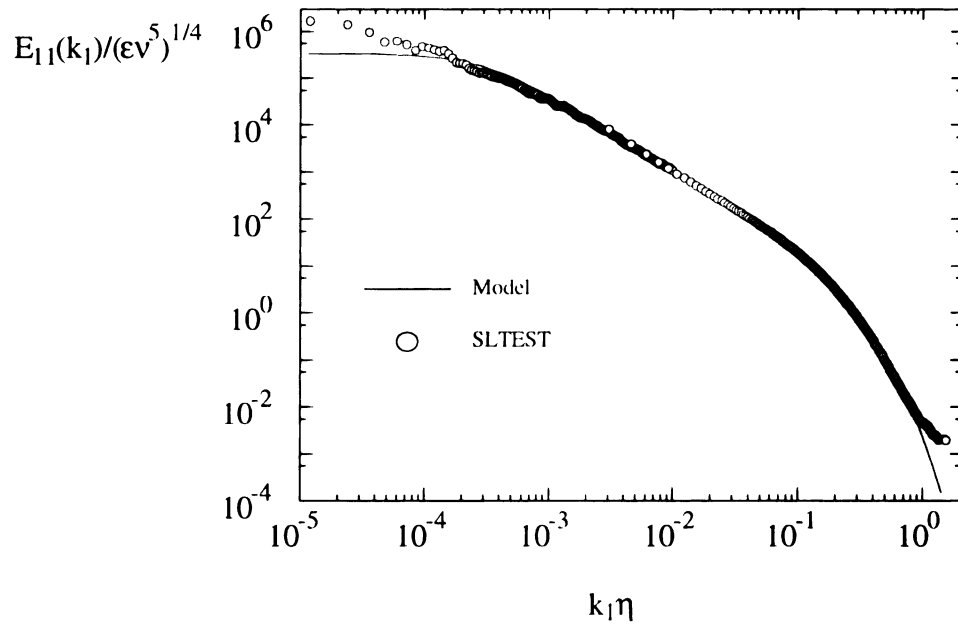


Figure 5.17 Normalized autospectral density of the u-velocity fluctuation (19-July).

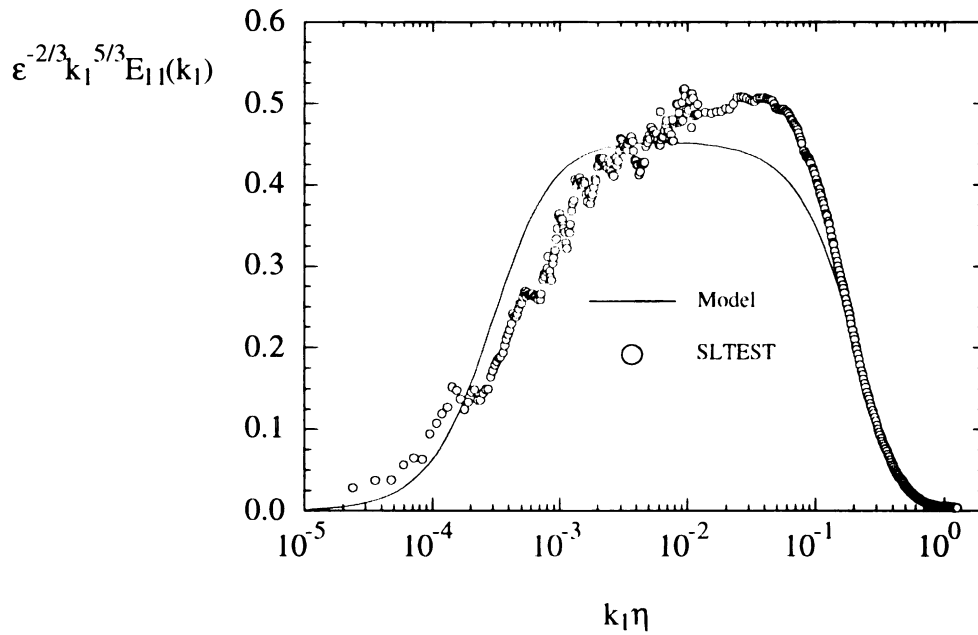


Figure 5.18 Compensated autospectral density of the u-velocity fluctuation (19-July).



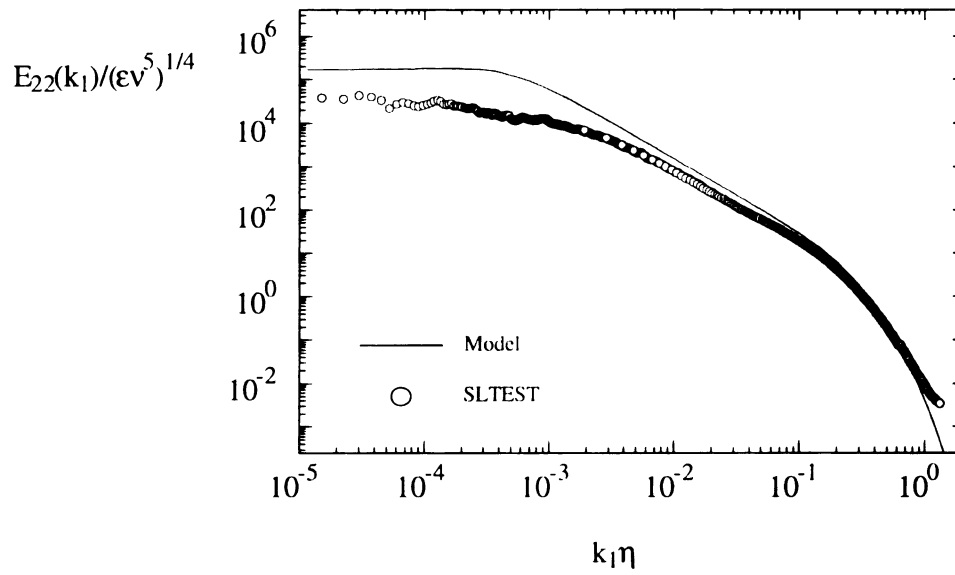


Figure 5.19 Normalized autospectral density of the v-velocity fluctuation (25-July).

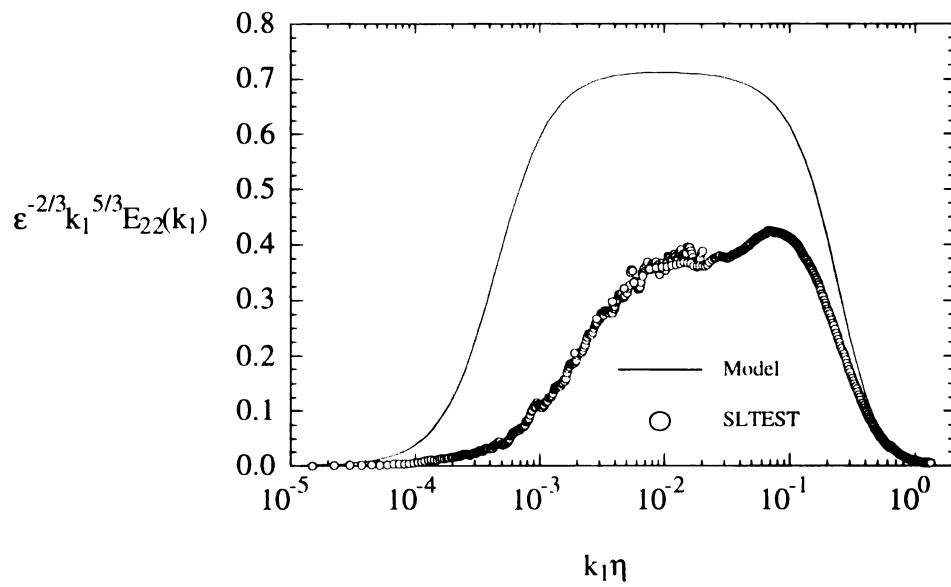


Figure 5.20 Compensated autospectral density of the v-velocity fluctuation (25-July).

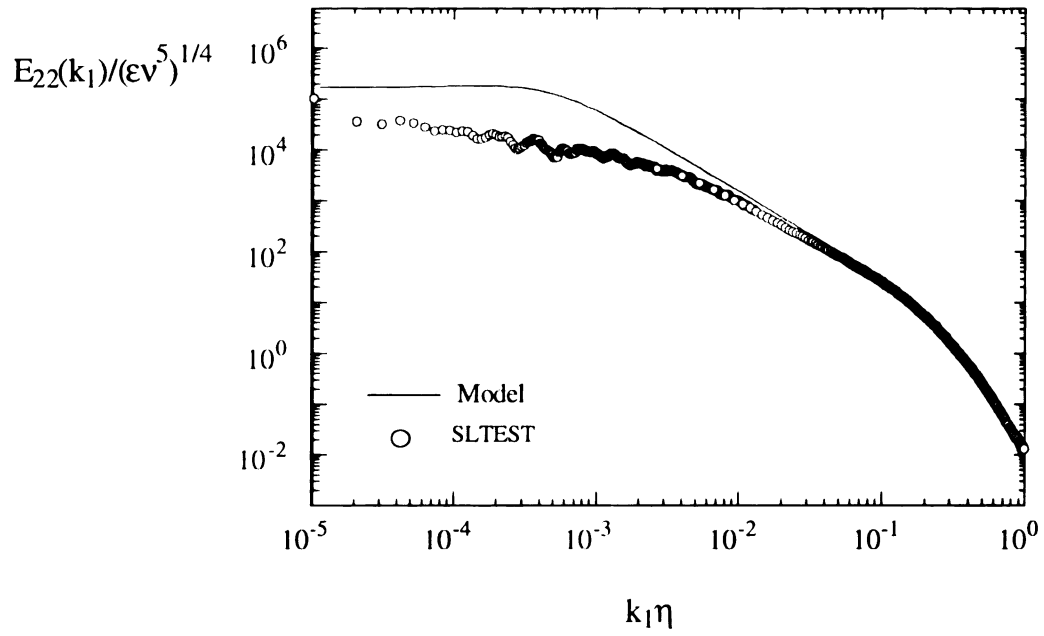


Figure 5.21 Normalized autospectral density of the v-velocity fluctuation (18-July).

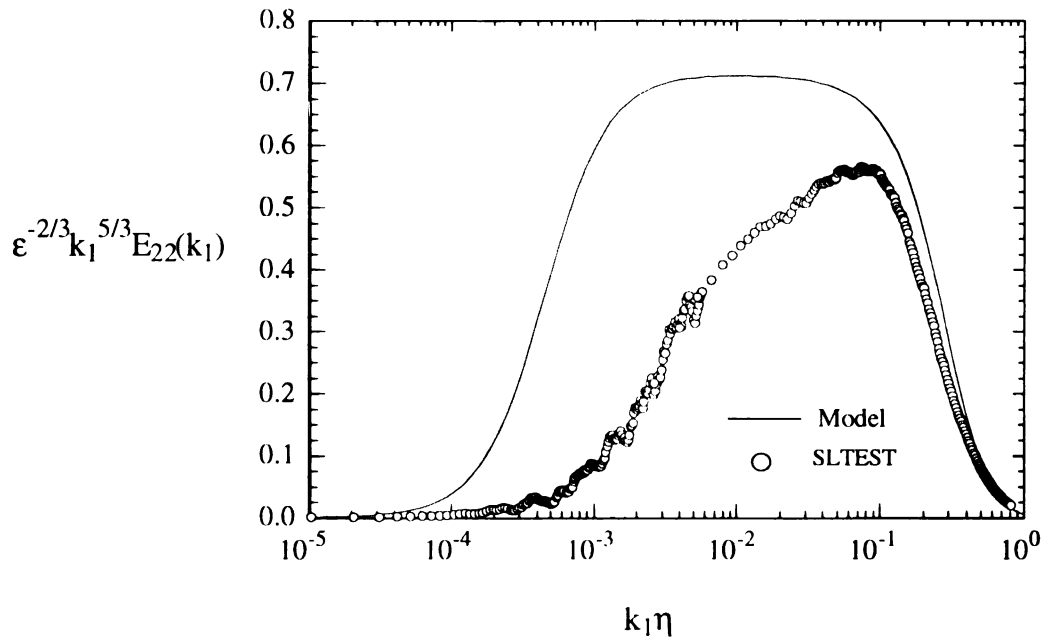


Figure 5.22 Compensated autospectral density of the v-velocity fluctuation (18-July).

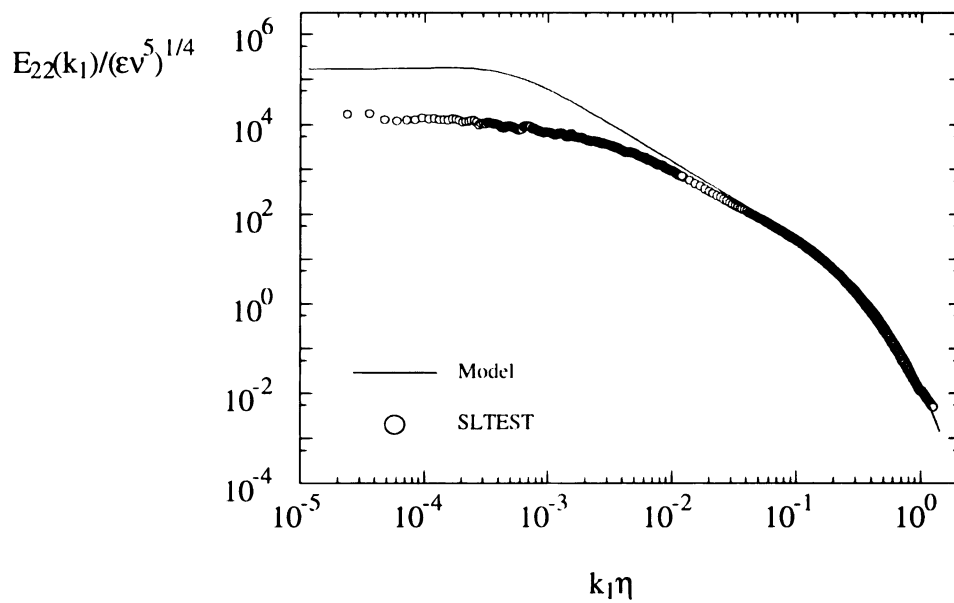


Figure 5.23 Normalized autospectral density of the v-velocity fluctuation (19-July).

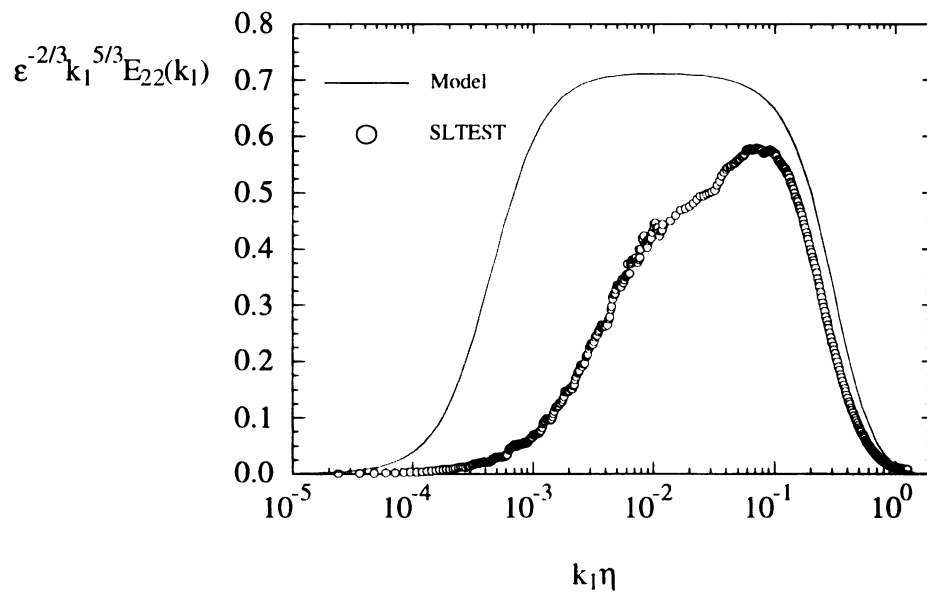


Figure 5.24 Compensated autospectral density of the v-velocity fluctuation (19-July).

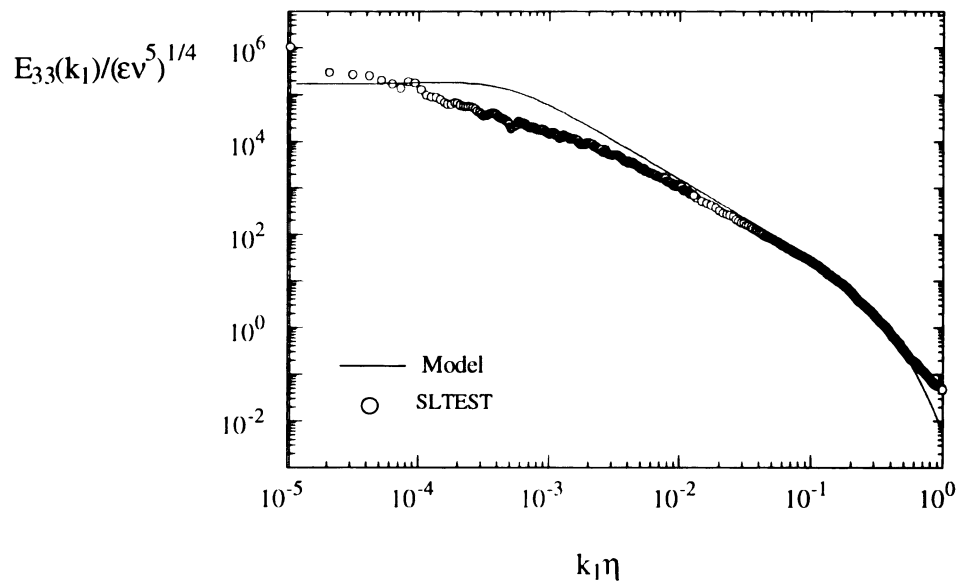


Figure 5.25 Normalized autospectral density of the w-velocity fluctuation (18-July).

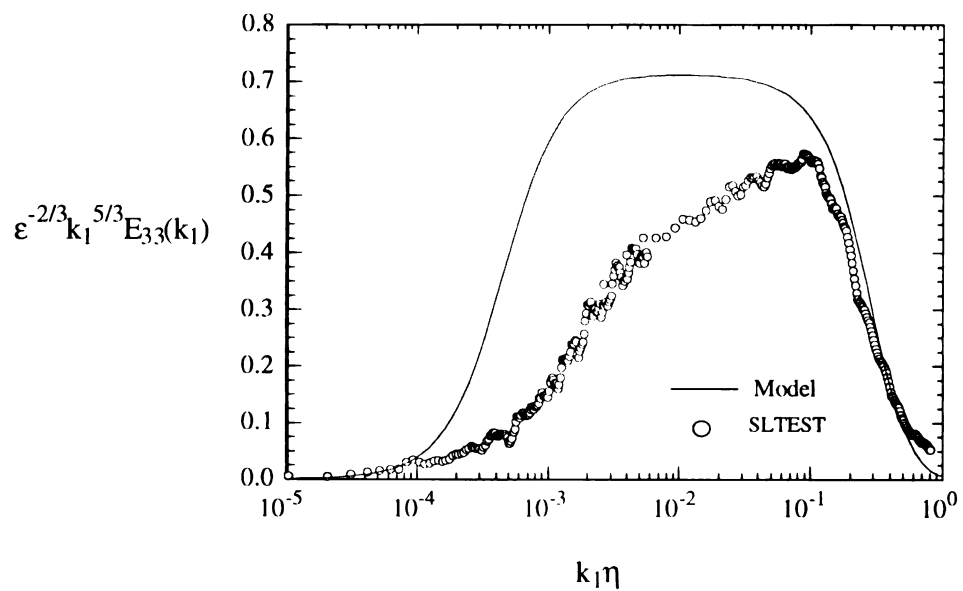


Figure 5.26 Compensated autospectral density of the w-velocity fluctuation (18-July).

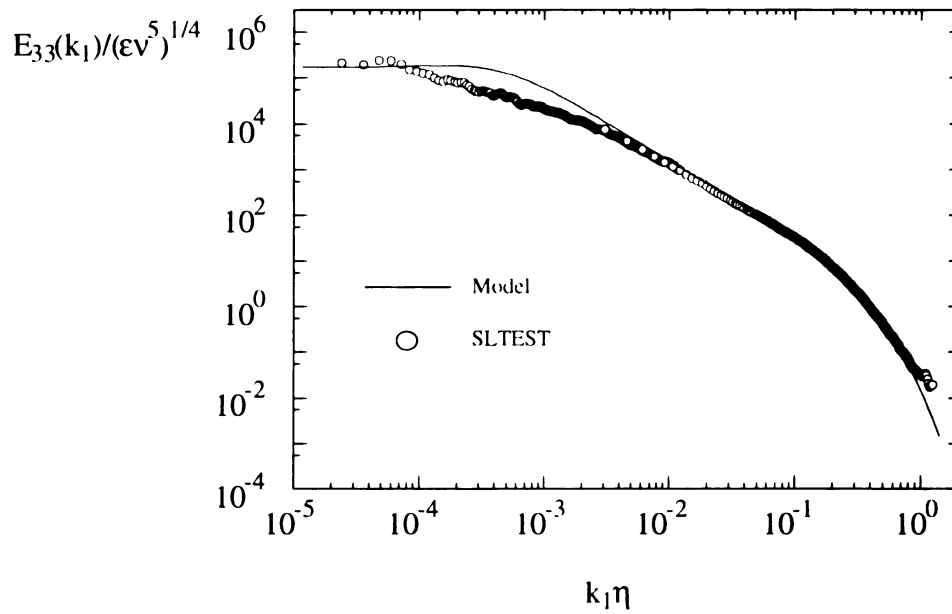


Figure 5.27 Normalized autospectral density of the w-velocity fluctuation (19-July).

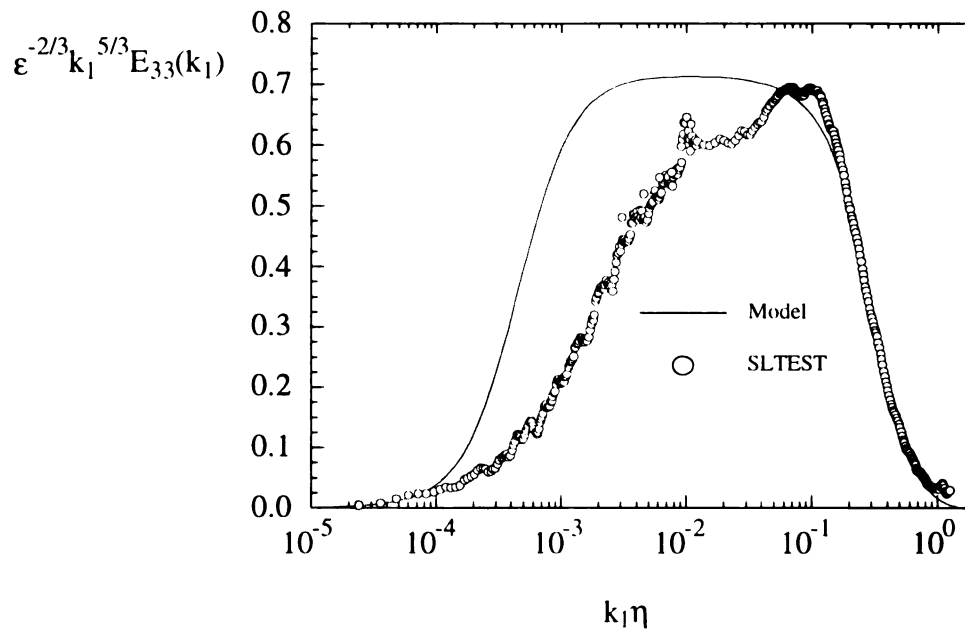


Figure 5.28 Compensated autospectral density of the w-velocity fluctuation (19-July).

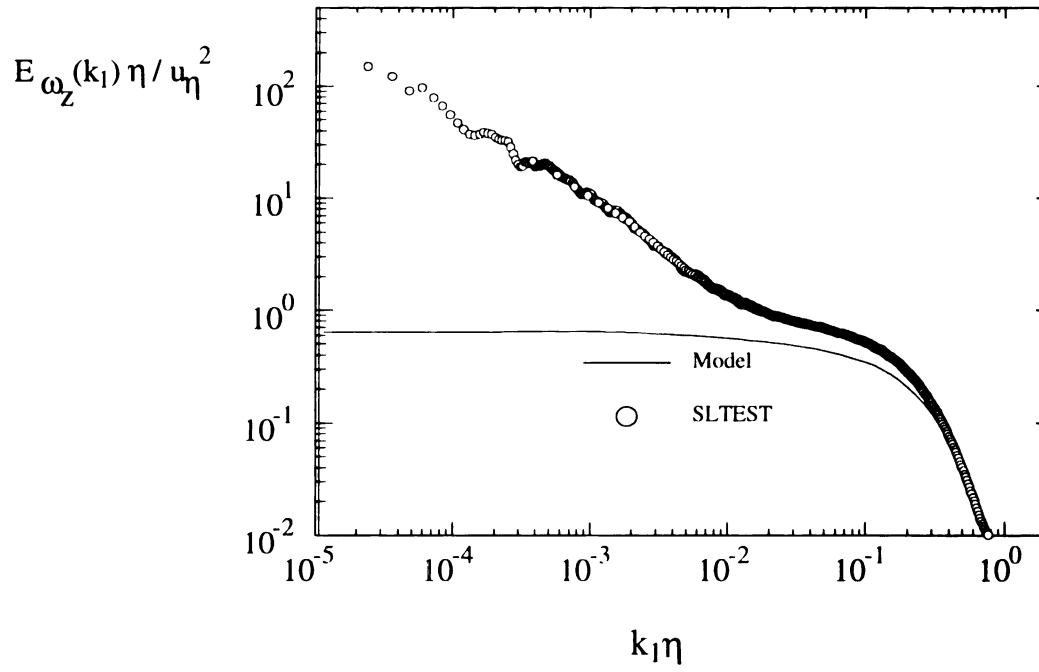


Figure 5.29 Normalized autospectral density of the  $\langle \omega_z \rangle$  vorticity (25-July).

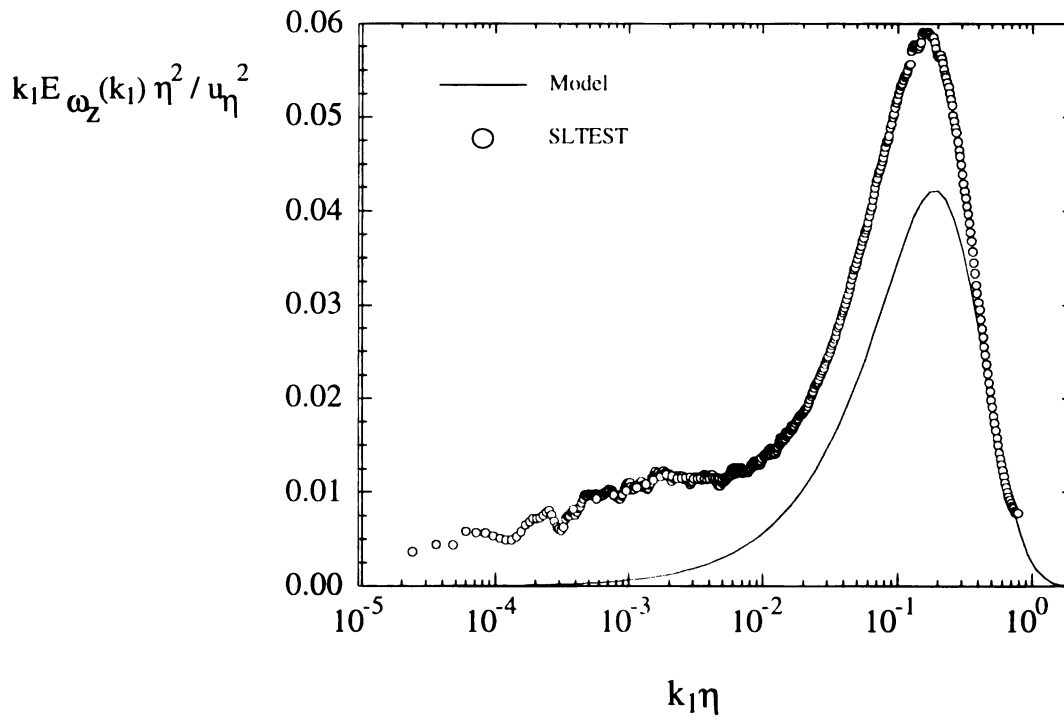


Figure 5.30 Compensated autospectral density of the  $\langle \omega_z \rangle$  vorticity (25-July).

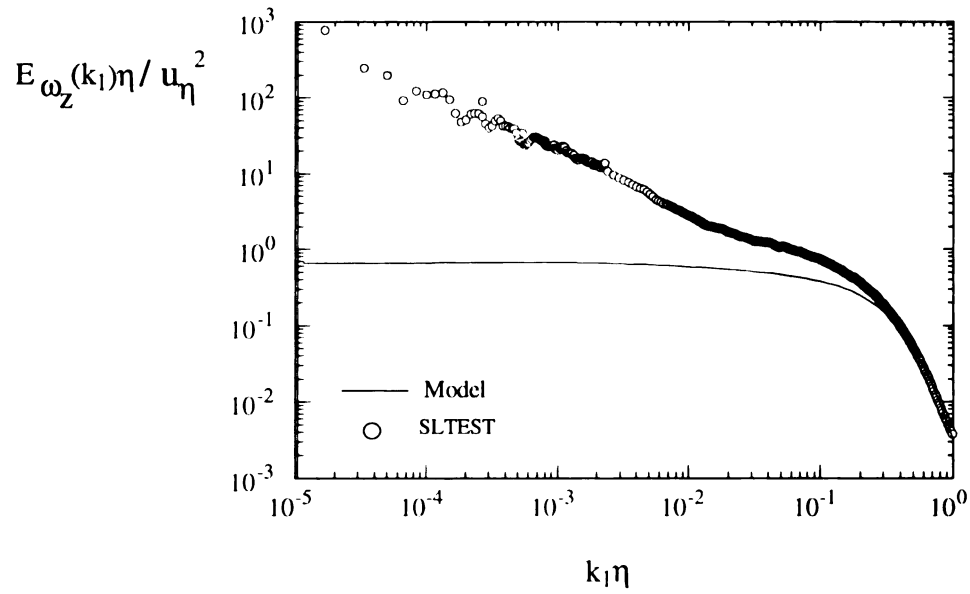


Figure 5.31 Normalized autospectral density of the  $\langle \omega_z \rangle$  vorticity (18-July).

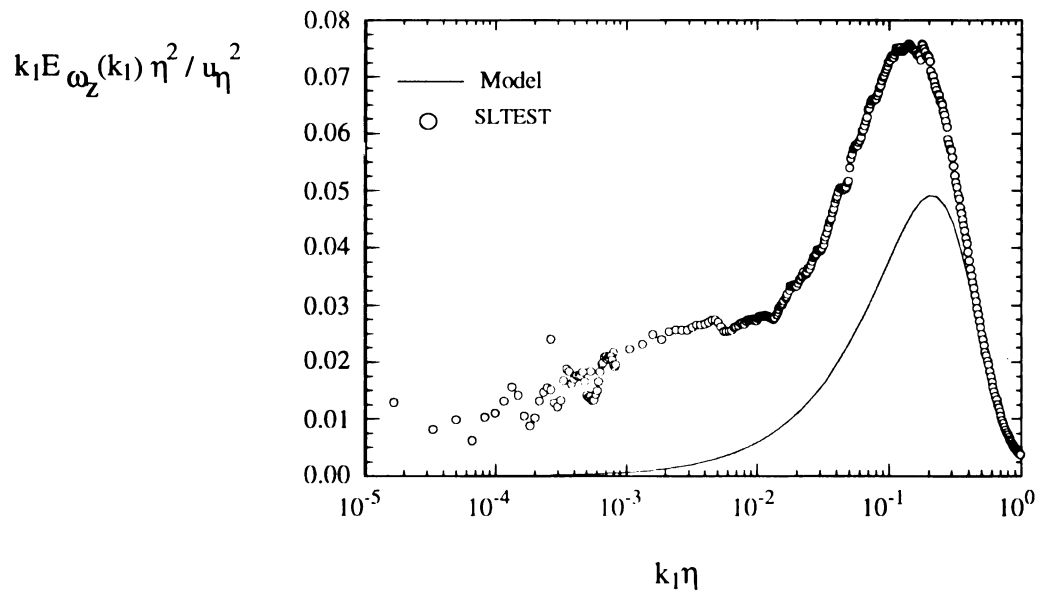


Figure 5.32 Compensated autospectral density of the  $\langle \omega_z \rangle$  vorticity (18-July).

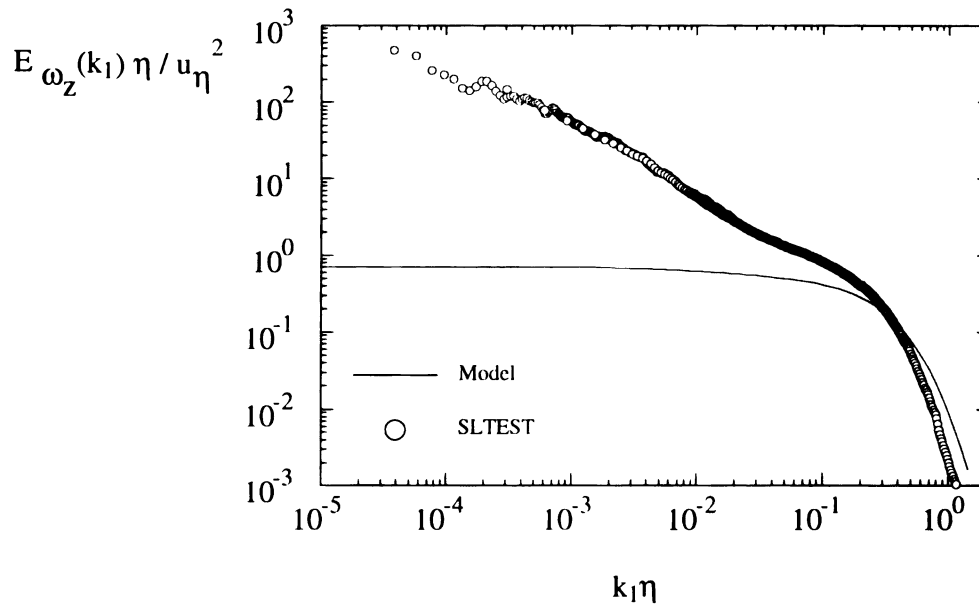


Figure 5.33 Normalized autospectral density of the  $\langle \omega_z \rangle$  vorticity (19-July).

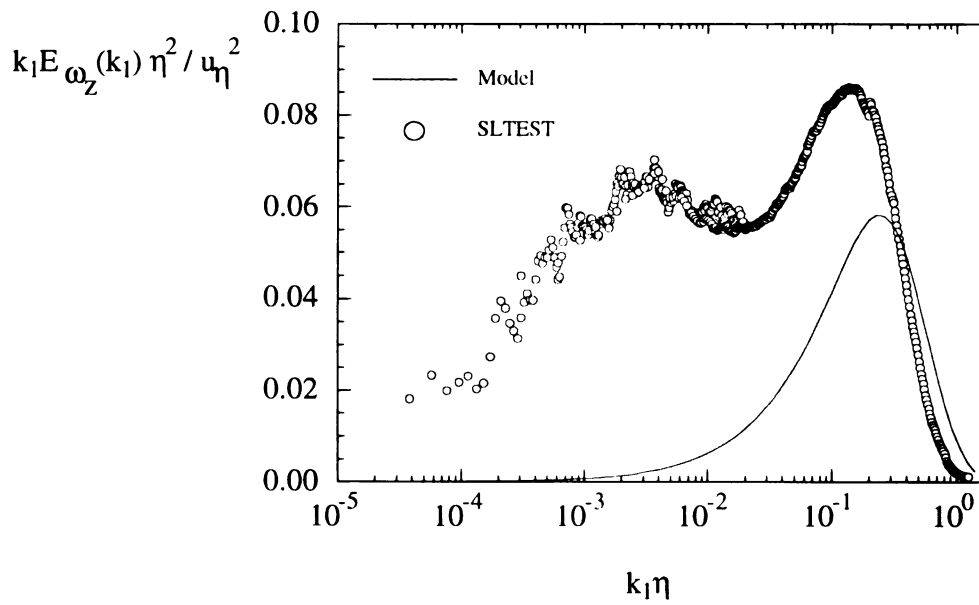


Figure 5.34 Compensated autospectral density of the  $\langle \omega_z \rangle$  vorticity (19-July).



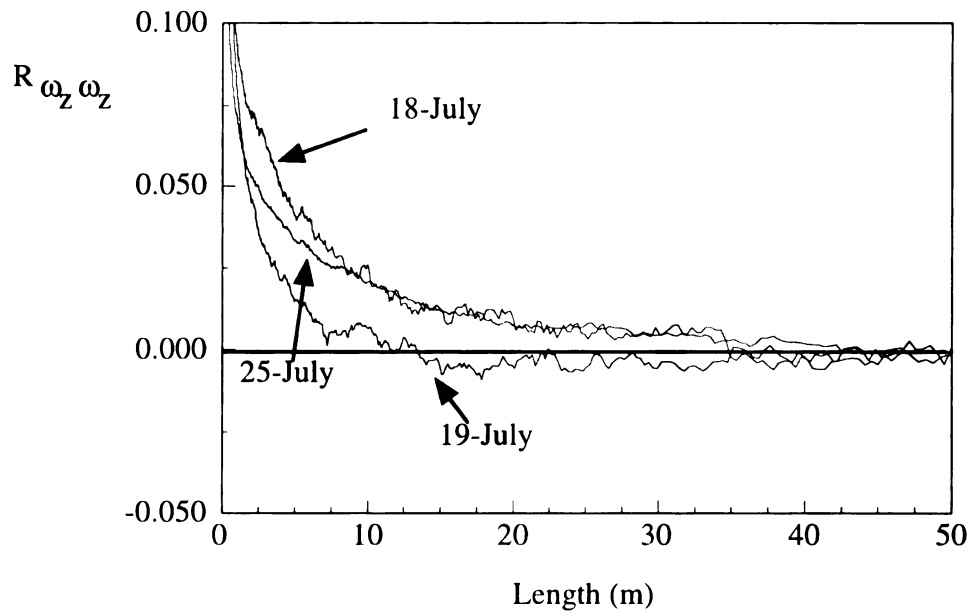


Figure 5.35 Autocorrelation of the  $\langle \omega_z \rangle$  vorticity for each day.

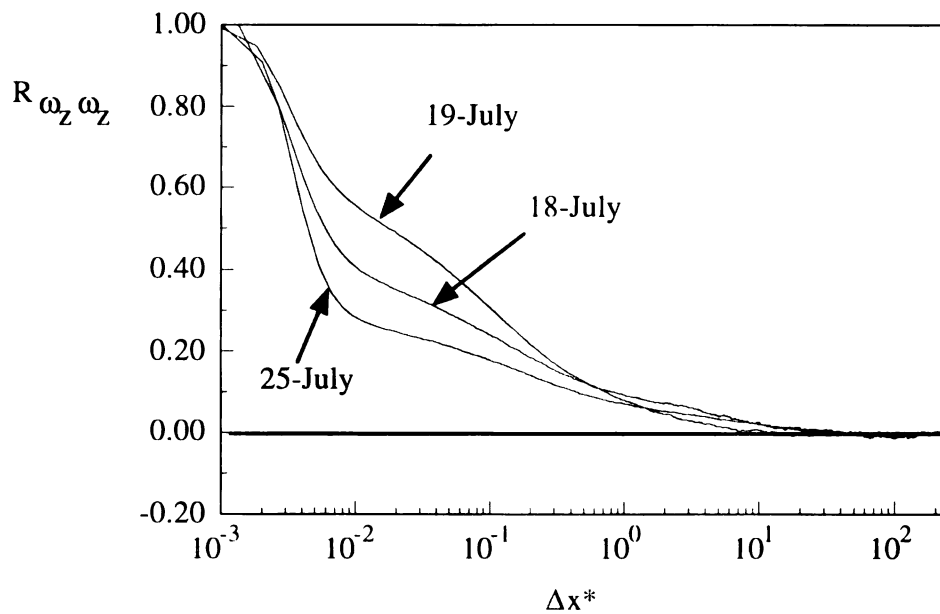


Figure 5.36 Autocorrelation of the  $\langle \omega_z \rangle$  vorticity in semilog format, where  $\Delta x^* = [(\Delta x)/(1m)]$ .

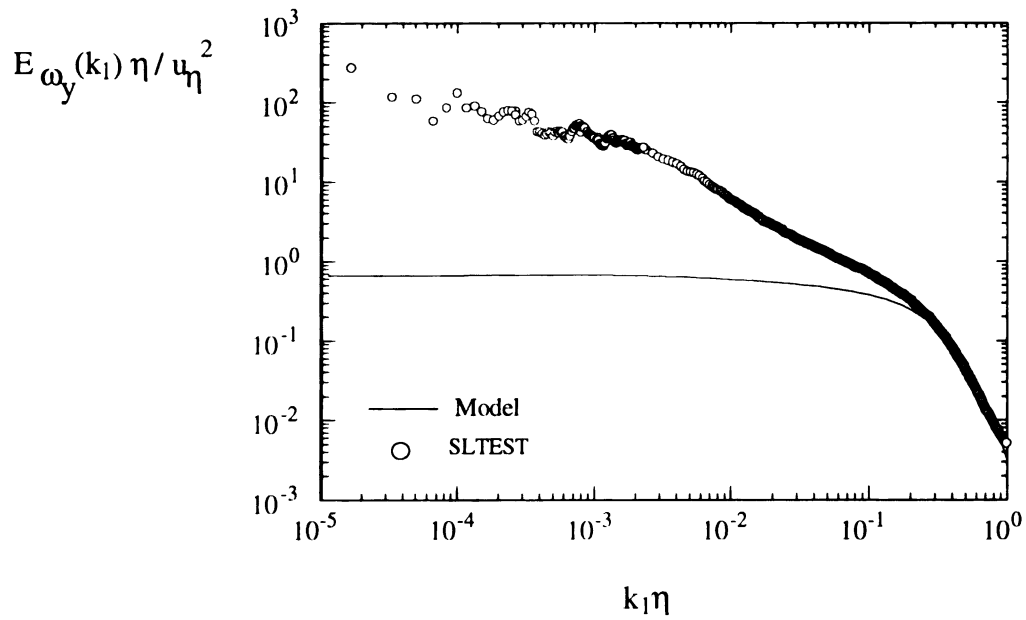


Figure 5.37 Normalized autospectral density of the  $\langle \omega_y \rangle$  vorticity (18-July).

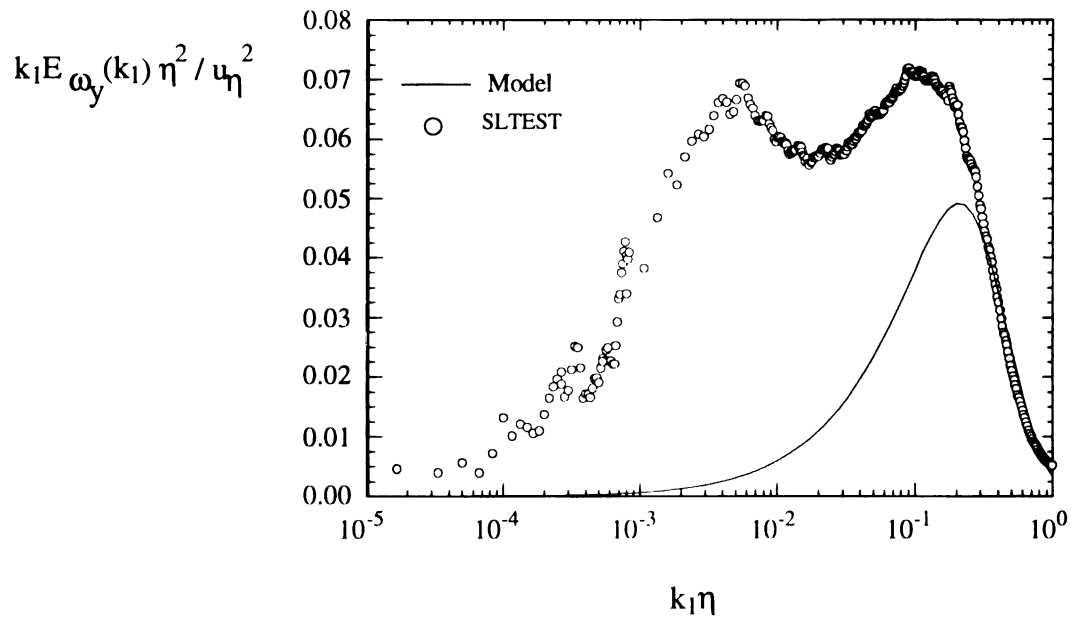


Figure 5.38 Compensated autospectral density of the  $\langle \omega_y \rangle$  vorticity (18-July).

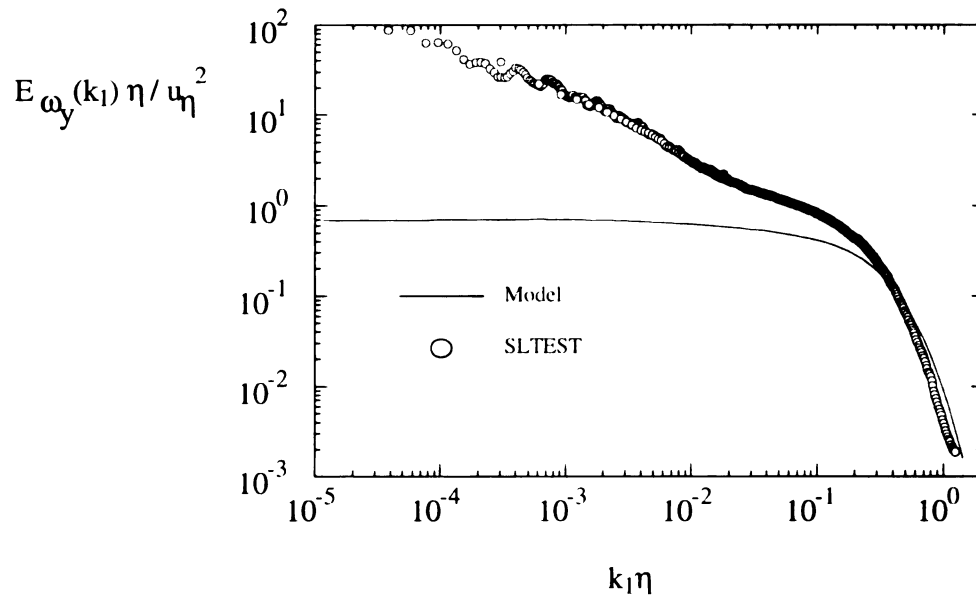


Figure 5.39 Normalized autospectral density of the  $\langle \omega_y \rangle$  vorticity (19-July).

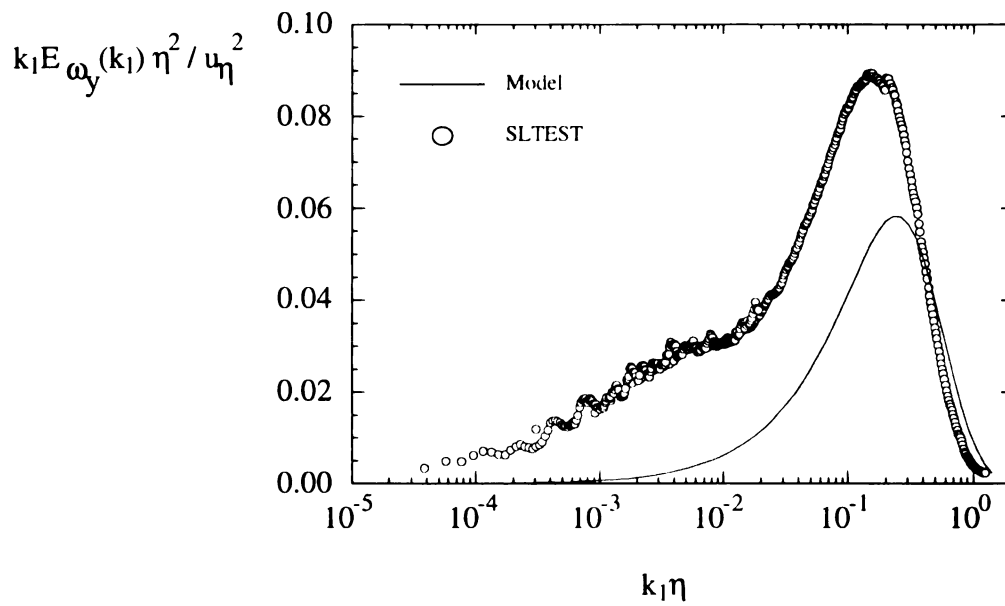


Figure 5.40 Compensated autospectral density of the  $\langle \omega_y \rangle$  vorticity (19-July).

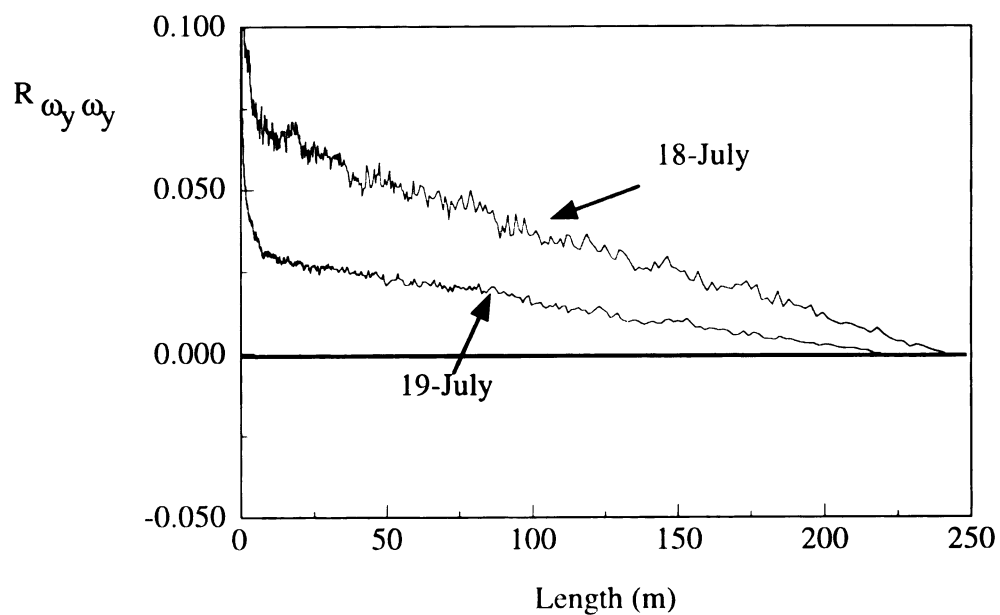


Figure 5.41 Autocorrelation of the  $\langle \omega_y \rangle$  vorticity for each day.

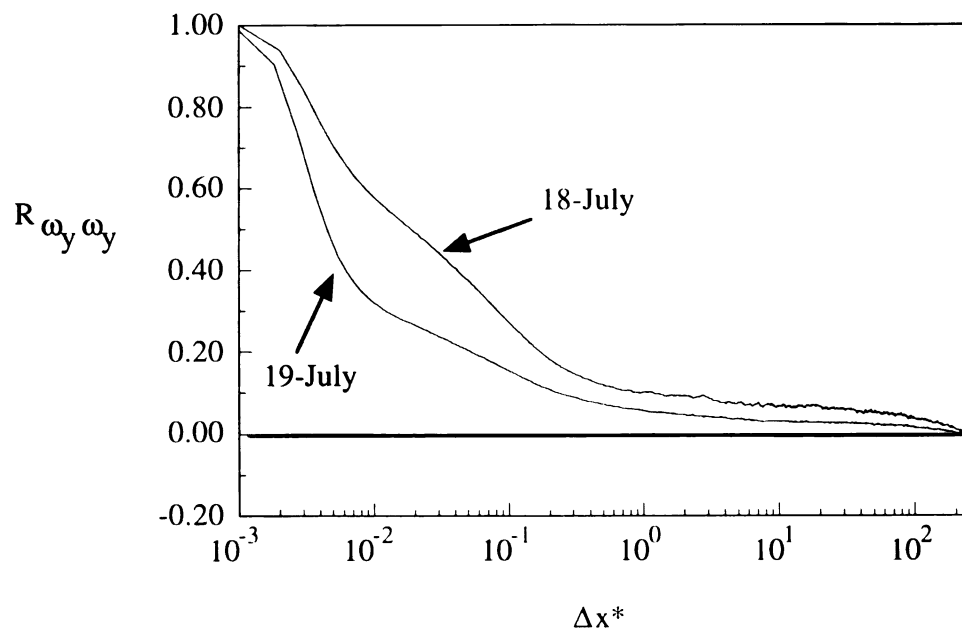


Figure 5.42 Autocorrelation of the  $\langle \omega_y \rangle$  vorticity in semilog format, where  $\Delta x^* = [(\Delta x)/(1m)]$ .

**Table 5.7 Dimensional Flow Statistics**

	18-July	19-July	25-July
$\overline{u'v'} \text{ (m}^2/\text{s}^2\text{)}$	-0.09	-0.07	-0.11
$\overline{u'w'} \text{ (m}^2/\text{s}^2\text{)}$	-0.014	-0.03	N/A
$\overline{u'\omega'_z} \text{ (m/s}^2\text{)}$	16.8	-2.46	11.9
$\overline{v'\omega'_z} \text{ (m/s}^2\text{)}$	0.59	-0.9	-0.14
$\overline{w'\omega'_y} \text{ (m/s}^2\text{)}$	11.9	7.56	N/A

**Table 5.8 Normalized Flow Statistics**

	18-July	19-July	25-July
$\frac{\overline{u'v'}}{u_\tau^2}$	-0.96	-0.77	-0.67
$\frac{\overline{u'v'}}{\tilde{u}\tilde{v}}$	-0.26	-0.30	-0.24
$\frac{\overline{u'w'}}{u_\tau^2}$	-0.15	-0.26	N/A
$\frac{\overline{u'w'}}{\tilde{u}\tilde{w}}$	-0.03	-0.06	N/A
$\frac{\overline{u'\omega'_z}}{u_\tau^2/l^+}$	$9.7 \times 10^{-3}$	$-1.4 \times 10^{-3}$	$2.7 \times 10^{-3}$
$\frac{\overline{u'\omega'_z}}{\tilde{u}\tilde{\omega}_z}$	0.22	-0.04	0.14
$\frac{\overline{v'\omega'_z}}{u_\tau^2/l^+}$	$3.4 \times 10^{-4}$	$-5.0 \times 10^{-4}$	$-3.2 \times 10^{-4}$
$\frac{\overline{v'\omega'_z}}{\tilde{v}\tilde{\omega}_z}$	0.02	-0.03	-0.004
$\frac{\overline{w'\omega'_y}}{u_\tau^2/l^+}$	0.01	0.004	N/A
$\frac{\overline{w'\omega'_y}}{\tilde{w}\tilde{\omega}_y}$	0.22	0.20	N/A

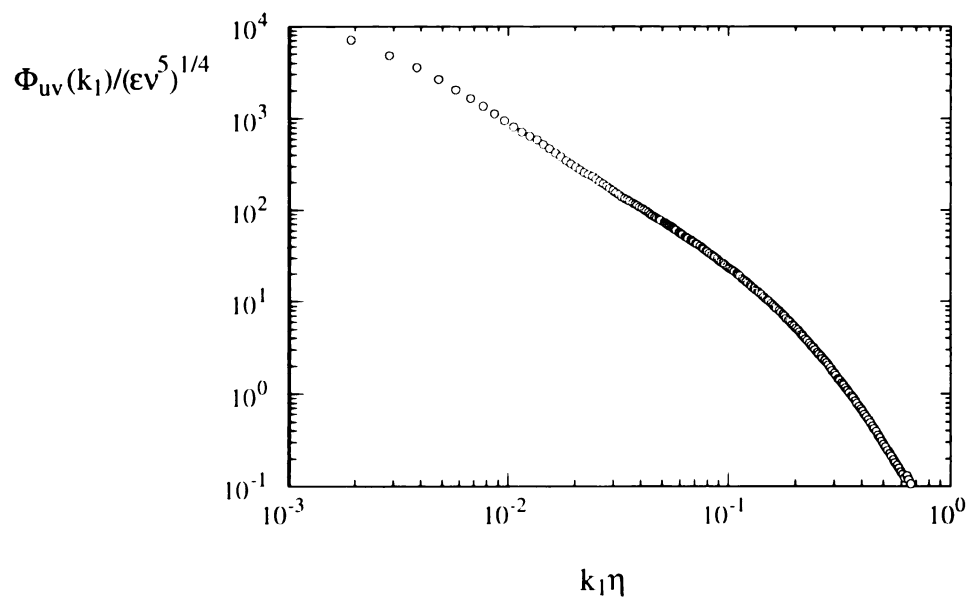


Figure 5.43 Normalized autospectral density of the  $u'v'$  product (25-July).

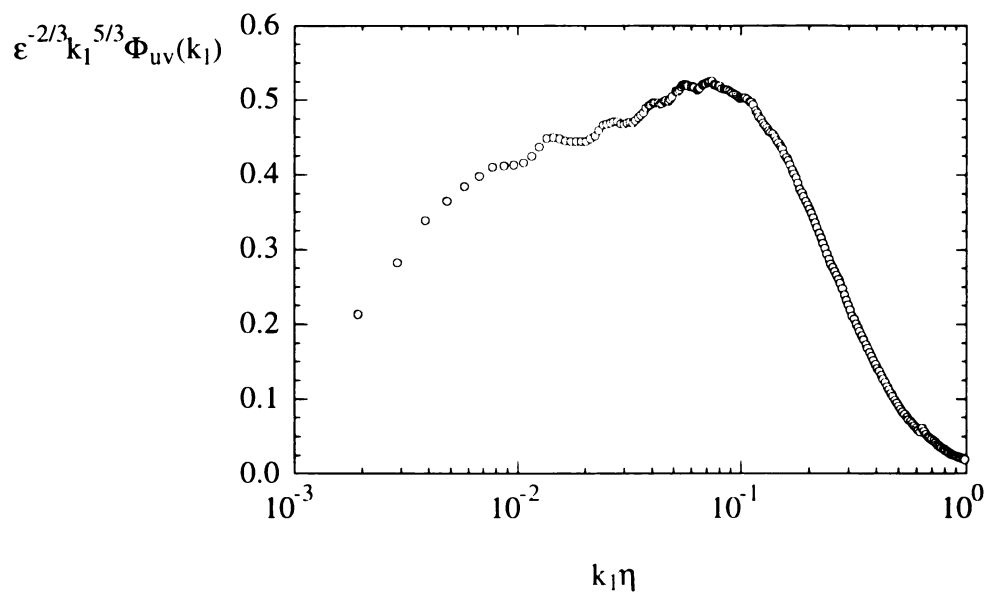


Figure 5.44 Compensated autospectral density of the  $u'v'$  product (25-July).

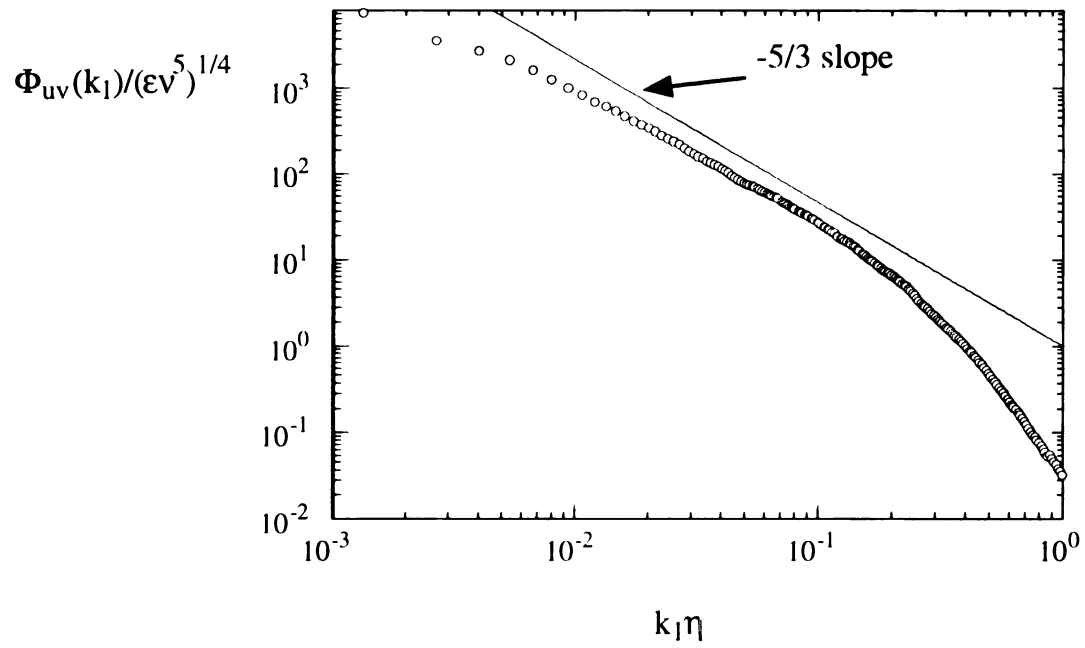


Figure 5.45 Normalized autospectral density of the  $u'v'$  product (18-July).

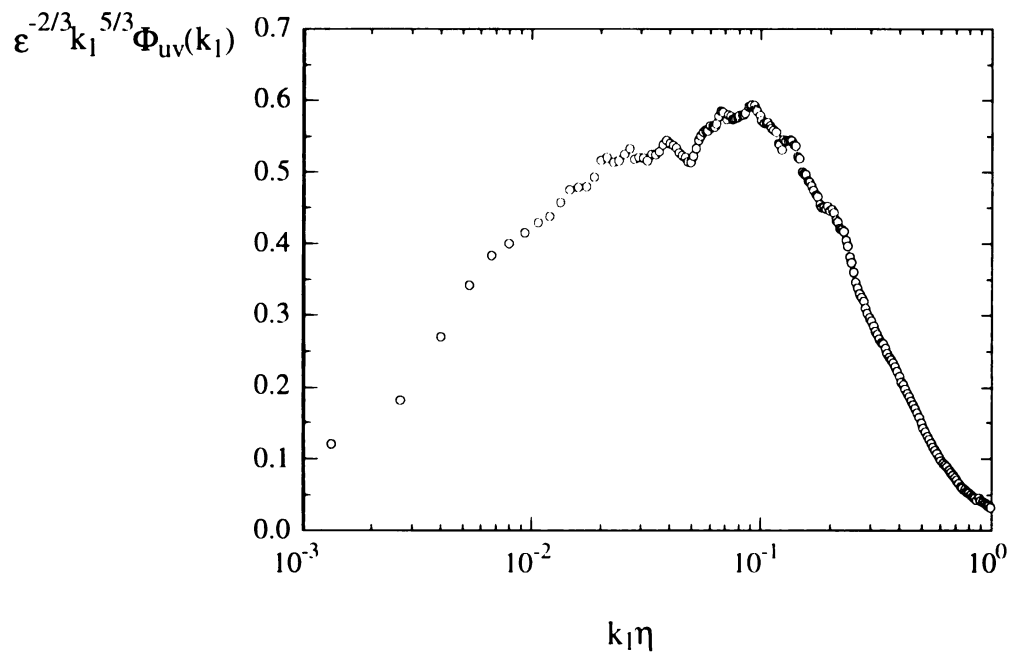


Figure 5.46 Compensated autospectral density of the  $u'v'$  product (18-July).



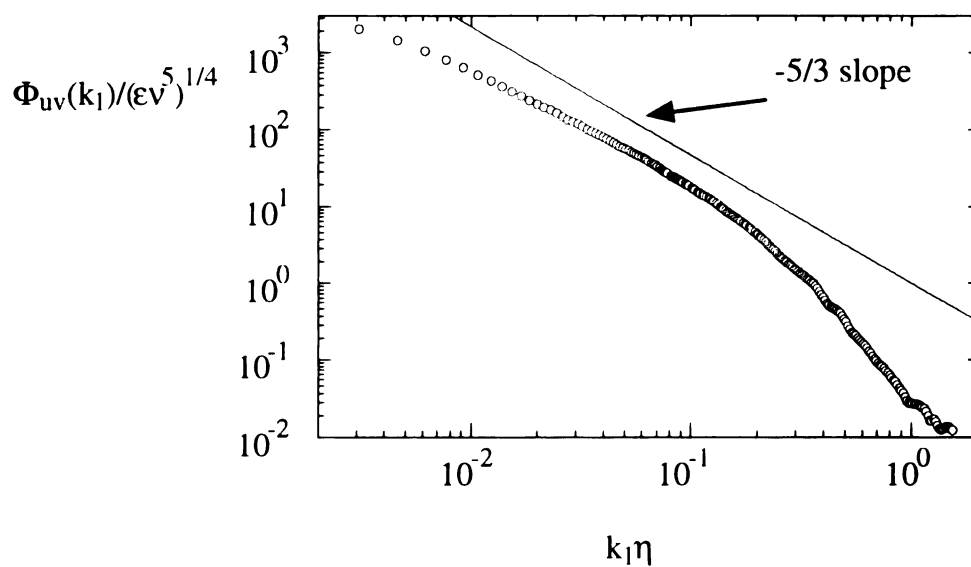


Figure 5.47 Normalized autospectral density of the  $u'v'$  product (19-July).

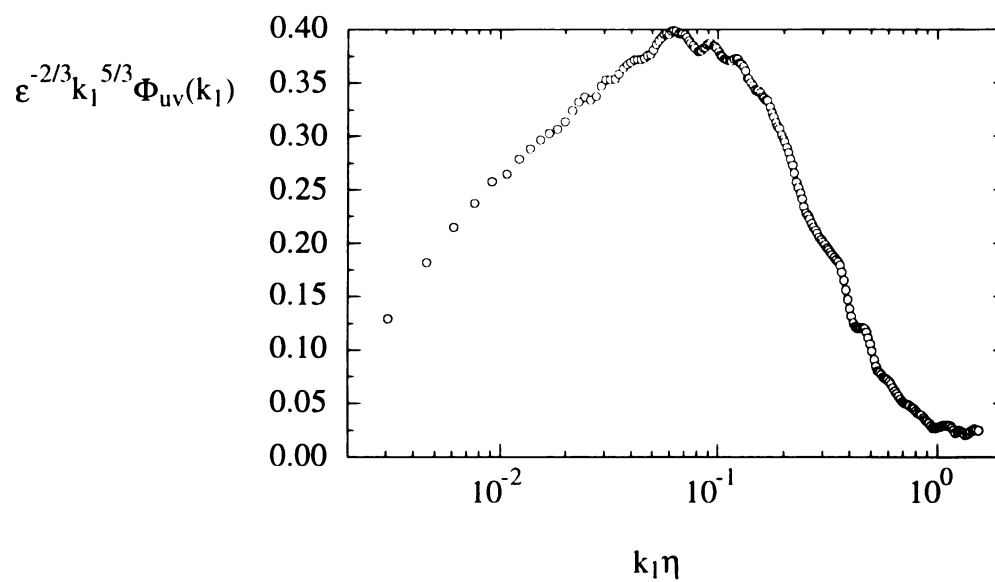


Figure 5.48 Compensated autospectral density of the  $u'v'$  product (19-July).

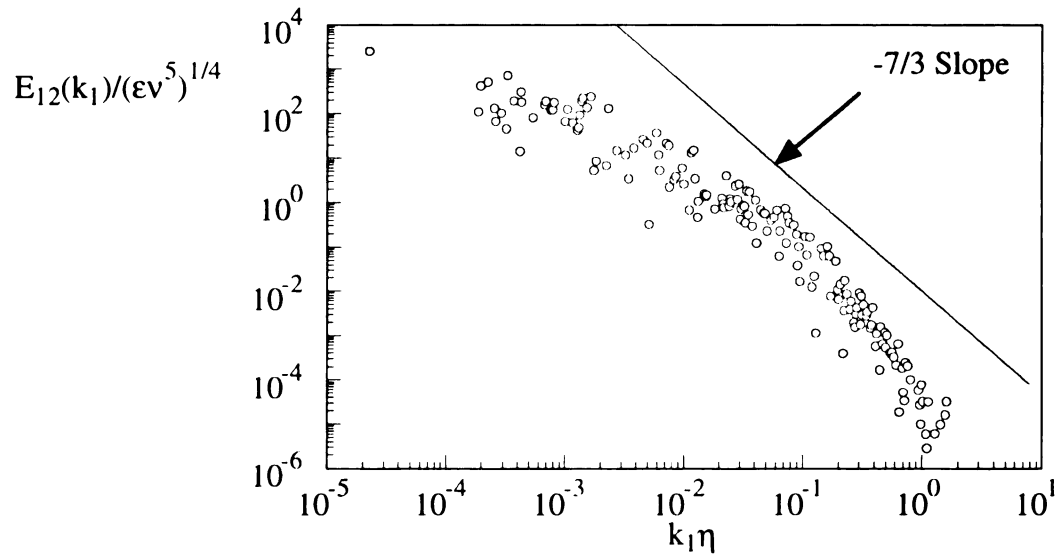


Figure 5.49 Normalized co-spectral density of the  $u'$  and  $v'$  velocity components (25-July).

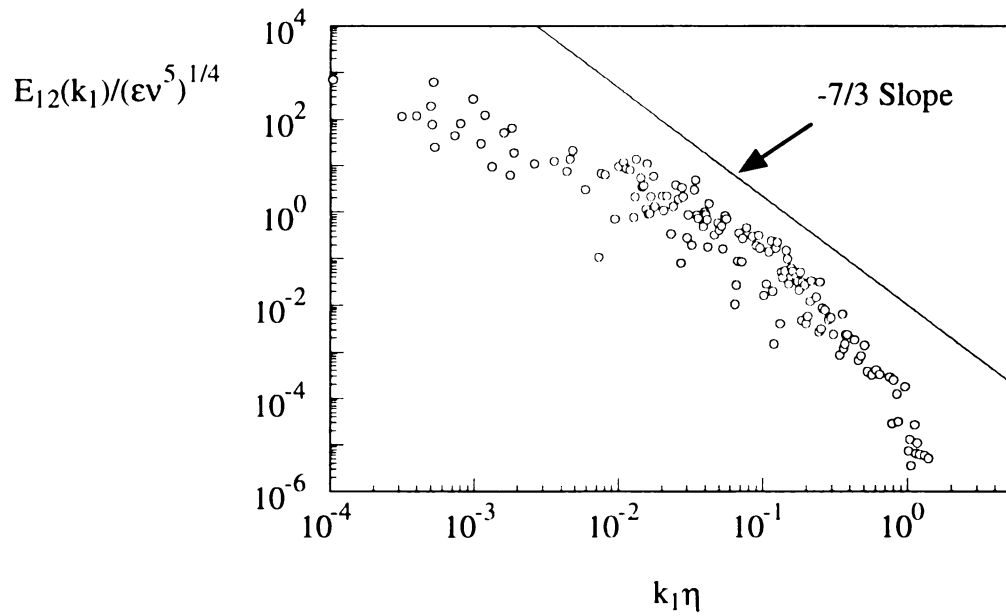


Figure 5.50 Normalized co-spectral density of the  $u'$  and  $v'$  velocity components (18-July).

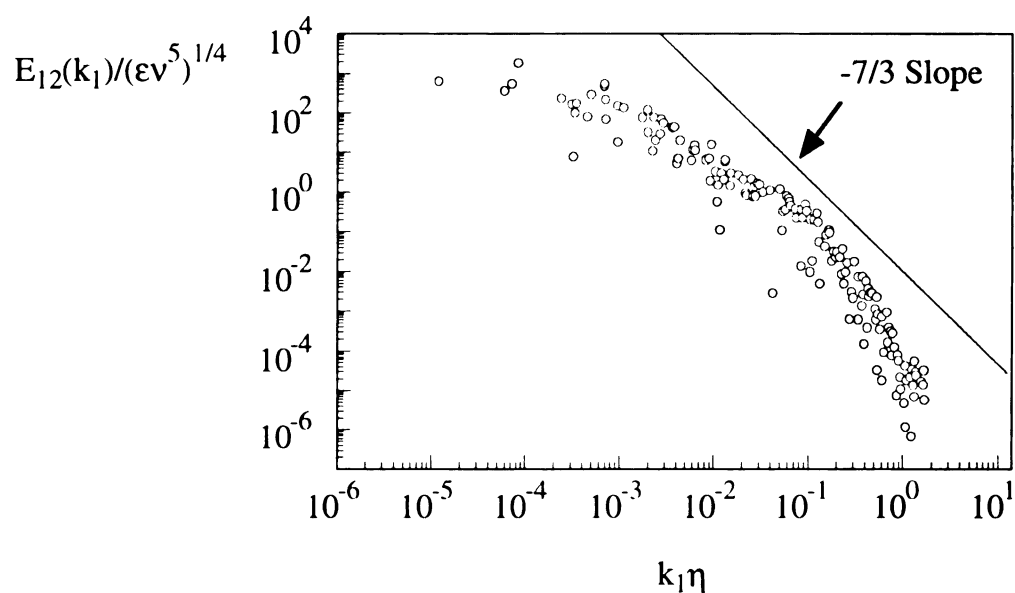


Figure 5.51 Normalized co-spectral density of the  $u'$  and  $v'$  velocity components (19-July).

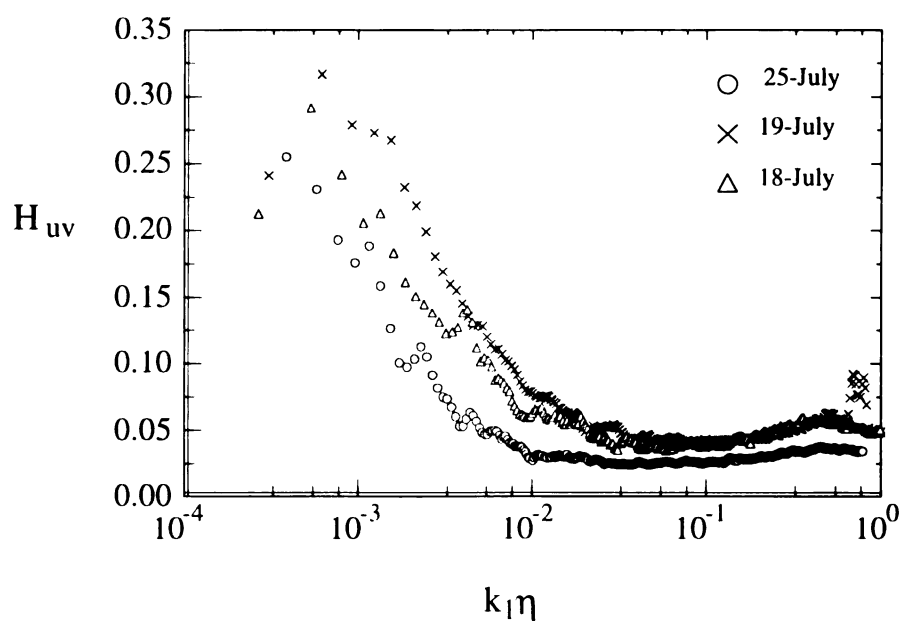


Figure 5.52 Coherence of the  $u'$  and  $v'$  velocity components for all three data sets.

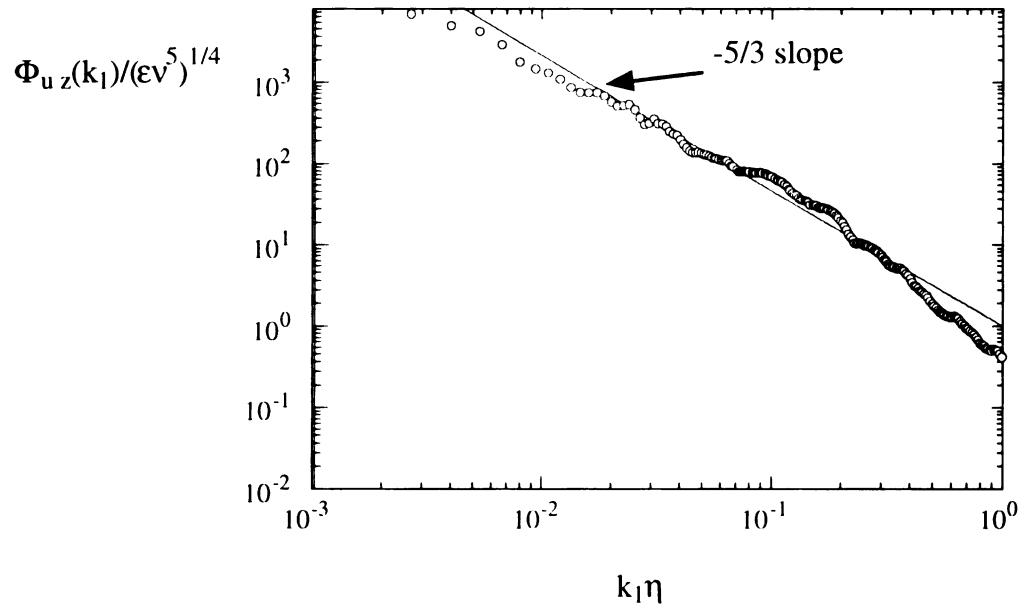


Figure 5.53 Normalized autospectral density of the  $u'w'$  product (18-July).

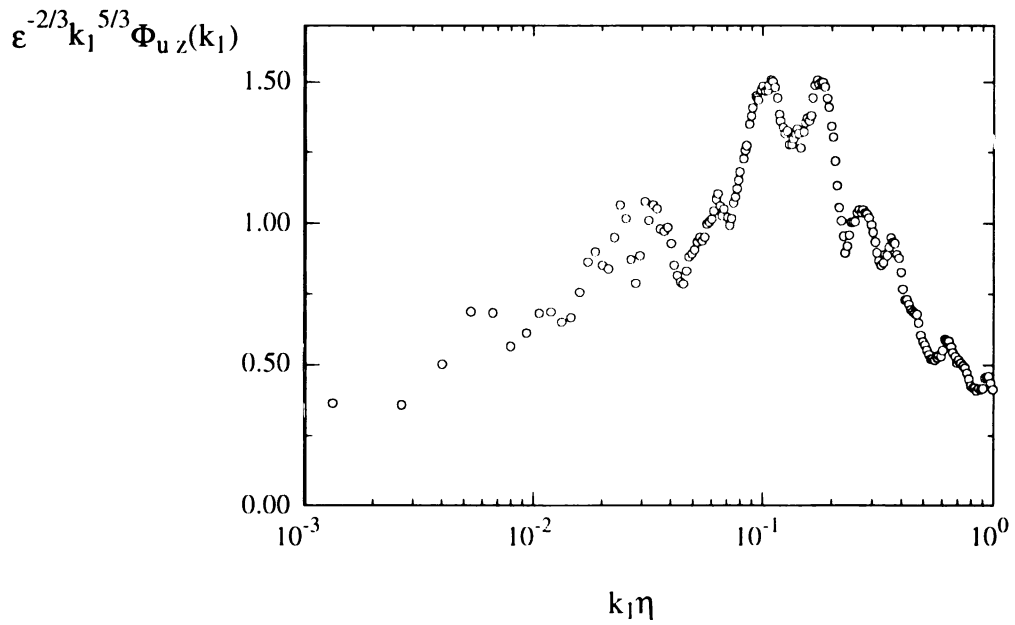


Figure 5.54 Compensated autospectral density of the  $u'w'$  product (18-July).

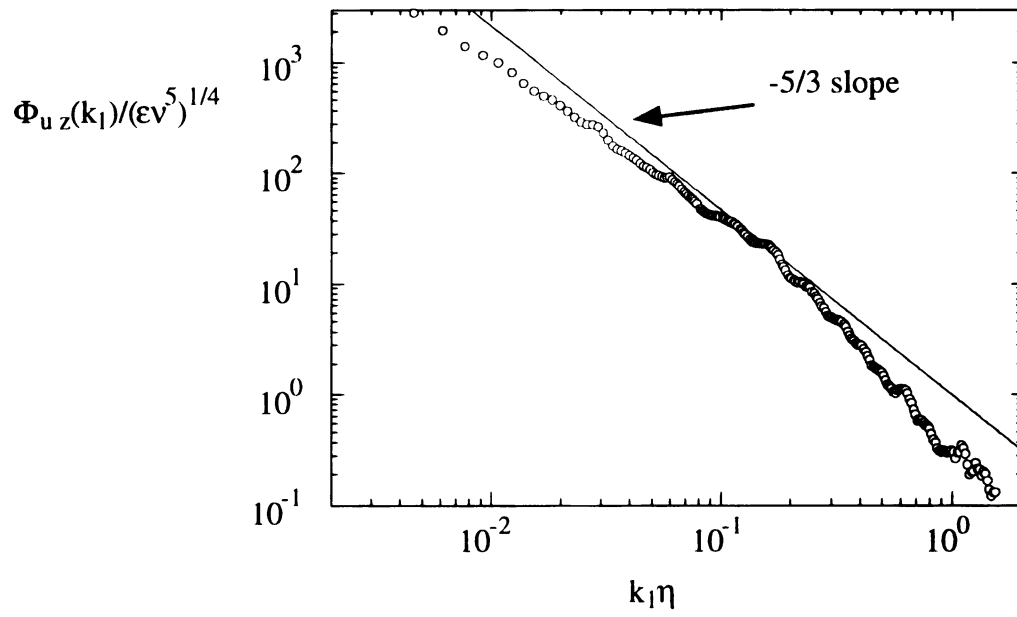


Figure 5.55 Normalized autospectral density of the  $u'w'$  product (19-July).

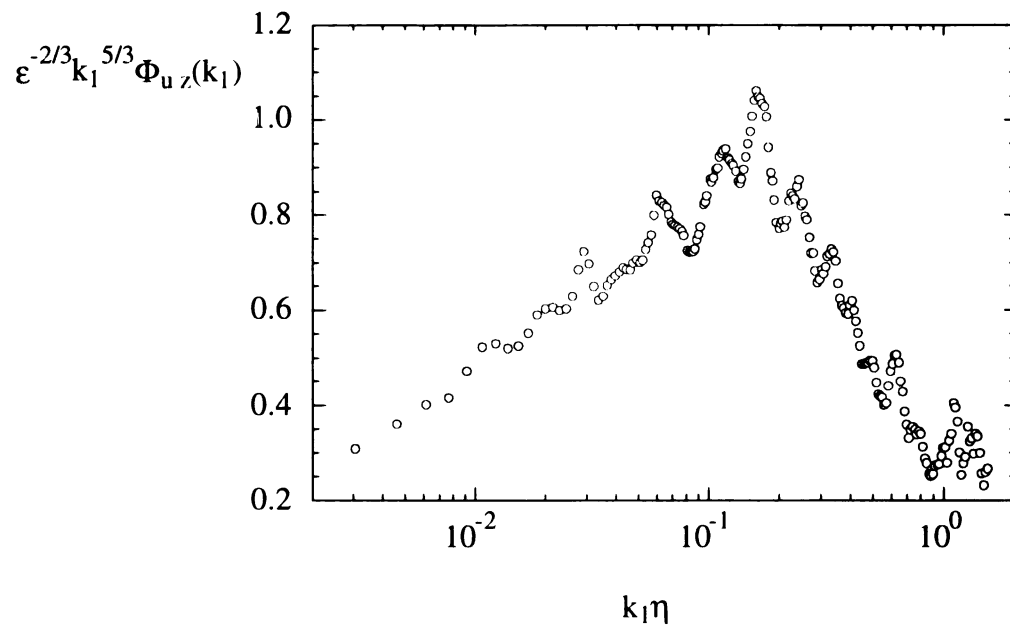


Figure 5.56 Compensated autospectral density of the  $u'w'$  product (19-July).

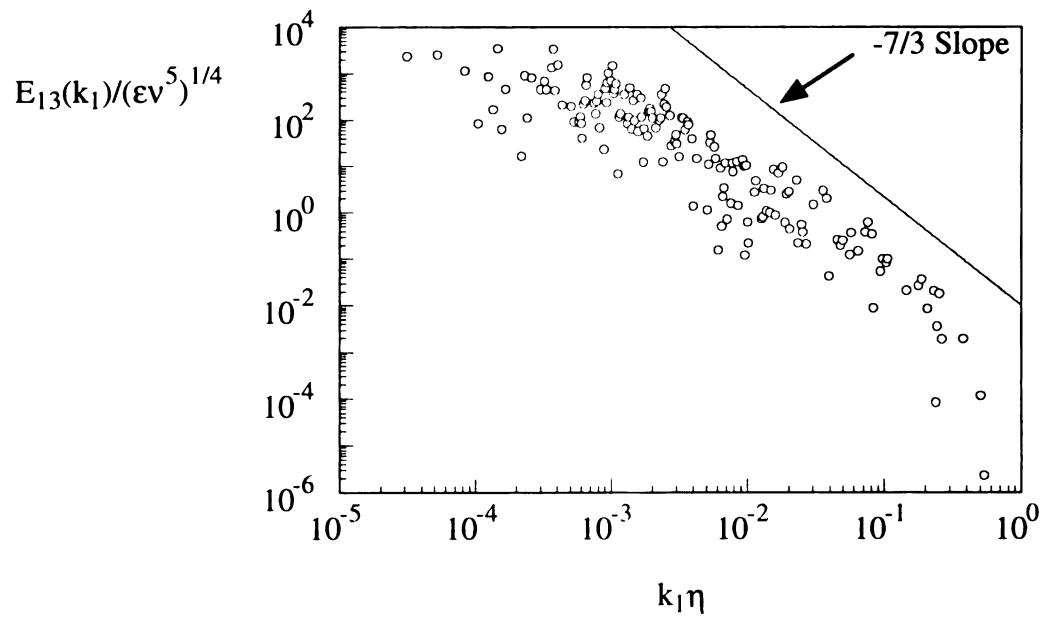


Figure 5.57 Normalized co-spectral density of the  $u'$  and  $w'$  velocity components (18-July).

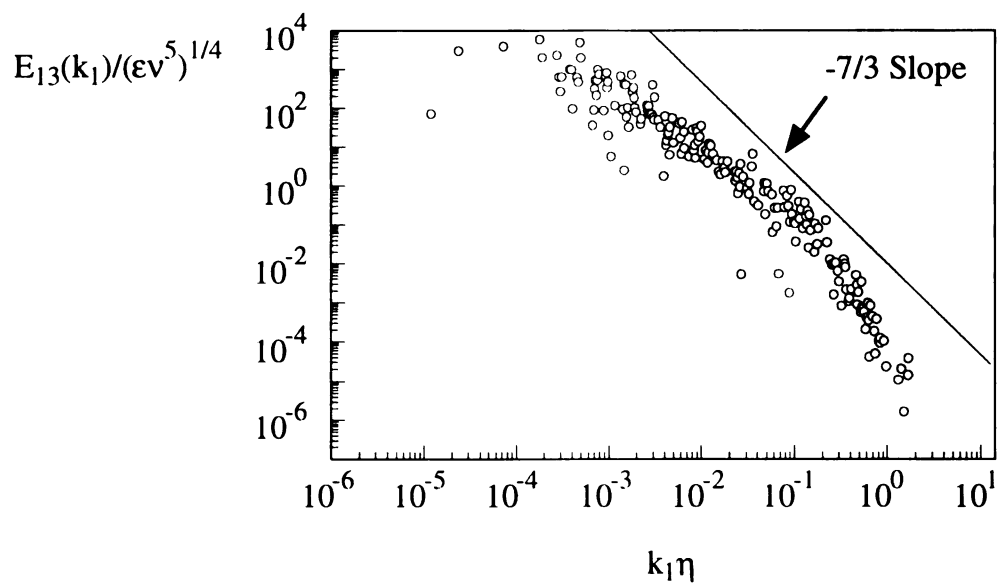


Figure 5.58 Normalized co-spectral density of the  $u'$  and  $w'$  velocity components (19-July).

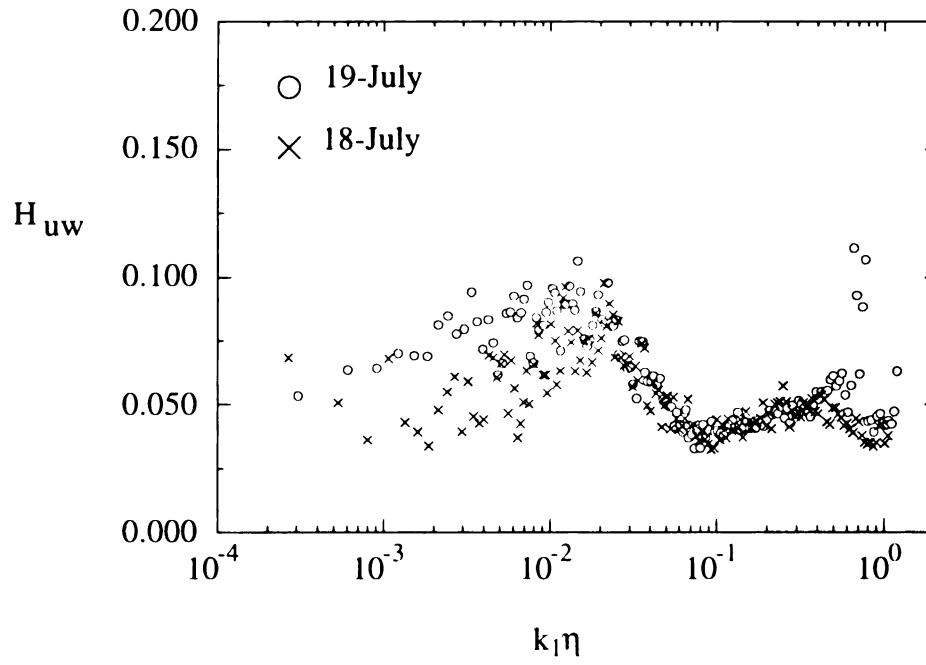


Figure 5.59 Coherence of the  $u'$  and  $w'$  velocity components (18, 19-July).

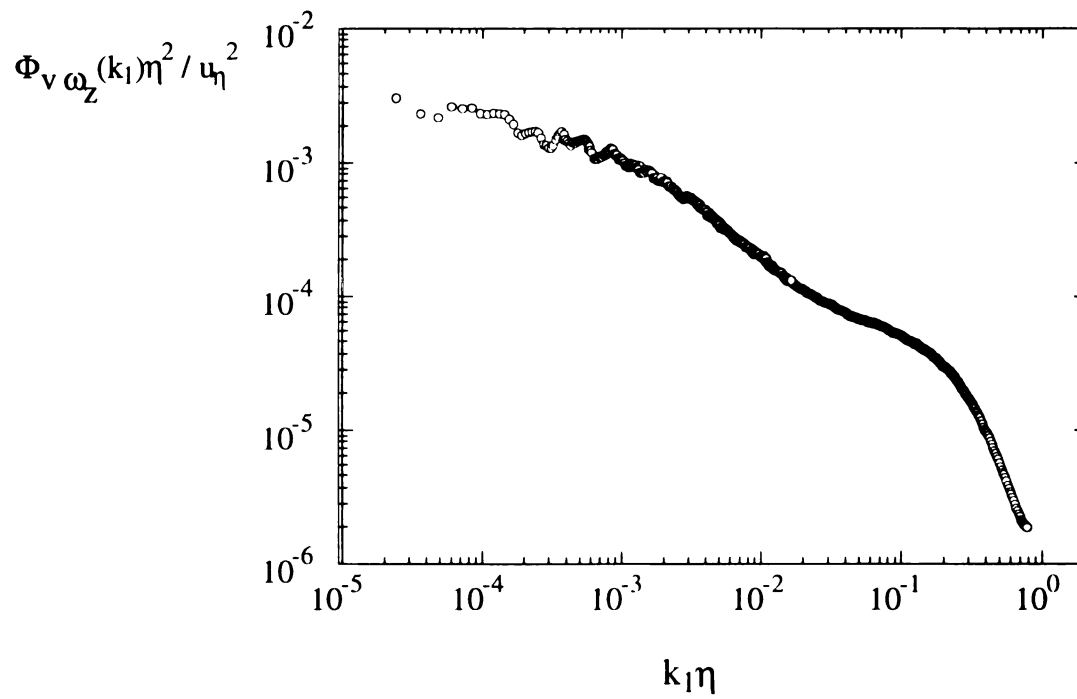


Figure 5.60 Normalized autospectral density of the  $v' \langle \omega_z' \rangle$  product (25-July).

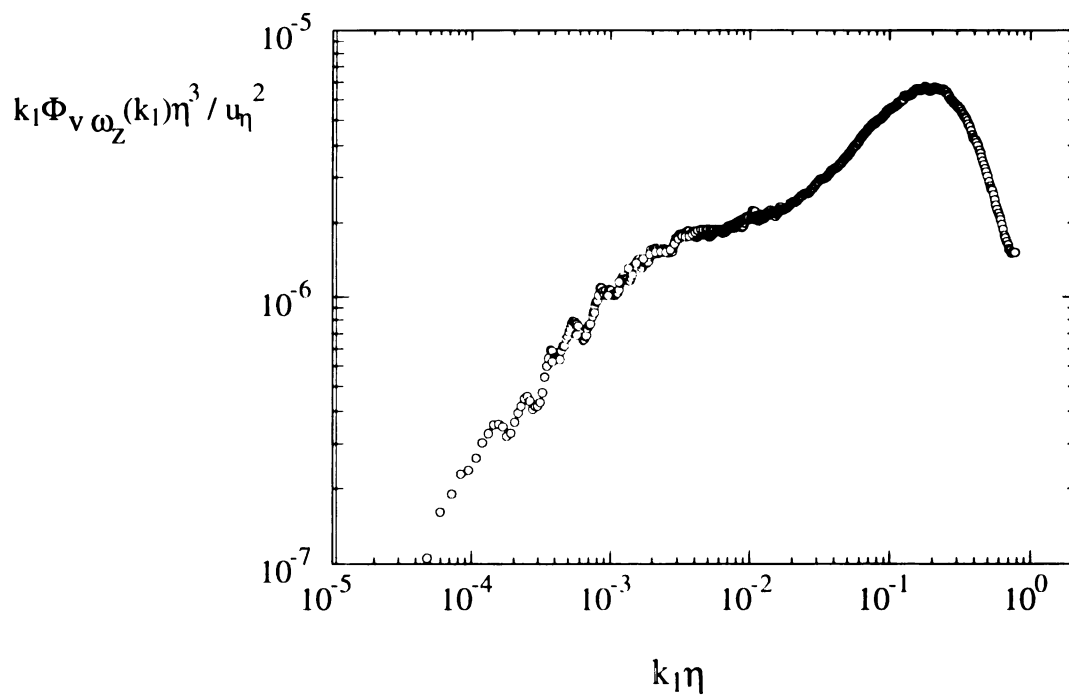


Figure 5.61 Compensated autospectral density of the  $v' < \omega_z' >$  product (25-July).

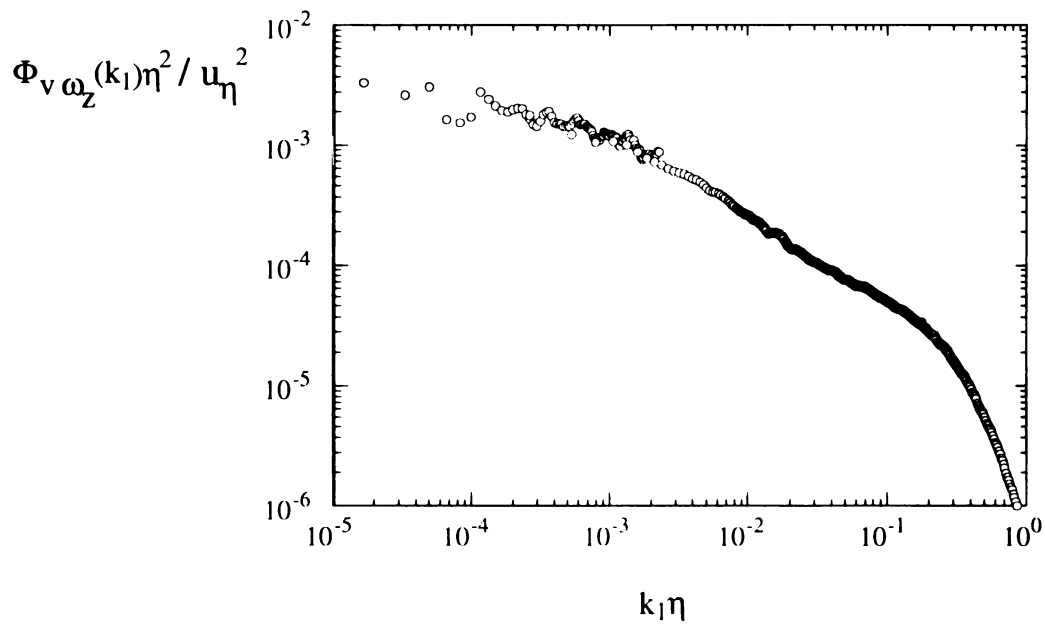


Figure 5.62 Normalized autospectral density of the  $v' < \omega_z' >$  product (18-July).



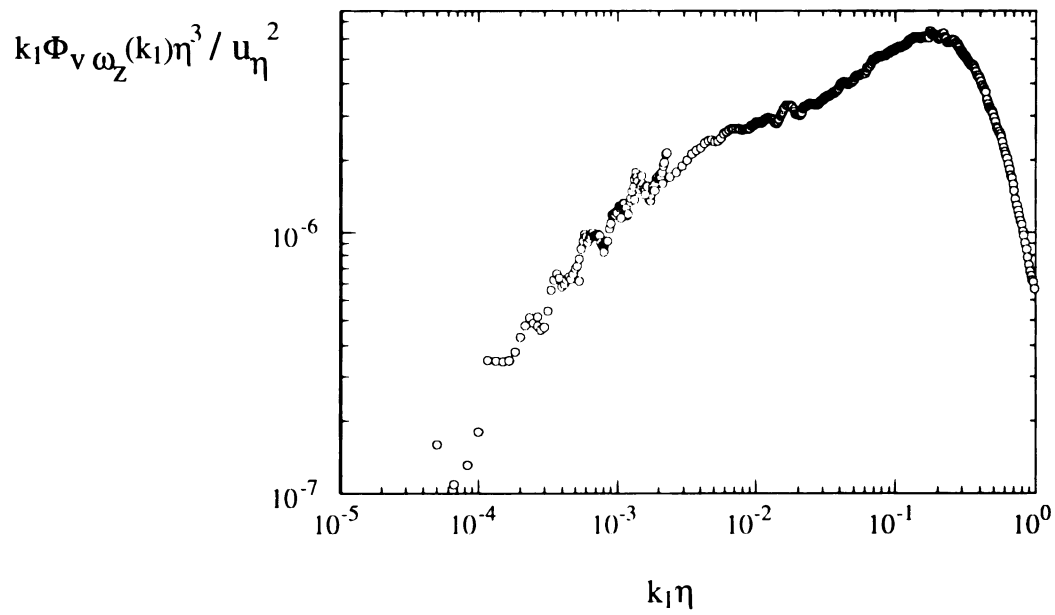


Figure 5.63 Compensated autospectral density of the  $v' < \omega_z' >$  product (18-July).

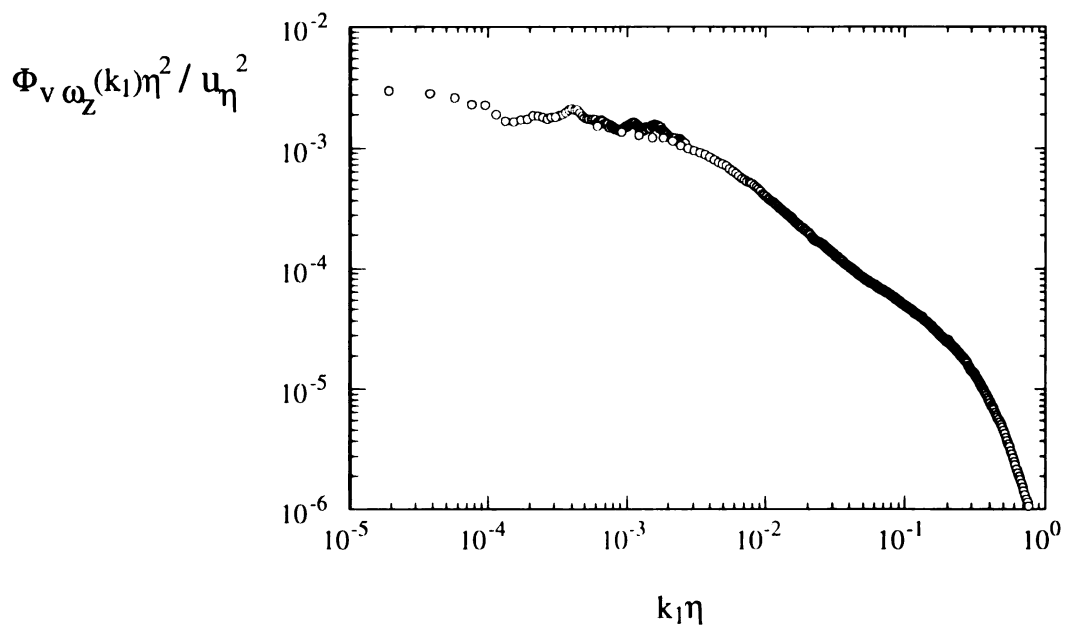


Figure 5.64 Normalized autospectral density of the  $v' < \omega_z' >$  product (19-July).

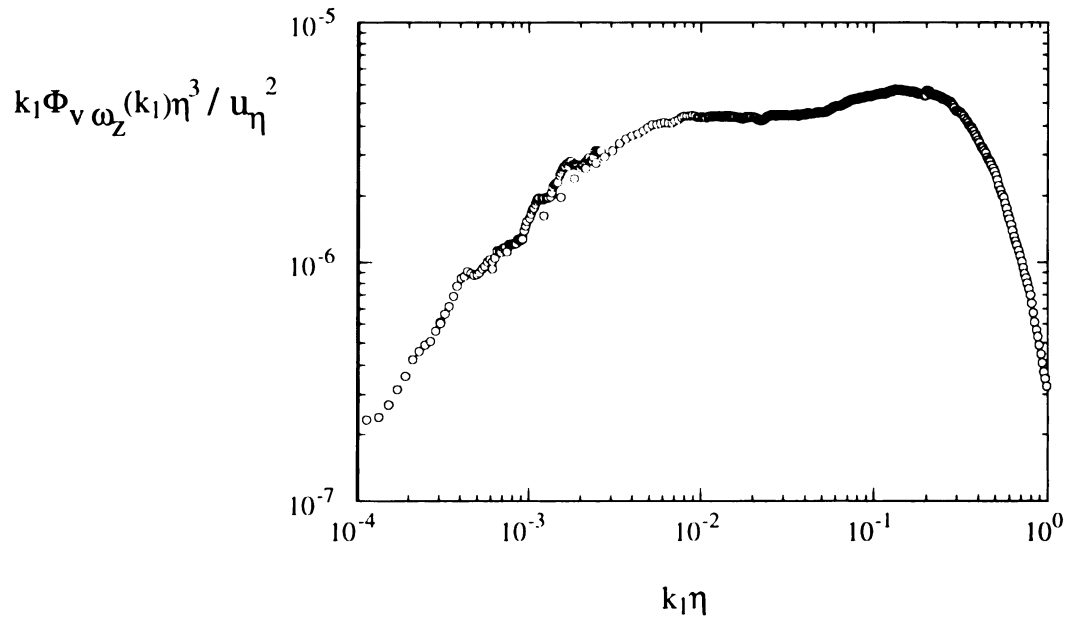


Figure 5.65 Compensated autospectral density of the  $v' \langle \omega_z' \rangle$  product (19-July).

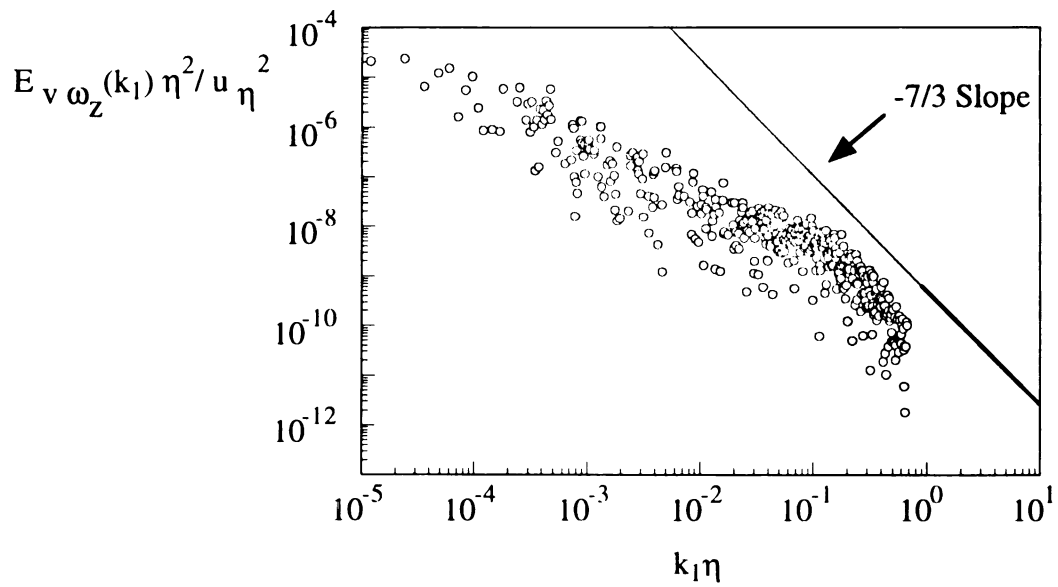


Figure 5.66 Normalized co-spectral density of  $v'$  and  $\langle \omega_z' \rangle$  (25-July).

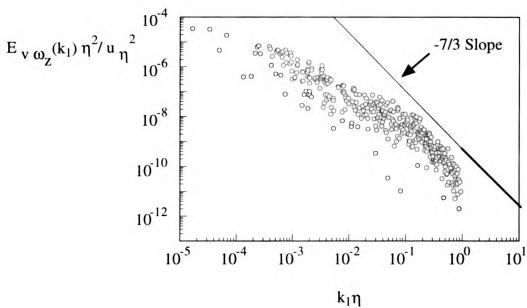


Figure 5.67 Normalized co-spectral density of  $v'$  and  $\langle \omega_z' \rangle$  (18-July).

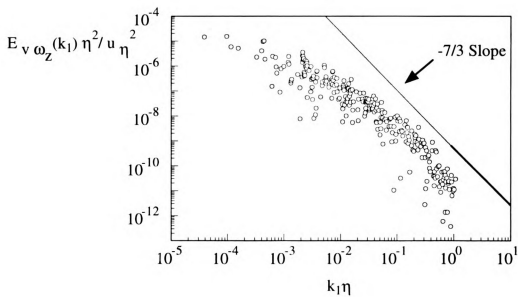


Figure 5.68 Normalized co-spectral density of  $v'$  and  $\langle \omega_z' \rangle$  (19-July).

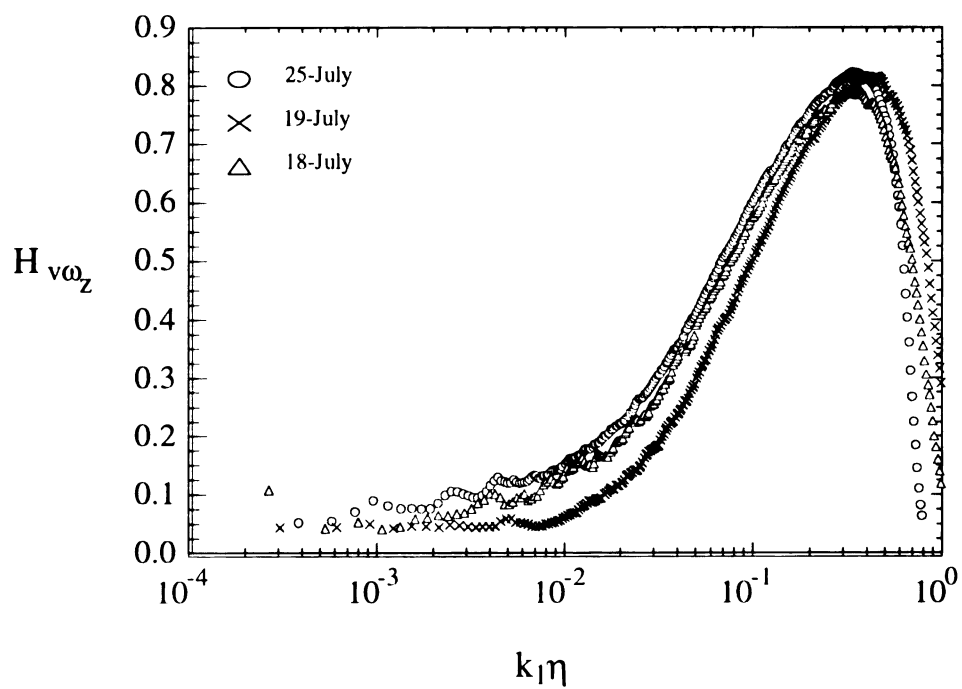


Figure 5.69 Coherence of  $v'$  and  $\langle \omega_z' \rangle$  over all three evenings.

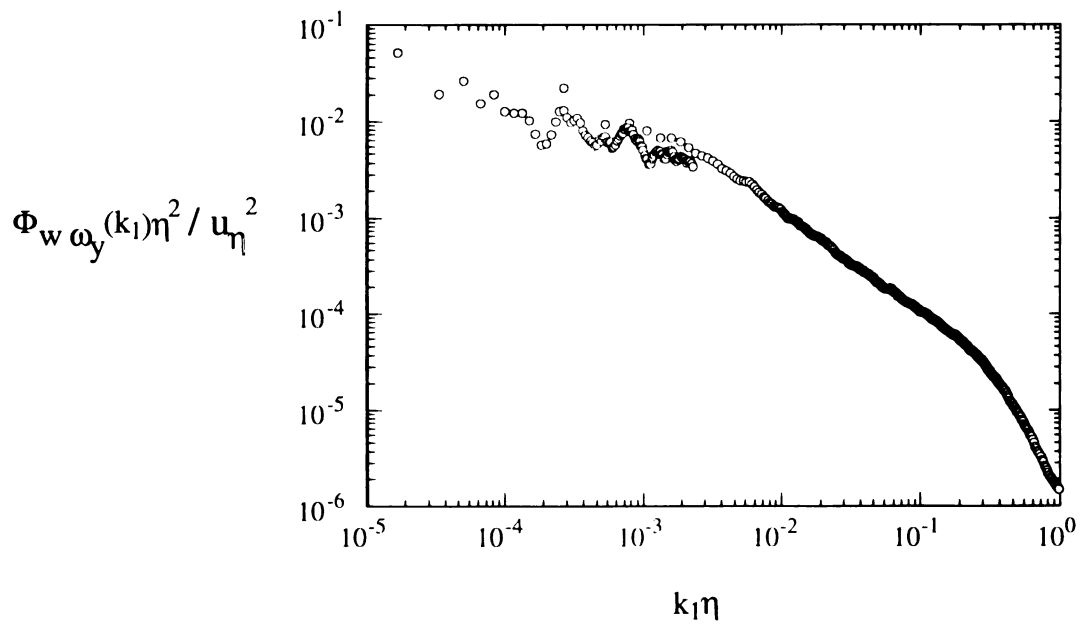


Figure 5.70 Normalized autospectral density of the  $w'\langle \omega_y' \rangle$  product (18-July).

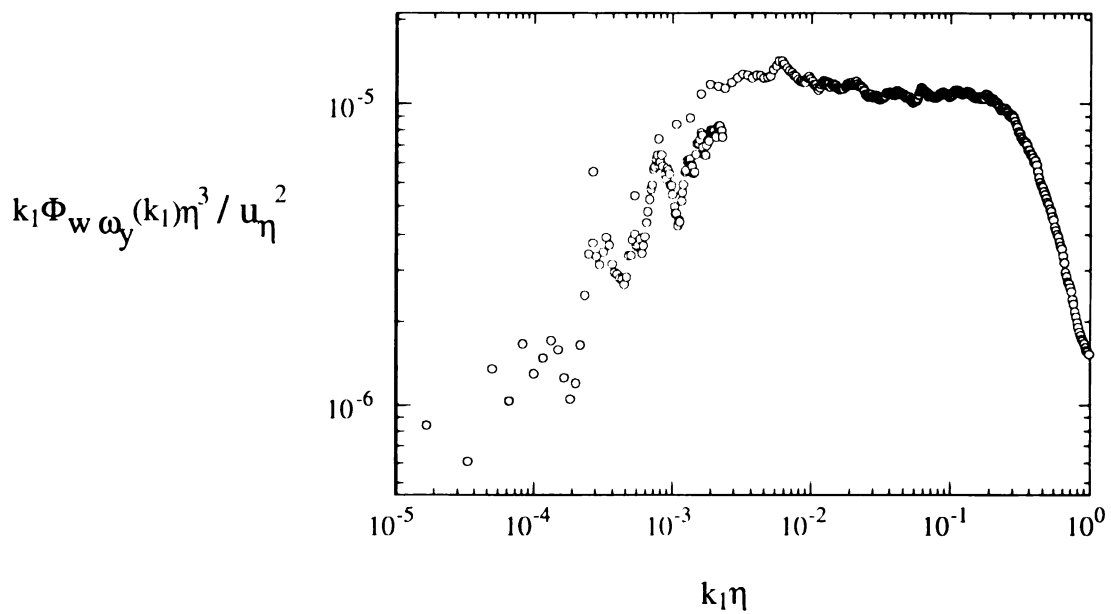


Figure 5.71 Compensated autospectral density of the  $w' \langle \omega_y' \rangle$  product (18-July).

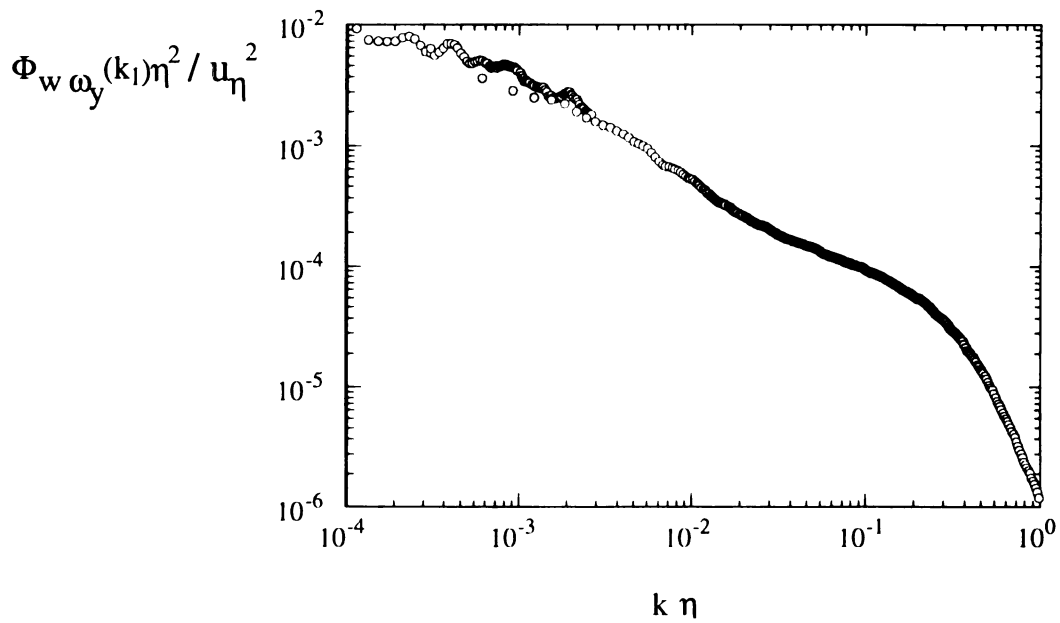


Figure 5.72 Normalized autospectral density of the  $w' \langle \omega_y' \rangle$  product (19-July).

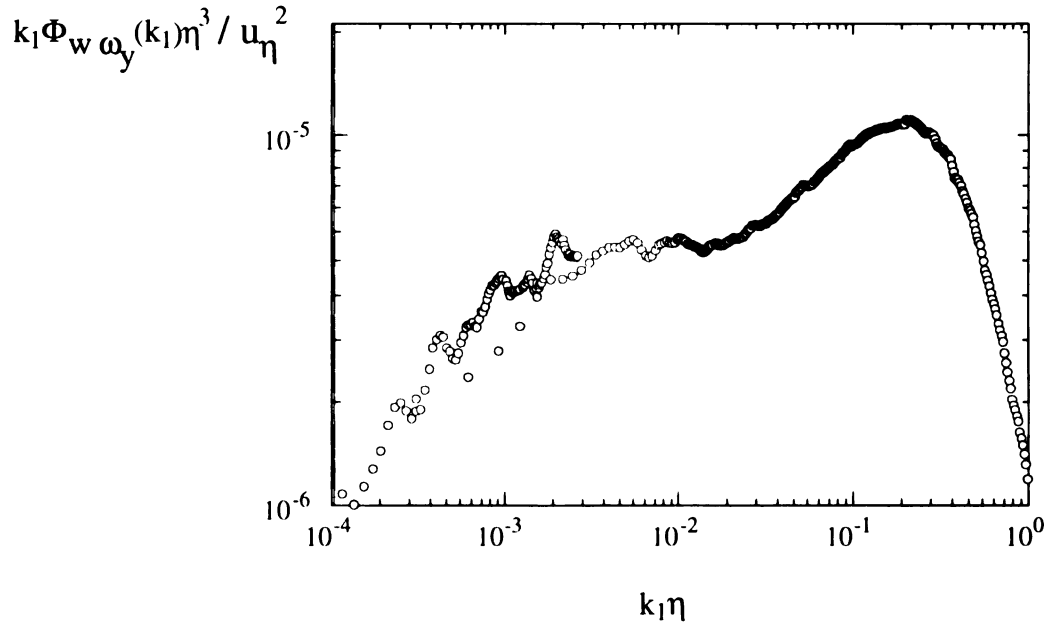


Figure 5.73 Compensated autospectral density of the  $w' \langle \omega_y' \rangle$  product (19-July).

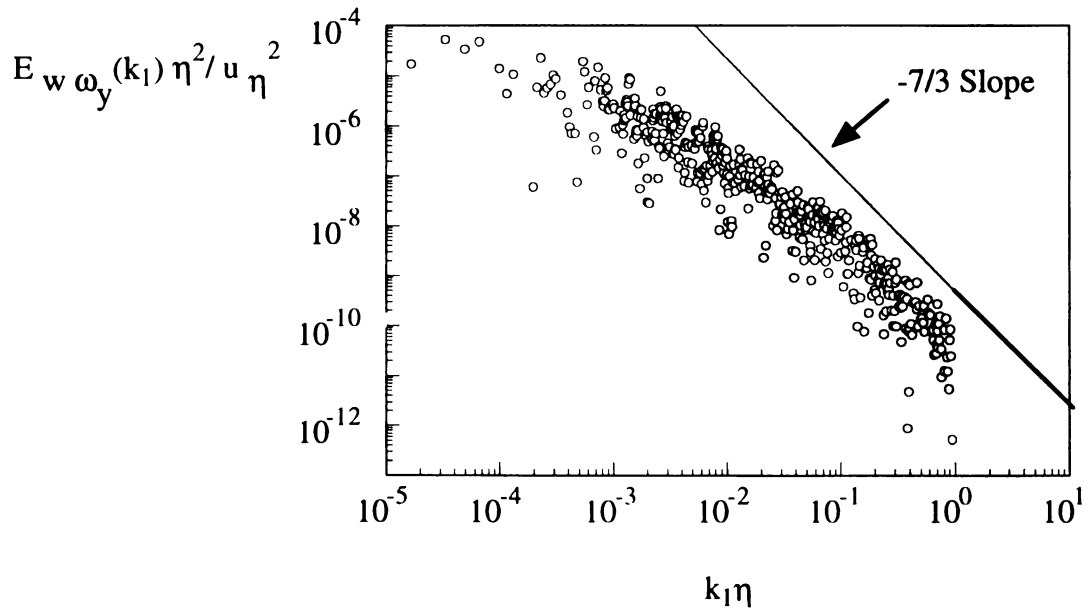


Figure 5.74 Normalized co-spectral density of  $w'$  and  $\langle \omega_y' \rangle$  (18-July).

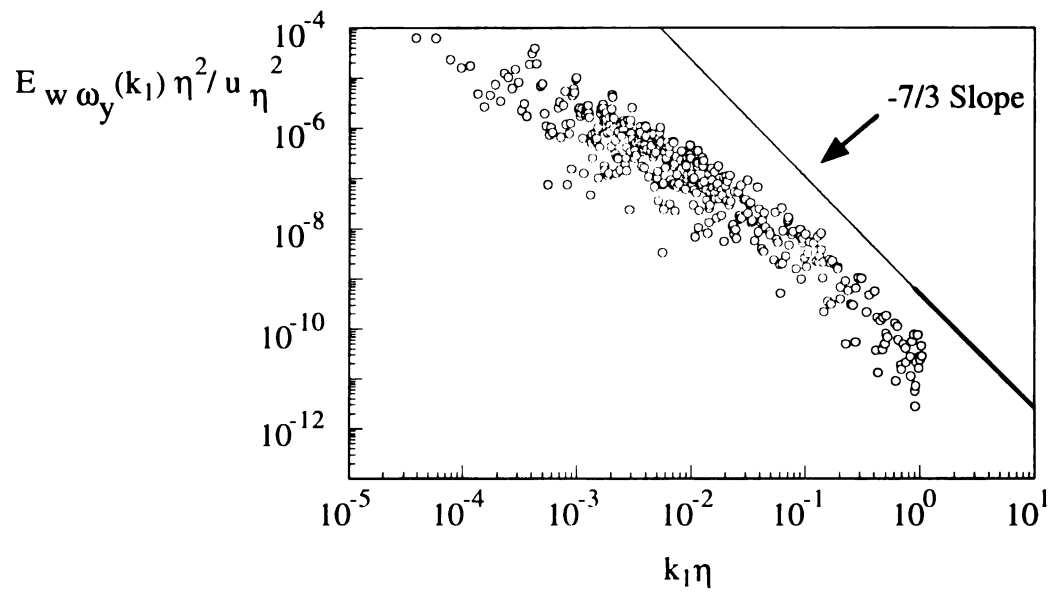


Figure 5.75 Normalized co-spectral density of  $w'$  and  $\langle \omega_y' \rangle$  (19-July).

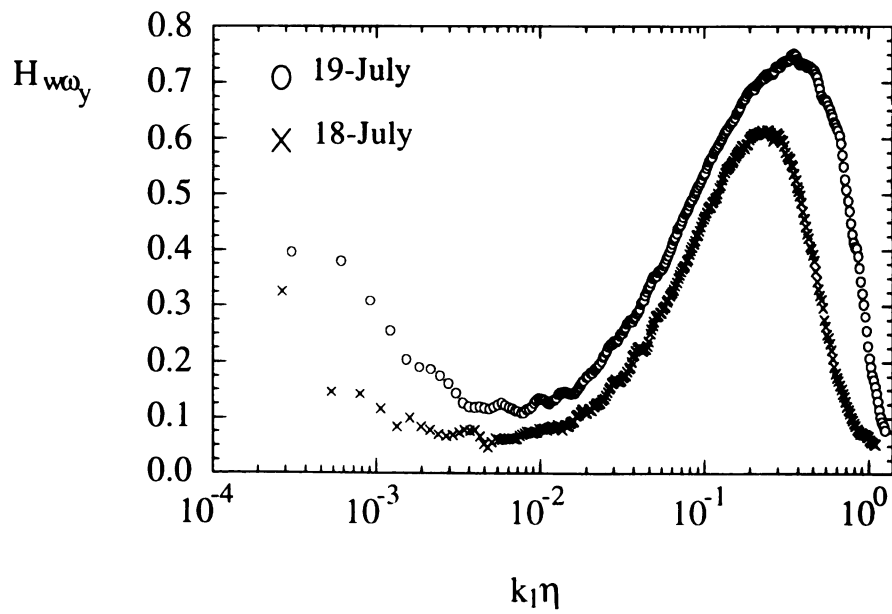


Figure 5.76 Coherence of  $w'$  and  $\langle \omega_y' \rangle$  for 18, 19-July.

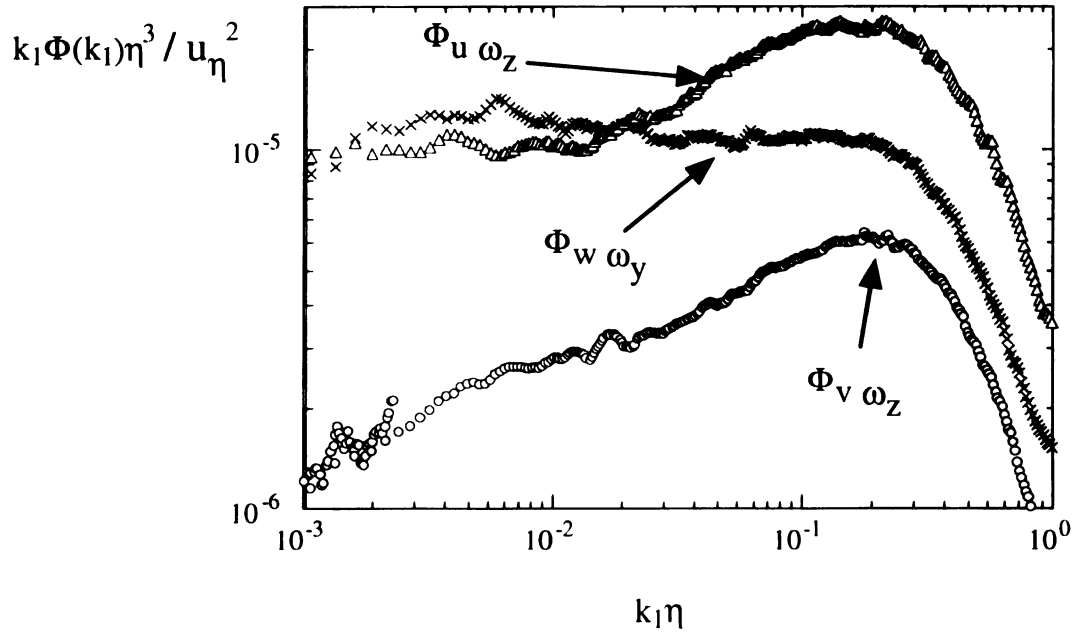


Figure 5.77 Compensated autospectral densities of the velocity-vorticity products for 18-July.

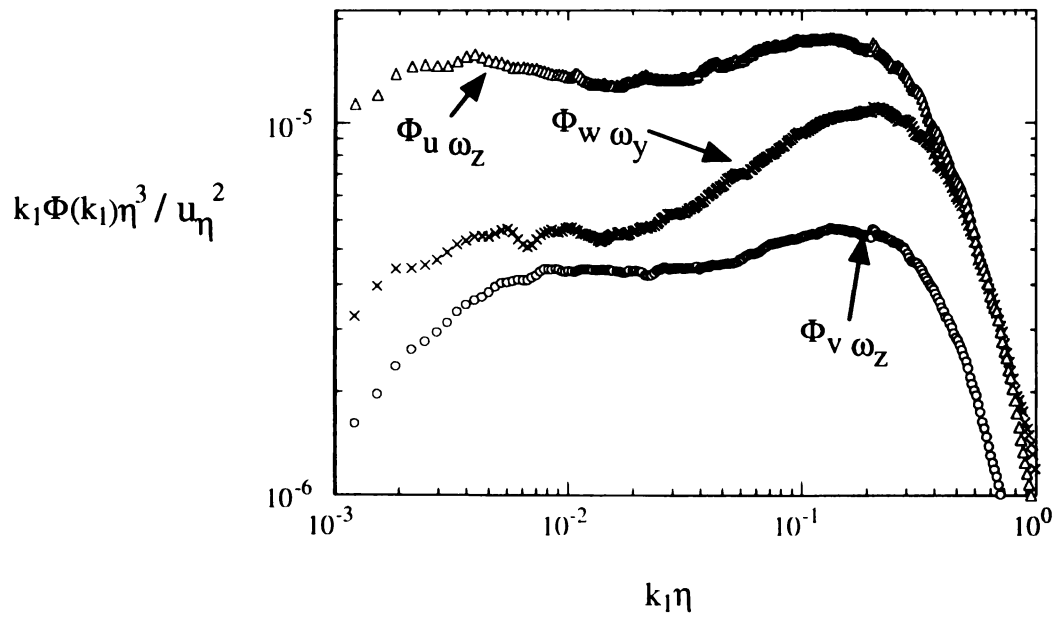


Figure 5.78 Compensated autospectral densities of the velocity-vorticity products for 19-July.



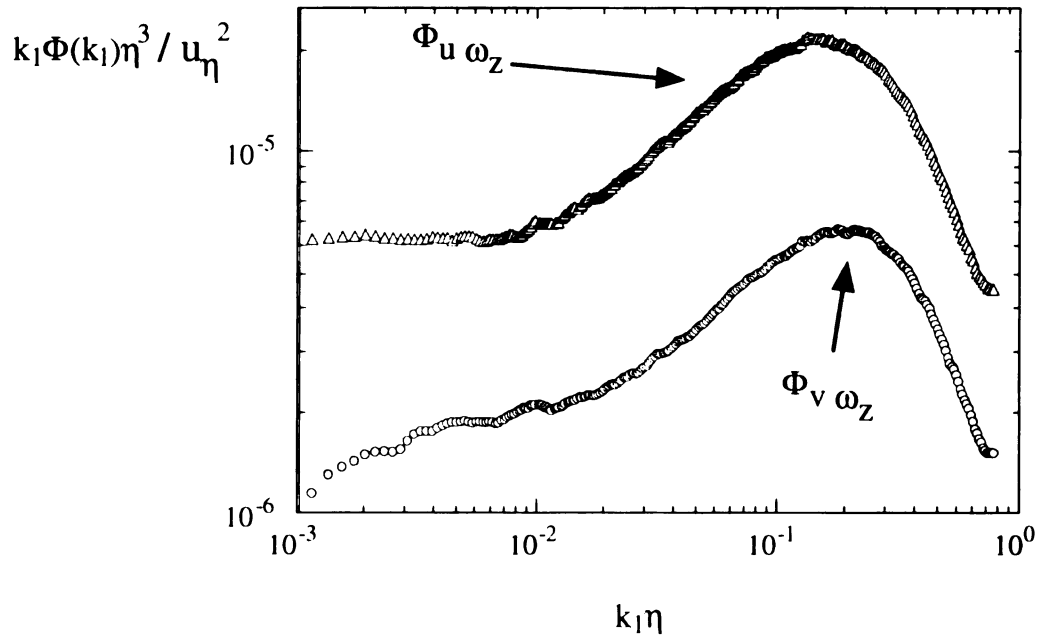


Figure 5.79 Compensated autospectral densities of the velocity-vorticity products for 25-July.

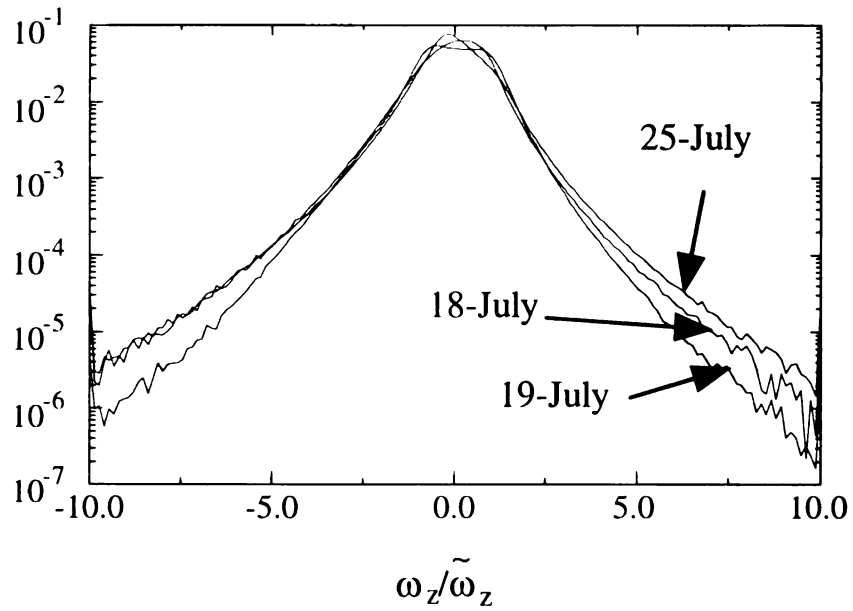


Figure 5.80 Normalized PDF of the  $\langle \omega_z' \rangle$  vorticity for each day.

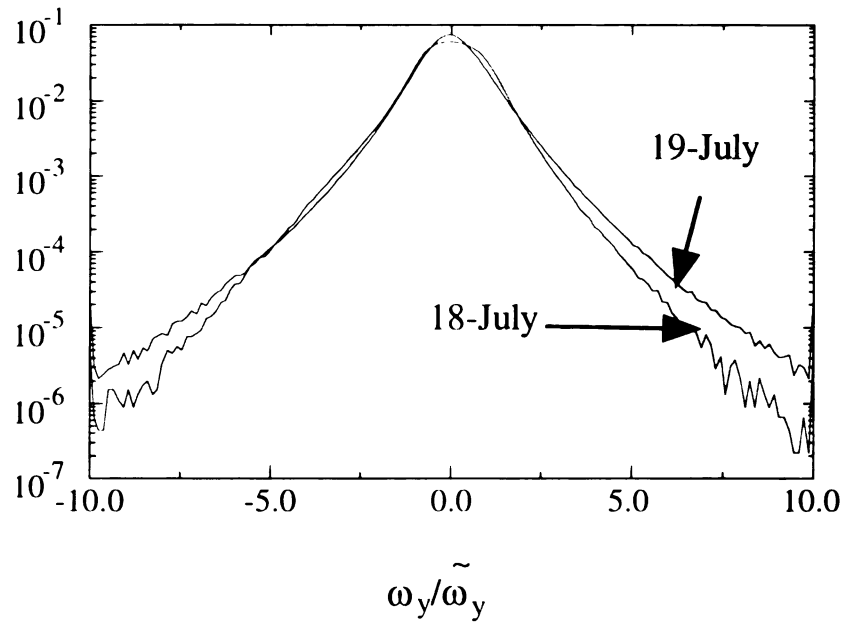


Figure 5.81 Normalized PDF of the  $\langle \omega_y' \rangle$  vorticity for each day.

**Table 5.9  $\omega_z$  PDF Statistics**

	18-July	19-July	25-July
RMS	84.5	94.1	84.7
Skewness	-0.49	-0.26	-0.09
Kurtosis	7.6	5.09	8.66

**Table 5.10  $\omega_y$  PDF Statistics**

	18-July	19-July	25-July
RMS	97.0	75.3	N/A
Skewness	-0.26	0.14	N/A
Kurtosis	6.06	8.53	N/A

## 6.0 Conclusions

This section presents conclusions made based on the data taken at the SLTEST site and presented in the previous chapters. The conclusions are presented in numbered order followed by a discussion of the relevant information needed to justify each conclusion.

1. The SLTEST data support Kolmogorov's hypothesis of local isotropy at very high wavenumbers. Large excursions from local isotropy for low wavenumbers was also documented.

The spectral representation of the velocity field was presented in Section 5.3.1. All three velocity components agreed well with the isotropic model spectra for very high wavenumbers. The coherence of the  $u$  and  $v$  velocity components dropped to near zero for almost two decades of high wavenumbers ( $10^{-2} \leq k_1 \eta \leq 10^0$ ). This lack of coherence between the  $u$  and  $v$  velocity components is a necessary condition for the presence of local isotropy. Similarly, the coherence of the  $u$  and  $w$  velocity components was nominally zero over all recorded wavelengths, as expected for a flow that is "two-dimensional" in the time averaged sense.

The condition of local isotropy did not appear to exist in the moderate to lower wavenumbers. The autospectral densities of these data appeared to deviate from the isotropic model at a range of moderate wavenumbers ( $k_1 \eta \approx 10^{-2}$ ). The effect of the wall was more evident in the 18- and 19-July data because these probes were located much closer to the wall. This anisotropic condition was also more prominent in the wall-normal

velocity component, where the magnitude of the experimental spectra was far below the isotropic model spectra.

2. A large range of values were initially found when computing the dissipation estimate. However, self consistent results could be obtained from several dissipation estimates.

The dissipation estimates were described in Section 5.2.3 and displayed in Table 5.4. Seven dissipation estimates were computed covering a range of assumptions. The estimates were computed in the assumptions of homogeneous isotropic turbulence and semi-isotropic, or axi-symmetric, turbulence. The dissipation estimates ranged from  $0.2 \leq \epsilon \leq 1.1$  (18-July),  $0.2 \leq \epsilon \leq 1.0$  (19-July), and  $0.28 \leq \epsilon \leq 1.4$  (25-July). However, with the exclusion of one estimate ( $\epsilon_b$ ), the range of the 25-July data was reduced to  $0.28 \leq \epsilon \leq 0.34$  for the three remaining estimates (two estimates were unavailable since only one probe was used on 25-July). Similar results for 18-July and 19-July were observed. On 18-July, with two estimates excluded ( $\epsilon_b$  and  $\epsilon_c$ ), the range was decreased to  $0.2 \leq \epsilon \leq 0.34$  for the five remaining estimates. On 19-July, with three estimates excluded ( $\epsilon_b$ ,  $\epsilon_c$  and  $\epsilon_e$ ), the range was decreased to  $0.2 \leq \epsilon \leq 0.43$  for the four remaining estimates.

3. Buoyancy had a small effect on the measurement of the velocity spectra.

The measurements of the velocity spectra were presented in Section 5.5 for all three days. Data from 25-July were acquired under thermally neutral conditions, data

from 18-July were acquired under thermally unstable conditions, and data from 19-July were acquired under the thermally stable condition. The autospectral densities of the three components of the velocity did not appear to be affected by the buoyancy condition. This was seen in the very similar character of the 18- and 19-July data. These data were acquired at the same probe location but acquired under different buoyancy conditions.

4. The gradient of the Reynolds shear stress appears to be dominated by the  $\overline{w'\omega_y'}$  component.

The gradient of the Reynolds shear stress is discussed in Section 5.3.3.3. Using a tensor identity, this gradient can be decomposed into two velocity-vorticity products:  $\overline{v'\omega_z'}$  and  $\overline{w'\omega_y'}$  (see equation 5.44). The correlation coefficient of the  $\overline{v'\omega_z'}$  component was found to be a relative small number for each of the three days ( $-0.03 \leq \overline{v'\omega_z'}/\tilde{v}\tilde{\omega}_z \leq 0.02$ ; see Table 5.8). The other velocity-vorticity component present in the gradient of the Reynolds shear stress,  $\overline{w'\omega_y'}$ , was found to consistently display a relatively large correlation between its velocity and vorticity parts ( $\overline{w'\omega_y'}/\tilde{w}\tilde{\omega}_y = 0.2$  for both data sets).

Spectral analyses of these velocity-vorticity components showed large coherence over very high wave numbers. Figure 5.69 demonstrates the coherence of the  $v'$  and  $\langle\omega_z'\rangle$  flow components. The coherence peaks at a value of 0.8 for a wavenumber of  $k_1\eta \approx 0.35$ . This trend is evident for each data set. Figure 5.76 shows the spectral correlation between the  $w'$  and  $\langle\omega_y'\rangle$  flow components. The large coherence at high wave-

numbers is again evident, peaking at a coherence of 0.76 and a wavenumber of  $k_1 \eta \approx 0.4$  (19-July). However, the  $w'$  and  $\langle \omega_y' \rangle$  coherence also has a significant low wavenumber contribution ( $\sim 0.4$  at a wavenumber  $k_1 \eta \sim O(10^{-4})$ ) that was not observed in the  $v'$  and  $\langle \omega_z' \rangle$  coherence spectra.

5. There is a large contribution to the vorticity autospectral densities from very low wavenumbers.

The autospectral representations of the  $\langle \omega_z \rangle$  vorticity field for the three days are presented in Section 5.3.2. In all three cases, the experimental spectra continued to increase as the wavenumber decreased. This character was not observed in the model spectrum which leveled off for lower wavenumbers. The autocorrelation of the vorticity time signal showed correlations over very large time periods. The length corresponding to the first zero crossing of the  $\langle \omega_z \rangle$  vorticity autocorrelation varied from day to day. It ranged from 13m (19-July) to 43m (25-July). The correlation appeared to show a dependence on  $R_\lambda$  (as  $R_\lambda$  increased, the length of the first zero crossing also increased), but effects from the different thermal stabilities cannot be excluded.

The same large scale correlations were observed in the  $\langle \omega_y \rangle$  vorticity data (section 5.3.2), except with much larger correlation values. The lengths corresponding to the first zero crossing of the  $\langle \omega_y \rangle$  vorticity autocorrelation were 225m (19-July) and 240m (18-July). These motions are on the order of a boundary layer thickness ( $\delta \approx 150m$ ). A

dependence on  $R_\lambda$ , the thermal stability, or both cannot be established given the limited observations.

6. The kurtosis (flatness) of the probability density function of the  $\langle \omega_z \rangle$  vorticity displays a dependence on  $R_\lambda$ . This is a result of the “tails” of the PDF, which “rise” with an increase in  $R_\lambda$ .

Section 5.4 discusses the PDF's of the  $\langle \omega_z \rangle$  vorticity. The flatness of the  $\langle \omega_z \rangle$  vorticity PDF appears to increase with higher  $R_\lambda$  values. This is evident in Table 5.9 as well as Figure 5.80. As the Reynolds number is increased, the number of large excursions in the vorticity fluctuations also increases. This increase in large excursions brings the “tails” of the PDF “up”, in turn flattening out the shape. It should be noted that this dependence on  $R_\lambda$  cannot be separated from buoyancy effects (which may also contribute to the skewness of the probability distribution functions) given this limited data set. The same trends do not hold true for the  $\langle \omega_y \rangle$  vorticity.

## Appendix A: Pre-Post Calibration Comparison

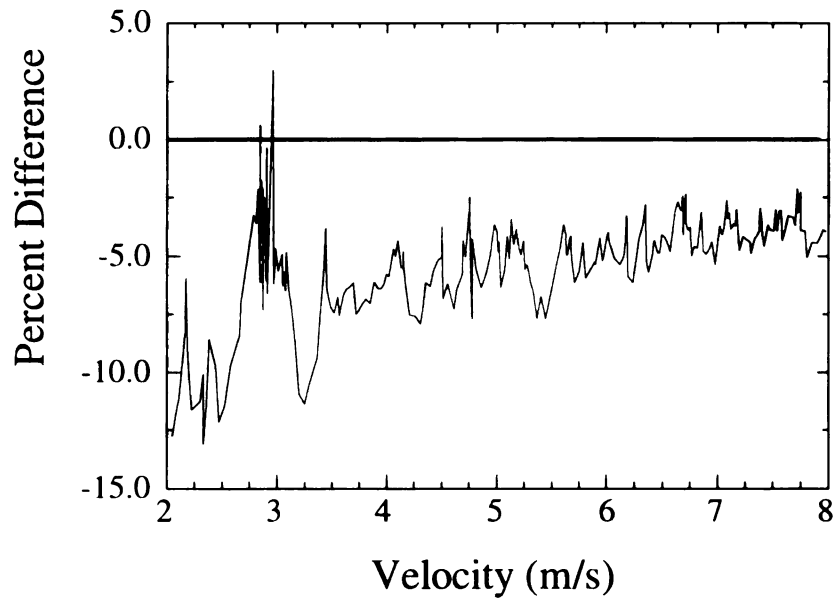


Figure A.1 Drift determination comparison taken on 18-July ( $\langle \omega_z \rangle$  probe, first straight wire).

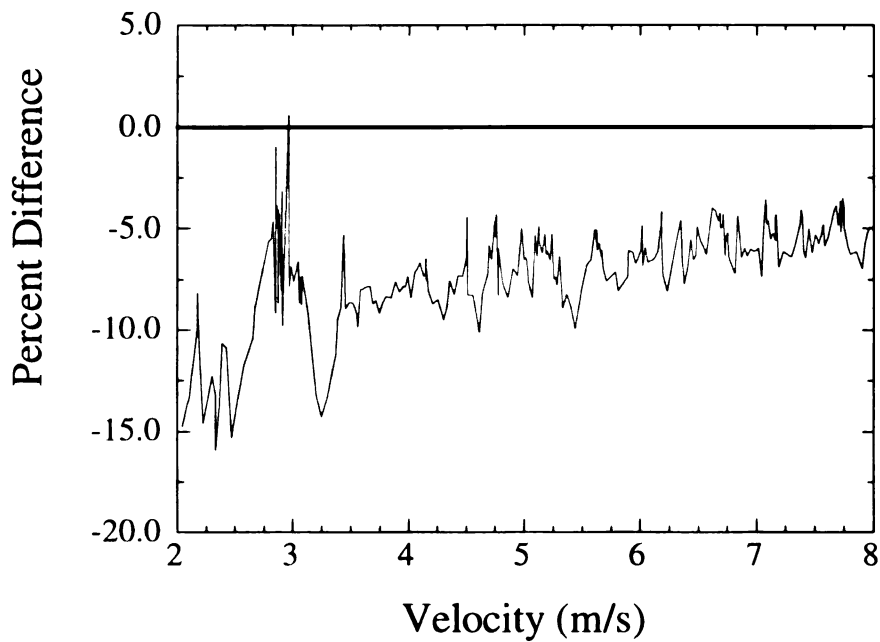


Figure A.2 Drift determination comparison taken on 18-July ( $\langle \omega_z \rangle$  probe, second straight wire).



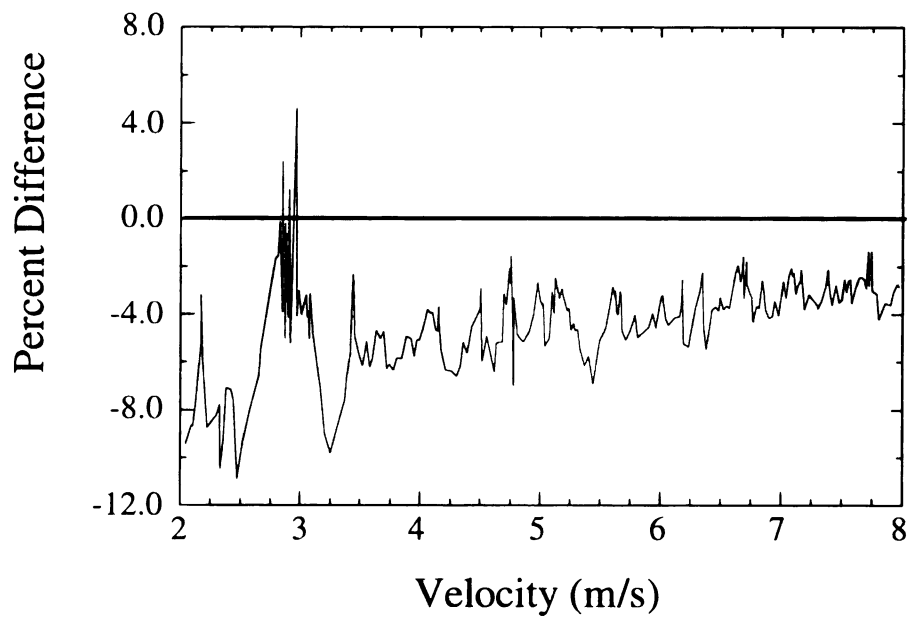


Figure A.3 Drift determination comparison taken on 18-July ( $\langle \omega_y \rangle$  probe, first straight wire).

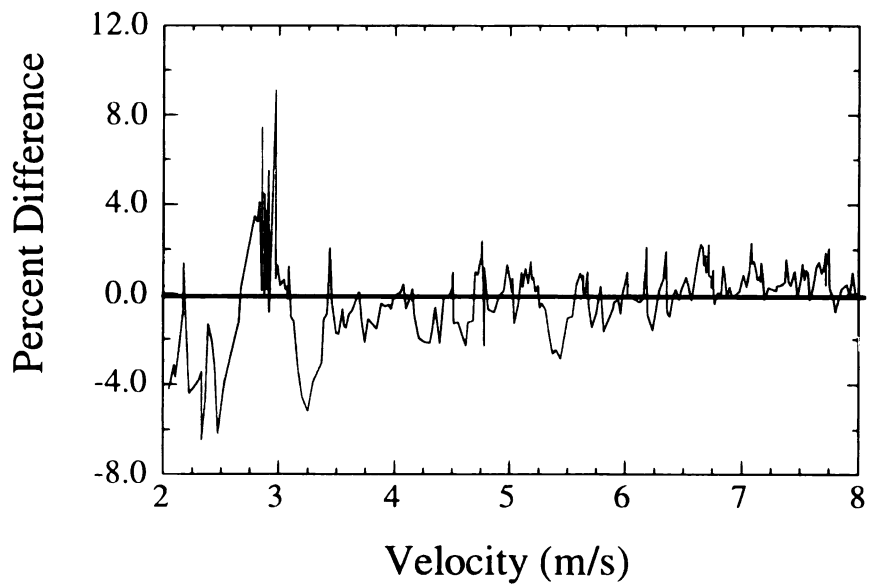


Figure A.4 Drift determination comparison taken on 18-July ( $\langle \omega_y \rangle$  probe, second straight wire).

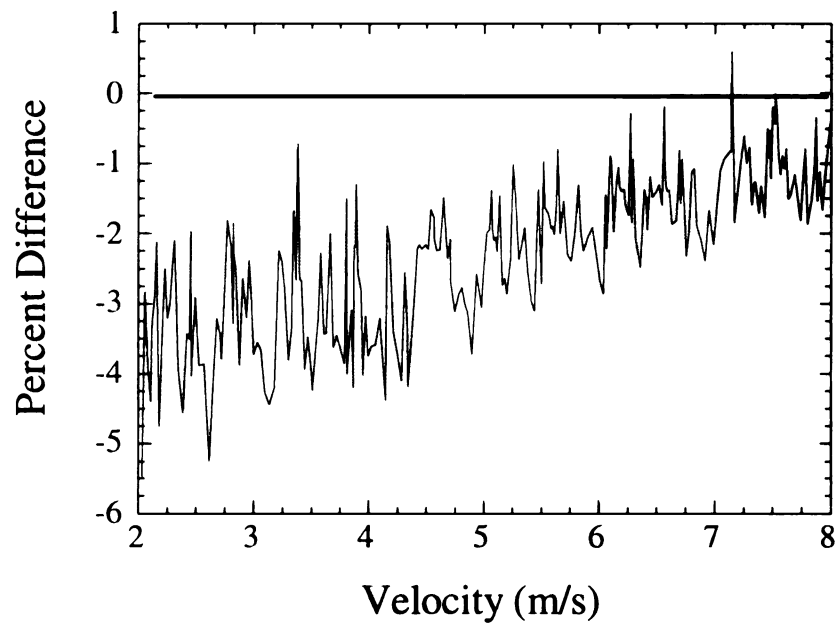


Figure A.5 Drift determination comparison taken on 19-July ( $\langle \omega_z \rangle$  probe, first straight wire).

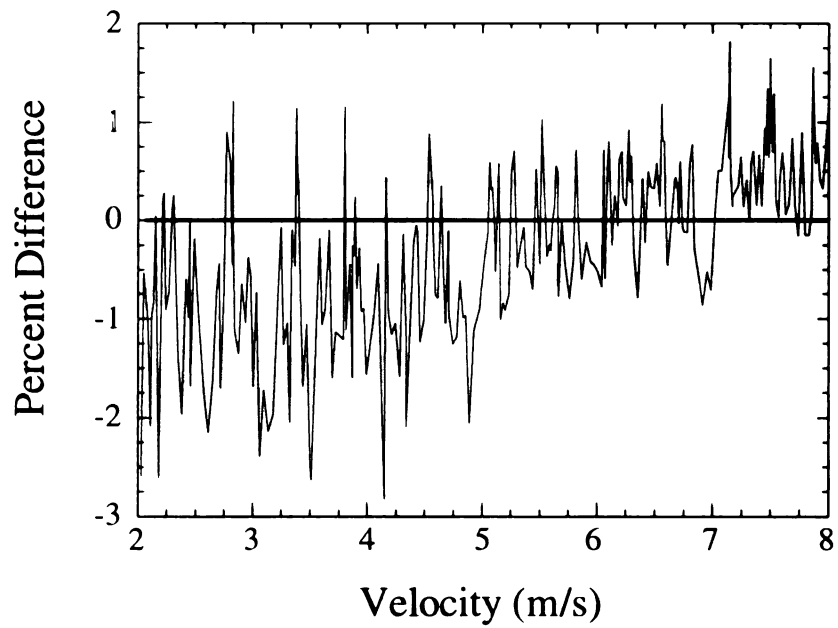


Figure A.6 Drift determination comparison taken on 19-July ( $\langle \omega_z \rangle$  probe, second straight wire).

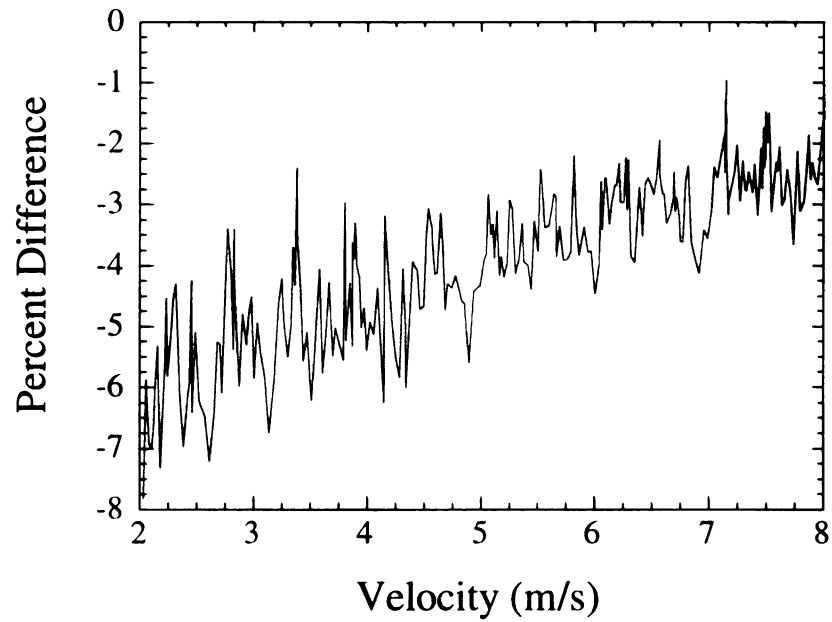


Figure A.7 Drift determination comparison taken on 19-July ( $\langle \omega_y \rangle$  probe, first straight wire).

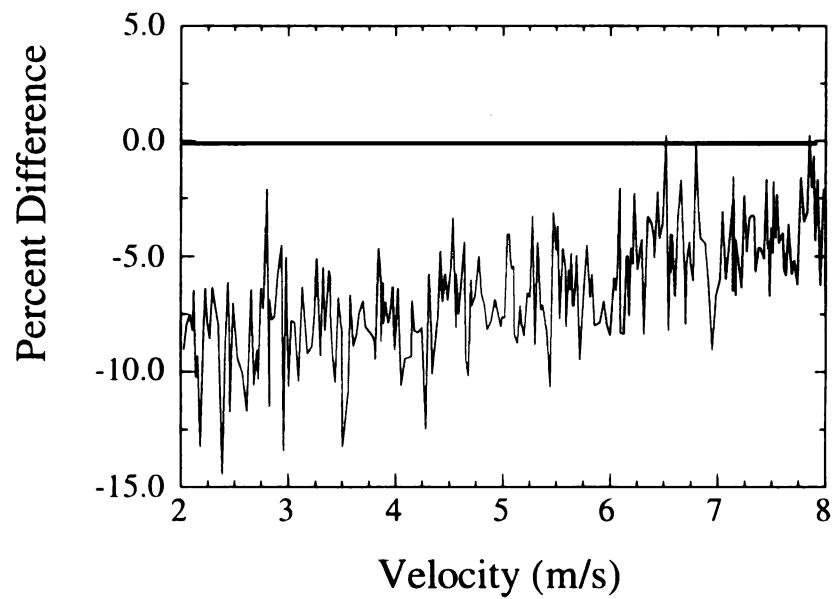


Figure A.8 Drift determination comparison taken on 19-July ( $\langle \omega_y \rangle$  probe, second straight wire).

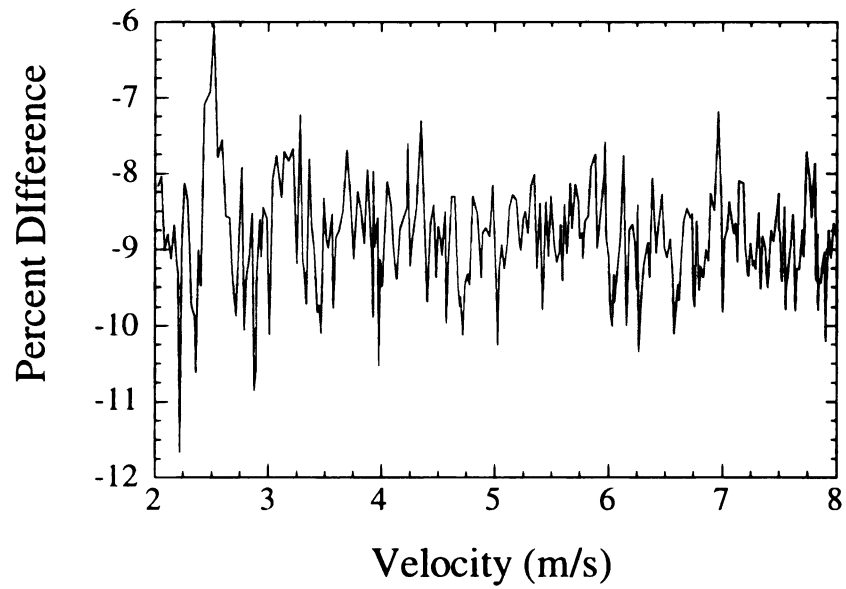


Figure A.9 Drift determination comparison taken on 25-July ( $\langle \omega_z \rangle$  probe, first straight wire).

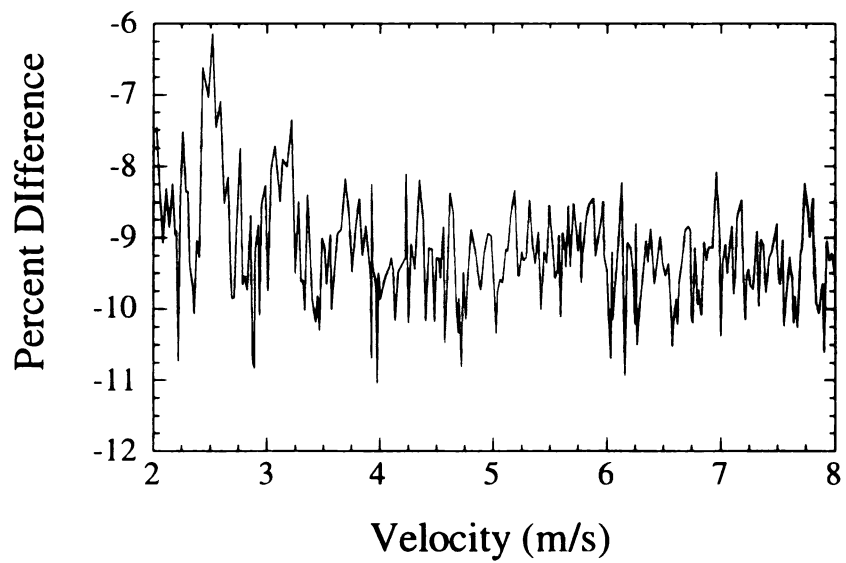


Figure A.10 Drift determination comparison taken on 25-July ( $\langle \omega_z \rangle$  probe, second straight wire).

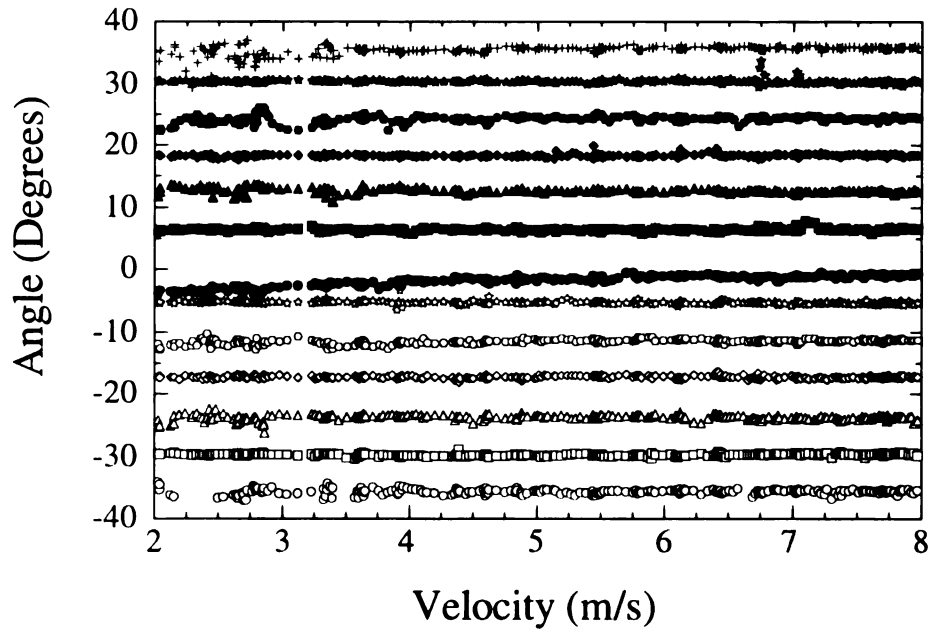


Figure A.11 X-wire drift determination comparison taken on 18-July ( $\langle \omega_z \rangle$  probe).

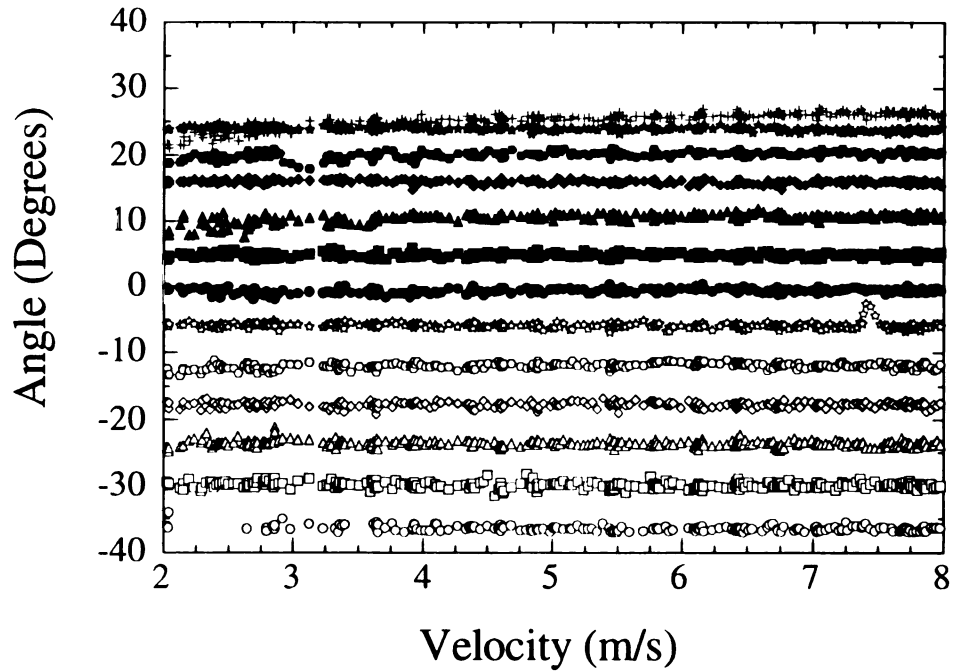


Figure A.12 X-wire drift determination comparison taken on 18-July ( $\langle \omega_y \rangle$  probe).

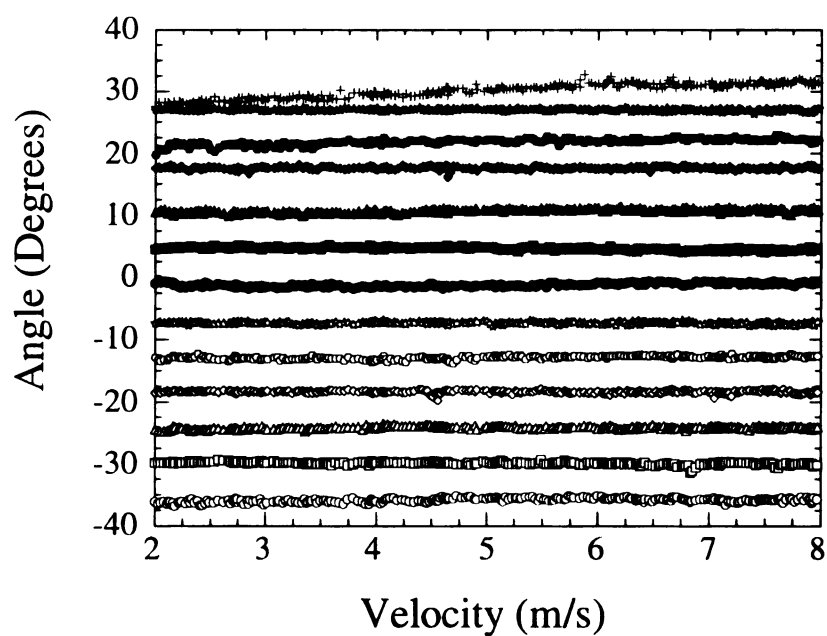


Figure A.13 X-wire drift determination comparison taken on 19-July ( $\langle \omega_z \rangle$  probe).

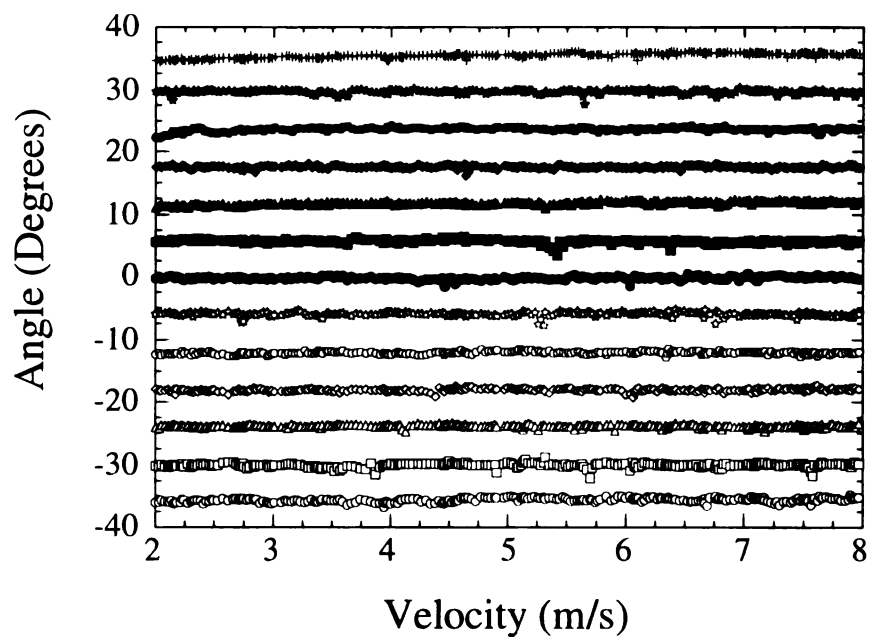


Figure A.14 X-wire drift determination comparison taken on 19-July ( $\langle \omega_y \rangle$  probe).

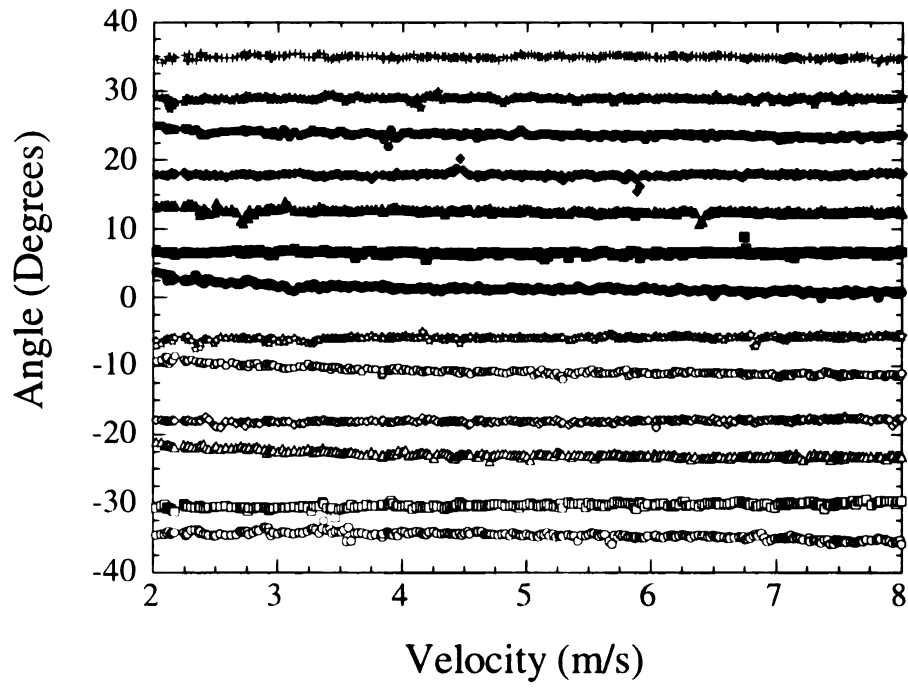


Figure A.15 X-wire drift determination comparison taken on 25-July ( $\langle \omega_z \rangle$  probe).

## Appendix B: Combined Calibration Plots

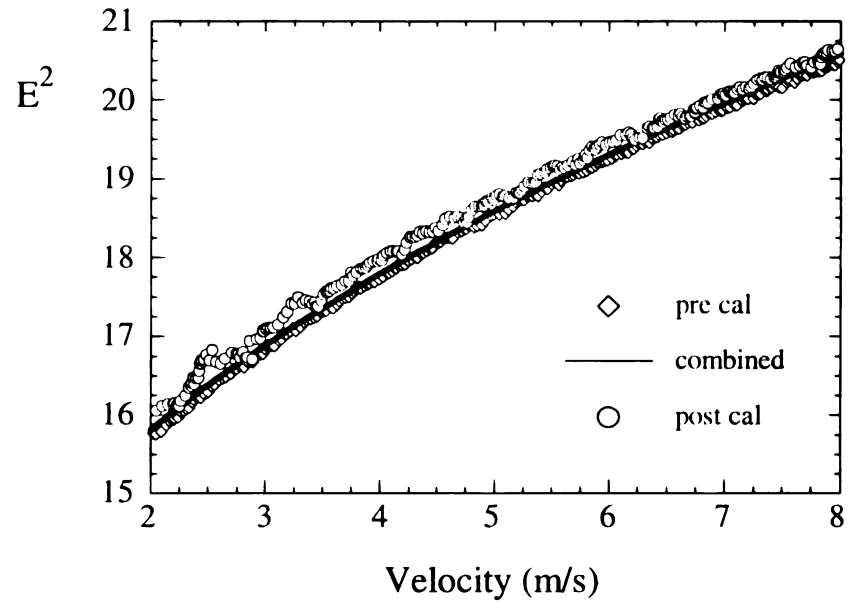


Figure B.1 Combined calibration data for 18-July ( $\langle \omega_z \rangle$  probe, first straight wire).

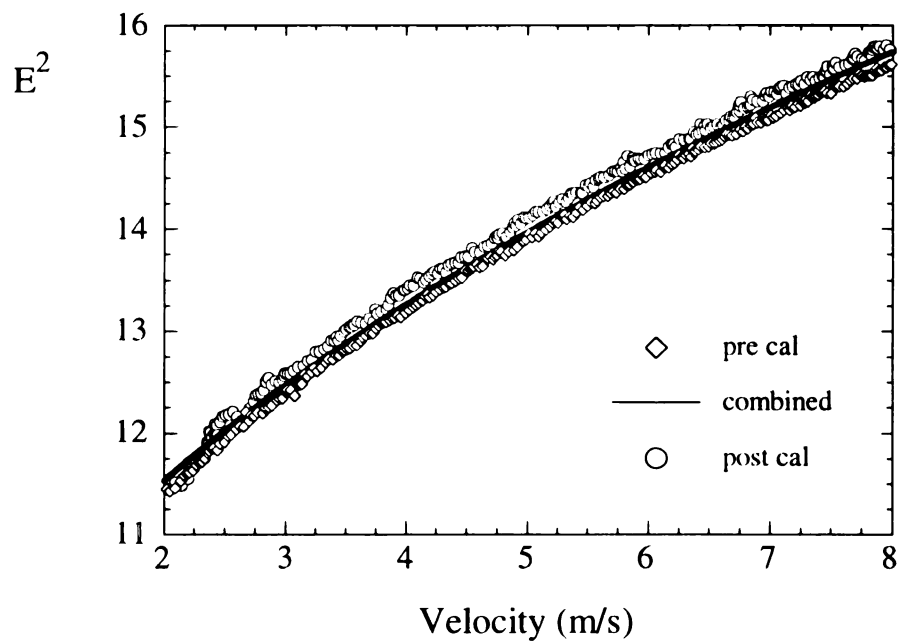


Figure B.2 Combined calibration data for 18-July ( $\langle \omega_z \rangle$  probe, second straight wire).



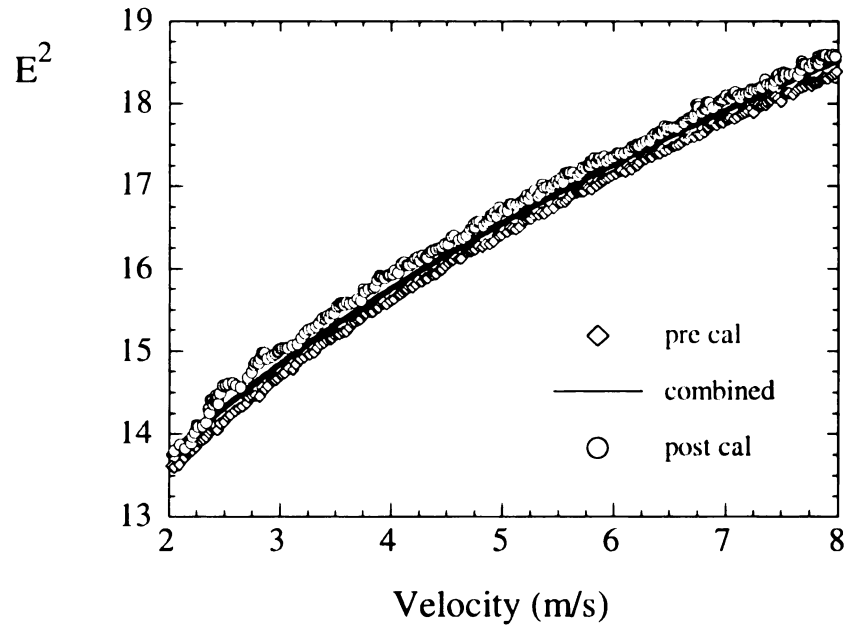


Figure B.3 Combined calibration data for 18-July ( $\langle \omega_z \rangle$  probe, first X-wire).

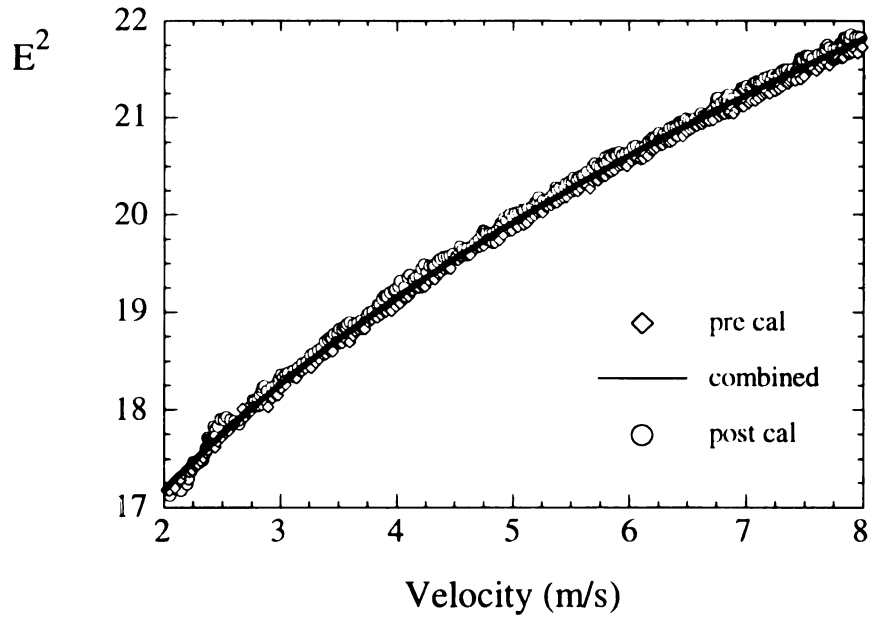


Figure B.4 Combined calibration data for 18-July ( $\langle \omega_z \rangle$  probe, second X-wire).

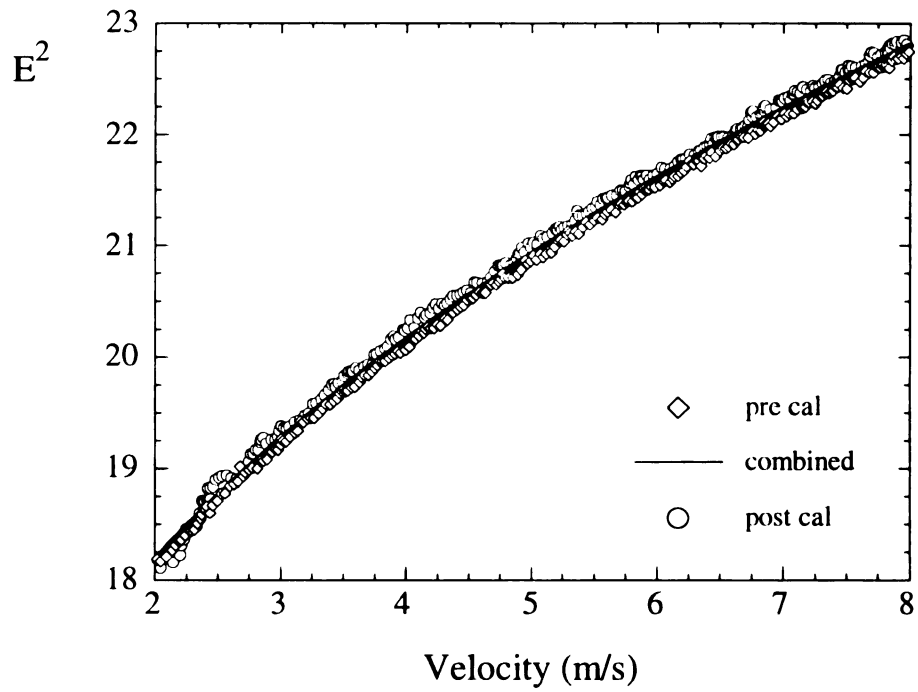


Figure B.5 Combined calibration data for 18-July ( $\langle \omega_y \rangle$  probe, first straight wire).

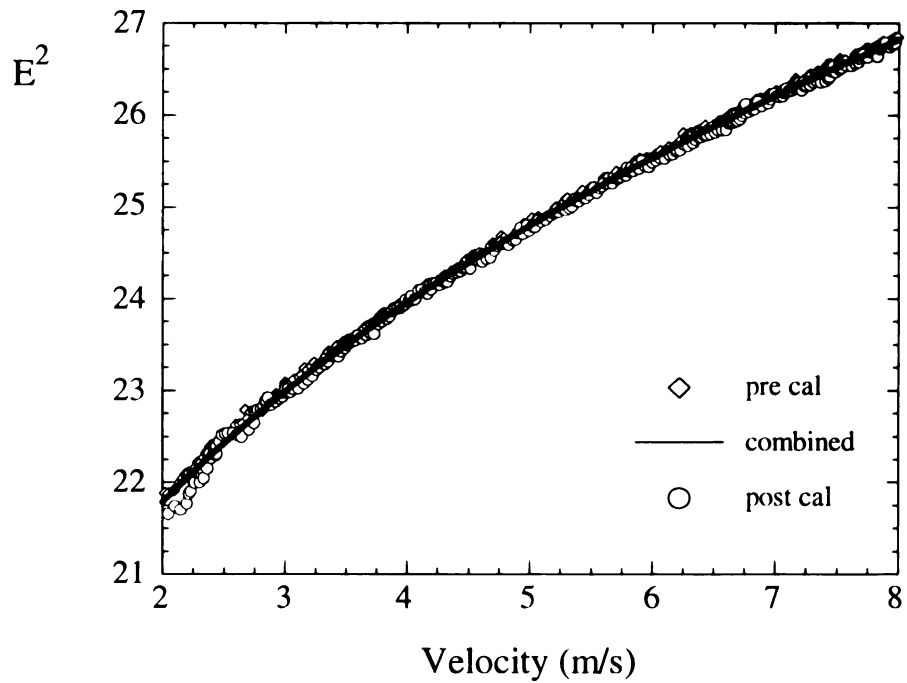


Figure B.6 Combined calibration data for 18-July ( $\langle \omega_y \rangle$  probe, second straight wire).

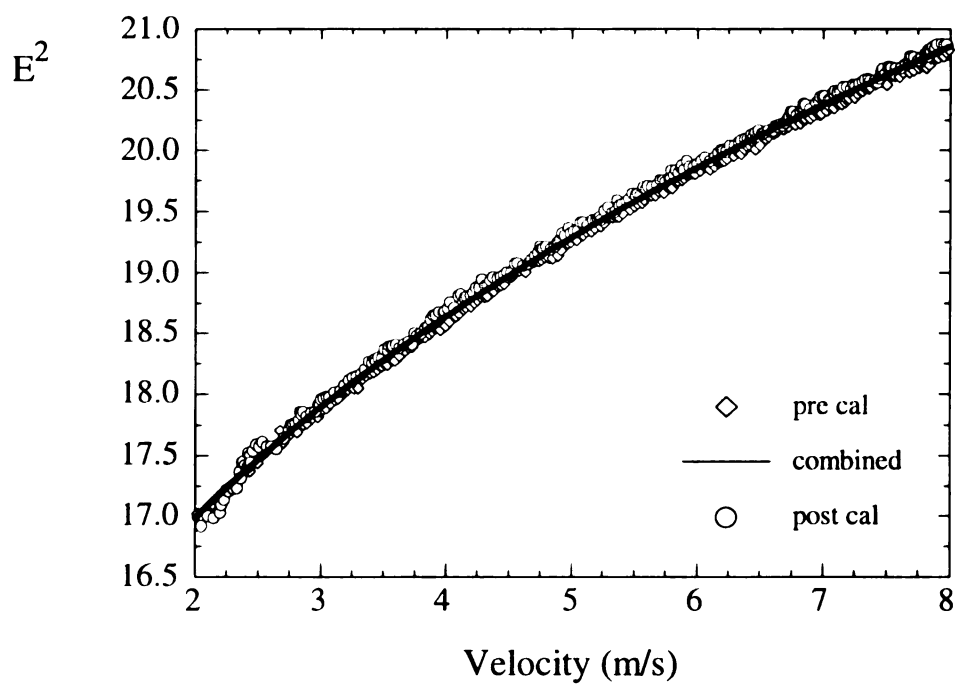


Figure B.7 Combined calibration data for 18-July ( $\langle \omega_y \rangle$  probe, first X-wire).

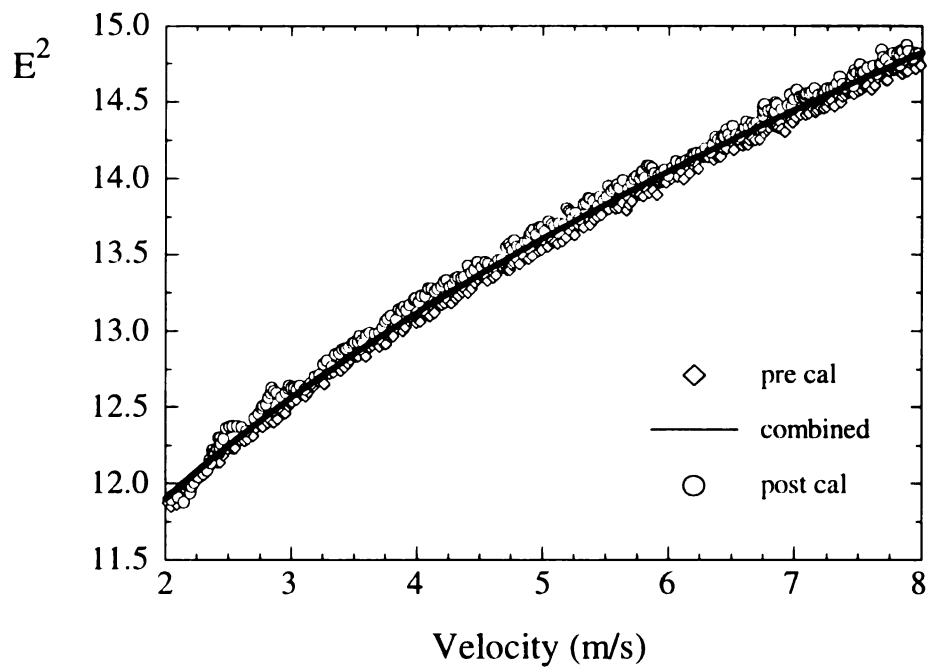


Figure B.8 Combined calibration data for 18-July ( $\langle \omega_y \rangle$  probe, second X-wire).

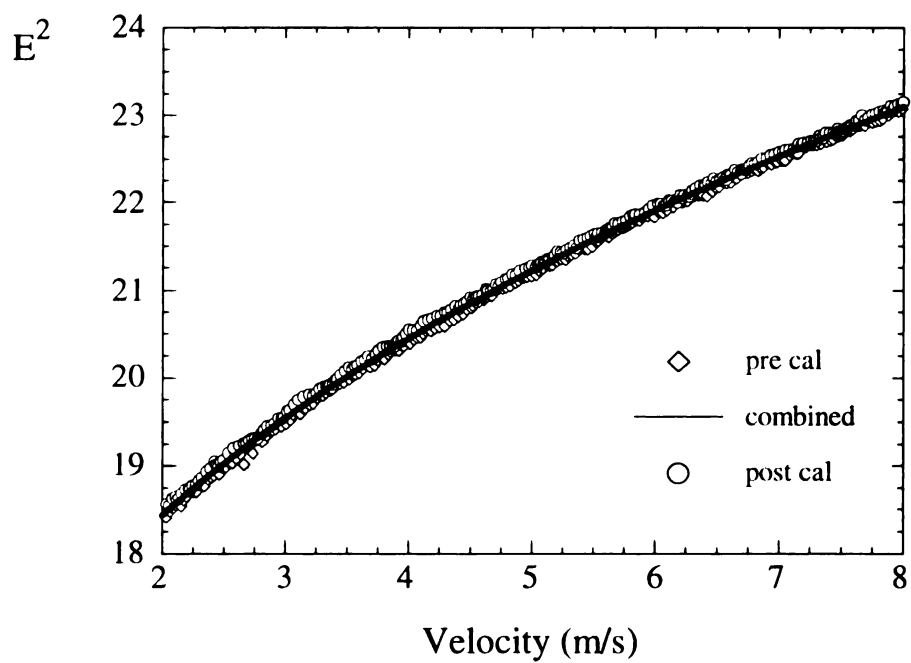


Figure B.9 Combined calibration data for 19-July ( $\langle \omega_z \rangle$  probe, first straight wire).

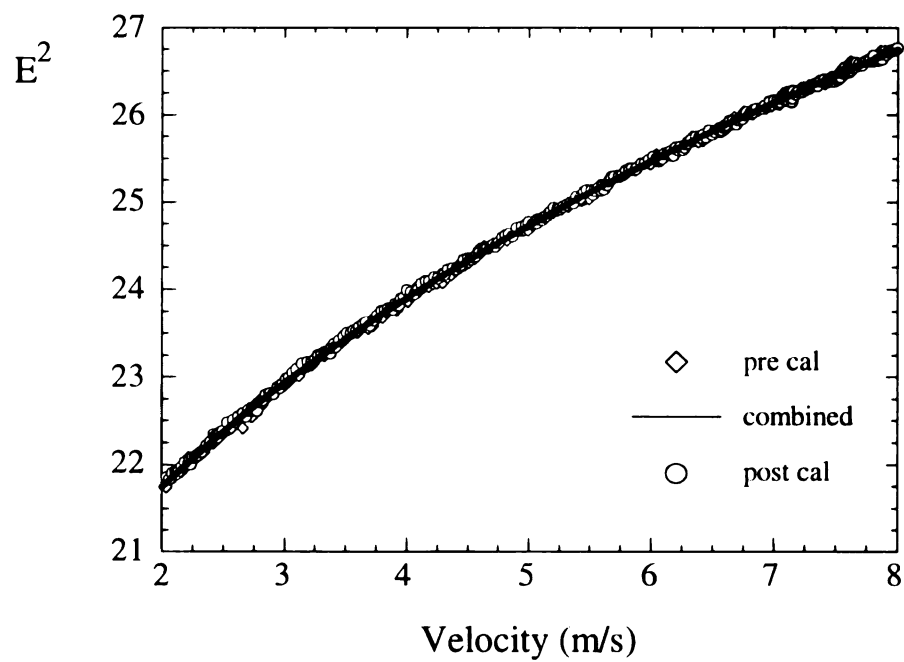


Figure B.10 Combined calibration data for 19-July ( $\langle \omega_z \rangle$  probe, second straight wire).

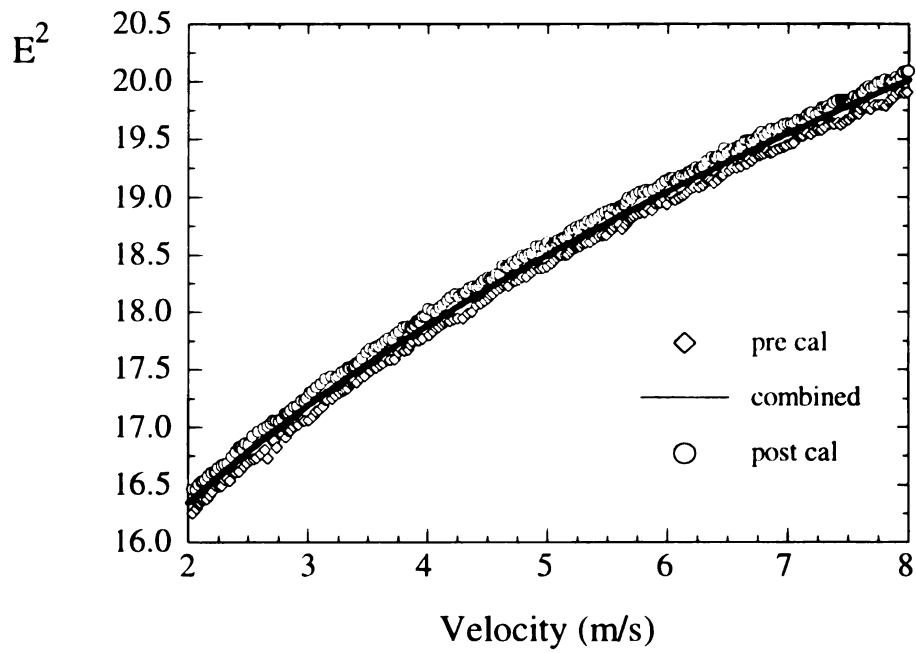


Figure B.11 Combined calibration data for 19-July ( $\langle \omega_z \rangle$  probe, first X-wire).

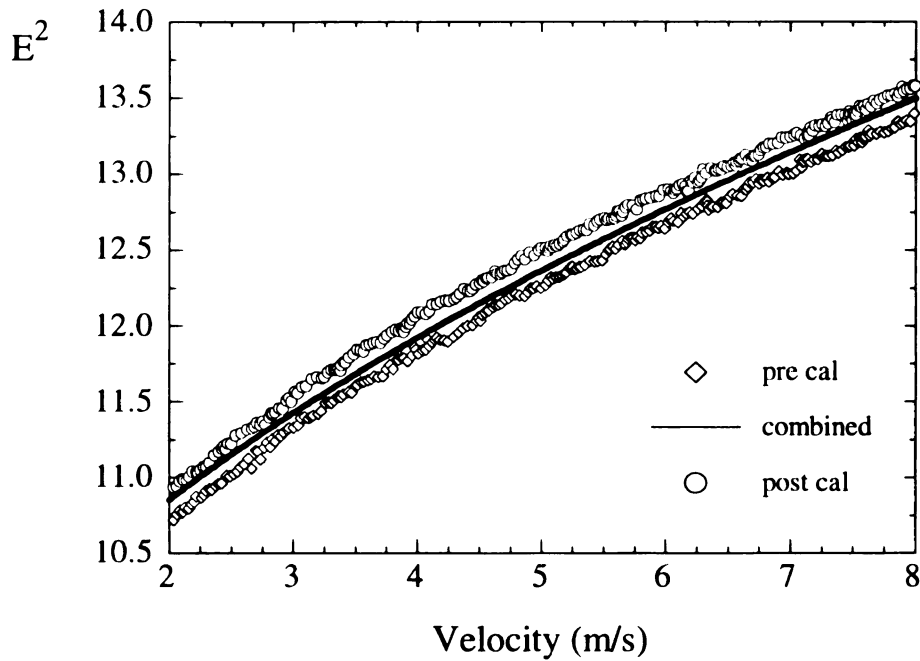


Figure B.12 Combined calibration data for 19-July ( $\langle \omega_z \rangle$  probe, second X-wire).

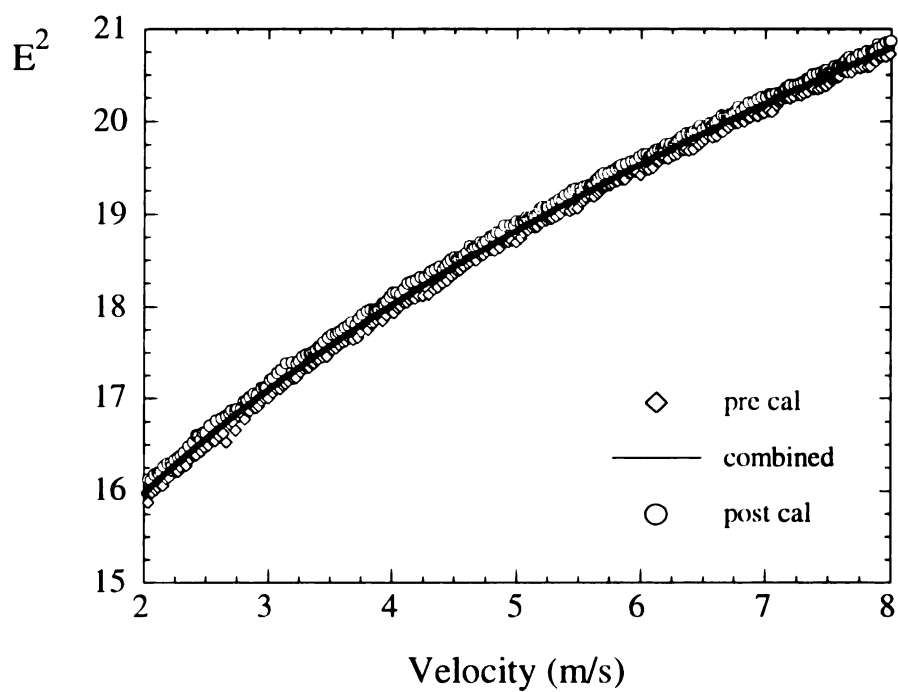


Figure B.13 Combined calibration data for 19-July ( $\langle \omega_y \rangle$  probe, first straight wire).

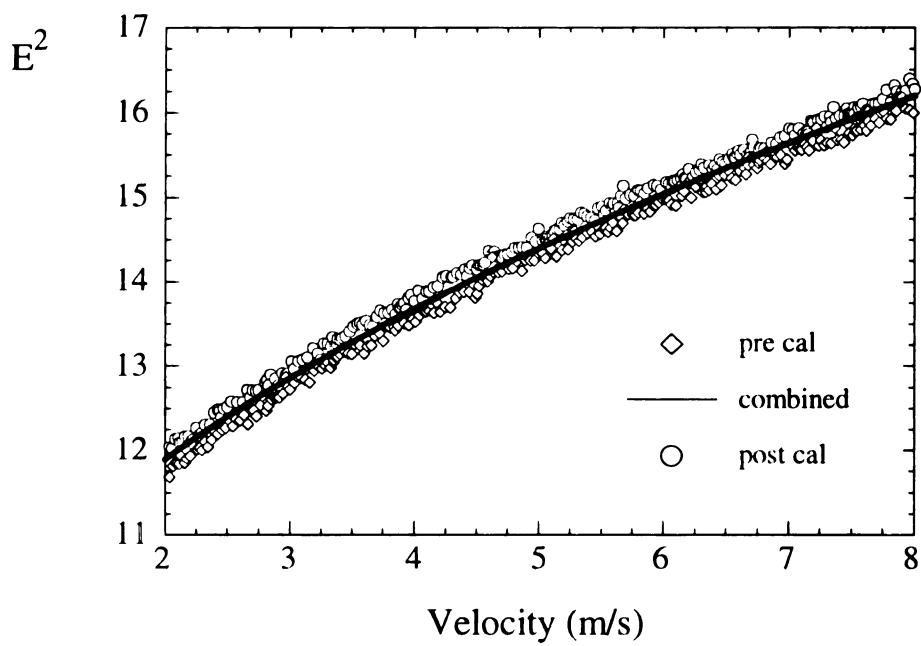


Figure B.14 Combined calibration data for 19-July ( $\langle \omega_y \rangle$  probe, second straight wire).

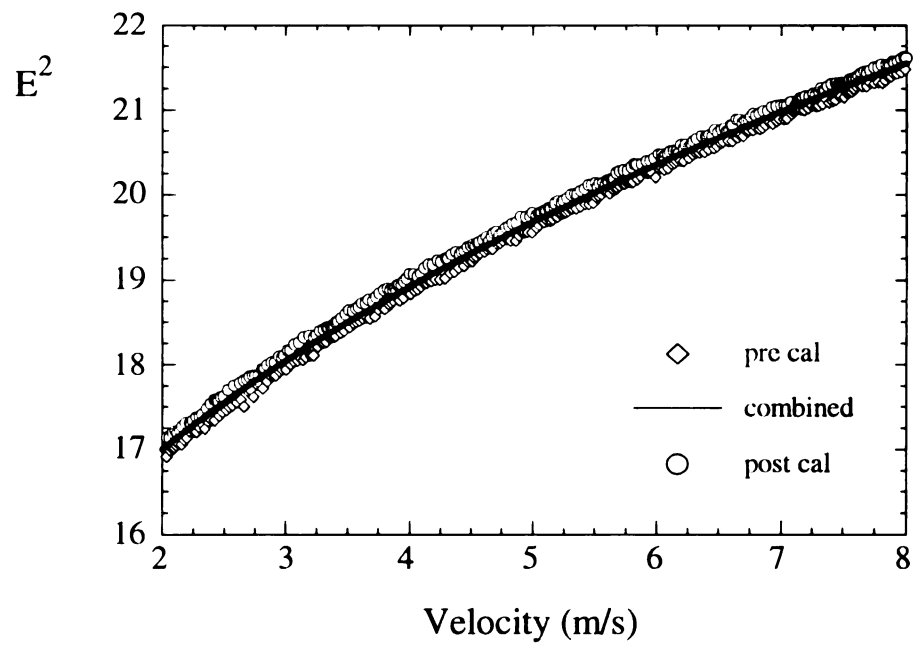


Figure B.15 Combined calibration data for 19-July ( $\langle \omega_y \rangle$  probe, first X-wire).

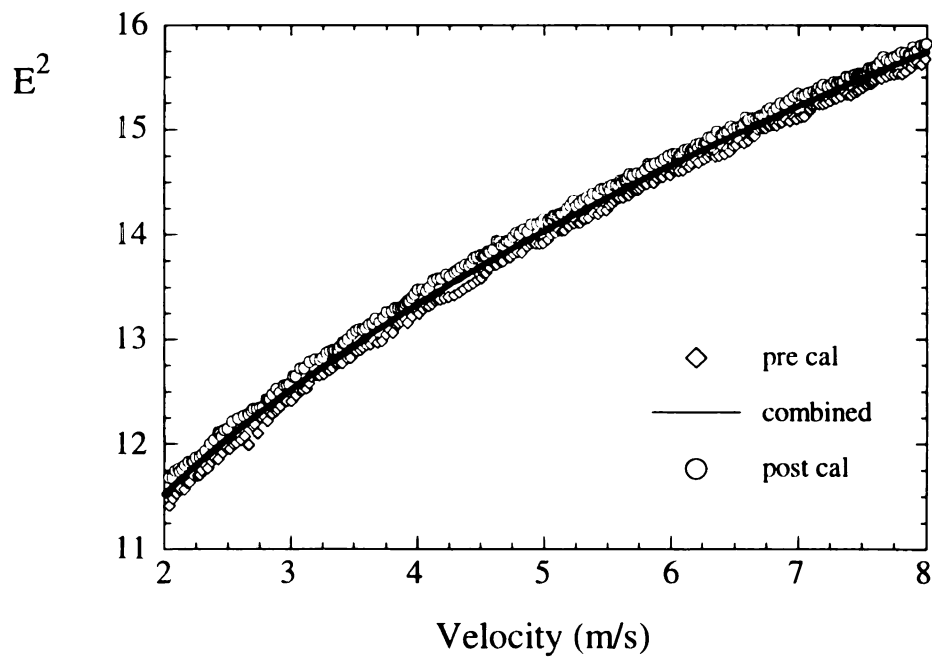


Figure B.16 Combined calibration data for 19-July ( $\langle \omega_y \rangle$  probe, second X-wire).

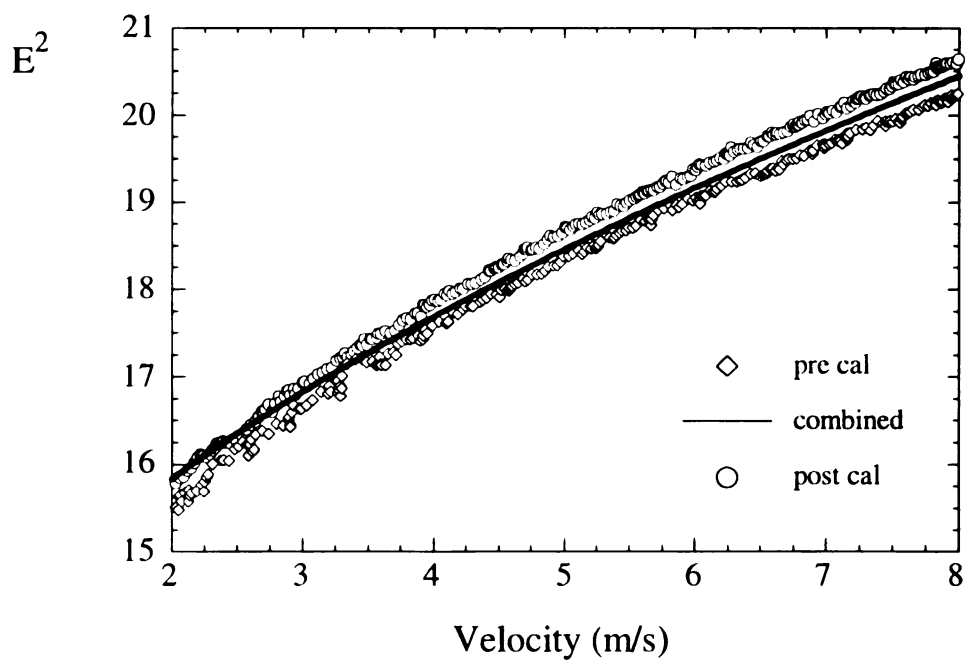


Figure B.17 Combined calibration data for 25-July ( $\langle \omega_z \rangle$  probe, first straight wire).

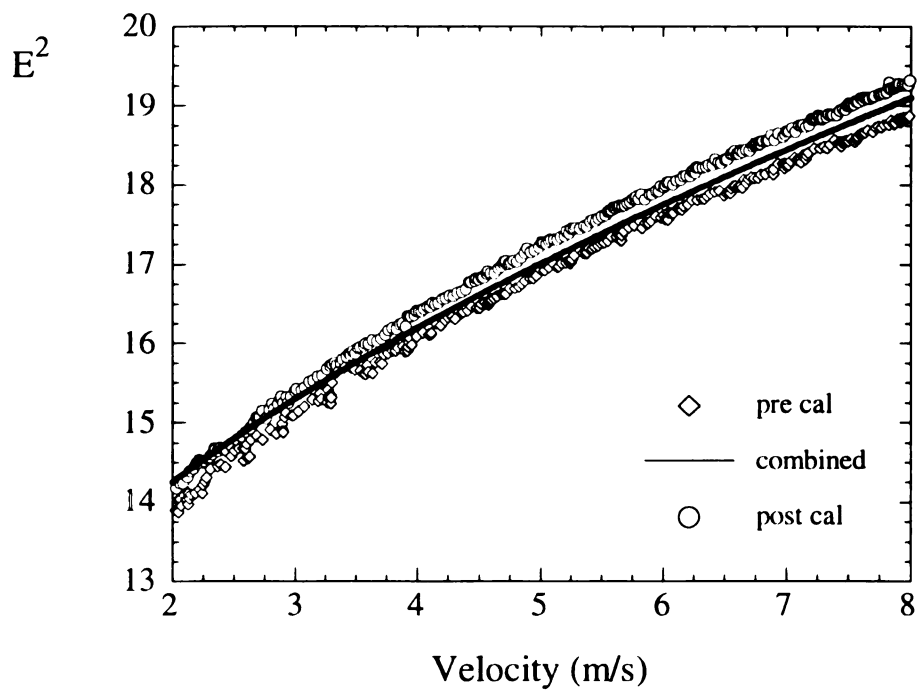


Figure B.18 Combined calibration data for 25-July ( $\langle \omega_z \rangle$  probe, second straight wire).



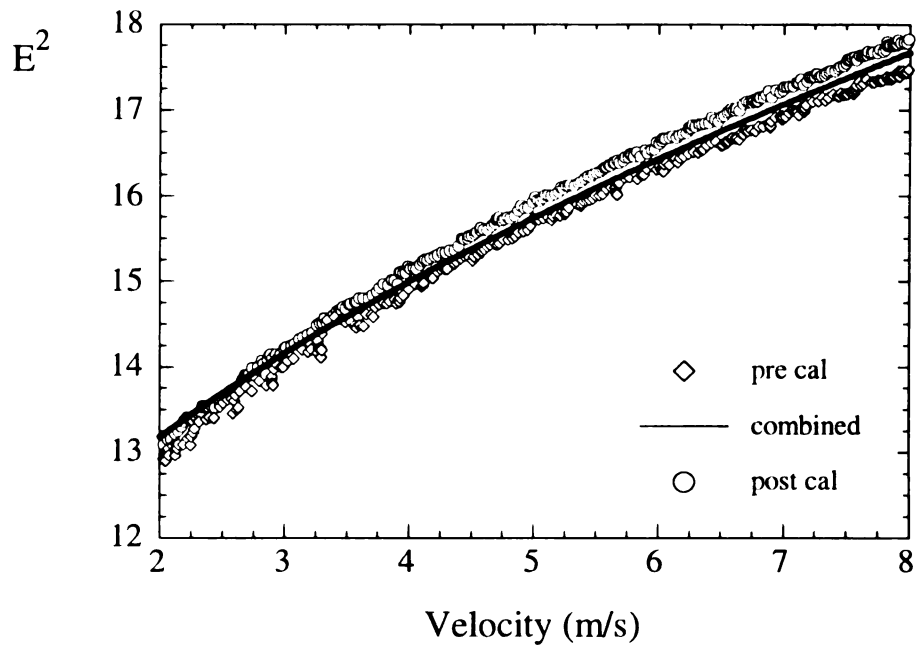


Figure B.19 Combined calibration data for 25-July ( $\langle \omega_z \rangle$  probe, first X-wire).

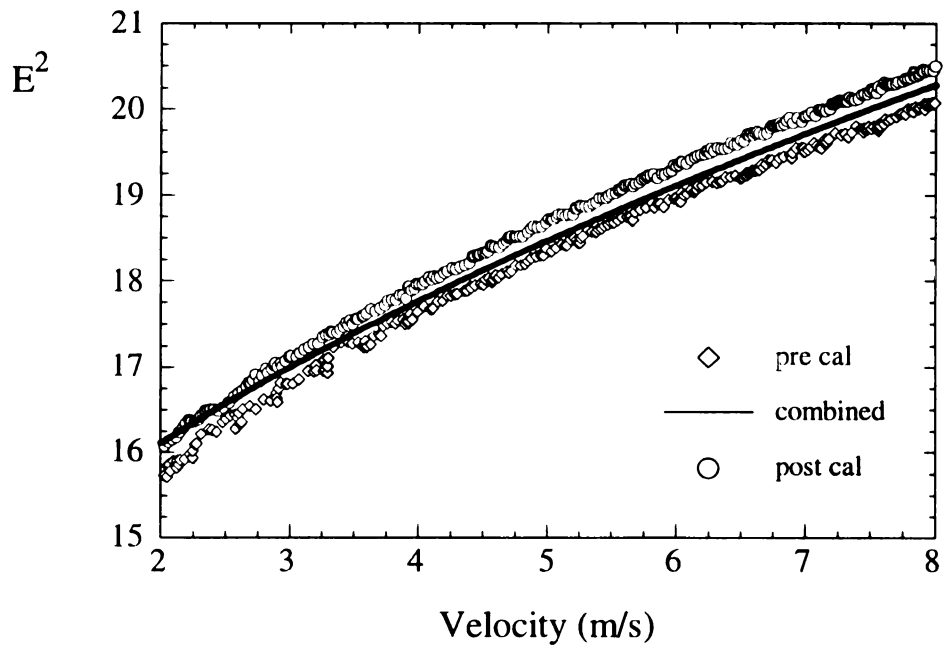


Figure B.20 Combined calibration data for 25-July ( $\langle \omega_z \rangle$  probe, second X-wire).

## REFERENCES

- [1] Andreopoulos, J., and Agui, J. H. 1997 "Wall-vorticity flux dynamics in a two-dimensional turbulent boundary layer." *J. Fluid Mech.* **309**, 45-84.
- [2] Andreopoulos, J., and Honkan, A. 1997 "An experimental study of the dissipative and vortical motion in turbulent boundary layers." *J. Fluid Mech.* **439**, 131-163.
- [3] Antonia, R.A., Browne, L.W., Shah, D.A., 1987, "Characteristics of vorticity fluctuations in a turbulent wake." *J. Fluid Mech.* 189, 346-365.
- [4] Bejan, Adrian. Convection Heat Transfer. John Wiley & Sons, Inc., New York, 1995.
- [5] Bendat, J.S., and Piersol, A.G. Random Data: Analysis and Measurement Procedures. John Wiley & Sons, Canada, 1968.
- [6] Browne, L.W.B., Antonia, R.A., and Shah, D.A., 1987, "Turbulent energy dissipation in a wake." *J. Fluid Mech.* 179, 307-326.
- [7] Bruun, H. H., Hot-Wire Anemometry Principles and Signal Analysis, Oxford University Press, New York, 1995.
- [8] Cerutti, S. and Meneveau, C. 1999 "Hot-wire array for turbulence research in sub-grid-scale modeling." Proceedings of FEDSM'99, ASME.
- [9] Foss, J.F., 1981, "Advanced techniques for transverse vorticity measurements." Proceedings, 7th Biennial Symposium on Turbulence, Univ. of Missouri-Rolla.
- [10] Foss, J.F., Bohl, D.G., and Kleis, S.J., 1995, "Activity Intermittency in a two-stream shear layer." Proceedings of the Tenth Symposium on Turbulent Shear Flows, The Pennsylvania State University, University Park, PA.

- [11] Foss, J. F., Davis, E. D., Haw, R. C., Ali, S. K., "Coherent Motion Induced Fluctuations in the Primary Transition Region of a Plane Shear Layer." Forum on Turbulent Flows, ASME, FED Vol. 51, 1987
- [12] Foss, J.F., and Haw, R.C., 1990, "Transverse vorticity measurements using a compact array of four sensors." In The Heuristics of Thermal Anemometry, ed. DE STock, SA Sherif, AJ Smits, ASME-FED 97: 71-76, pp98.
- [13] Hogstrom, U. 1988 "Non-Dimensional Wind and Temperature Profiles in the Atmospheric Surface Layer: A Re-Evaluation." *Boundary Layer Meteorology*. **42**, 55-78.
- [14] Honkan, A. and Andreopoulos, J. 1997 "Vorticity, strain-rate and dissipation characteristics in the near-wall region of turbulent boundary layers." *J. Fluid Mech.* **350**, 29-96.
- [15] Klewicki, J.C., Priyadarshana, P., Foss, J.F., Sreenivasen, K.R., "Boundary Layer Turbulence Measurements at Submarine Scale Reynolds Numbers to Support RANS Model Validation and Development." First Year Progress Report, ONR
- [16] Klewicki, J.C. and Metzger, M.M., 2001, "A comparative study of near-wall turbulence in high and low Reynolds number boundary layers." *Physics of Fluids* Vol. 13, issue 3, 692-701.
- [17] Klewicki, J. C., Sreenivasan, K. R., Foss, J. F. "Spatially and Temporally Resolved Wall Layer Measurements of Rough Wall Turbulence at  $R_\theta \approx 10^7$ ." Meeting abstract for the 2001 ONR review.
- [18] Mestayer, P., 1982, "Local isotropy and anisotropy in a high-reynolds-number turbulent boundary layer." *J. Fluid Mech.* 125, 475-503.
- [19] Metzger, M., "Scalar dispersion in high Reynolds number turbulent boundary layers." Ph.D. dissertation, University of Utah, Salt Lake City, Utah, 2002.
- [20] Morris, S.C., "Experimental Investigation of an Aerodynamic Shroud for Cooling Fan Applications." M.S. dissertation, Michigan State University, East Lansing, MI, 1997

- [21] Morris, S.C., "The Velocity and Vorticity Fields of a Single Stream Shear Layer." Ph.D. dissertation, Michigan State University, East Lansing, MI, 2002
- [22] Ong, L. and Wallace, J.M., 1998, "Joint probability density analysis of the structure and dynamics of the vorticity field in a turbulent boundary layer." *J. Fluid Mech.* 367, 291-328.
- [23] Panton, Ronald L. Incompressible Flow. John Wiley & Sons, Canada, 1984.
- [24] Pope, Stephen NB. Turbulent Flows. Cambridge University Press, United Kingdom, 2000.
- [25] Potter, M. C. and Foss, J.F. Fluid Mechanics. Great Lakes Press, Michigan, 1982.
- [26] Saddoughi, S. and Veeravalli, S. 1994 "Local isotropy in turbulent boundary layers at high Reynold's number." *J. Fluid Mech.* **268**, 333-372.
- [27] Schetz, Joseph A. Boundary Layer Analysis. Prentice Hall, New Jersey, 1993.
- [28] Schlichting, H. Boundary Layer Theory. McGraw-Hill, New York, 1960.
- [29] Stull, Roland B. An Introduction to Boundary Layer Meteorology. Kluwer Academic Publishers, The Netherlands, 1988.
- [30] Surface Layer Turbulence and Environmental Test Facility home page. <http://www.mech.utah.edu/sltest/>
- [31] Tennekes, H and Lumley, J.L. A First Class in Turbulence. The MIT Press, 1972.
- [32] Wallace, J.M., and Foss, J.F., 1995. "The Measurement of Vorticity in Turbulent Flows." *Annual Review of Fluid Mechanics*, 27: 469-514.
- [33] Wygnanski, J.C., Fiedler, H.E., 1970, "The two-dimensional mixing region." *J. Fluid Mech.* 41, 327-361.





MICHIGAN STATE UNIVERSITY LIBRARIES



3 1293 02372 0414